A Note on Carborundum.

To the Editors of Electrical World:

SIRS:—During an investigation of the unsymmetrical passage of current through a contact of carborundum and other substances a curious phenomenon was noted. On applying a potential of 10 volts between two points on a crystal of carborundum, the crystal gave out a yellowish light. Only one or two specimens could be found which gave a bright glow on such a low voltage, but with 110 volts a large number could be found to glow. In some crystals only edges gave the light and others gave instead of a yellow light green, orange or blue. In all cases tested the glow appears to come from the negative pole, a bright blue-green spark appearing at the positive pole. In a single crystal, if contact is made near the center with the negative pole, and the positive pole is put in contact at any other place, only one section of the crystal will glow and that the same section wherever the positive pole is placed.

There seems to be some connection between the above effect and the e.m.f. produced by a junction of carborundum and another conductor when heated by a direct or alternating current; but the connection may be only secondary as an obvious explanation of the e.m.f. effect is the thermoelectric one. The writer would be glad of references to any published account of an investigation of this or any allied phenomena.

NEW YORK, N. Y. H. J. ROUND.

Fig. 1.1. Publication reporting on a "curious phenomenon", namely the first observation of electroluminescence from a SiC (carborundum) light-emitting diode. The article indicates that the first LED was a Schottky diode rather than a p-n-junction diode (after H. J. Round, *Electrical World* **49,** 309, 1907).

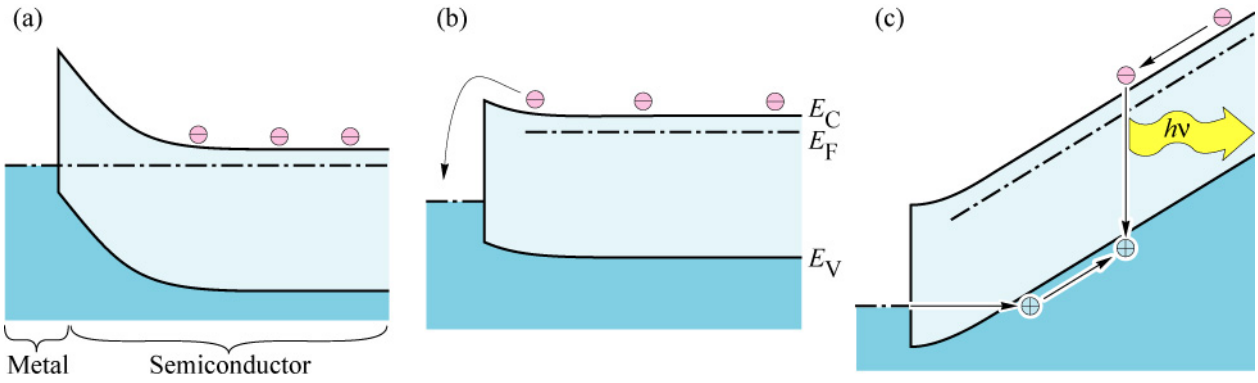

Fig. 1.2. Band diagram of a Schottky diode under (a) equilibrium conditions, (b) forward bias, and (c) strong forward bias. Under strong forward bias, minority carrier injection occurs making possible near-bandgap light emission.

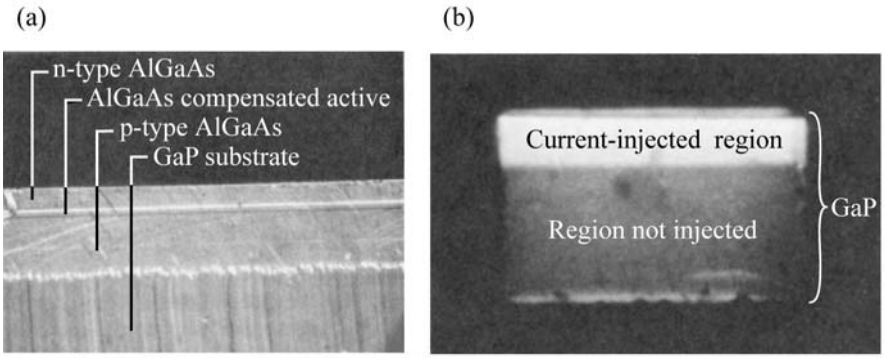

Fig. 1.3. (a) Cross section micrograph of AlGaAs LED grown on transparent GaP substrate. (b) Electroluminescence originating from current-injected region located under stripe-shaped contact viewed through transparent GaP substrate (after Woodall *et al.*, 1972).

Fig. 1.4. This classic 1964 mainframe computer IBM System 360 used high-voltage gas-discharge lamps to indicate the status of the arithmetic unit. In later models, the lamps were replaced by LEDs. The cabinet-sized 360 had a performance comparable to a current low-end laptop computer.

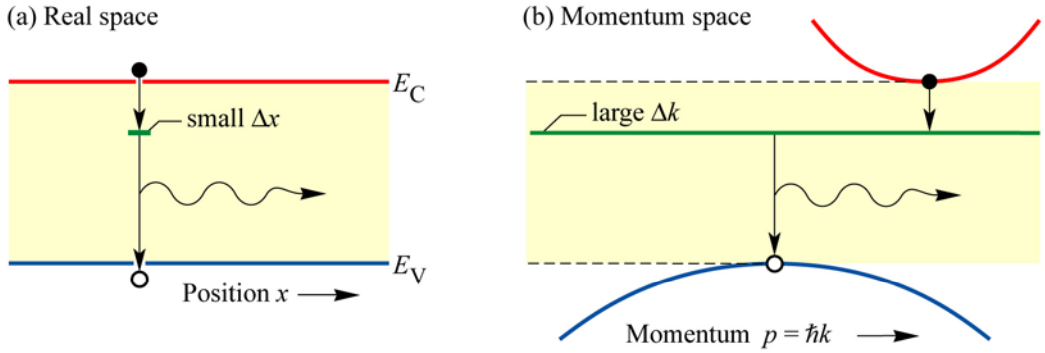

Fig. 1.5. (a) Real-space and (b) momentum-space optical transitions in GaP doped with an optically active impurity such as O or N, emitting in the red and green parts of the spectrum, respectively. GaP LEDs employ the *uncertainty principle* ($\Delta x\,\Delta p \geq h/2\pi$) which predicts that an electron wave function localized in real space is delocalized in momentum space, thereby making momentum-conserving (vertical) transitions possible.

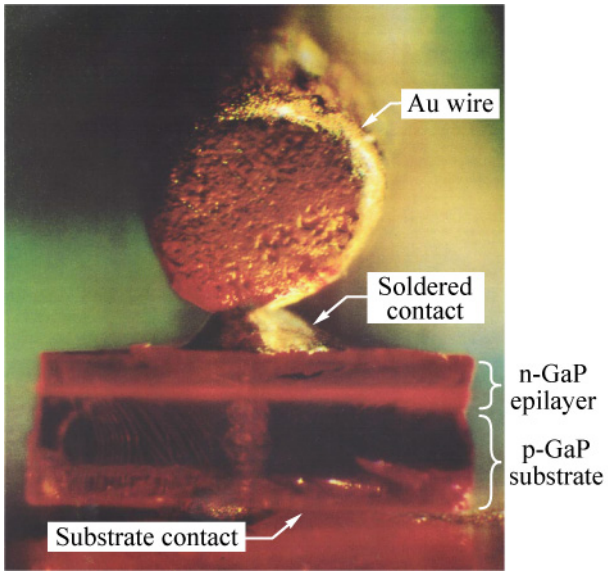

Fig. 1.6. GaP light-emitting di-ode grown by liquid-phase epi-taxy emitting "brilliant red light" from the Zn- and O-doped p-n junction region (courtesy of Pilkuhn, 2000).

Fig. 1.7. AT&T telephone set ("Trimline" model) with the dial pad illuminated by two green N-doped GaP LEDs. The illumina-ted dial pad was one of the first applications of green GaP:N LEDs.

Fig. 1.8. Pulsar calculator watch with LED display released in 1975 by Hamilton Corporation. The first Pulsar LED watch (without calculator) was offered in 1972. It was based on GaInP LEDs (after Seiko, 2004).

Fig. 1.9. Programmable pocket calculators Model SR-56 of the Texas Instruments Corporation and Model HP-67 of the Hewlett-Packard Corporation, both first manufactured in 1976. Seven-segment numeric characters composed of GaAsP LEDs were used in the display. The SR-56 came with a "huge" program memory of 100 steps. The HP-67 came with a magnetic card reader and had several freely programmable keys.

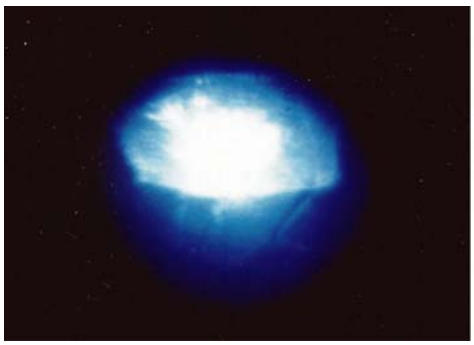

Fig. 1.10. Blue light emission found in 1972 caused by recombining electron-hole pairs created in a highly resistive GaN structure doped with Si and Mg (courtesy of Maruska, 2000)

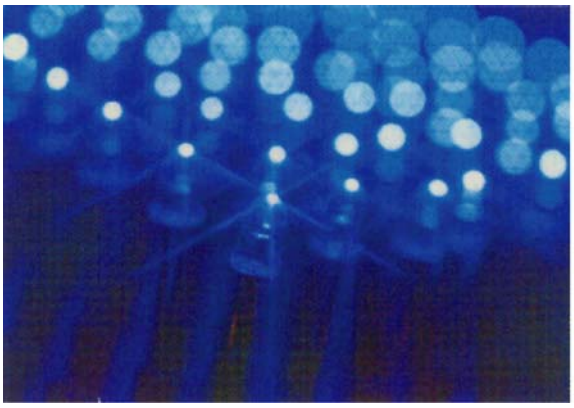

Fig. 1.11. Array of GaInN/GaN blue LEDs manufactured by the Nichia Corporation (after Nakamura and Fasol, 1997).

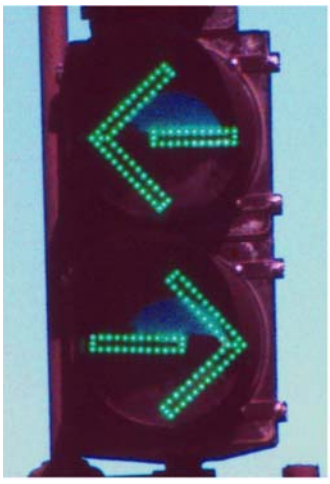

Fig. 1.12. Green traffic signals are one of the ubiquitous applications of GaInN/GaN green LEDs.

Fig. 1.13. Examples of red and amber AlGaInP/GaAs LEDs used in signage applications.

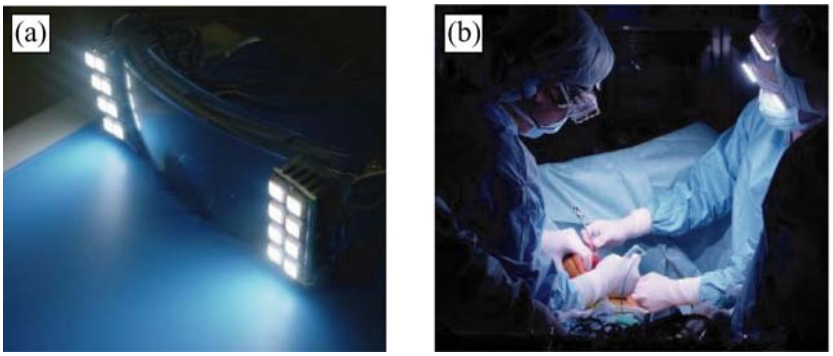

Fig. 1.14. (a) First goggle with integrated white LEDs used for (b) illumination during medical surgery (after Shimada *et al.*, 2001; Shimada *et al.*, 2003)

Fig. 1.15. First automotive daytime running lights based on LEDs.

Fig. 1.16. LED display consisting of 18 million LEDs covering front of building, located in New York City.

Fig. 1.17. Pedestrian sign indicating number of seconds left to cross street, located in Taipei, Taiwan.

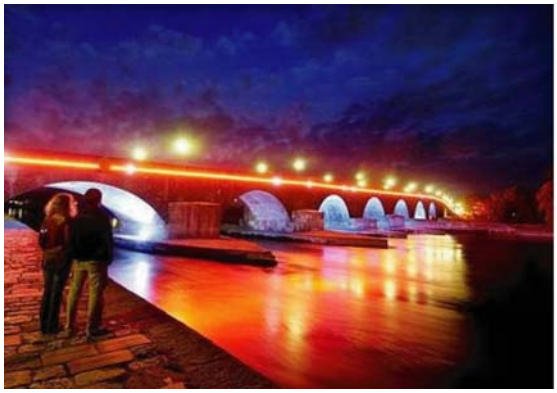

Fig. 1.18. Stone Bridge located in Regensburg, Germany, illuminated by LEDs.

Fig. 1.19. Artistic accent lighting at the main gate of the Science Based Industrial Park located in Hsin Chu, Taiwan (courtesy of K. R. Wang and L.-W. Tu, 2005).

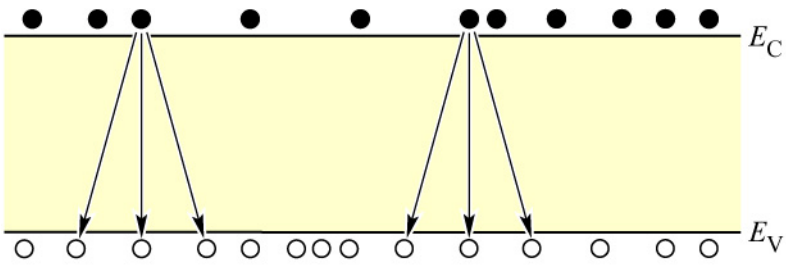

Fig. 2.1. Illustration of electron-hole recombination. The number of recombination events per unit time per unit volume is proportional to the product of electron and hole concentrations, *i. e.* $R \propto n\,p$.

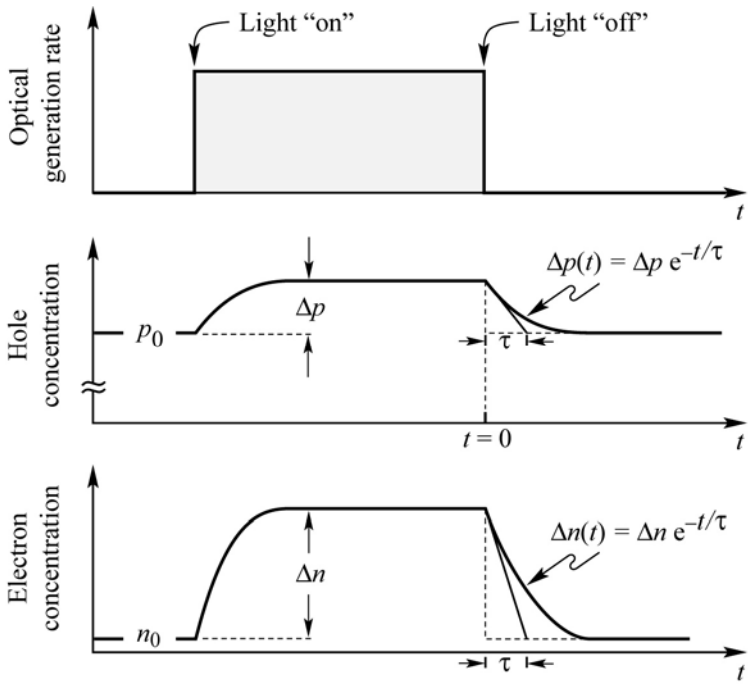

Fig. 2.2. Carrier concentration as a function of time before, during, and after an optical excitation pulse. The semiconductor is assumed to be p-type and thus it is $p_0 >> n_0$. Electrons and holes are generated in pairs, thus $\Delta p = \Delta n$. Under low-level excitation as shown here, it is $\Delta n << p_0$. In most practical cases the equilibrium minority carrier concentration is extremely small so that $n_0 << \Delta n$.

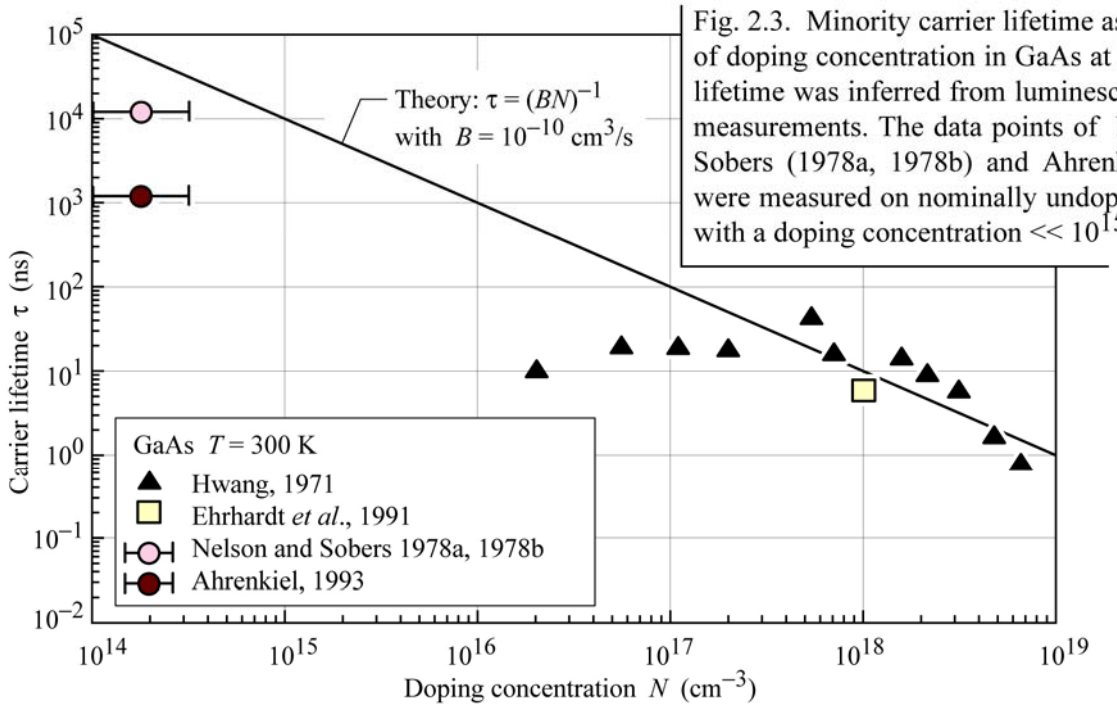

Fig. 2.3. Minority carrier lifetime as a function of doping concentration in GaAs at 300 K. The lifetime was inferred from luminescence decay measurements. The data points of Nelson and Sobers (1978a, 1978b) and Ahrenkiel (1993) were measured on nominally undoped material with a doping concentration $<< 10^{15}$ cm^{-3}.

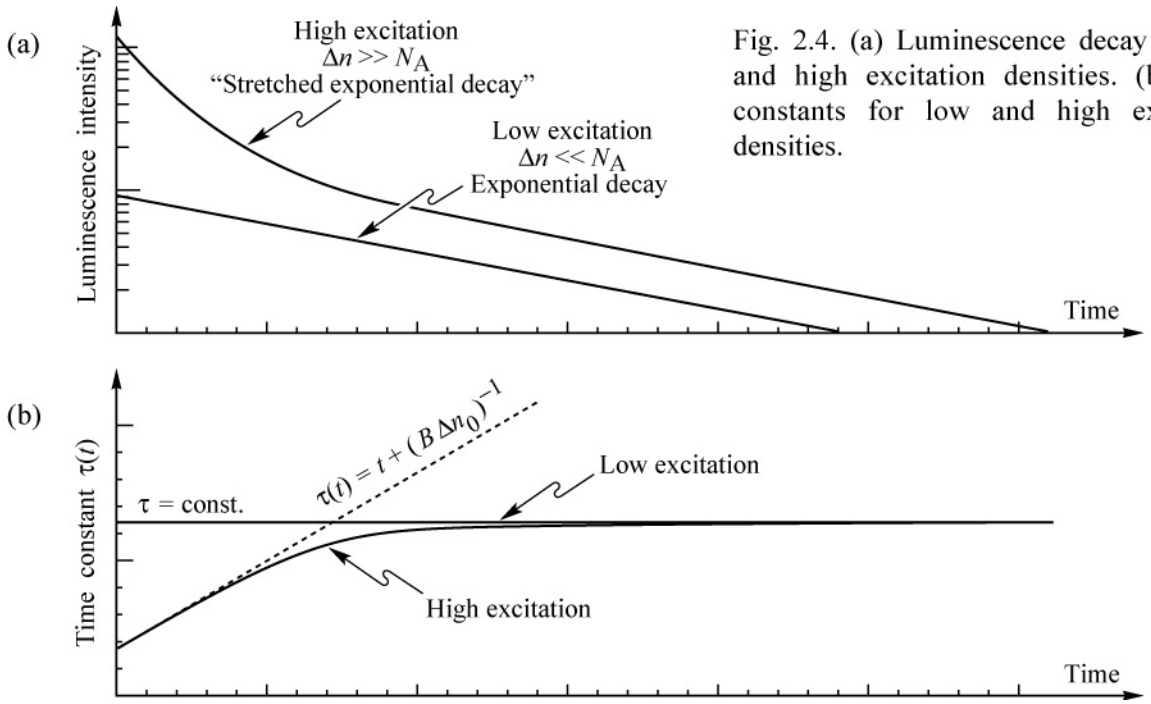

Fig. 2.4. (a) Luminescence decay for low and high excitation densities. (b) Time constants for low and high excitation densities.

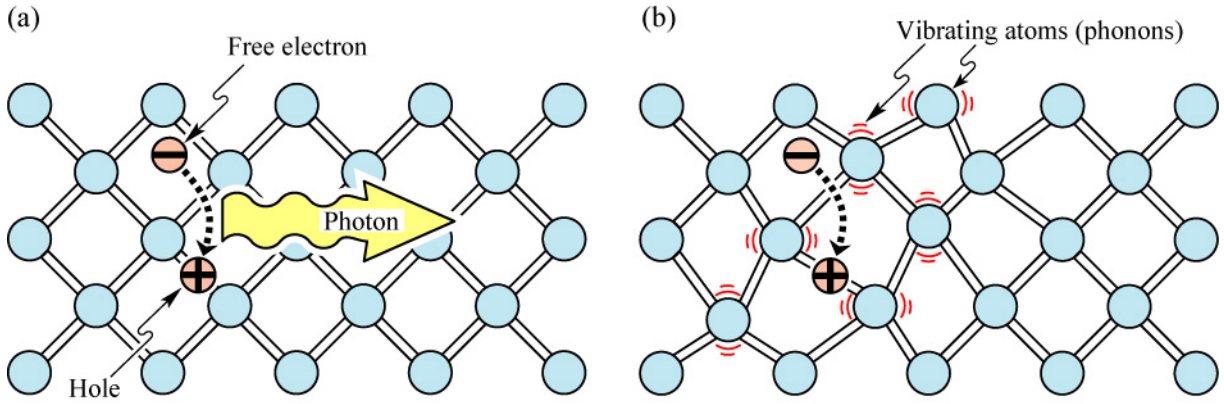

Fig. 2.5. (a) Radiative recombination of an electron-hole pair accompanied by the emission of a photon with energy $h\nu \approx E_g$. (b) In non-radiative recombination events, the energy released during the electron-hole recombination is converted to phonons (adopted from Shockley, 1950).

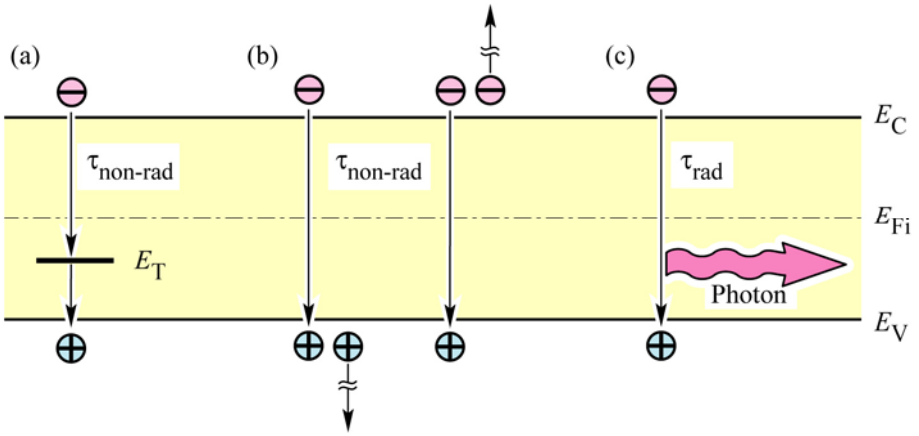

Fig. 2.6. Band diagram illustrating recombination: (a) non-radiative via deep level, (b) non-radiative via Auger process and (c) radiative.

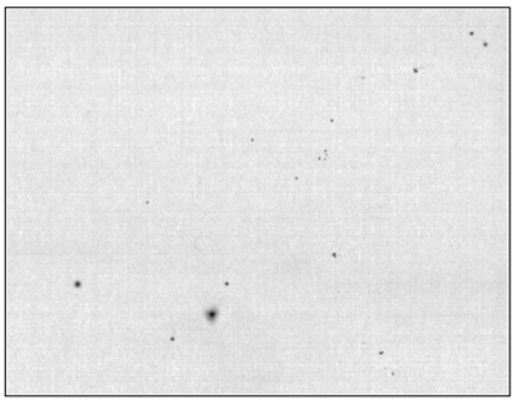

Fig. 2.7. Cathodoluminescence micrograph of a GaAs epitaxial layer. The dark spots are due to large clusters of non-radiative recombination centers (after Schubert, 1995).

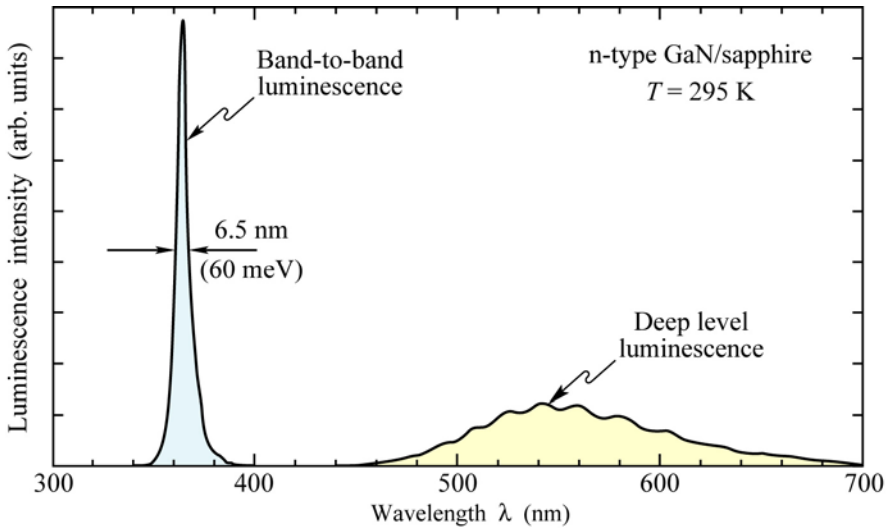

Fig. 2.8. Room-temperature photoluminescence spectrum of GaN with a band-to-band optical transition at 365 nm and a second transition at 550 nm identified as an optically active deep-level transition (after Grieshaber *et al*., 1996).

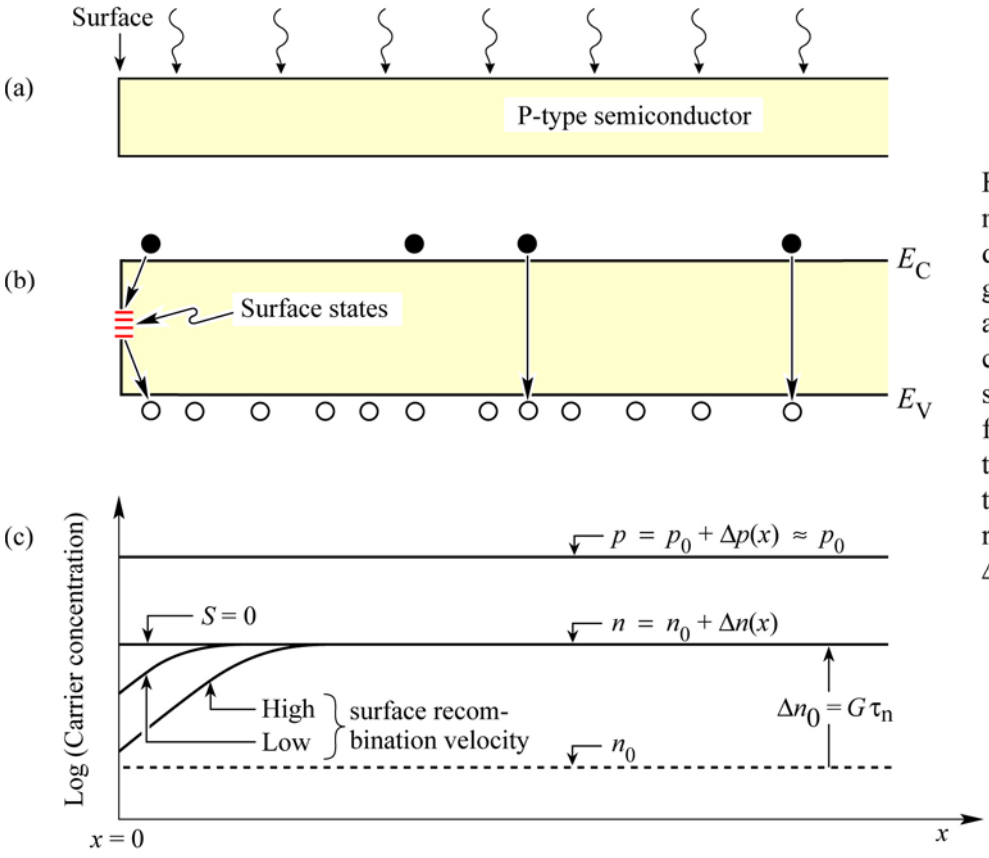

Fig. 2.9. (a) Illuminated p-type semiconductor, (b) band diagram, and (c) minority and majority carrier concentration near the surface assuming uniform carrier generation due to illumination. The excess carrier concentrations are Δn and Δp.

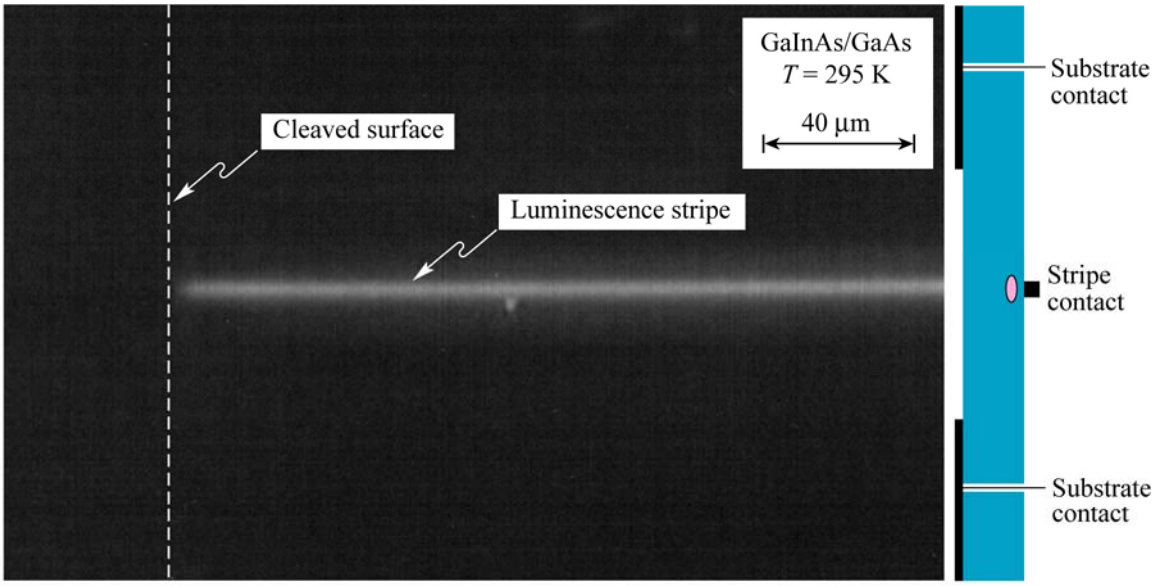

Fig. 2.10. (a) Micrograph and (b) schematic frontal view of a GaInAs/GaAs structure with a stripe-shaped top contact and contact window on substrate side under current injection conditions. The luminescence emanating from active region located below the stripe clearly decreases in the vicinity of the surface due to surface recombination.

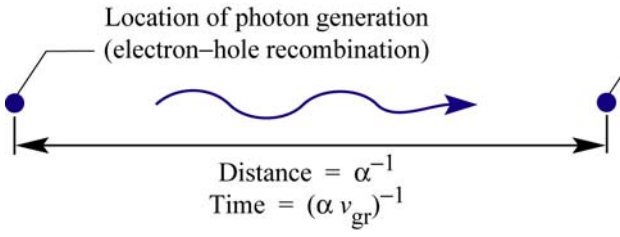

Fig. 3.1. Illustration of distance and elapsed time between a photon generation and absorption event.

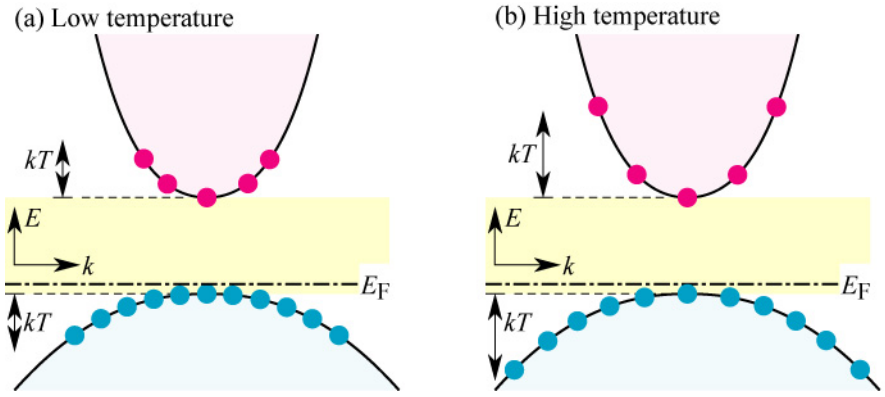

Fig. 3.2. Carrier distribution at (a) low and (b) high temperatures. Recombination probability decreases at high temperatures due to reduced number of carriers per dk interval.

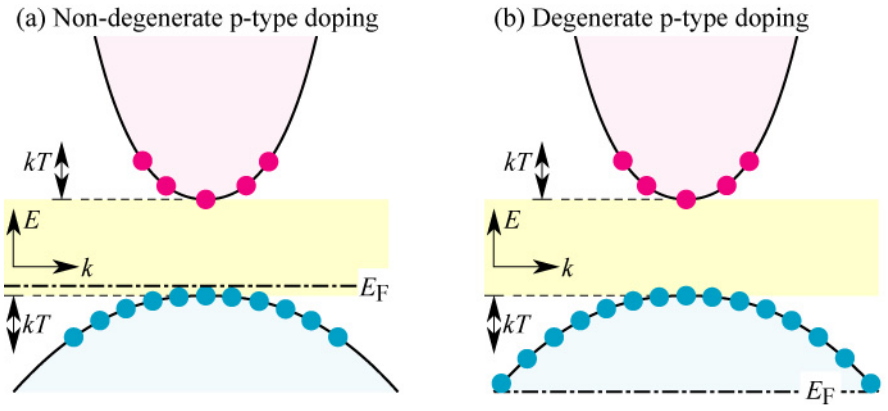

Fig. 3.3. Carrier distribution in (a) non-degenerately and (b) degenerately doped p-type semiconductor. Degenerate doping does not increase overlap between electrons and holes with equal momentum.

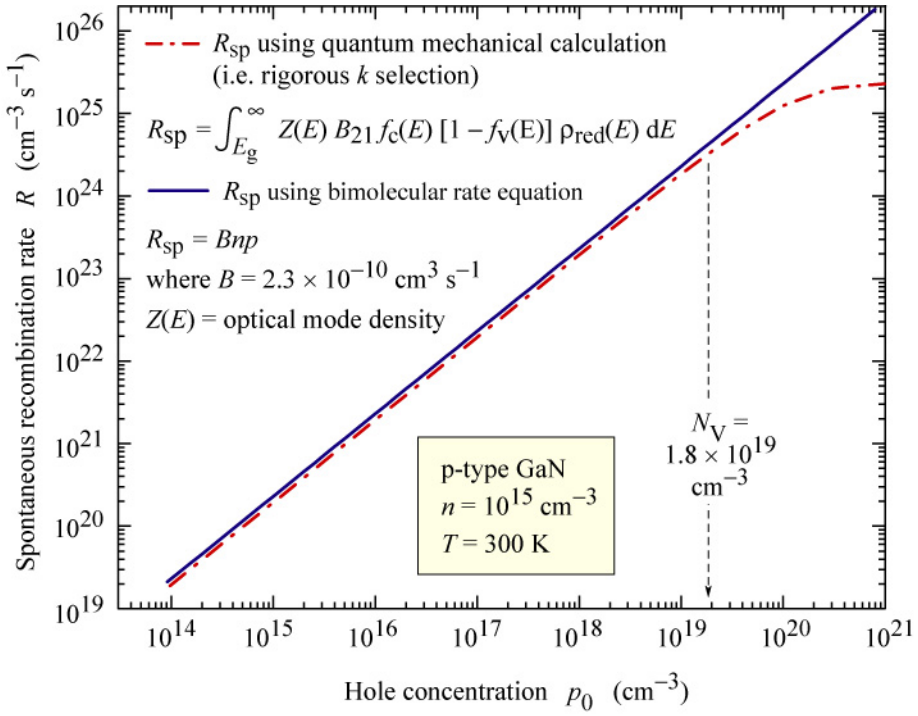

Fig. 3.4. Calculated spontaneous recombination rate in GaN at 300 K as a function of p-type doping concentration using a classical and quantum mechanical approach. The quantum mechanical approach (employing rigorous k selection) exhibits saturation in the degenerate doping regime (after Waldron, 2002).

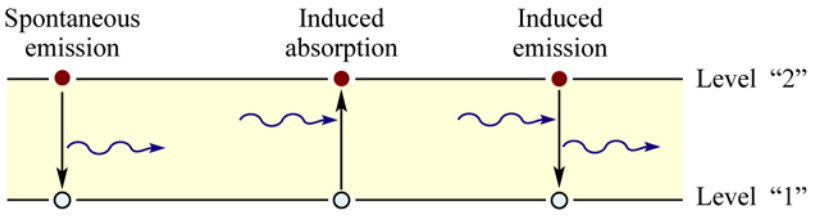

Fig. 3.5. Spontaneous emission, induced absorption, and induced emission events in the two-level atom model.

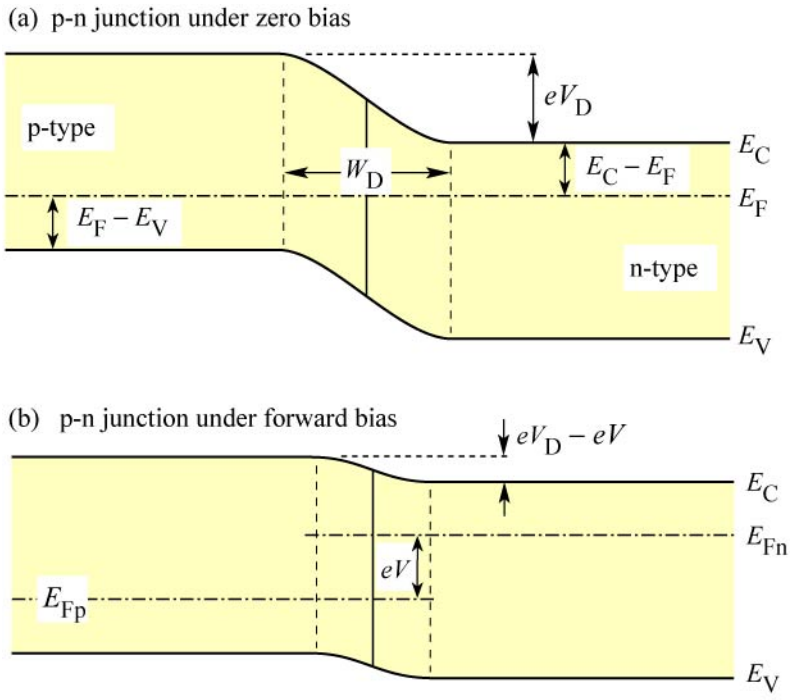

Fig. 4.1. P-n junction under (a) zero bias and (b) forward bias. Under forward bias conditions, minority carriers diffuse into the neutral regions where they recombine.

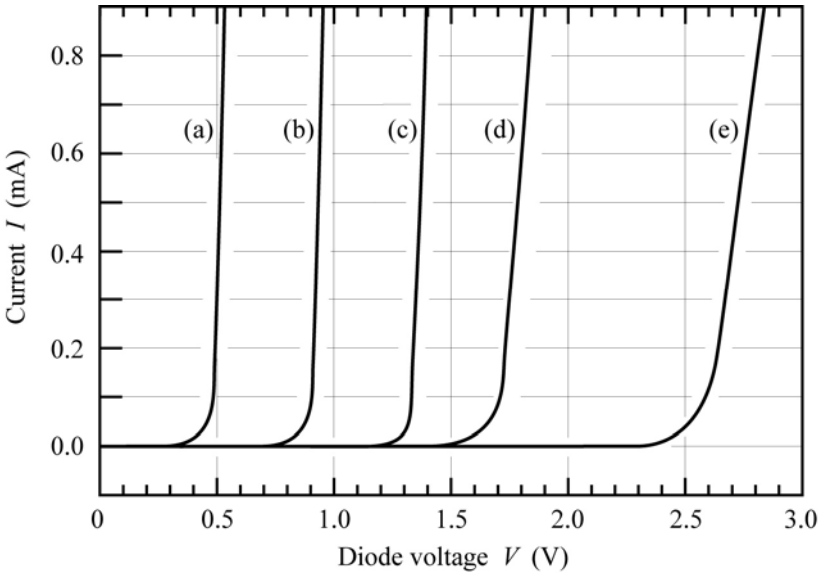

$T = 295$ K

(a)	Ge	$E_g \approx 0.7$ eV
(b)	Si	$E_g \approx 1.1$ eV
(c)	GaAs	$E_g \approx 1.4$ eV
(d)	GaAsP	$E_g \approx 2.0$ eV
(e)	GaInN	$E_g \approx 2.9$ eV

Fig. 4.2. Room-temperature current–voltage characteristics of p-n junctions made from different semiconductors.

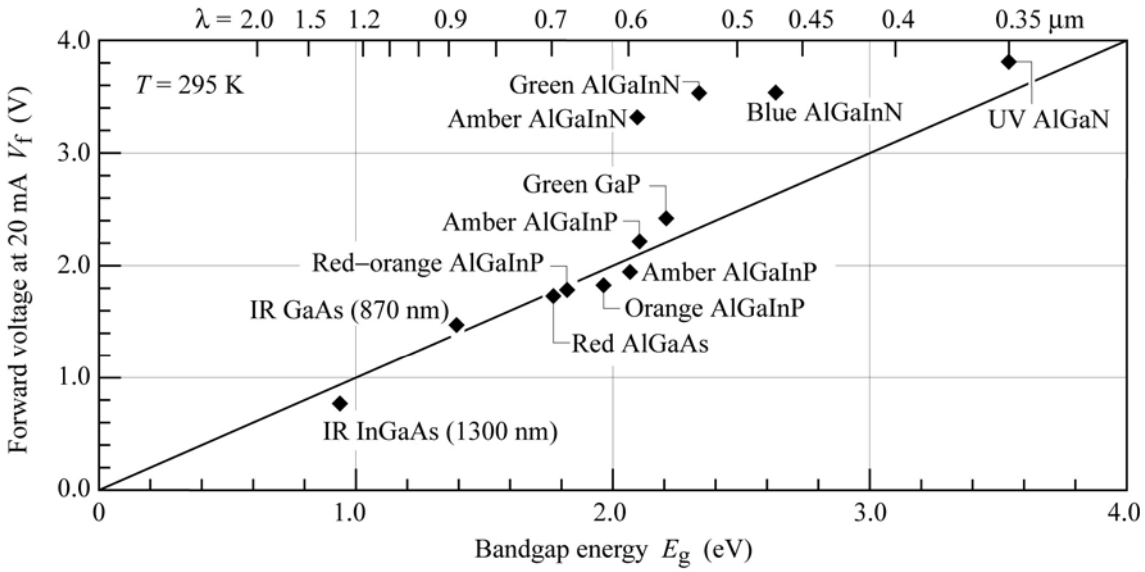

Fig. 4.3. iode forward voltage versus bandgap energy for LEDs made from different materials (after Krames *et al.*, 2000; updated with UV LED data of Emerson *et al.*, 2002).

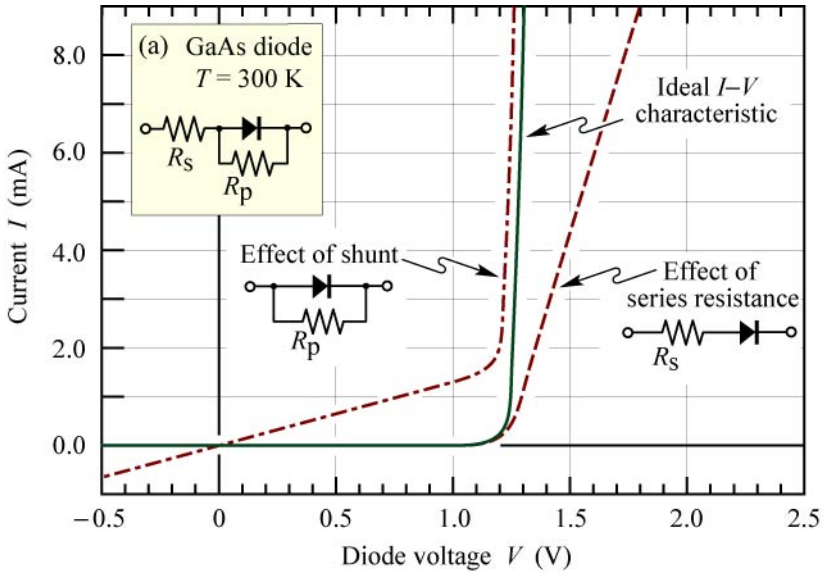

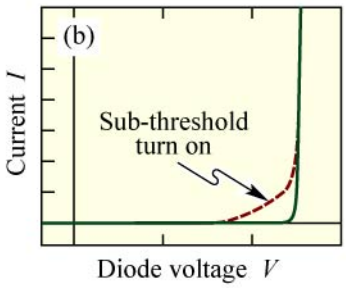

Fig. 4.4. (a) Effect of series and parallel resistance (shunt) on *I–V* characteristic. (b) *I–V* with with clearly discernable sub-threshold turn-on caused by defects or surface states.

Fig. 4.5 (a)

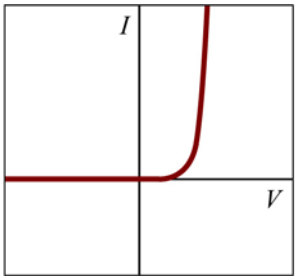

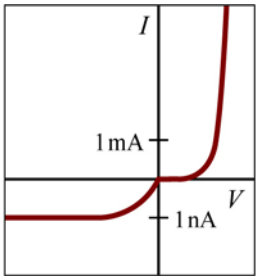

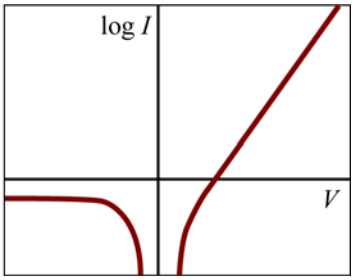

Fig. 4.5 (b)

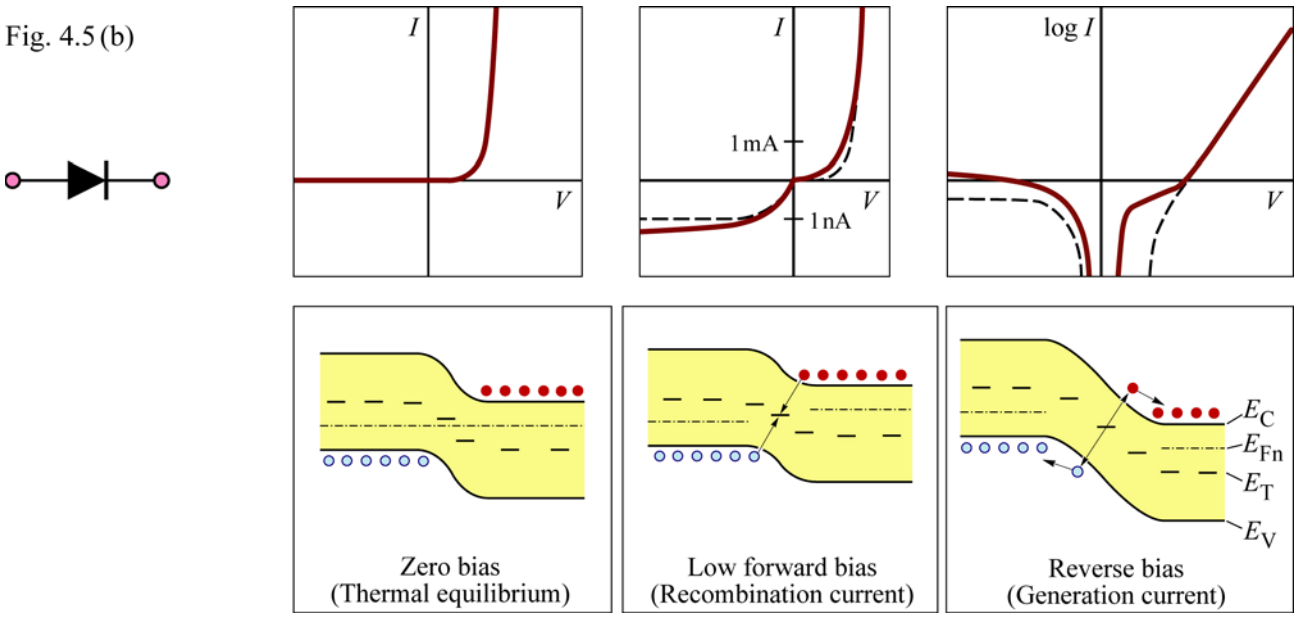

Fig. 4.5 (c)

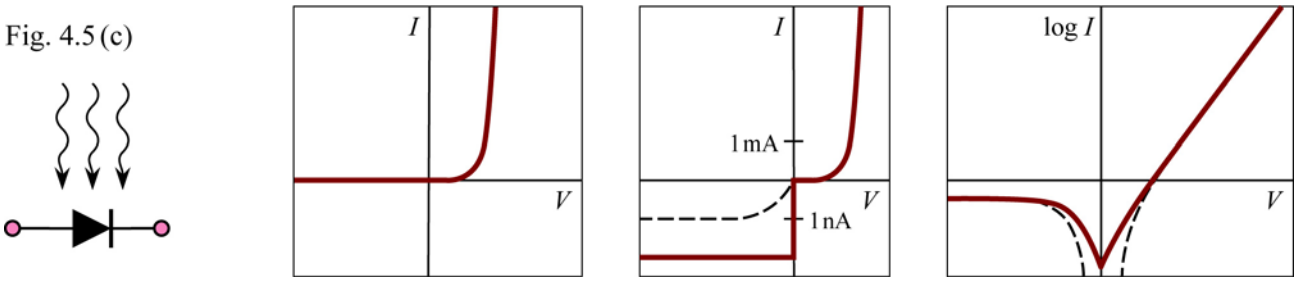

Fig. 4.5 (d)

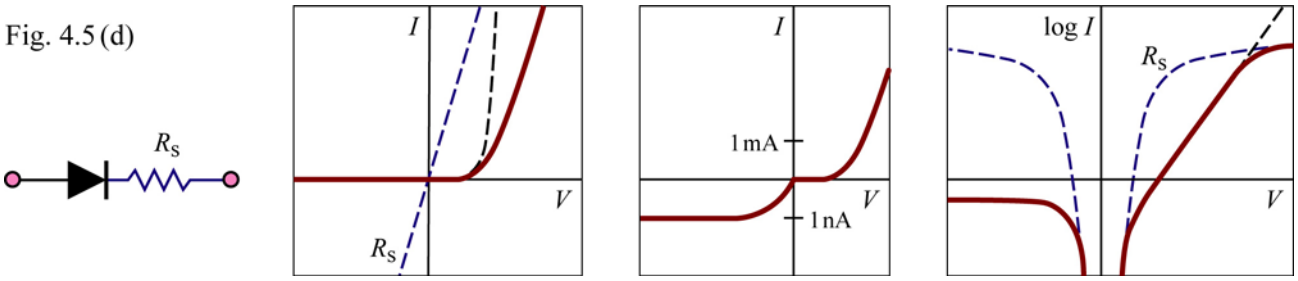

Fig. 4.5 (e)

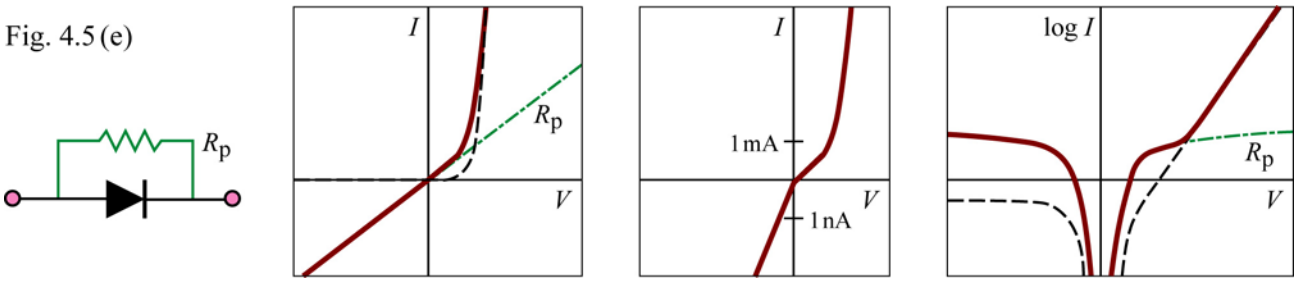

Fig. 4.5 (f)

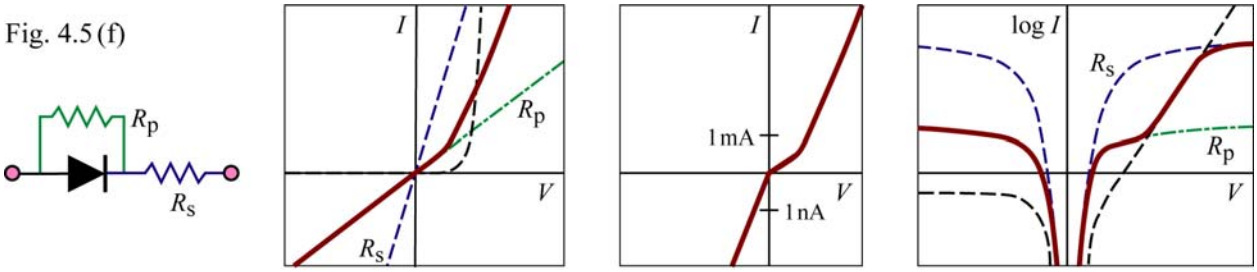

Fig. 4.5 (g)

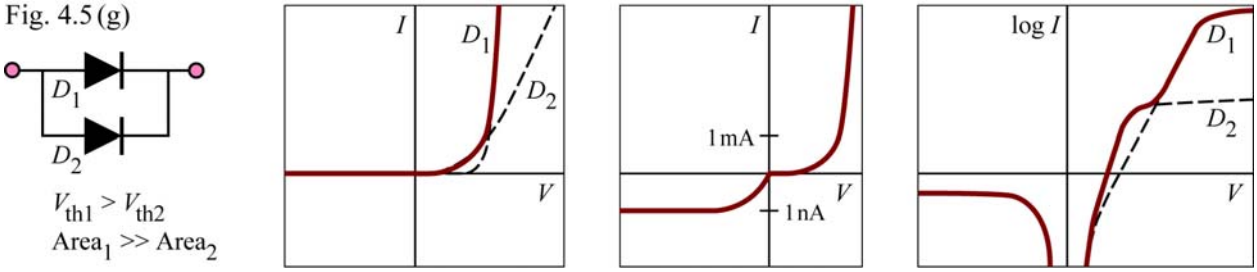

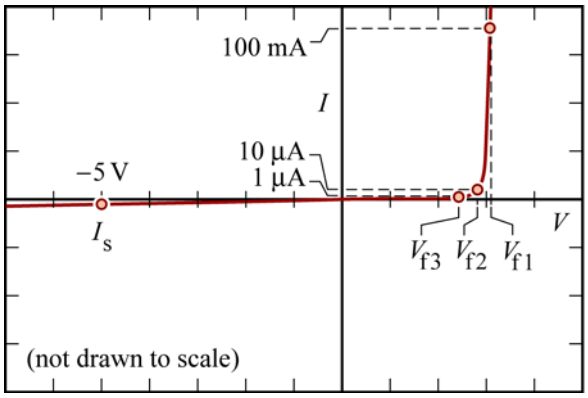

Fig. 4.6. Critical points of diode I–V characteristic, namely 'forward voltage one', V_{f1}, (measured at operating current, e.g. 100 mA), 'forward voltage two', V_{f2}, (measured at low current, e.g. 10 µA), 'forward voltage three', V_{f3}, (measured at very low current, e.g. 1 µA), and reverse saturation current (measured at e.g. – 5.0 V).

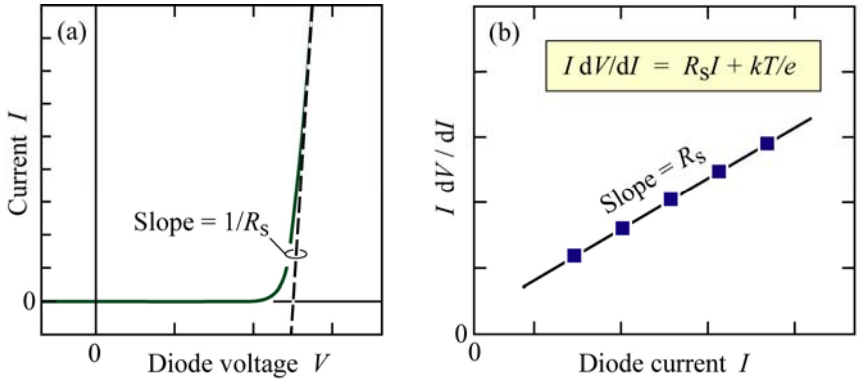

Fig. 4.7. Methods for evaluating diode series resistance. (a) Tangent for $V > V_{th}$ provides R_s. (b) Equation shown as inset is valid for forward bias ($V >> kT/e$).

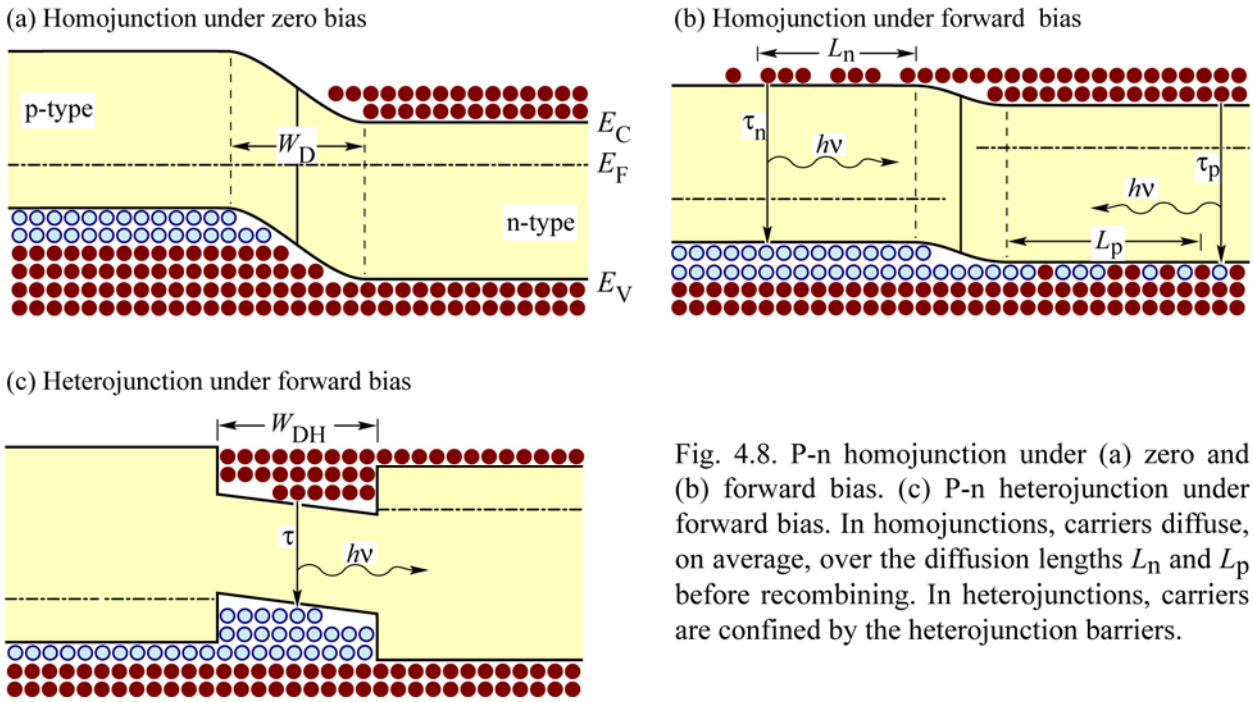

Fig. 4.8. P-n homojunction under (a) zero and (b) forward bias. (c) P-n heterojunction under forward bias. In homojunctions, carriers diffuse, on average, over the diffusion lengths L_n and L_p before recombining. In heterojunctions, carriers are confined by the heterojunction barriers.

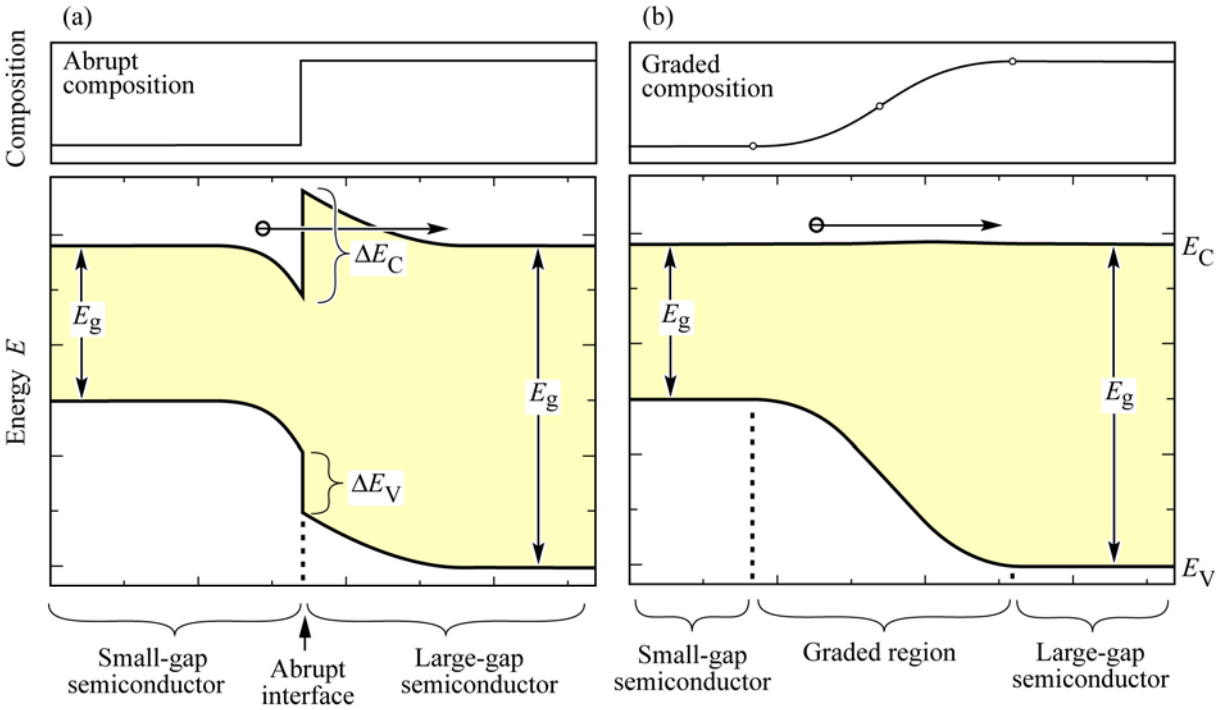

Fig. 4.9. Band diagram of (a) an abrupt n-type–n-type heterojunction and (b) a graded heterojunction of two semiconductors with different bandgap energy. The abrupt junction is more resistive than the graded junction due to the electron barrier forming at the abrupt junctions (after Schubert *et al*., 1992).

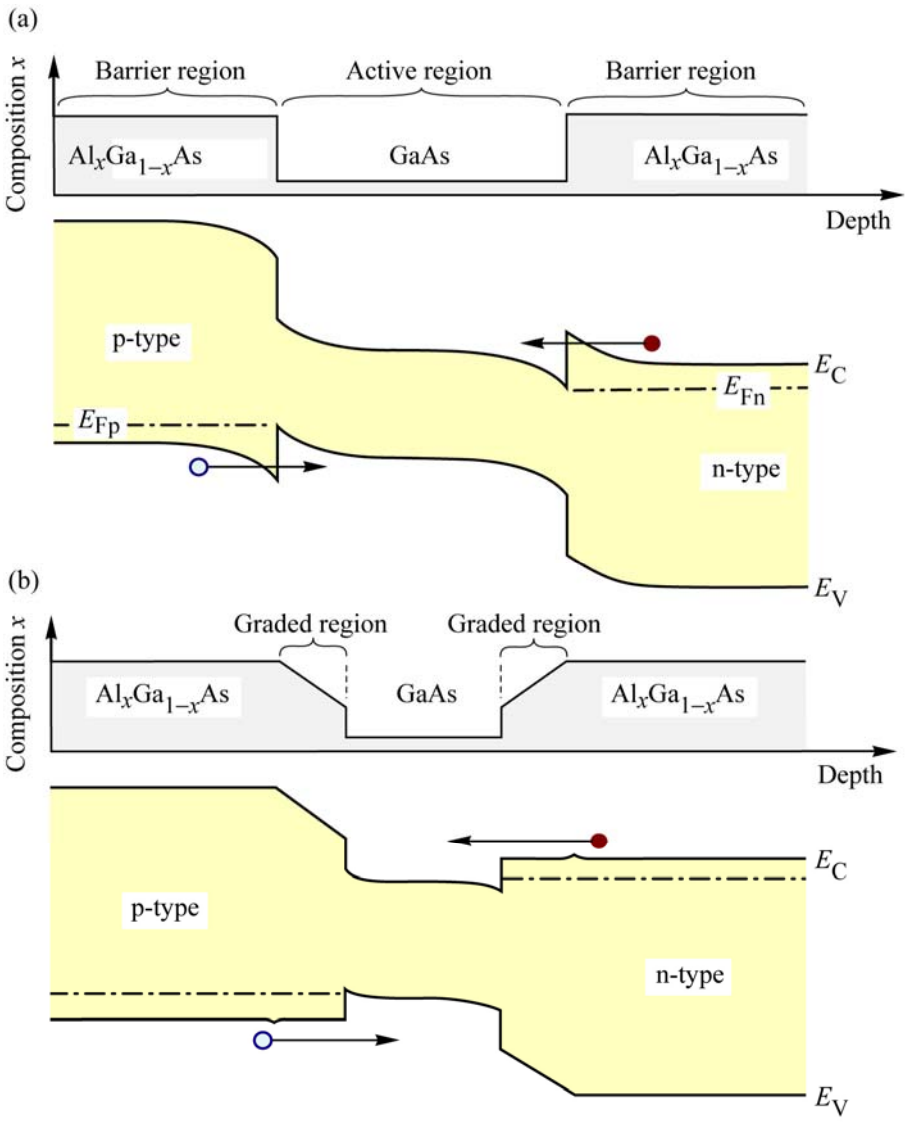

Fig. 4.10. Band diagram of (a) an abrupt double heterostructure and (b) a graded double heterostructure. The barrier–well interface of the abrupt junction is more resistive than the graded junction due to barriers forming at the interfaces.

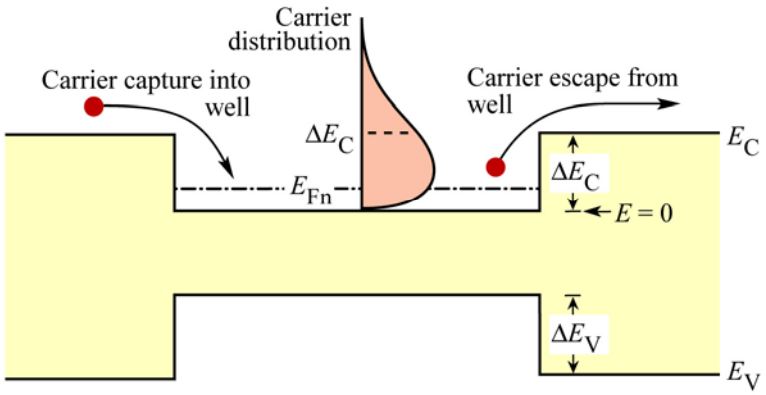

Fig. 4.11. Carrier capture and escape in a double heterostructure. Also shown is the carrier distribution in the active layer.

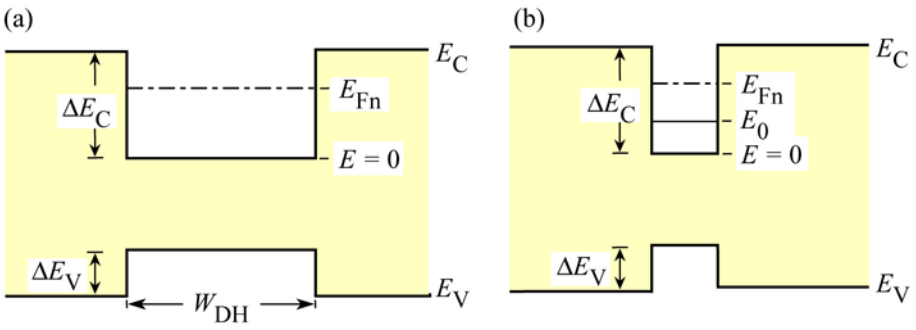

Fig. 4.12. Fermi level (E_{Fn}) and subband level (E_0) in (a) a double heterostructure and (b) a quantum well structure.

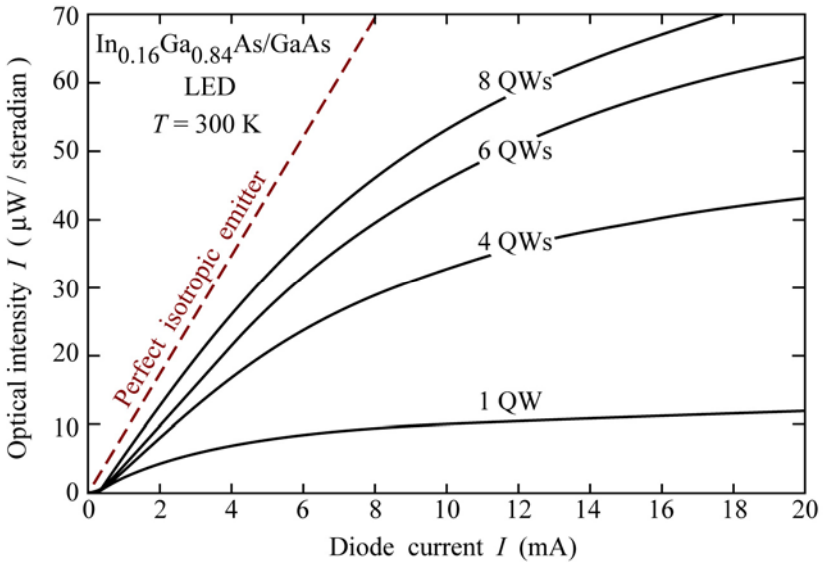

Fig. 4.13. Optical intensity emitted by $In_{0.16}Ga_{0.84}As/GaAs$ LEDs with active regions consisting of one, four, six, and eight quantum wells and theoretical intensity of a perfect isotropic emitter (dashed line) (after Hunt *et al.*, 1992).

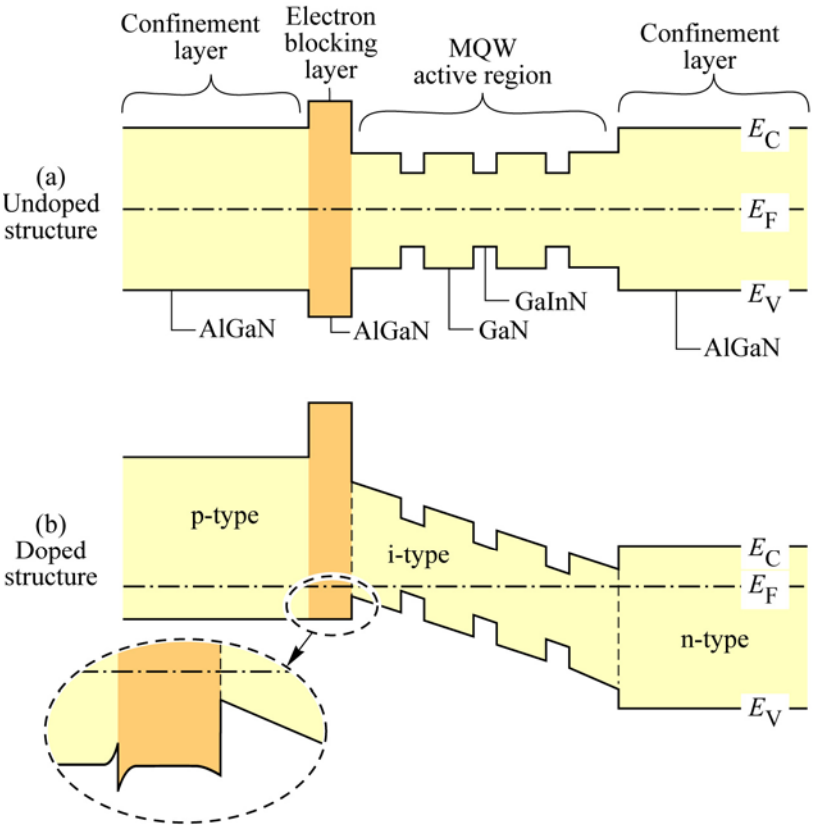

Fig. 4.14. AlGaN current-blocking layer in an AlGaN/GaN/GaInN multi quantum well structure. (a) Band diagram without doping. (b) Band diagram with doping. The Al content in the electron-blocking layer is higher than in the p-type confinement layer.

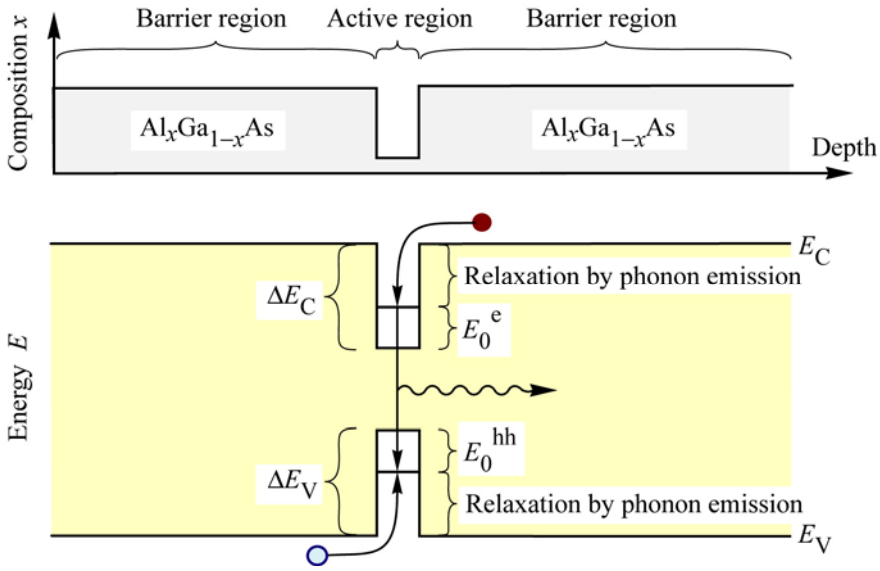

Fig. 4.15. (a) Chemical composition and (b) band diagram of a quantum well structure, illustrating the energy loss of carriers as they are captured into the quantum well.

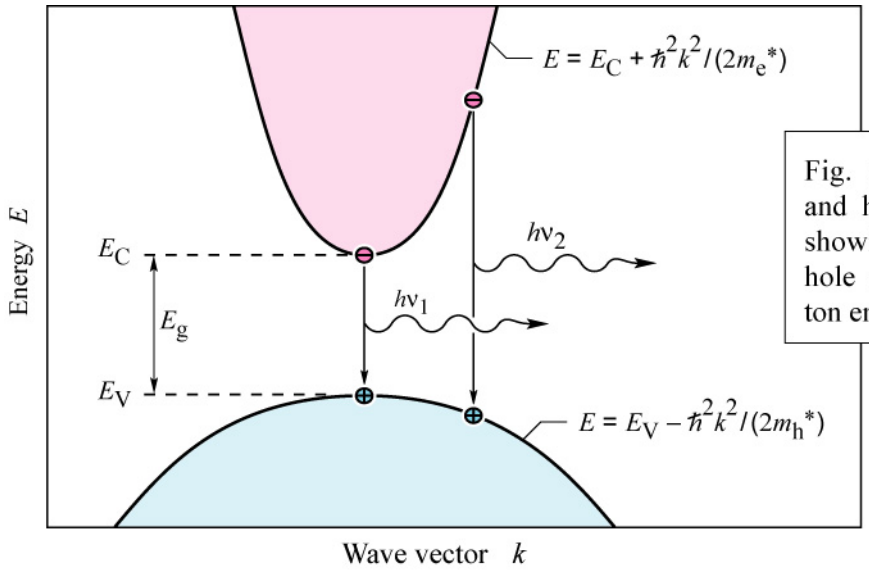

Fig. 5.1. Parabolic electron and hole dispersion relations showing "vertical" electron-hole recombination and photon emission.

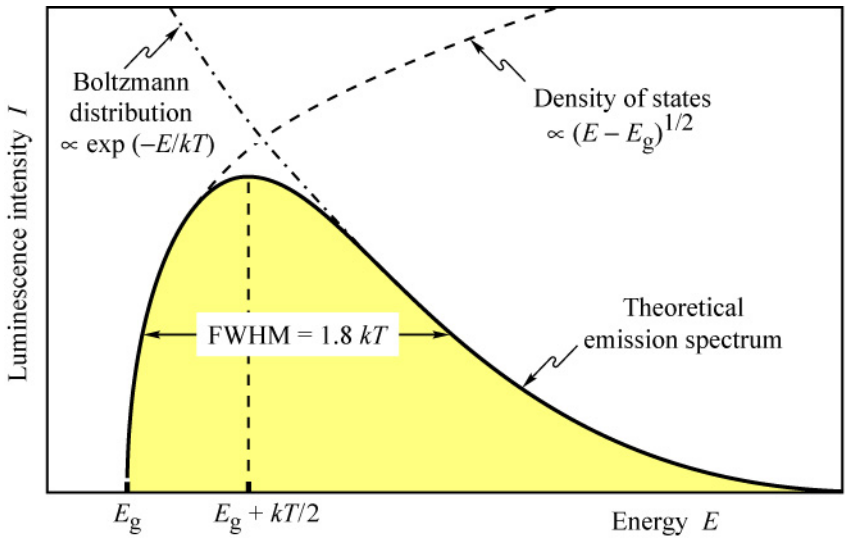

Fig. 5.2. Theoretical emission spectrum of an LED. The full width at half maximum (FWHM) of the emission line is 1.8 kT.

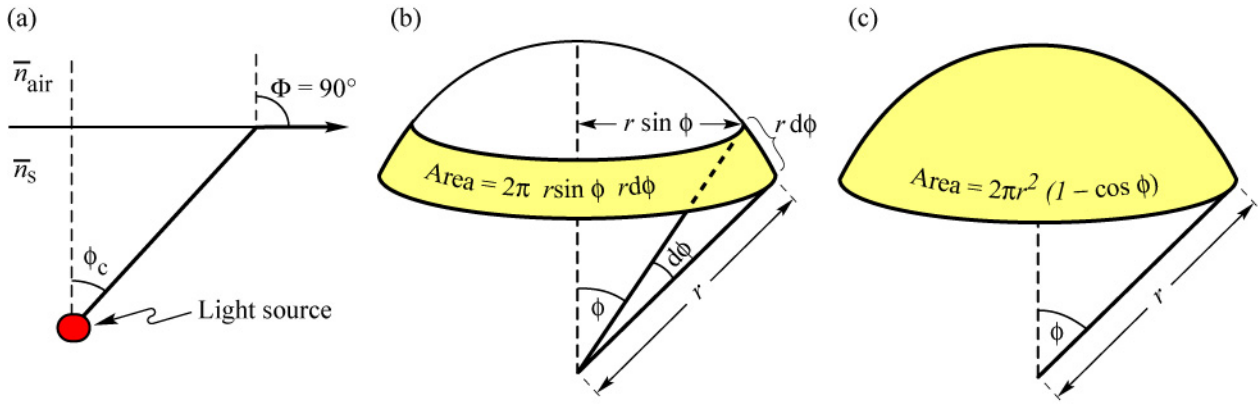

Fig. 5.3. (a) Definition of the escape cone by the critical angle ϕ_c. (b) Area element dA. (c) Area of calotte-shaped section of the sphere defined by radius r and angle ϕ_c.

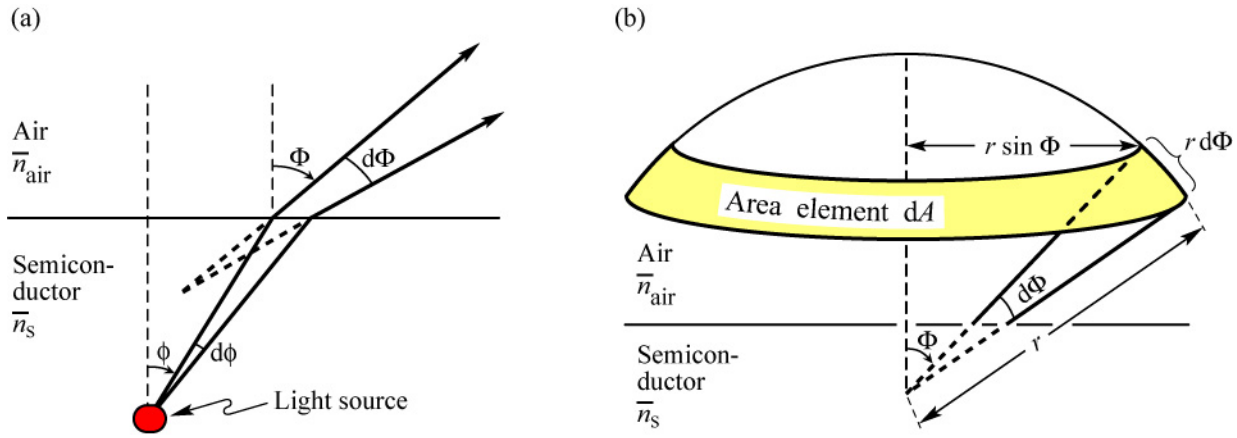

Fig. 5.4. Geometrical model used to derive the Lambertian emission pattern. (a) The light emitted into angle dϕ inside the semiconductor is emitted into the angle dΦ in air. (b)Illustration of the area element dA of the calotte-shaped section of the sphere.

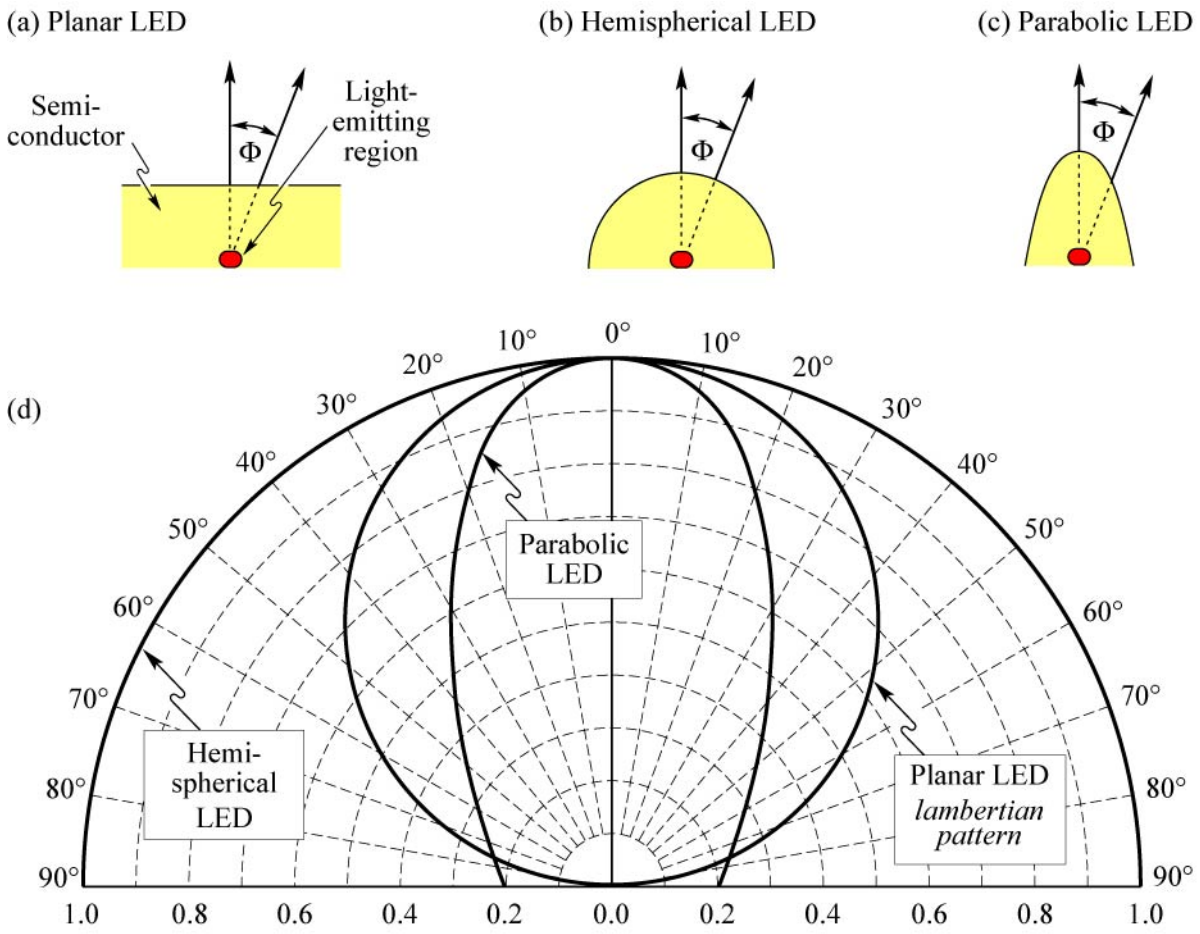

Fig. 5.5. Light-emitting diodes with (a) planar, (b) hemispherical, and (c) parabolic surfaces. (d) Far-field patterns of the different types of LEDs. At an angle of $\Phi = 60°$, the lambertian emission pattern decreases to 50 % of its maximum value occurring at $\Phi = 0°$. The three emission patterns are normalized to unity intensity at $\Phi = 0°$.

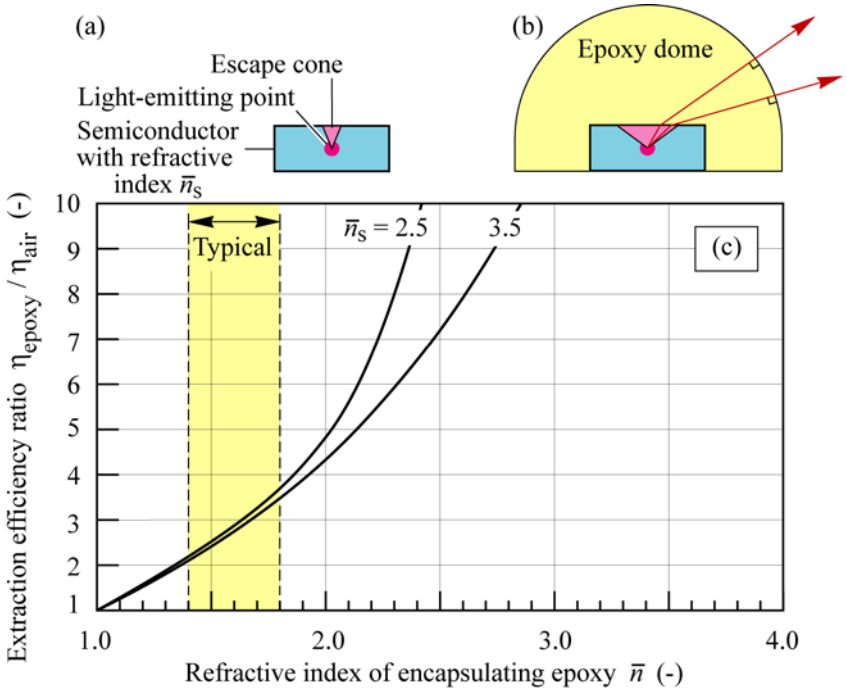

Fig. 5.6. (a) LED without and (b) with dome-shaped epoxy encapsulant. A larger escape angle is obtained for the LED with an epoxy dome. (c) Calculated ratio of light extraction efficiency emitted through the top surface of a planar LED with and without an epoxy dome. The refractive indices of typical epoxies range between 1.4 and 1.8 (adopted from Nuese *et al.*, 1969).

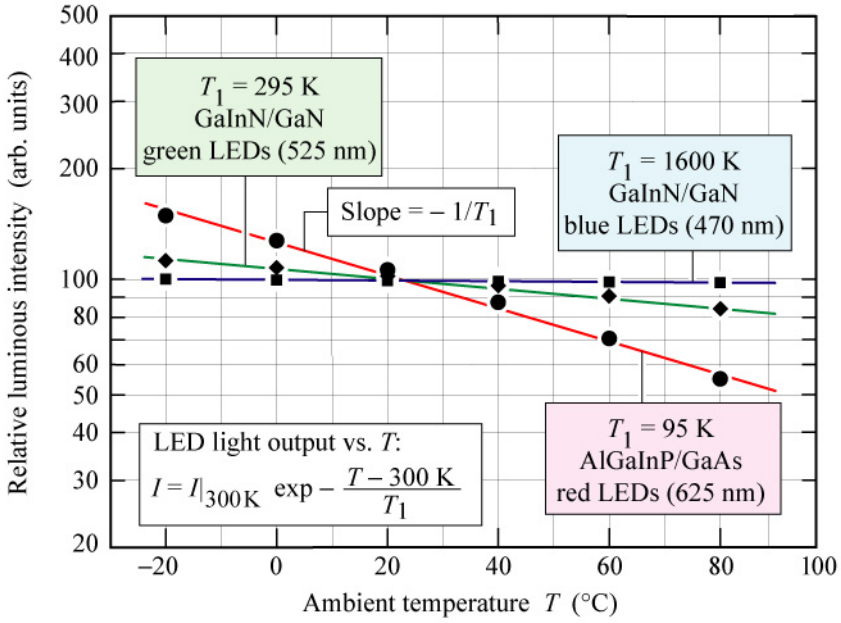

Fig. 5.7. Characteristic temperature T_1 of GaInN/GaN blue, GaInN/GaN green, and AlGaInP/GaAs red LEDs near room temperature (after data from Toyoda Gosei Corp., 2000). More recent data (Toyoda Gosei Corp., 2004) shows the following values for T_1: Blue GaInN LED, 460 nm, T_1 = 1600 K; Cyan GaInN LED, 505 nm, T_1 = 832 K; Green GaInN LED, 525 nm, T_1 = 341 K; Red AlGaInP LED, 625 nm, T_1 = 199 K.

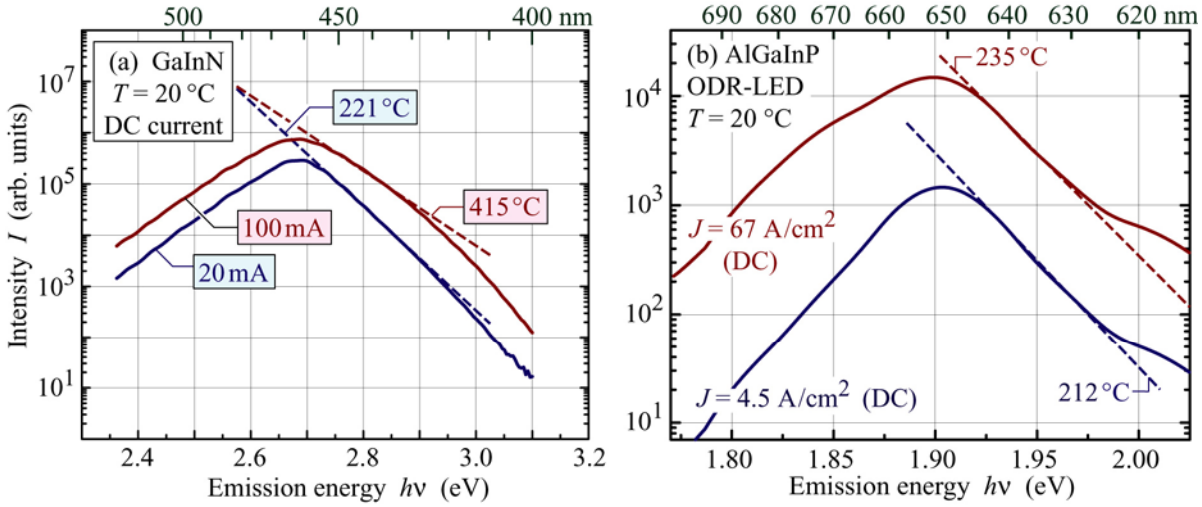

Fig. 6.1. Carrier temperatures in (a) GaInN blue and (b) AlGaInP red LEDs inferred from the high-energy slope of emission spectrum. Due to the alloy-broadening effect, the measured carrier temperatures overestimate the true carrier temperature (after Chhajed *et al.*, 2005; Gessmann *et al.*, 2003).

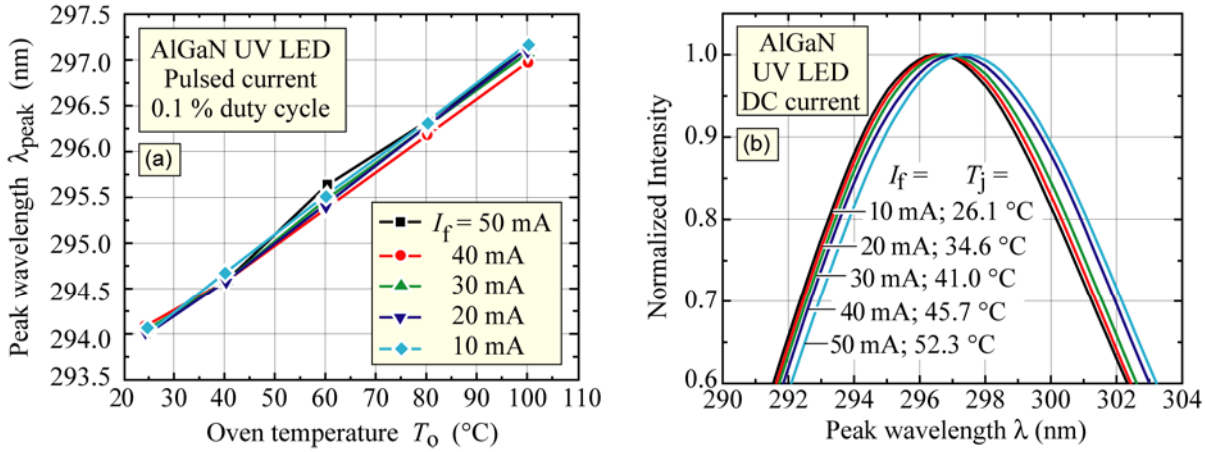

Fig. 6.2. (a) Peak emssion wavelength versus oven temperatureof an AlGaN UV LED for pulsed current injection with 0.1 % duty cycle. (b) Emssion spectra and junction temperatures for different DC currents (after Xi *et al*., 2005).

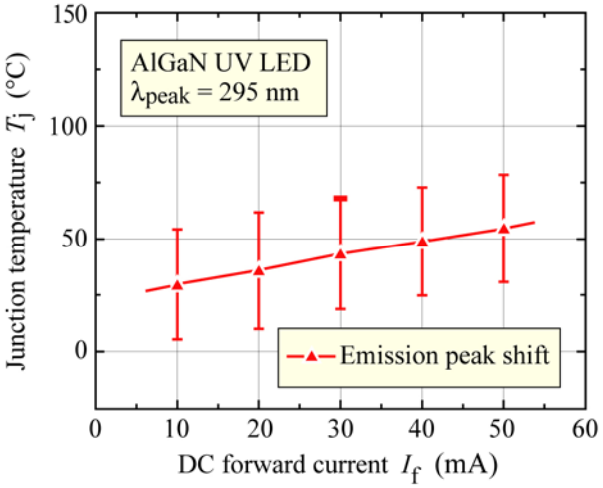

Fig. 6.3. Junction temperature inferred from emission peak energy as a function of DC injection current for a 300 µm × 300 µm deep UV LED emitting at 295 nm. The error bar stems from an uncertainty in the peak energy (after Xi *et al*., 2005).

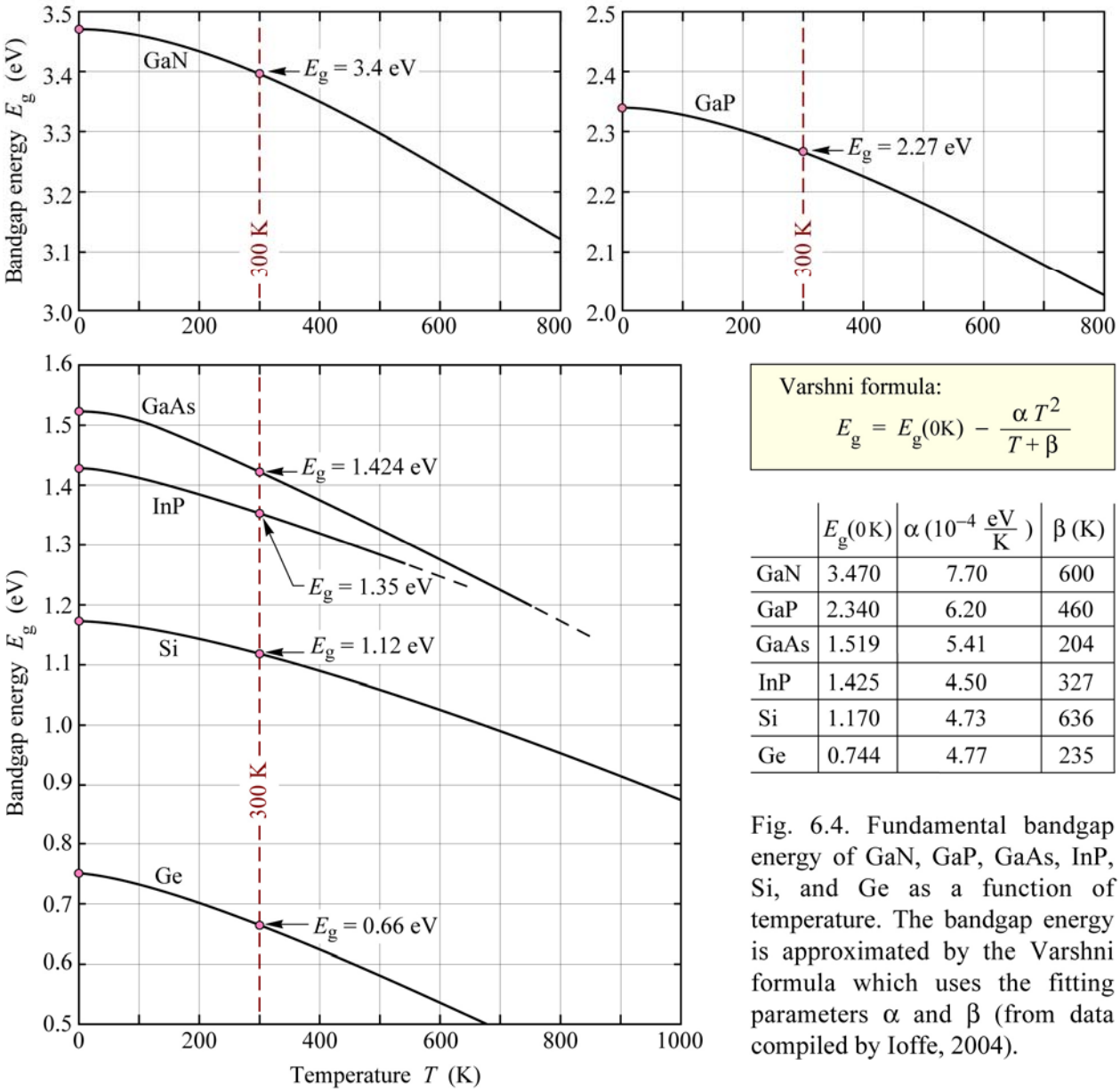

Varshni formula:

$$E_g = E_g(0\text{K}) - \frac{\alpha T^2}{T + \beta}$$

	E_g(0 K)	α (10^{-4} eV/K)	β (K)
GaN	3.470	7.70	600
GaP	2.340	6.20	460
GaAs	1.519	5.41	204
InP	1.425	4.50	327
Si	1.170	4.73	636
Ge	0.744	4.77	235

Fig. 6.4. Fundamental bandgap energy of GaN, GaP, GaAs, InP, Si, and Ge as a function of temperature. The bandgap energy is approximated by the Varshni formula which uses the fitting parameters α and β (from data compiled by Ioffe, 2004).

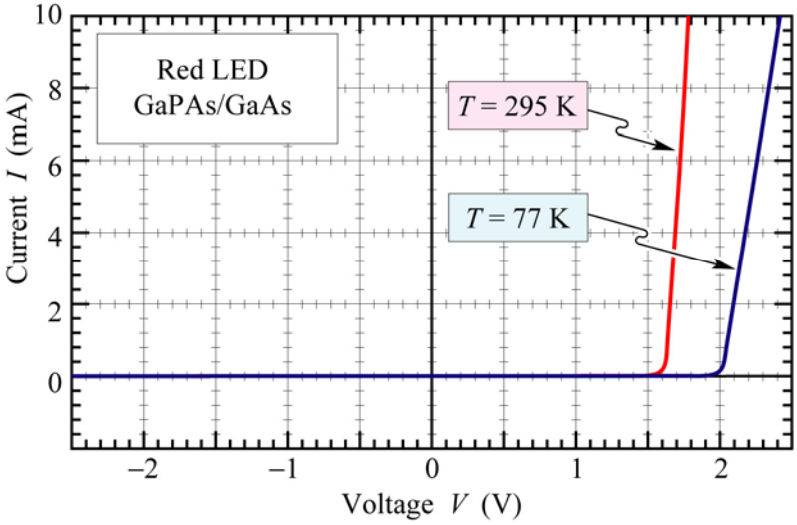

Fig. 6.5. Current–voltage characteristic of GaAsP/GaAs LED emitting in the red part of the visible spectrum, measured at 77 and 295 K. The threshold voltages are 2.0 and 1.6 V, at 77 and 300 K, respectively.

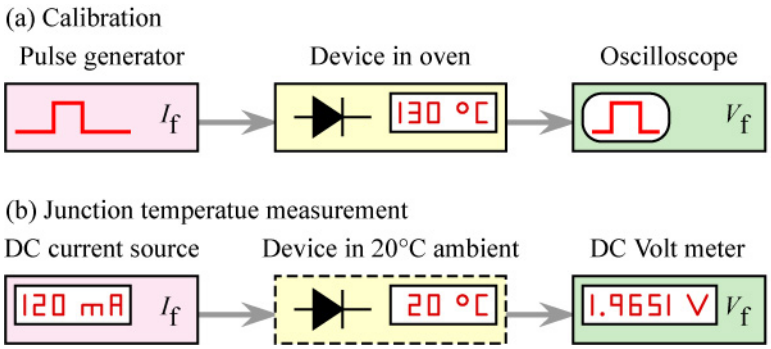

Fig. 6.6. (a) Pulsed calibration procedure establishing the forward voltage versus junction temperature (V_f vs. T_j) relation and (b) determination of junction temperature for different DC forward currents.

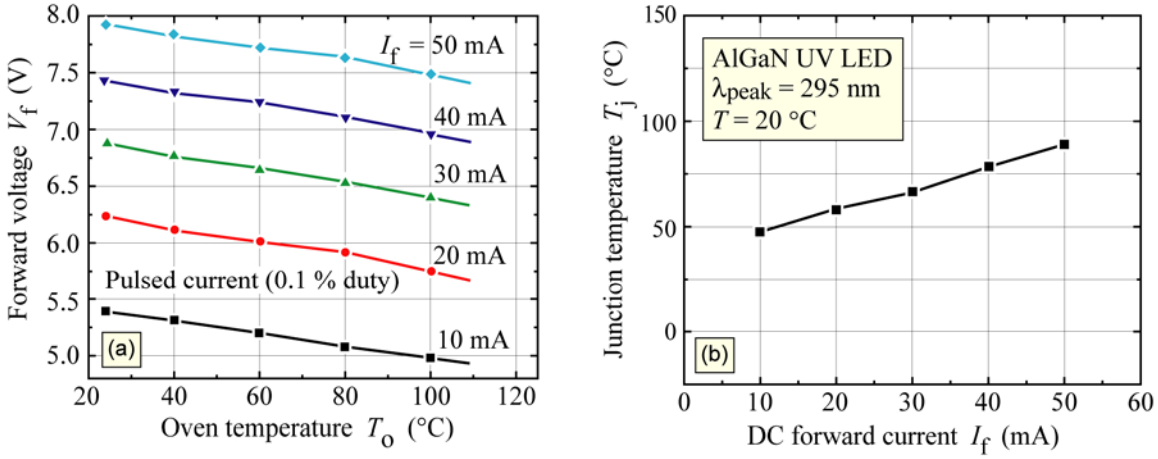

Fig. 6.7. (a) Pulsed calibration measurement (duty cycle 0.1 %) and (b) junction temperature (T_j) versus DC current of an AlGaN UV LED (after Xi *et al.*, 2005)

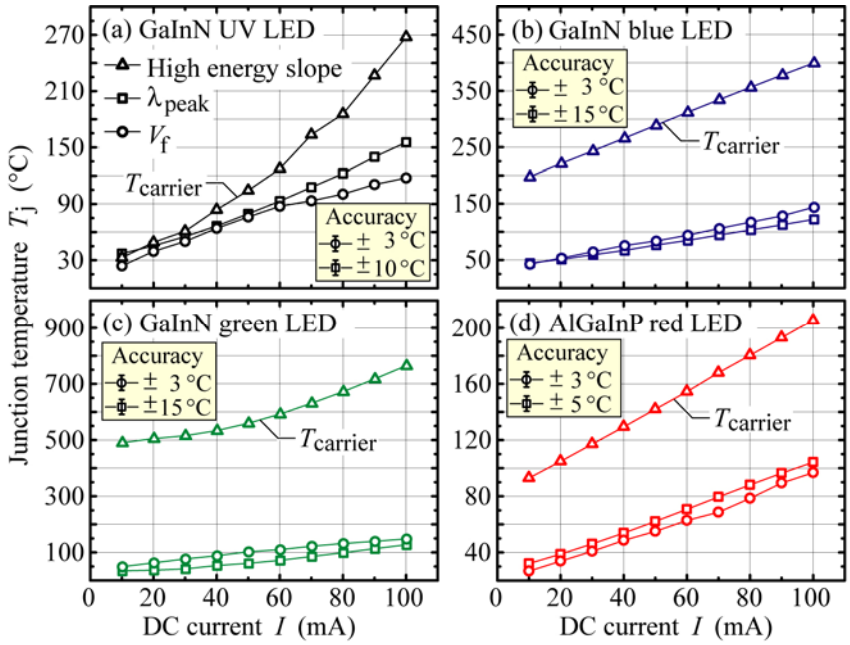

Fig. 6.8. Junction and carrier temperature of devices packaged in conventional 5 mm packages as a function of DC injection current. The measured carrier temperature over-estimates the true carrier temperature due to alloy broadening (after Chhajed *et al.*, 2005).

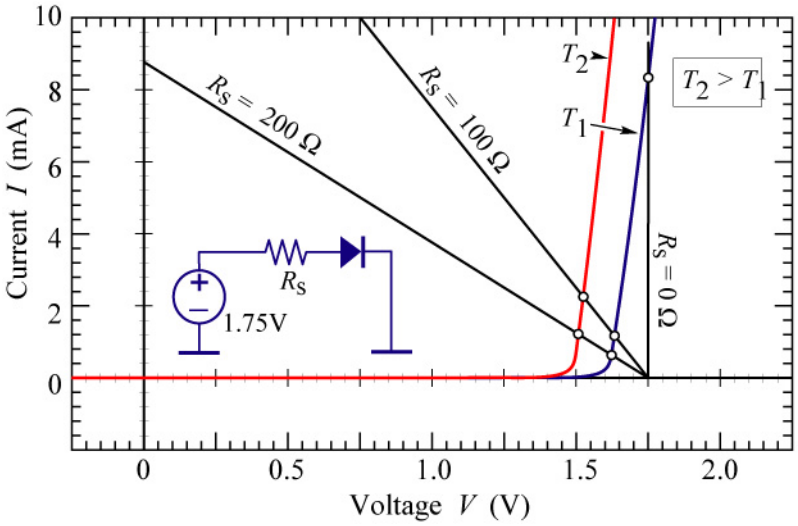

Fig. 6.9. LED drive circuit with series resistance R_S. The intersection between the diode I–V characteristics and the load lines are the points of operation. Small series resistances result in an increased diode current at high temperatures, thus allowing for compensation of a lower LED radiative efficiency.

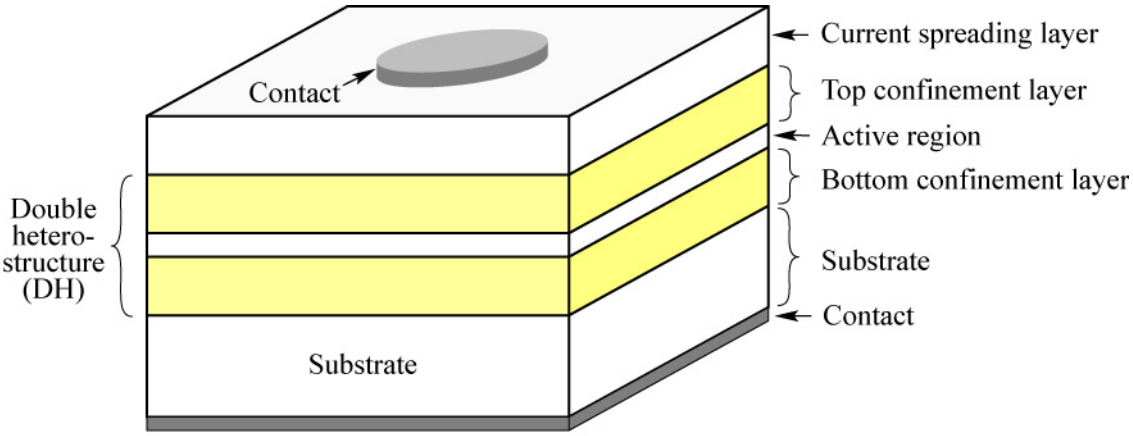

Fig. 7.1. Illustration of a double heterostructure consisting of a bulk or quantum well active region and two confinement layers. The *confinement* layers are frequently called *cladding* layers.

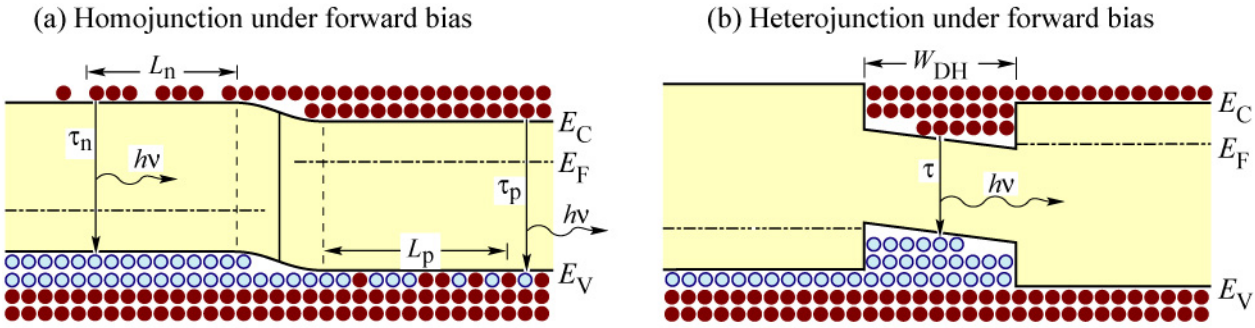

Fig. 7.2. Free carrier distribution in (a) a homojunction and (b) a heterojunction under forward bias conditions. In homojunctions, carriers are distributed over the diffusion length. In heterojunctions, carriers are confined to the well region.

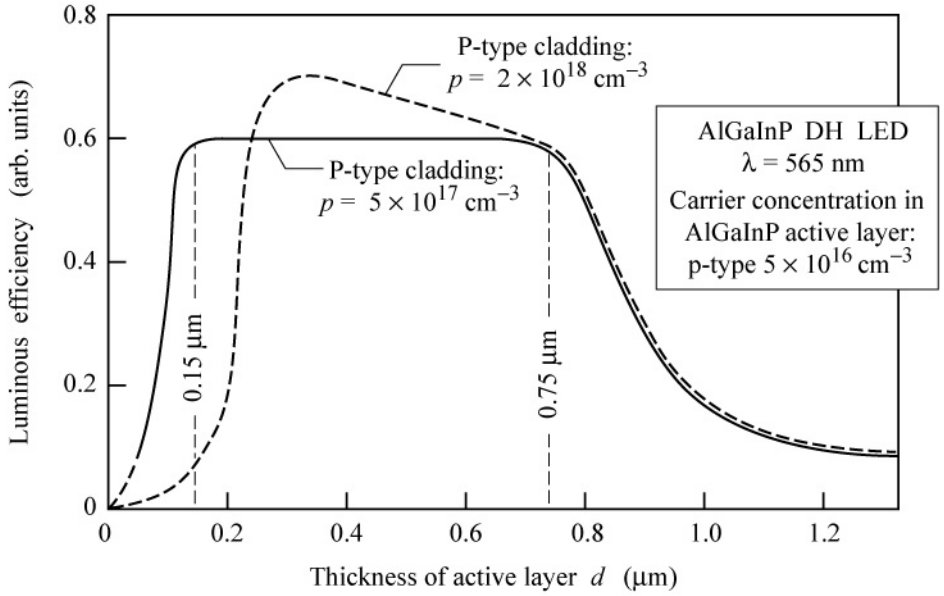

Fig. 7.3. Dependence of the luminous efficiency of an AlGaInP double heterostructure LED emitting at 565 nm on the active layer thickness. The figure reveals an optimum active region thickness of 0.15 – 0.75 µm (after Sugawara *et al*., 1992).

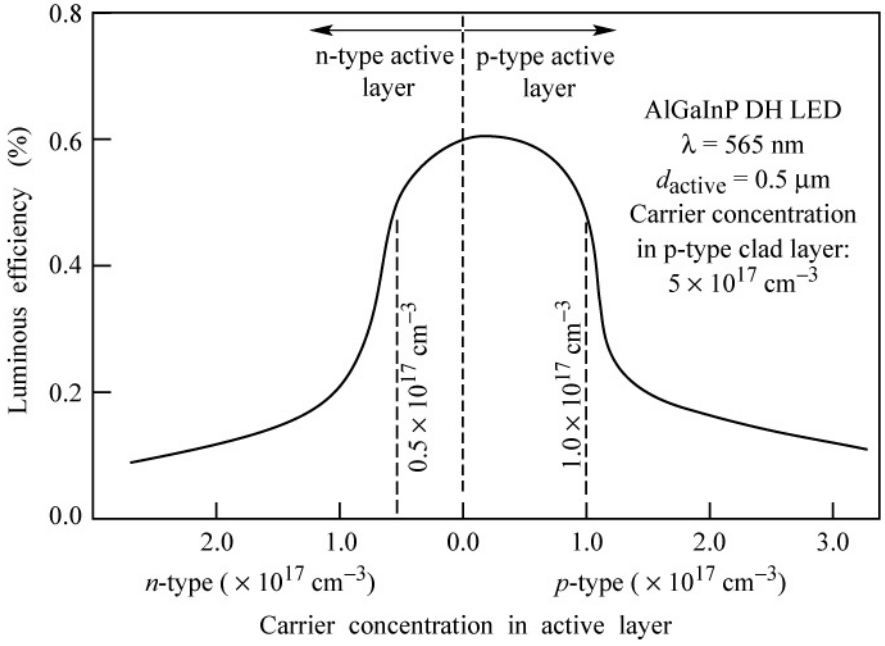

Fig. 7.4. Dependence of the luminous efficiency of an AlGaInP double heterostructure LED emitting at 565 nm on the active layer doping concentration (after Sugawara *et al*., 1992).

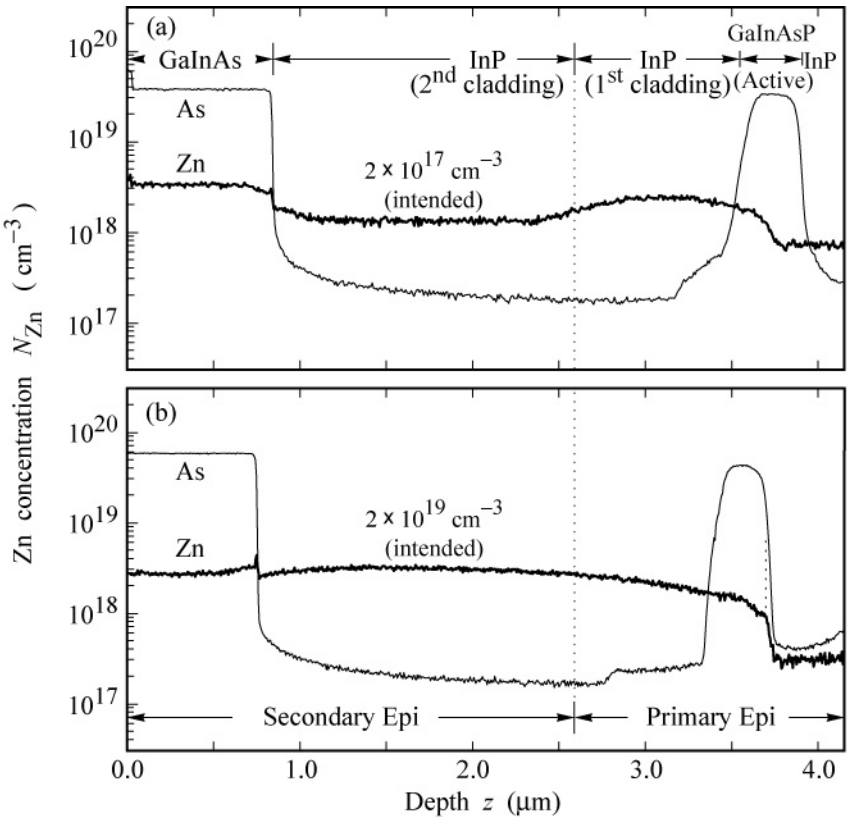

Fig. 7.5. Secondary ion mass spectrometry (SIMS) profile of Zn in a GaInAsP/InP double heterostructure. The structure uses Zn as a p-type dopant. Part (a) shows no p-n junction displacement. Part (b) shows p-n junction displacement caused by high Zn doping of the upper cladding region (after Schubert *et al.*, 1995).

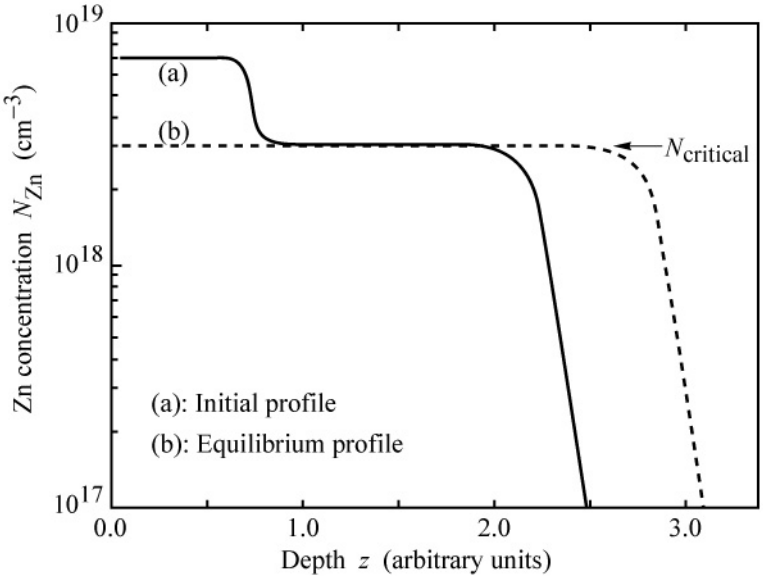

Fig. 7.6. P-n junction displacement process caused by excessive doping of the cladding region. If the acceptor dopant has a highly concentration-dependent diffusion constant and the diffusion constant increases strongly above a critical concentration, N_{critical}, p-n junction displacement occurs in the active region (after Schubert *et al.*, 1995).

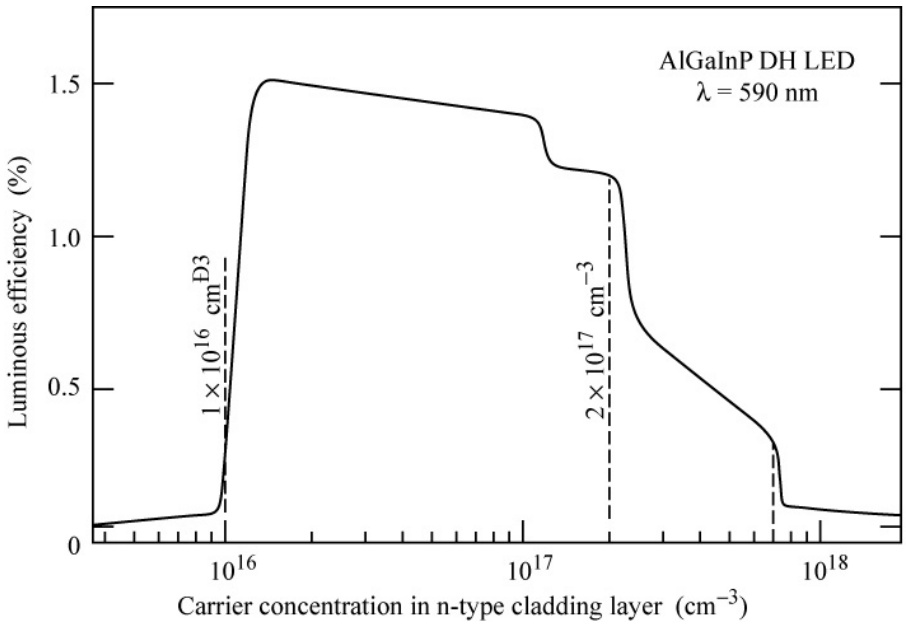

Fig. 7.7. Dependence of the luminous efficiency of an AlGaInP double heterostructure LED emitting at 565 nm on n-type confinement layer doping concentration (after Sugawara *et al*., 1992).

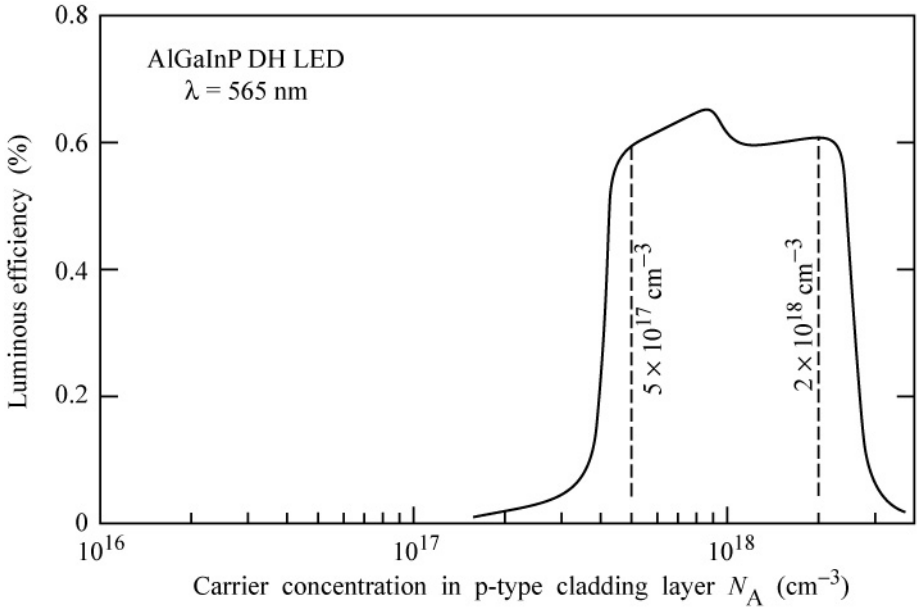

Fig. 7.8. Dependence of the luminous efficiency of an AlGaInP double heterostructure LED emitting at 565 nm on the p-type confinement layer doping concentration (after Sugawara *et al*., 1992).

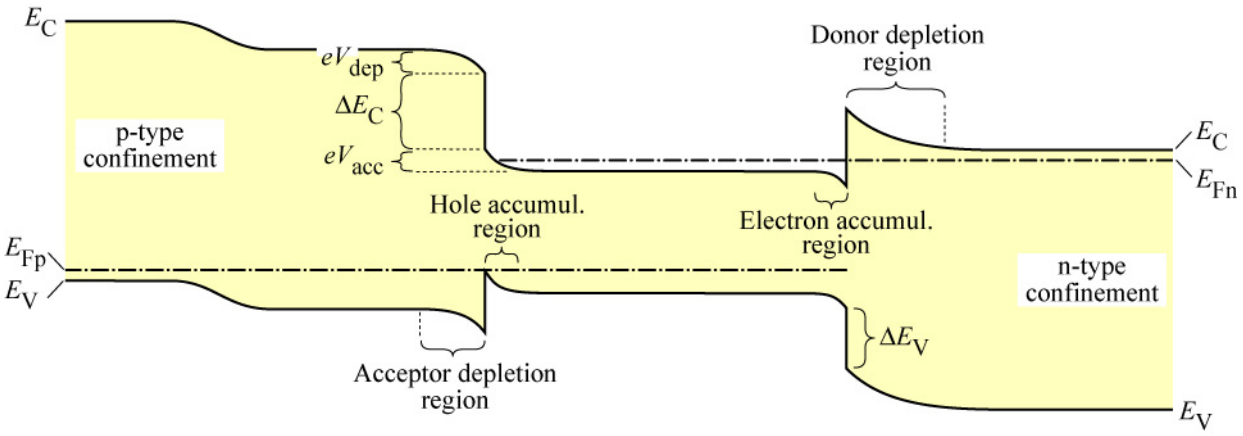

Fig. 7.9. Band diagram of a forward-biased double heterostructure. The p-type confinement layer consists of a lightly doped layer close to the active region and a higher doped layer further away from the active layer (adapted from Kazarinov and Pinto, 1994).

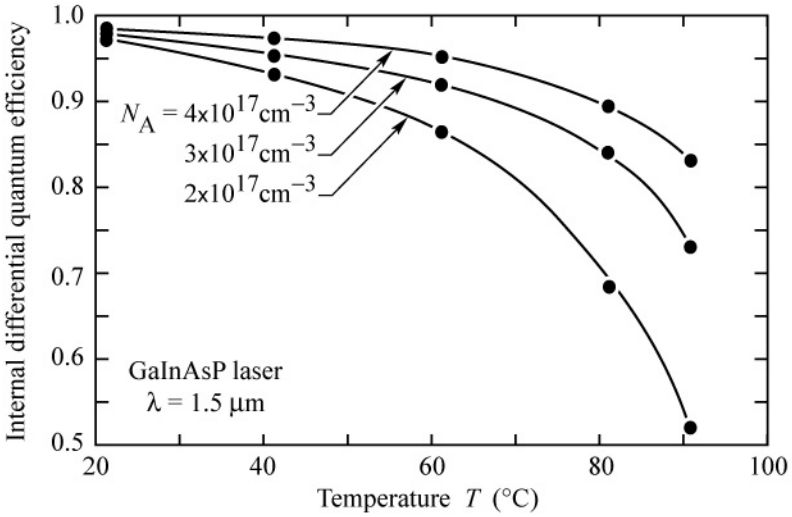

Fig. 7.10. Dependence of the internal differential quantum efficiency (emitted photons per injected electron) on temperature for different p-type doping levels in the cladding layer (after Kazarinov and Pinto, 1994).

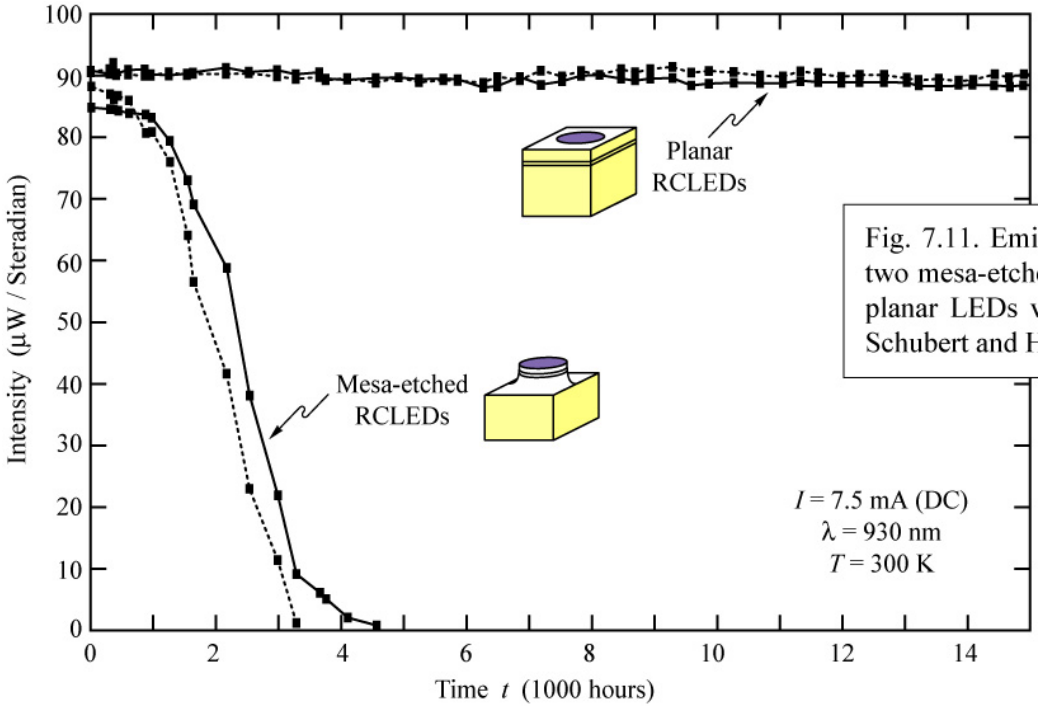

Fig. 7.11. Emission intensity of two mesa-etched LEDs and two planar LEDs versus time (after Schubert and Hunt, 1998)

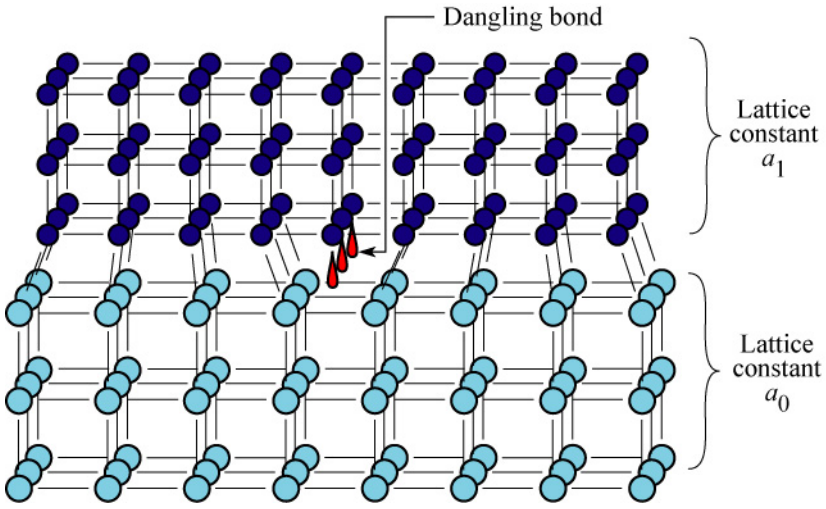

Fig. 7.12. Illustration of two crystals with mismatched lattice constant resulting in dislocations at or near the interface between the two semiconductors.

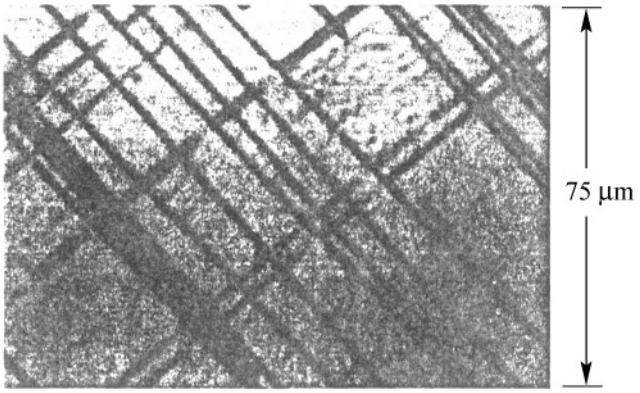

Fig. 7.13. Cathodo-luminescence image of a 0.35 μm thick $Ga_{0.95}In_{0.05}As$ layer grown on a GaAs substrate. The dark lines forming a cross-hatch pattern are due to misfit dislocations (after Fitzgerald *et al*., 1989).

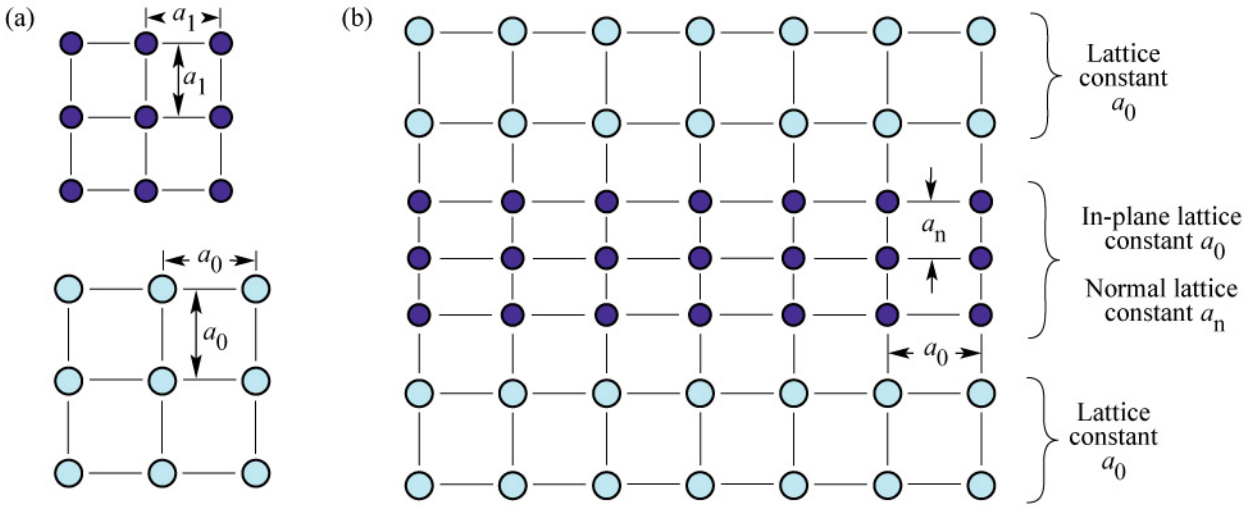

Fig. 7.14. (a) Cubic-symmetry crystals with equilibrium lattice constant a_1 and a_0. (b) Thin, coherently strained crystal layer with equilibrium lattice constant a_1 sandwiched between two semiconductors with equilibrium lattice constant a_0. The coherently strained layer assumes an in-plane lattice constant a_0 and a normal lattice constant a_n.

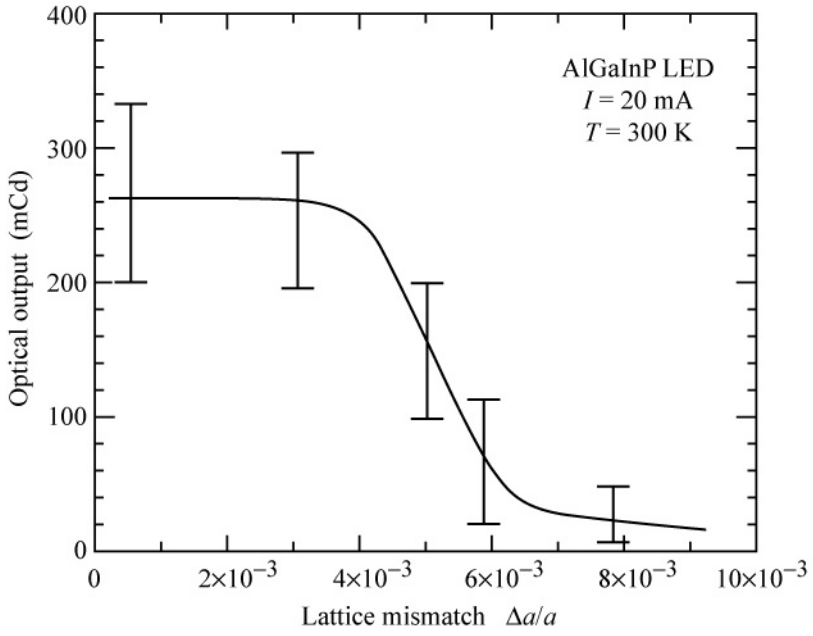

Fig. 7.15. Optical output intensity of an AlGaInP LED driven with an injection current of 20 mA versus the lattice mismatch between the AlInGaP active region and the GaAs substrate (after Watanabe and Usui, 1987).

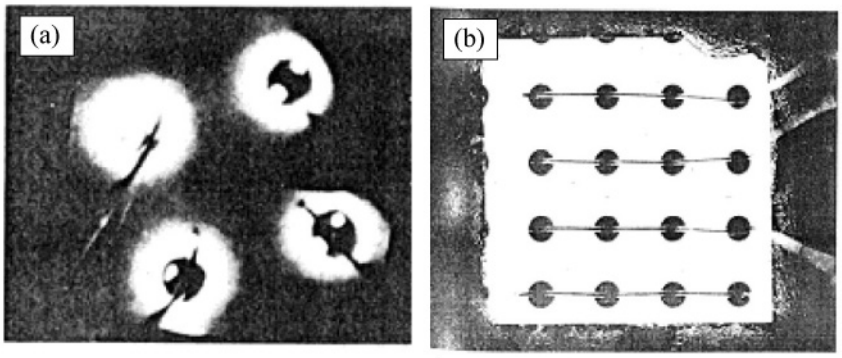

Fig. 8.1. Effect of the current-spreading layer on LED output. (a) Top view without a current-spreading layer. Emission occurs only near the perimeter of the contact. (b) Top view with a current-spreading layer (after Nuese *et al*., 1969).

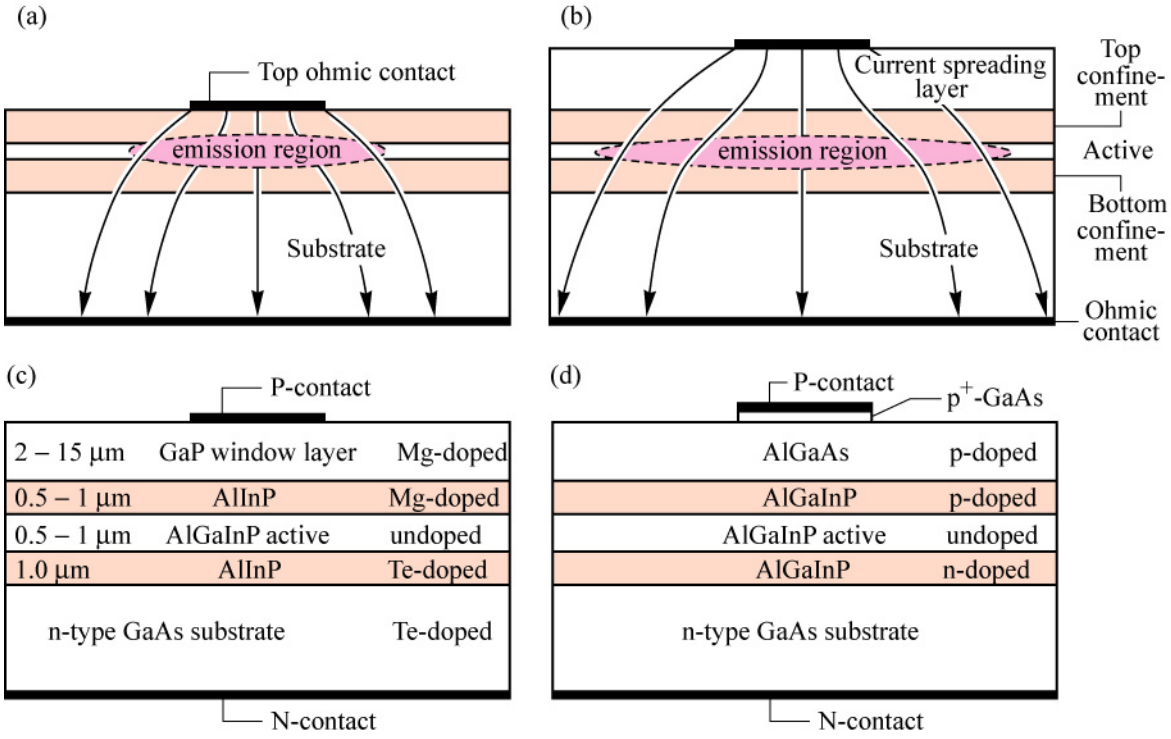

Fig. 8.2. Current-spreading structures in high-brightness AlGaInP LEDs. Illustration of the effect of a current-spreading layer for LEDs (a) without and (b) with a spreading layer on the light extraction efficiency. (c) GaP current-spreading structure (Fletcher *et al*., 1991a, 1991b). (d) AlGaAs currect-spreading structure (Sugawara *et al*., 1992a, 1992b).

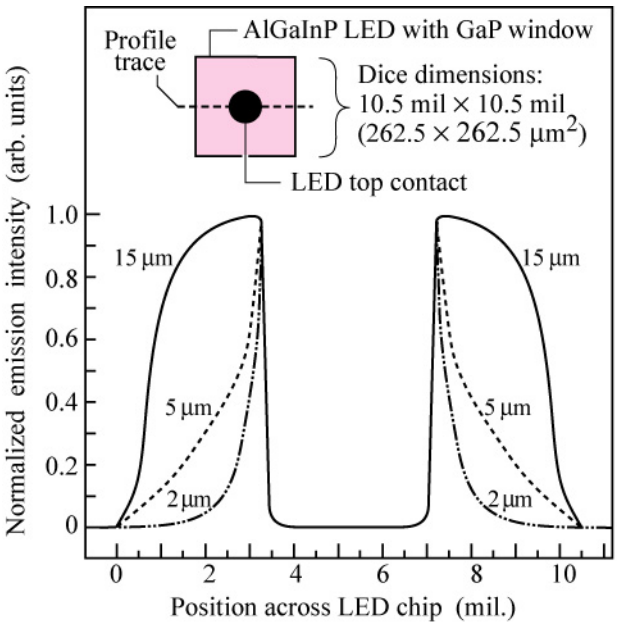

Fig. 8.3. The effect of GaP window thickness on current spreading is illustrated by surface light emission intensity profiles for three different AlGaInP LED chips with window layer thicknesses of 2, 5, and 15 μm. The profile is indicated by the dashed line in the inset. The dip in the middle of the profiles is due to the opaque ohmic contact pad. A microscope fitted with a video camara was used in the measurements (after Fletcher *et al*., 1991a).

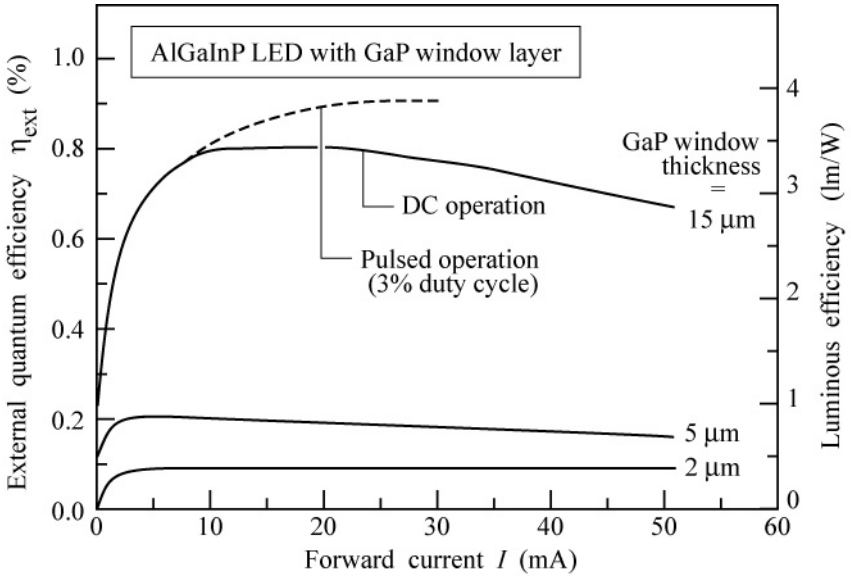

Fig. 8.4. Bare chip external quantum efficiency and luminous efficiency versus forward current for AlGaInP LEDs with GaP window layer thicknesses of 2, 5, and 15 μm. Solid curves are under DC conditions. Dashed curve is under pulsed condition using 400 ns pulses and a 3 % duty cycle. Heating is essentially eliminated in this case (after Fletcher *et al*., 1991a).

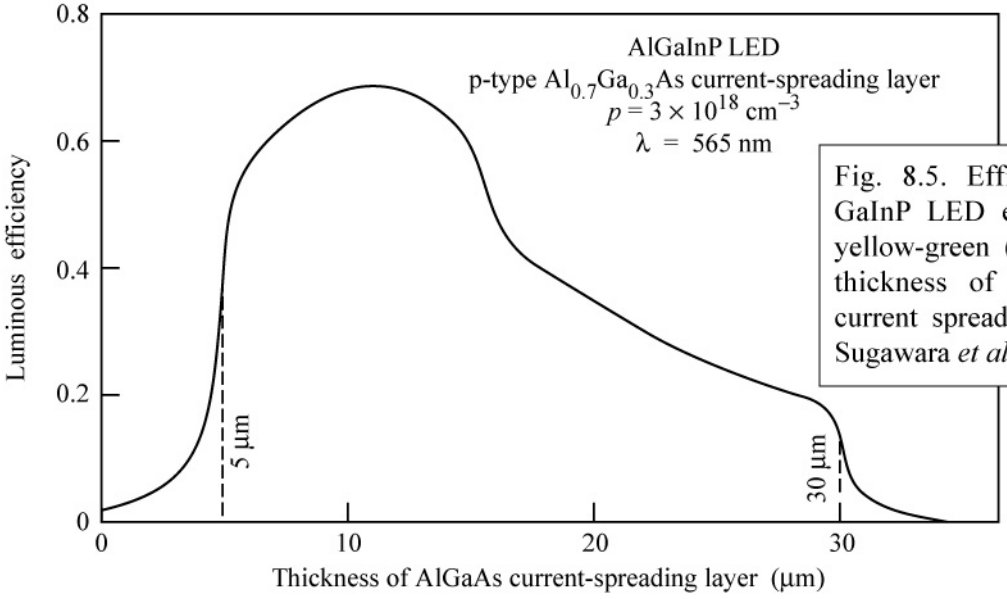

Fig. 8.5. Efficiency of AlGaInP LED emitting in the yellow-green (565nm) versus thickness of $Al_{0.70}Ga_{0.30}As$ current spreading layer (after Sugawara *et al*., 1992a).

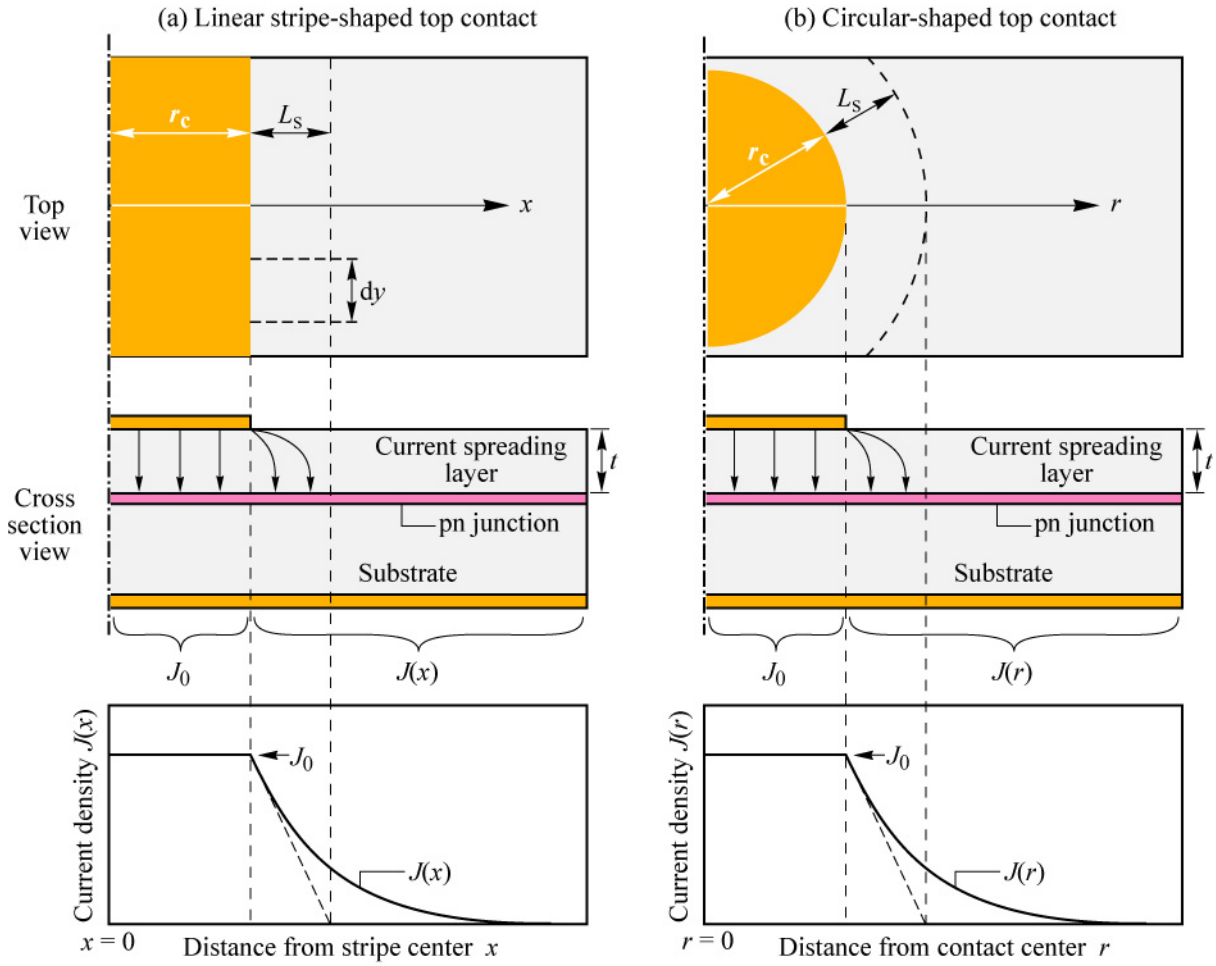

Fig. 8.6. Schematic illustration of current spreading in structures with different top contact geometries. (a) Linear stripe contact geometry. (b) Circular contact geometry.

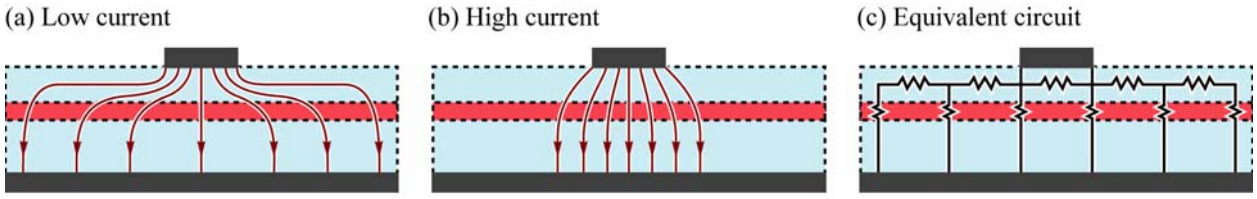

Fig. 8.7. Schematic current flow in device with current-spreading layer at (a) low and (b) high current. Current spreading generally decreases at very high current densities which results in current 'bunching' under the top contact as shown in (b).

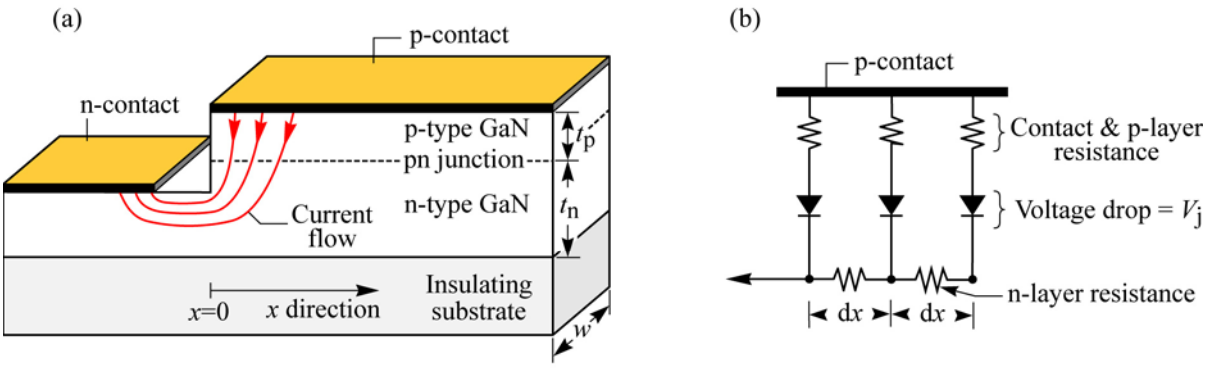

Fig. 8.8. (a) Current crowding in a mesa-structure GaN-based LED grown on an insulating substrate. (b) Equivalent circuit consisting of n-type and p-type layer resistances, p-type contact resistance, and ideal diodes representing the p-n junction.

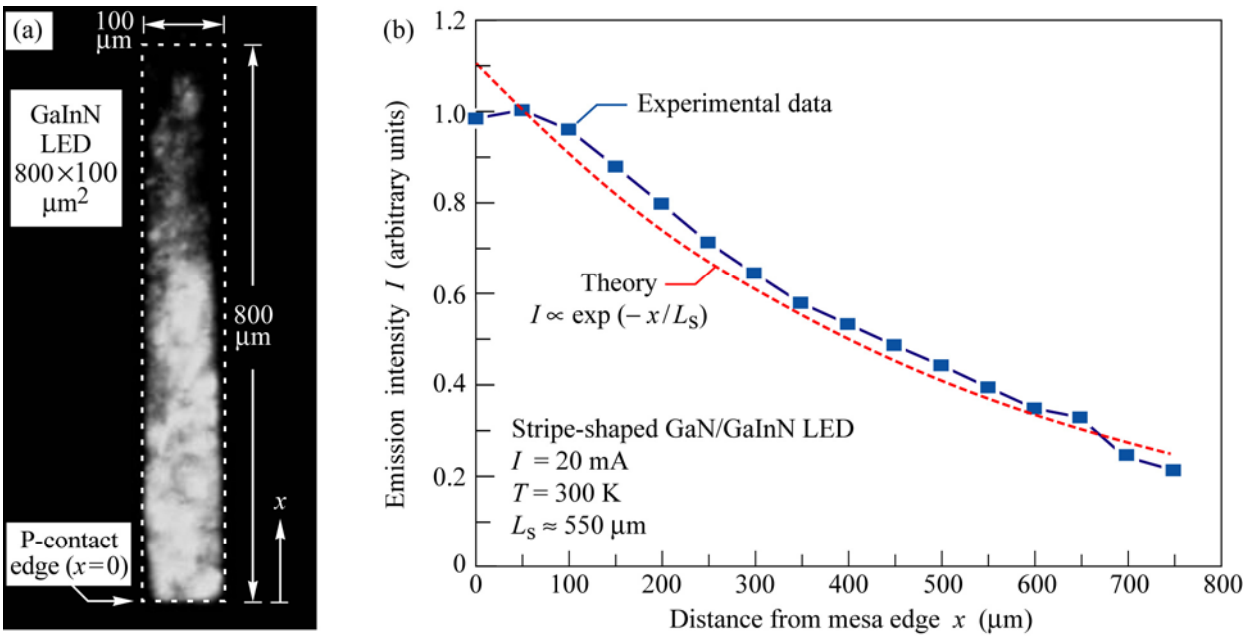

Fig. 8.9. (a) Micrograph of optical emission from mesa-structure GaInN/GaN LED grown on an insulating sapphire substrate. The LED has a stripe-shaped 800 µm × 100 µm p-type contact. (b) Theoretical and experimental emission intensity versus the distance from the mesa edge (after Guo and Schubert, 2001).

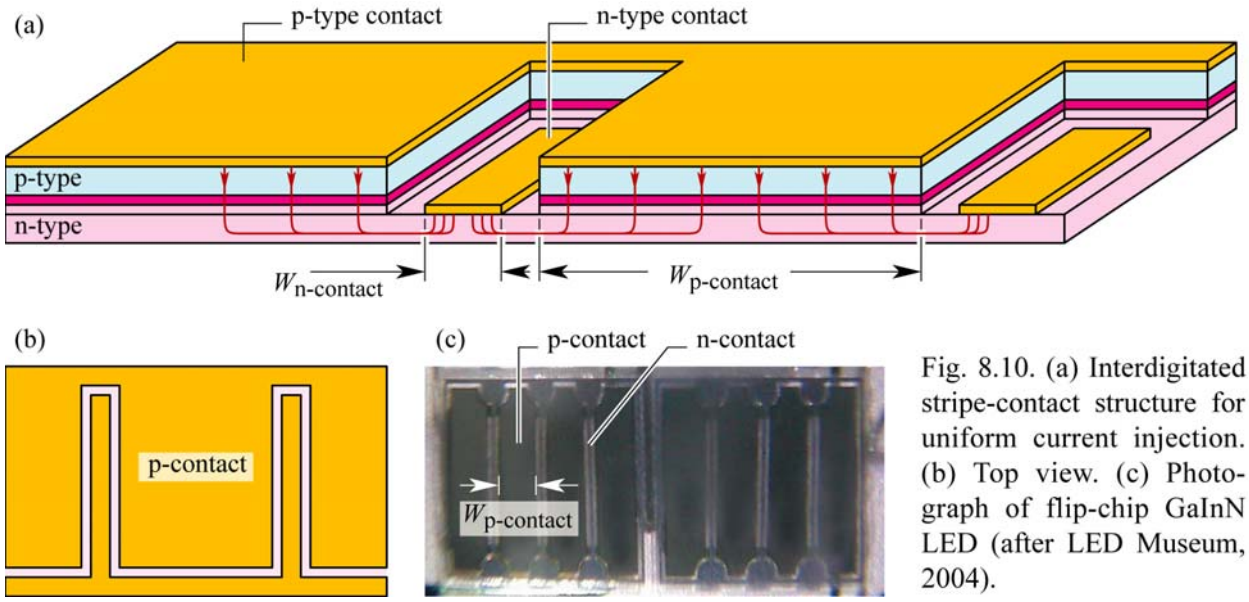

Fig. 8.10. (a) Interdigitated stripe-contact structure for uniform current injection. (b) Top view. (c) Photograph of flip-chip GaInN LED (after LED Museum, 2004).

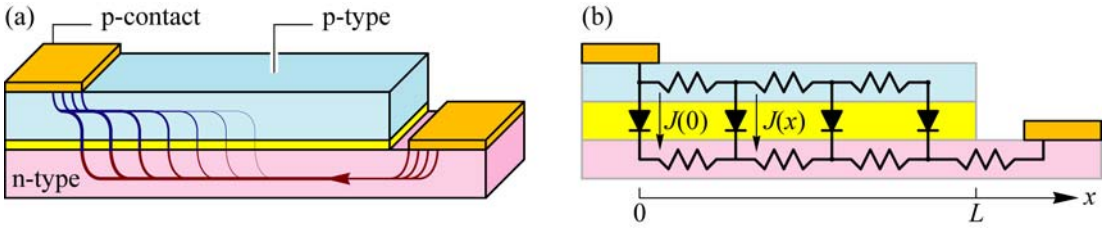

Fig. 8.11. (a) Lateral injection geometry and schematic current distribution for $\rho_n << \rho_p$. (b) Corresponding equivalent circuit.

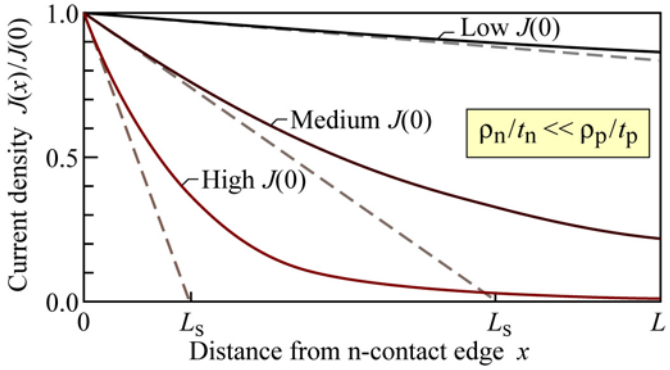

Fig. 8.12. Current density distribution at high, medium, and low current normalized to the initial current density for device with lateral injection geometry. The n-type sheet resistance is assumed to be lower than the p-type sheet resistance.

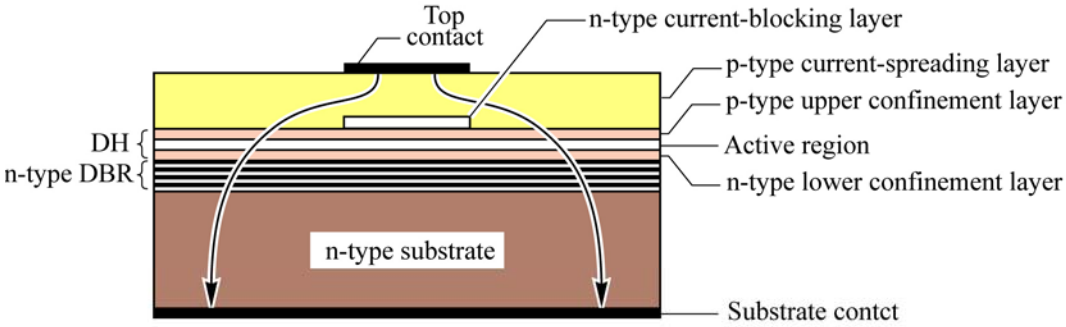

Fig. 8.13. LED with an n-type current-blocking layer located on the upper confinement layer. Light emission occurs in the regions not covered by the opaque top ohmic contact. The LED is fabricated by *epitaxial regrowth*. After growth of the current-blocking layer, the wafer is taken out of the growth system for etching. The wafer is then re-introduced into the epitaxial system for growth of the current-spreading layer.

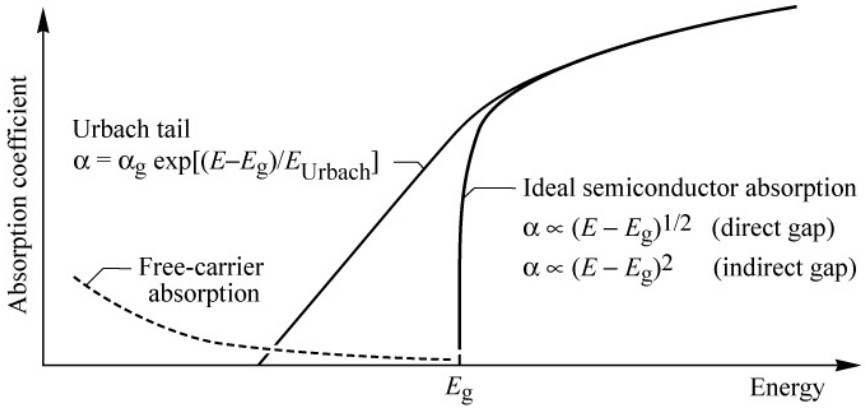

Fig. 9.1. Absorption coefficient of a semiconductor with bandgap E_g versus energy. The "Urbach tail" dominates absorption near but below the bandgap. Absorption further below the bandgap is dominated by free-carrier absorption.

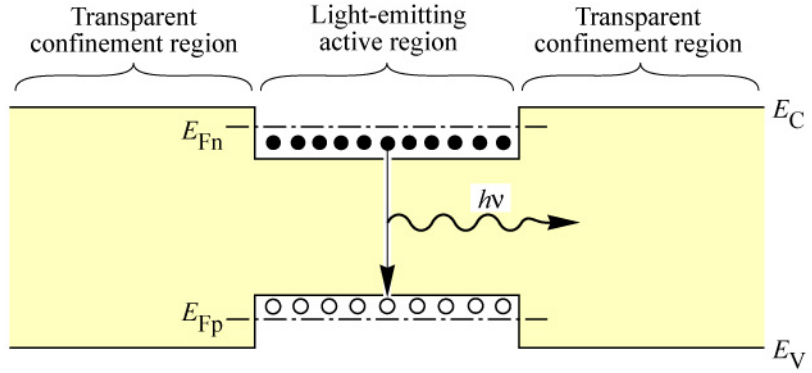

Fig. 9.2. Double hetero-structure with optically transparent confinement regions. Reabsorption in the active region is unlikely due to the high carrier concentration in the active region and the resulting Burstein–Moss shift of the absorption edge.

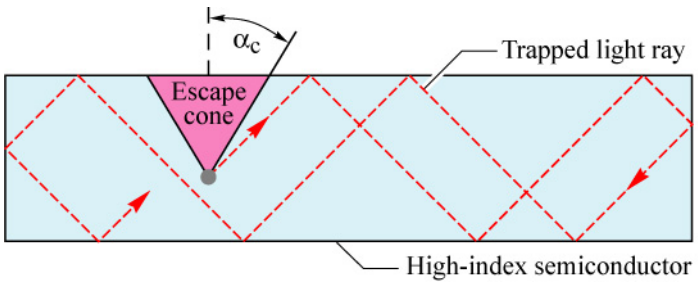

Fig. 9.3. "Trapped light" in a rectangular-parallelepiped-shaped semiconductor unable to escape for emission angles greater than α_c due to total internal reflection.

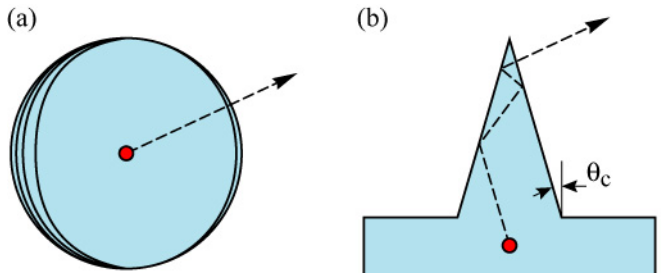

Fig. 9.4. Schematic illustration of different geometric shapes for LEDs with perfect extraction efficiency. (a) Spherical LED with a point-like light-emitting region at the center of the sphere. (b) A cone-shaped LED.

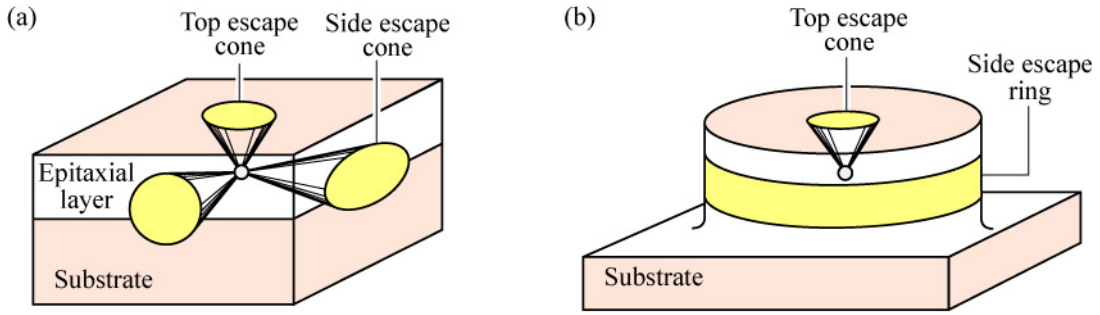

Fig. 9.5. Illustration of different geometric shapes of LEDs. (a) Rectangular parallelepipedal LED die with a total of six escape cones. (b) Cylindrical LED die with a top escape cone and a side escape ring.

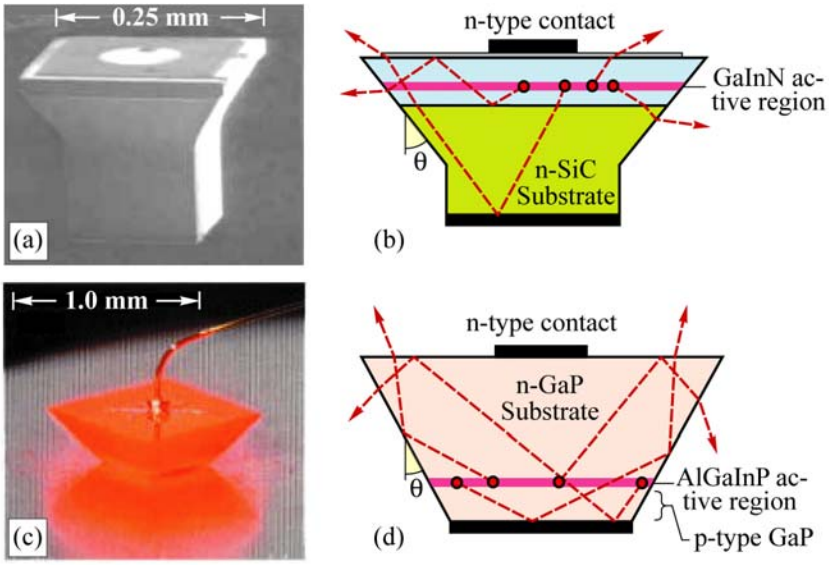

Fig. 9.6. Die-shaped devices: (a) Blue GaInN emitter on SiC substrate with trade name "Aton". (b) Schematic ray traces illustrating enhanced light extraction. (c) Micrograph of truncated inverted pyramid (TIP) AlGaInP/GaP LED. (d) Schematic diagram illustrating enhanced extraction (after Osram, 2001; Krames *et al.*, 1999).

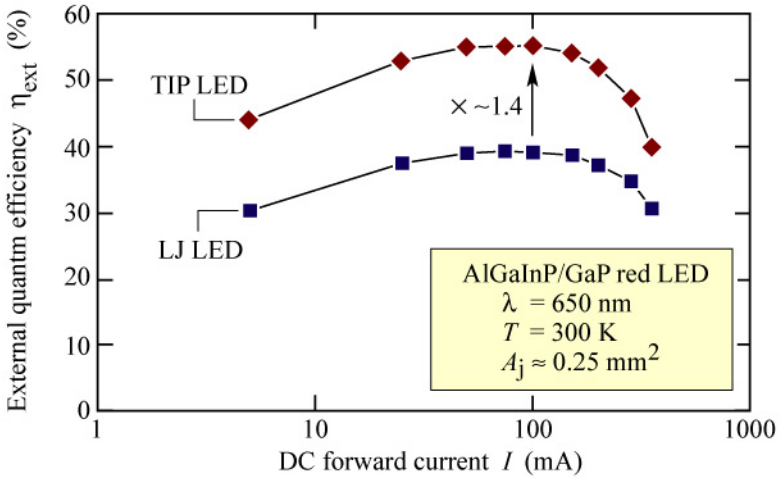

Fig. 9.7. External efficiency vs. forward current for red-emitting (650 nm) truncated inverted pyramid (TIP) LEDs and large junction (LJ) LEDs mounted in power-lamp packages. The TIP LED exhibits a 1.4 times improvement in extraction efficiency compared with the LJ device, resulting in a peak external quantum efficiency of 55 % at 100 mA (after Krames *et al*., 1999).

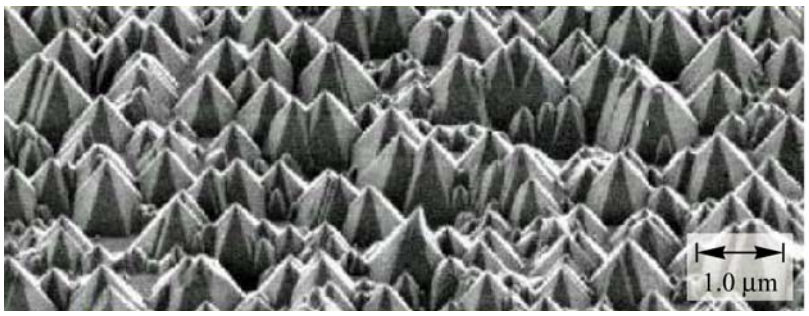

Fig. 9.8. Scanning electron micrograph of strongly textured GaN surface (after Haerle, 2004).

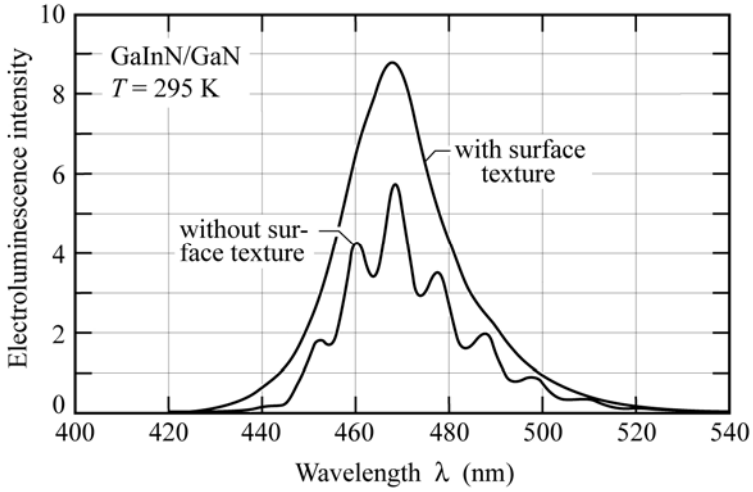

Fig. 9.9. Emission spectrum of GaInN blue LED with and without surface texture. The spectrum exhibits Fabry-Perot interference fringes for the device with a smooth surface (after Haerle, 2004).

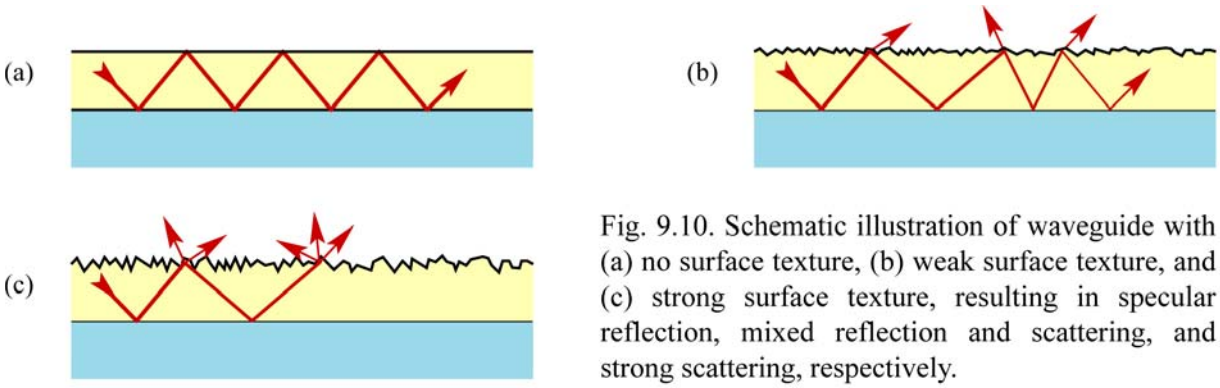

Fig. 9.10. Schematic illustration of waveguide with (a) no surface texture, (b) weak surface texture, and (c) strong surface texture, resulting in specular reflection, mixed reflection and scattering, and strong scattering, respectively.

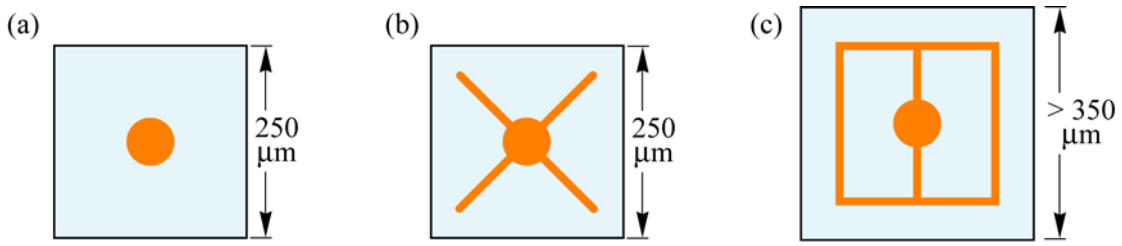

Fig. 9.11. Top view on an LED die with (a) a circular contact also serving as a bond pad and (b) a cross-shaped contact with a circular bond pad. (c) Typical contact geometry used for larger LED dies.

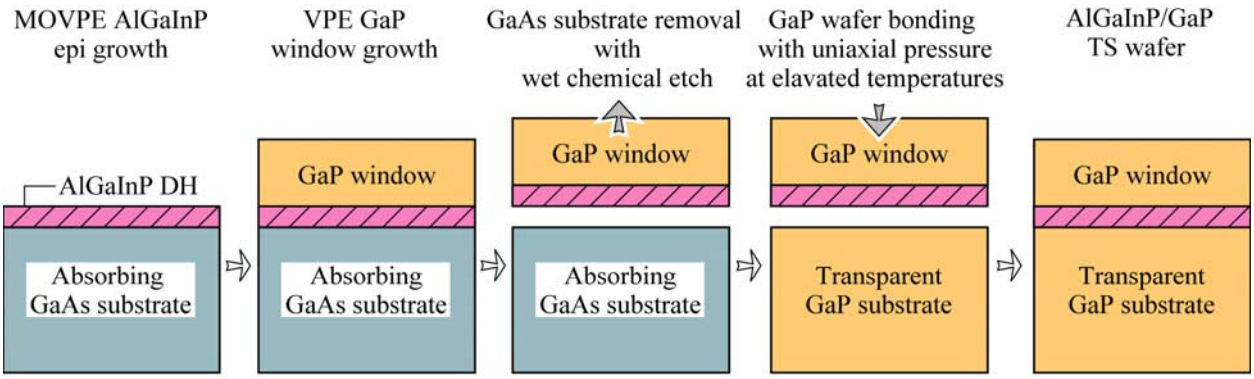

Fig. 9.12. Schematic fabrication process for wafer-bonded transparent substrate (TS) AlGaInP/GaP LEDs. After the selective removal of the original GaAs substrate, elevated temperature and uniaxial pressure are applied, resulting in the formation of a single TS LED wafer (adopted from Kish *et al*., 1994).

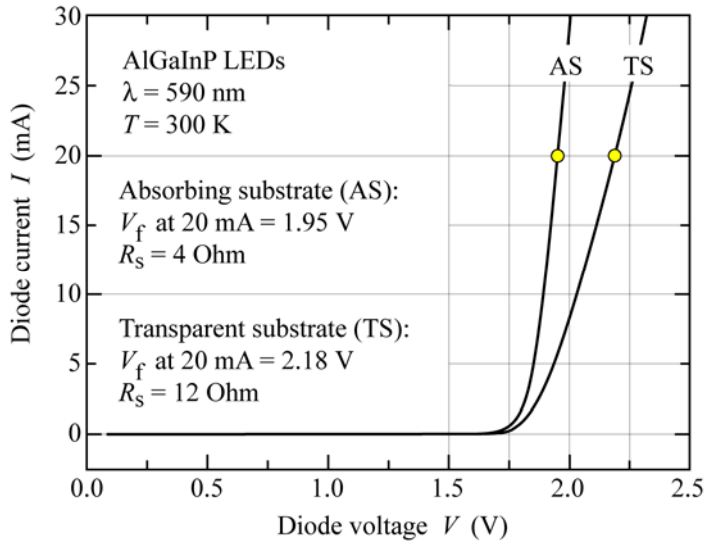

Fig. 9.13. Current–voltage characteristic, forward voltage, and series resistance of absorbing-substrate (GaAs) and transparent-substrate (GaP) LEDs with AlGaInP active regions.

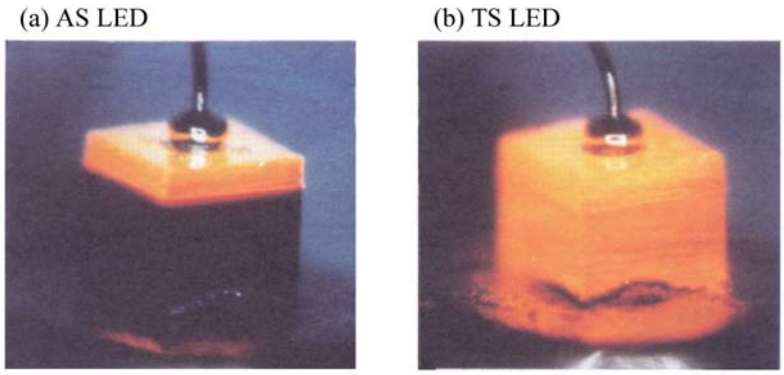

Fig. 9.14. (a) Amber AlGaInP LED with a GaP window layer and absorbing GaAs substrate (AS). (b) Amber AlGaInP LED with a GaP window layer and a transparent GaP substrate (TS) fabricated by wafer bonding. Conductive Ag-loaded die-attach epoxy can be seen at bottom (after Kish and Fletcher, 1997).

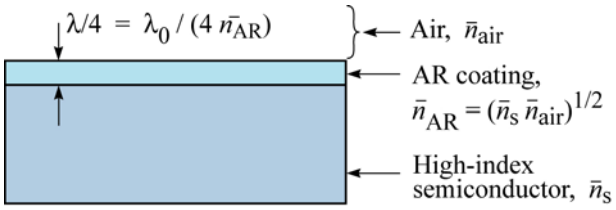

Fig. 9.15. Illustration of optimum thickness and refractive index of an anti-reflection (AR) coating.

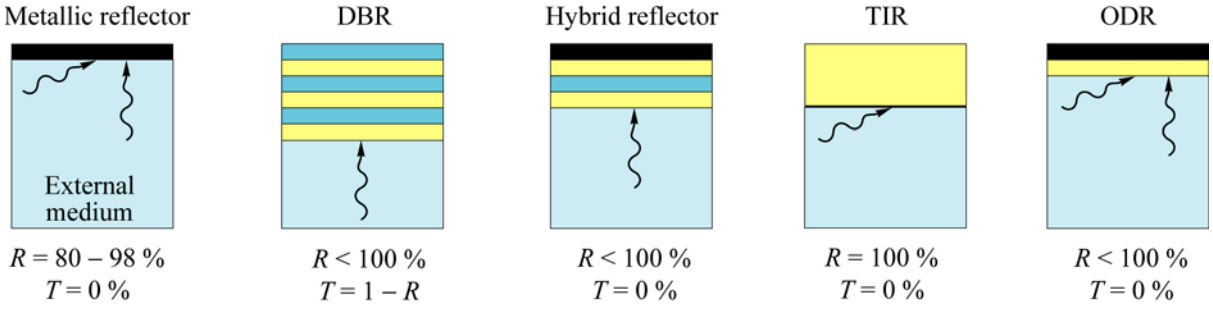

Fig. 10.1. Different types of reflectors including metallic reflector, distributed Bragg reflector (DBR), hybrid reflector, total internal reflector (TIR), and a triple-layer omni-directional reflector (ODR). Also given are angles of incidence for high reflectivity and typical reflectances and transmittances.

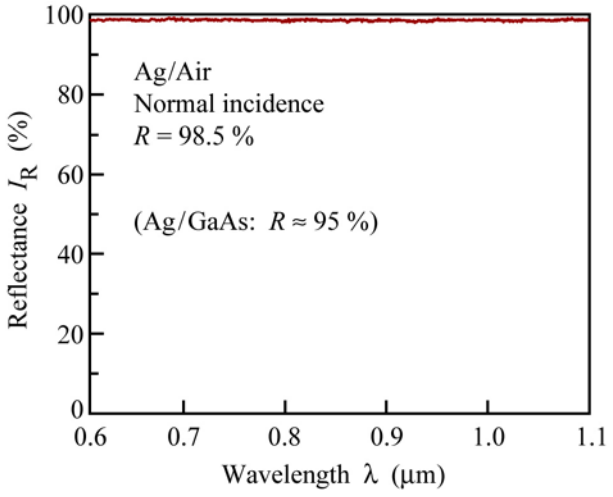

Fig. 10.2. Measured reflectance of a silver/air reflector for normal incidence. The average reflectivity in the visible spectrum is 98.5 %.

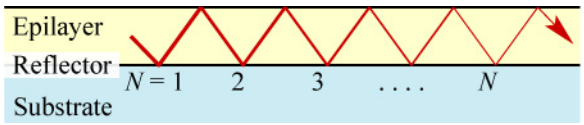

Fig. 10.3. Attenuation of waveguide mode due to lossy reflector.

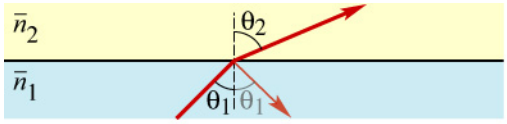

Fig. 10.4. Reflected and refracted light ray at the boundary between two media with refractive indices $\bar{n}_1$ and $\bar{n}_2$, where $\bar{n}_1 > \bar{n}_2$.

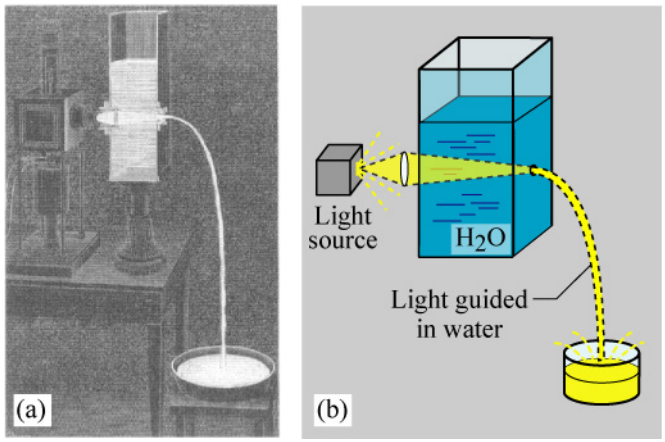

Fig. 10.5. (a) Historical drawing and (b) schematic illustration of apparatus used in 1841 by Swiss engineer Daniel Colladon to demonstrate the guiding of light by total internal reflection in a jet of water.

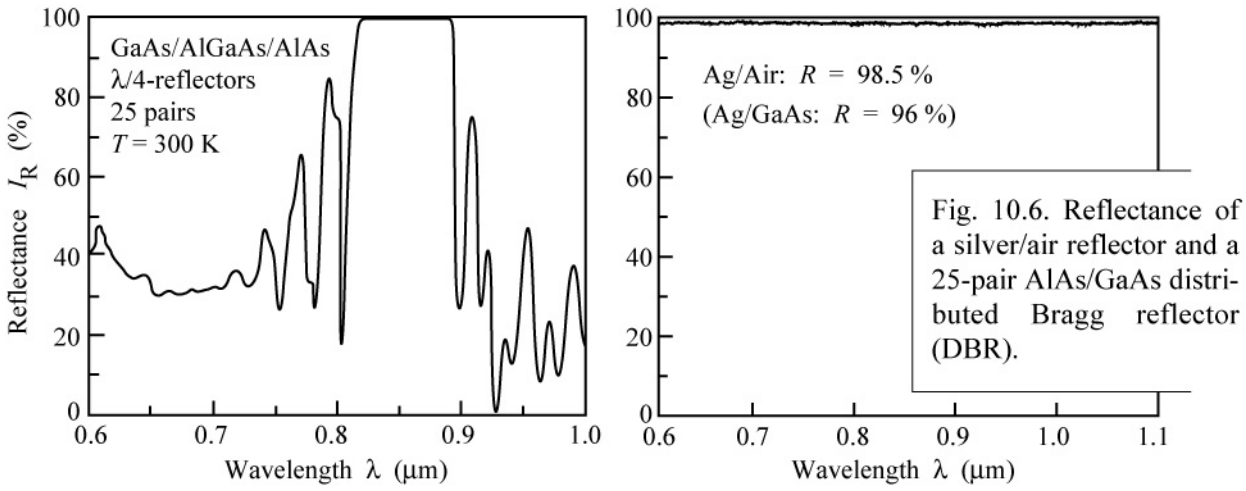

Fig. 10.6. Reflectance of a silver/air reflector and a 25-pair AlAs/GaAs distributed Bragg reflector (DBR).

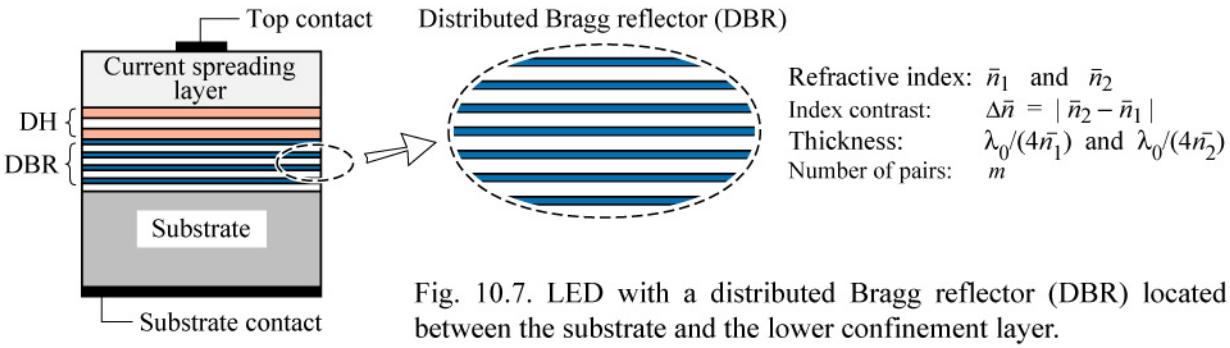

Fig. 10.7. LED with a distributed Bragg reflector (DBR) located between the substrate and the lower confinement layer.

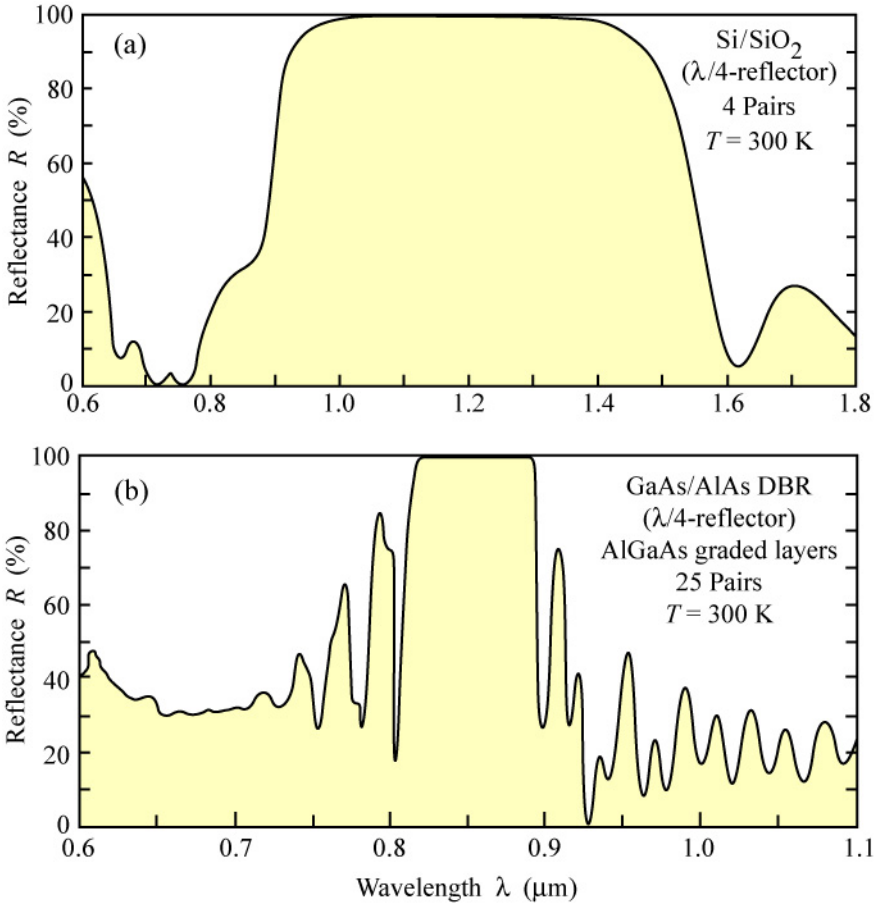

Fig. 10.8. Reflectance of two distributed Bragg reflectors (DBRs) versus wavelength. (a) Four-pair Si/SiO_2 reflector with high index contrast. (b) 25-pair AlAs/GaAs reflector. The high-index-contrast DBR only needs four pairs to attain high reflectivity. Note that the stop band of the high-index-contrast DBR is wider compared with the low-contrast DBR.

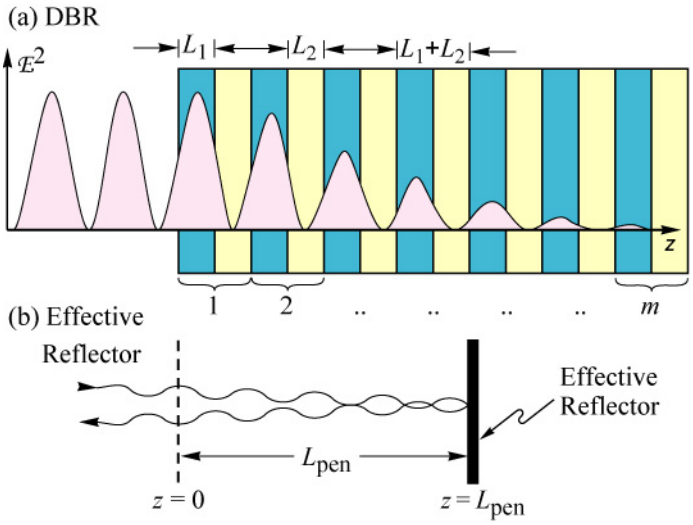

Fig. 10.9. Illustration of the DBR penetration depth. (a) DBR consis-ting of two materials with thickness L_1 and L_2. (b) Ideal (metallic) re-flector displaced from the DBR sur-face by the penetration depth.

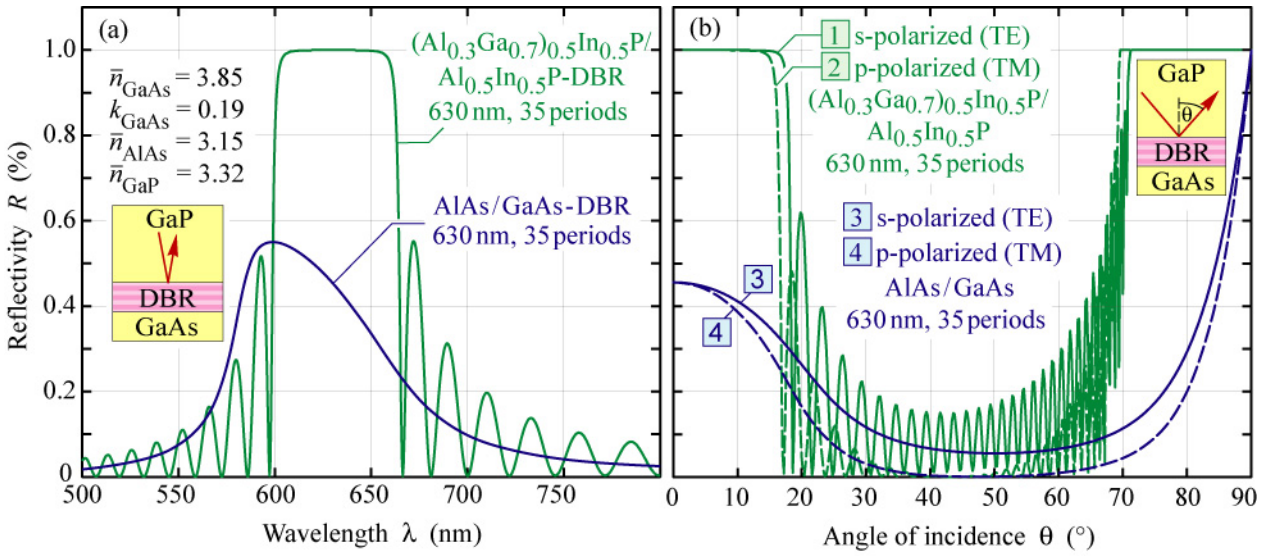

Fig. 10.10. Calculated reflectivity (inside the cladding GaP) versus (a) wavelength and (b) polar angle of a transparent AlGaInP/AlInP DBR and an absorbing AlAs/GaAs DBR.

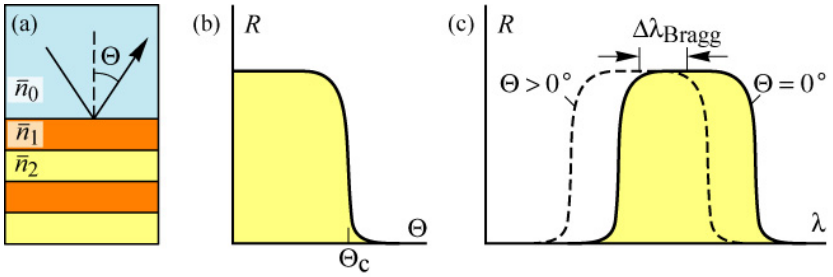

Fig. 10.11. (a) DBR stucture used in calculation. (b) Reflectivity versus angle of incidence and critical angle at which reflectivity decreases. (c) DBR reflectivity versus wavelength for two angles of incidence.

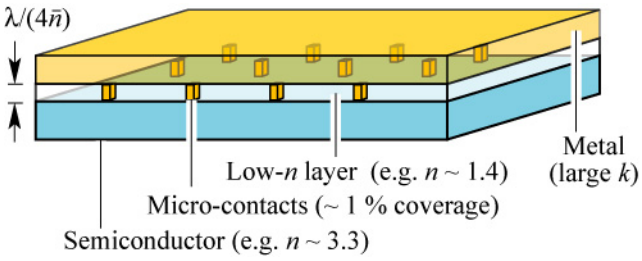

Fig. 10.12. Structure of omnidirectional reflector consisting of semiconductor, low-refractive index dielectric layer, and metal layer. The dielectric is perforated by an array of microcontacts providing electrical conductivity (after Gessmann *et al.*, 2003).

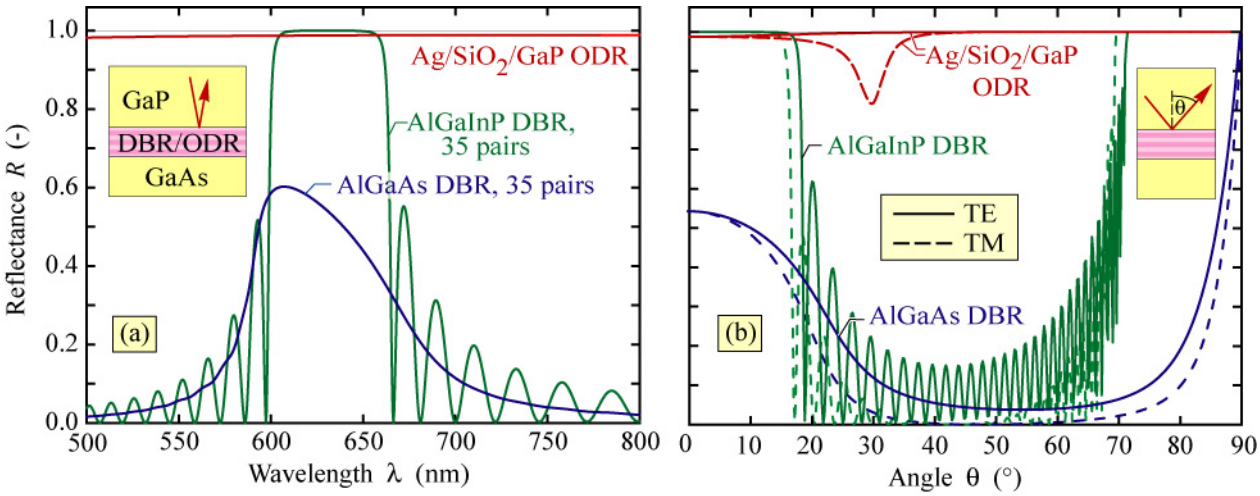

Fig. 10.13. (a) Calculated relflectivity at normal-incidence versus wavelength and (b) reflectivity versus angle of incidence for an omnidirectional reflcetor (ODR), a transparent AlGaInP/AlInP DBR, and an absorbing AlGaAs/GaAs DBR (after Gessmann et al., 2003).

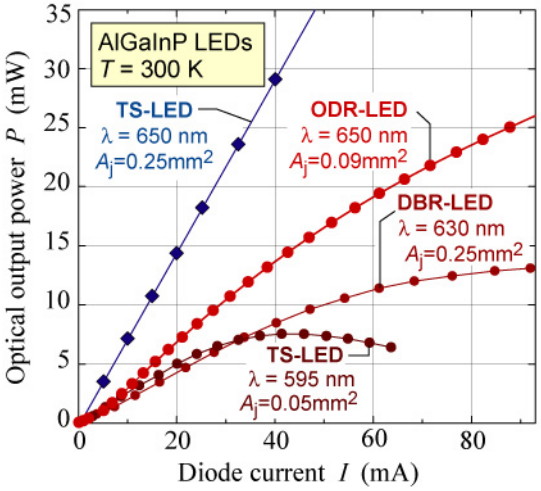

Fig. 10.14. Light-output power versus injection current of different types of LEDs. The ODR device has a higher output power than the DBR device (after Gessmann et al., 2003).

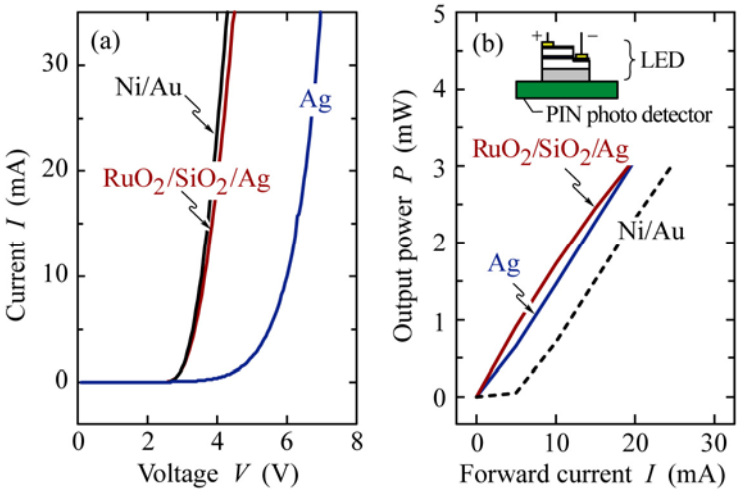

Fig. 10.15. Current-voltage and light-output-versus-current characteristic of a GaInN LED with a GaInN/RuO_2/SiO_2/Ag omnidirectional reflector (after Kim *et al.*, 2004).

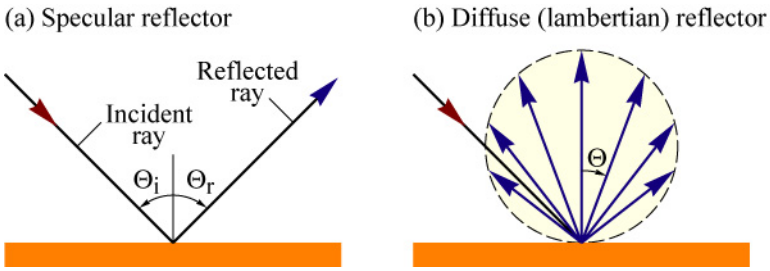

Fig. 10.16. Schematic of a specular and diffuse (lambertian) reflector. The reflected power distribution of a lambertian reflector follows a cos Θ dependence.

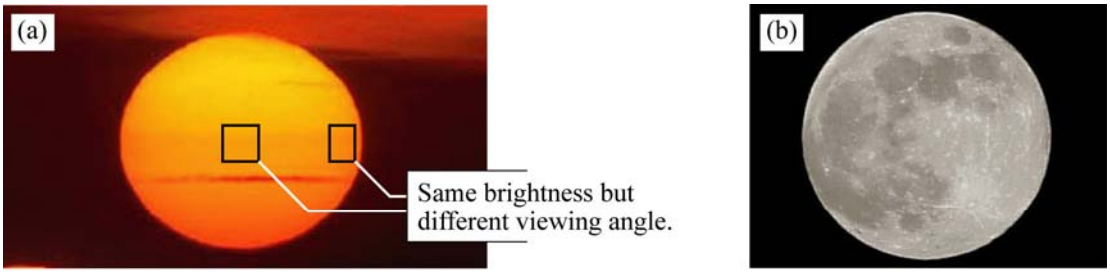

Fig. 10.17. (a) The sun's surface brightness is independent of viewing angle with respect to the sun's surface. It is a good example of a lambertian source. (b) The moon is a good example of a lambertian reflector.

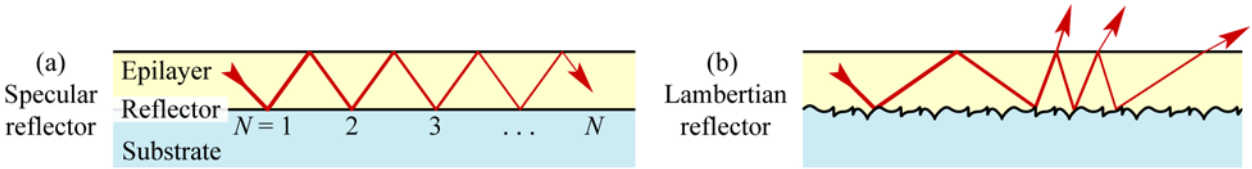

Fig. 10.18. (a) Optical mode guided by specular reflector at the epilayer/substrate interface and the epilayer/air interface. (b) Optical ray propagating in epilayer guided by lambertian reflector at the epilayer/substrate interface and the epilayer/air interface.

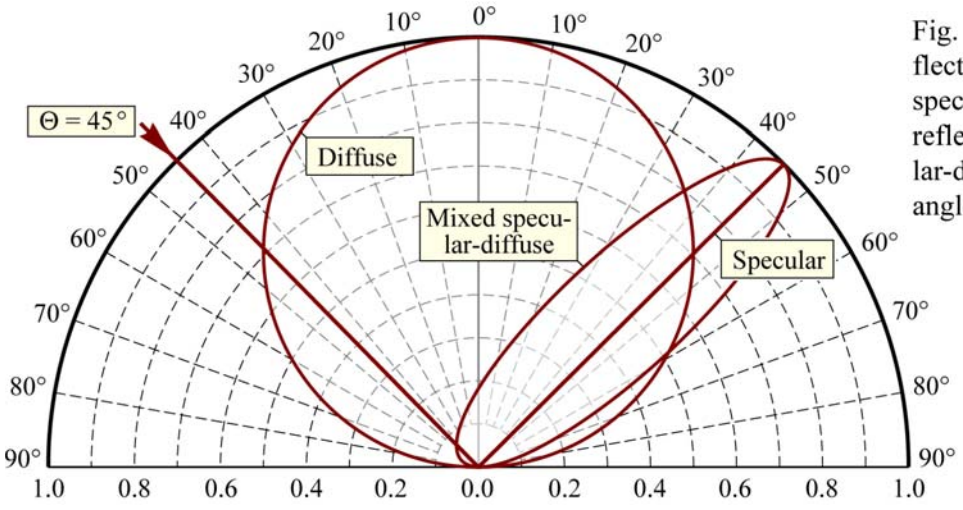

Fig. 10.19. Schematic reflection contour plots of a specular reflector, diffiuse reflector, and a mixed specular-diffuse reflector for an angle of incidence of 45°.

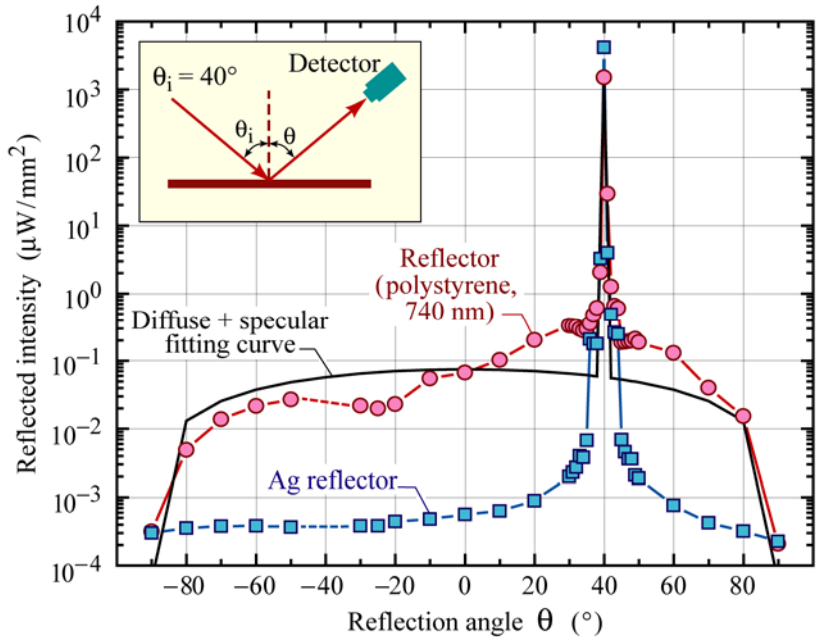

Smooth Ag reflector:
$P_{diff}/(P_{diff}+P_{spec}) < 1\%$

Textured Ag reflector:
$P_{diff}/(P_{diff}+P_{spec}) = 42.8\%$

Fig. 10.20. Reflected intensity versus angle for a smooth Ag reflector and a Ag reflector textured by using natural lithorgraphy with 700 nm diameter polystyrene spheres and subsequent ion-beam etching (after Xi *et al.*, 2005).

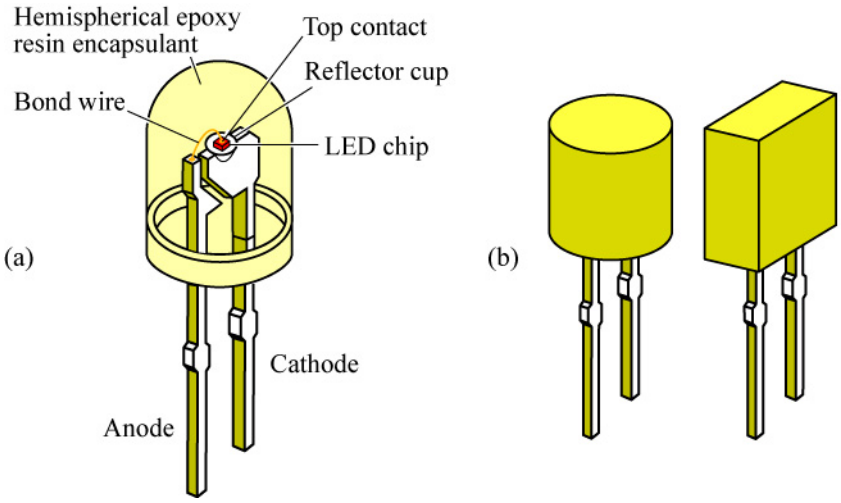

Fig. 11.1. Typical packages; (a) LED with hemispherical encapsulant; (b) LEDs with cylindrical and rectangular encapsulant.

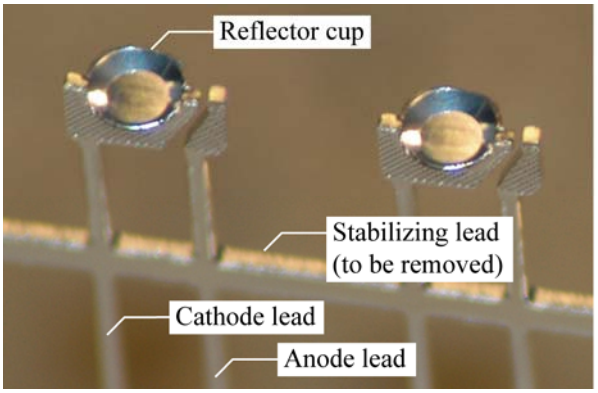

Fig. 11.2. Leadframe of a conventional 5 mm package for mounting and connecting LED chips. The stabilizing lead is cut off, once mechanical stability between the anode and cathode lead has been established by the epoxy encapsulant.

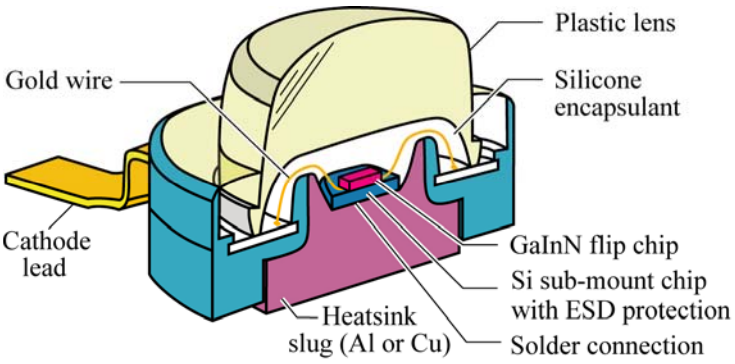

Fig. 11.3. Cross section through high-power package. The heatsink slug can be soldered to a printed circuit board for efficient heat removal. This package, called *Barracuda package,* was introduced by Lumileds Corp. (adopted from Krames, 2003).

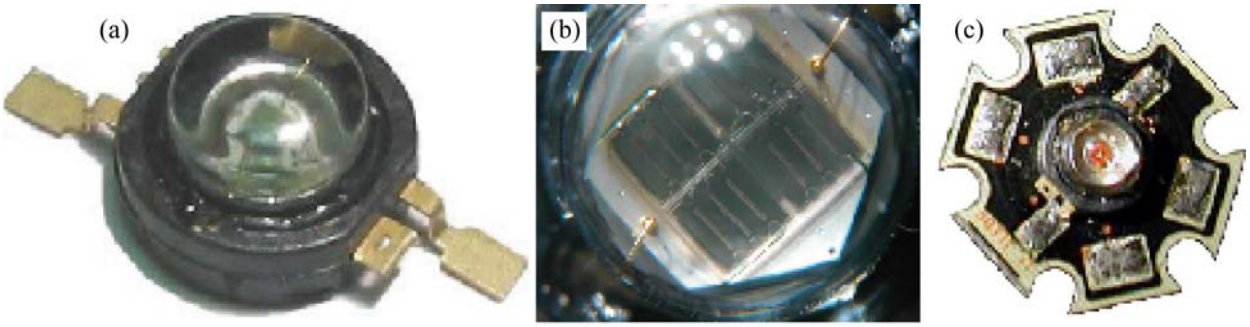

Fig. 11.4. (a) High-power package; (b) LED die in package; (c) package on printed circuit board with high thermal conductivity. ((a) after Krames, 2003; (b), (c) after after LED Museum, 2003).

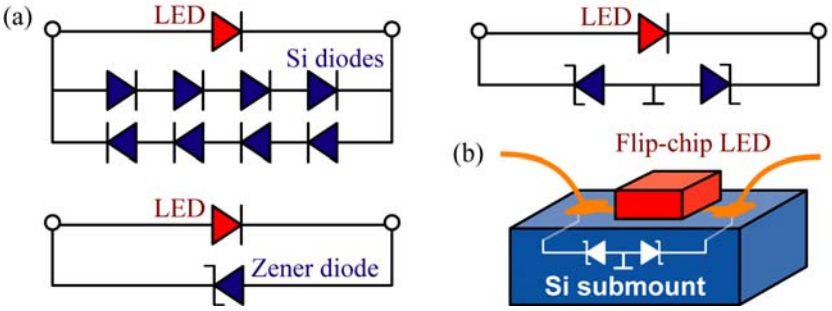

Fig. 11.5. (a) Electrostatic discharge (ESD) protection circuits using multiple Si pn junctions, one Zener diode, and two Zener diodes. (b) ESD protection integrated into a Si submount (two-Zender diode circuit after Lumileds, 2004).

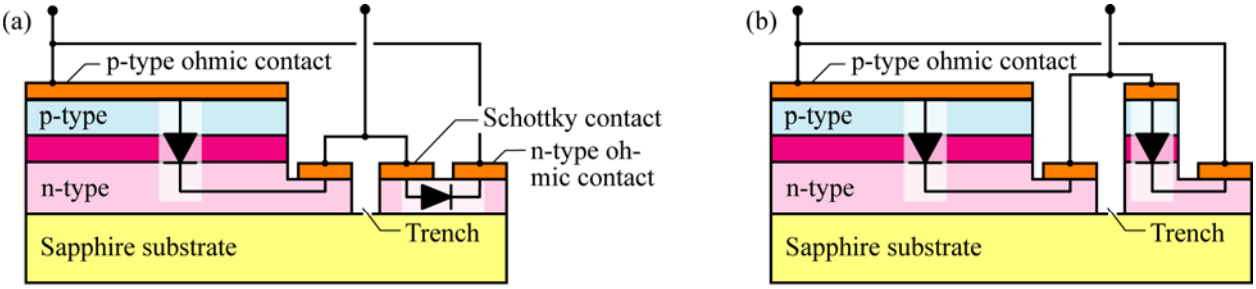

Fig. 11.6. On-chip ESD protection using (a) a small-area Schottky diode on the n-type buffer layer of a GaInN device and (b) a small-area pn-junction diode (Schottky diode circuit after Sheu, 2003).

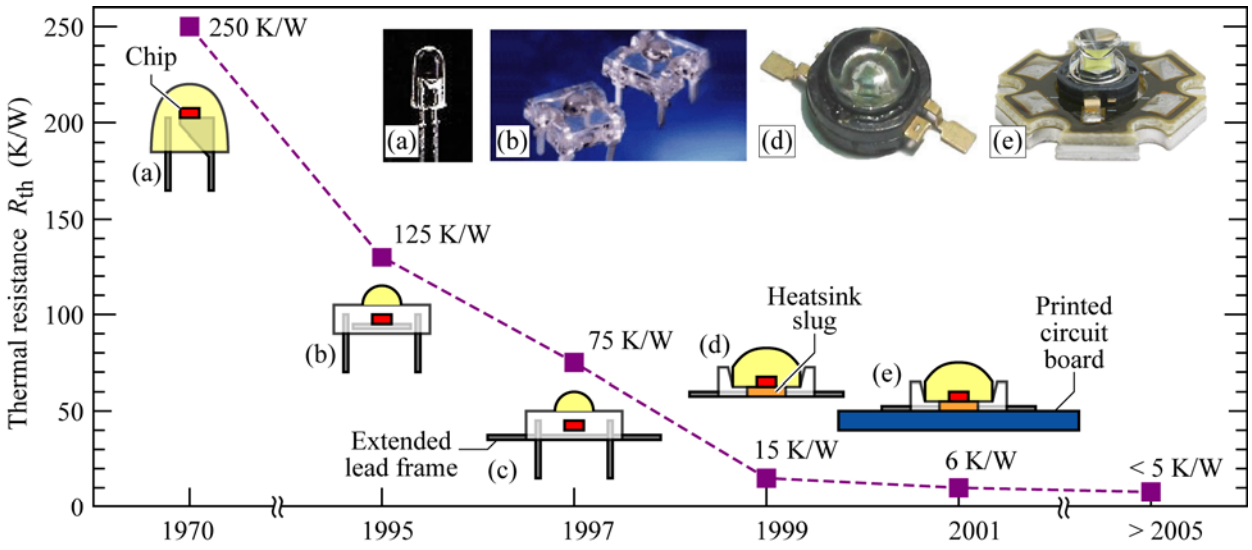

Fig. 11.7. Thermal resistance of LED packages: (a) 5mm (b) low-profile (c) low-profile with extended lead frame (d) heatsink slug (e) heatsink slug mounted on printed circuit board (PCB). Trade names for these packages are "Piranha" (b and c, Hewlett Packard Corp.), "Barracuda" (d and e, Lumileds Corp.), and "Dragon" (d and e, Osram Opto Semiconductors Corp.) (adopted from Arik *et al*., 2002).

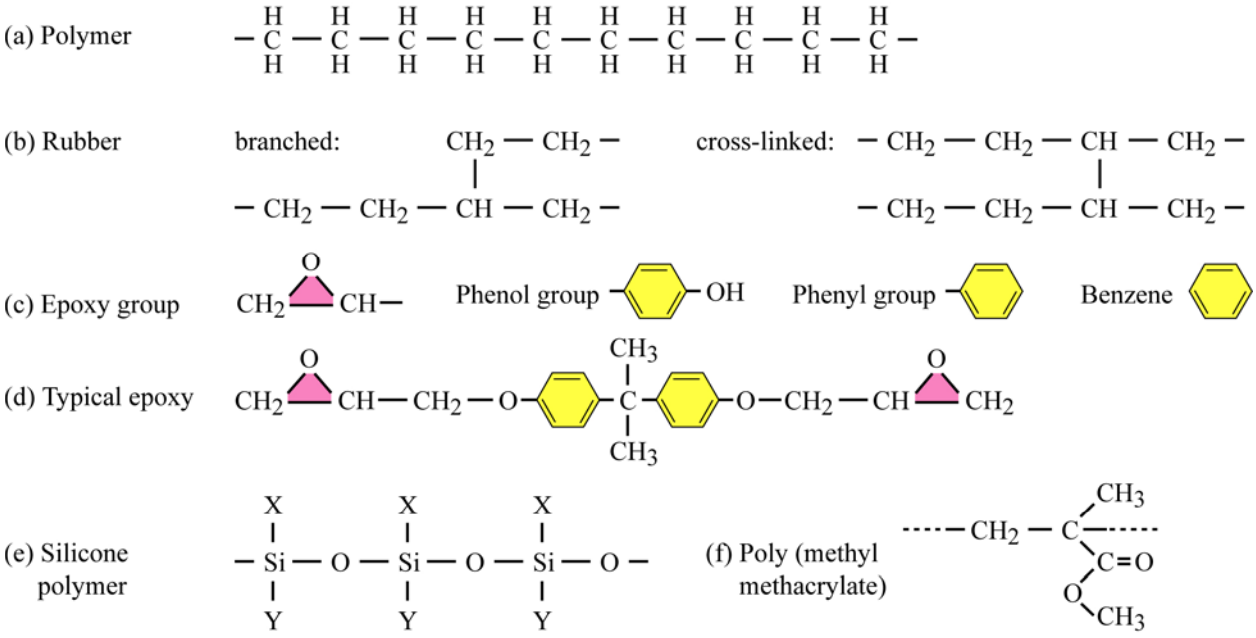

Fig. 11.8. Chemical structures of polymers. Epoxy resins, silicone polymers, and poly methyl methacrylate (PMMA) are used as LED encapsulants. In the silicone structure, X and Y represent atoms or molecules such as H, CH_3 (methyl), C_6H_5 (phenyl).

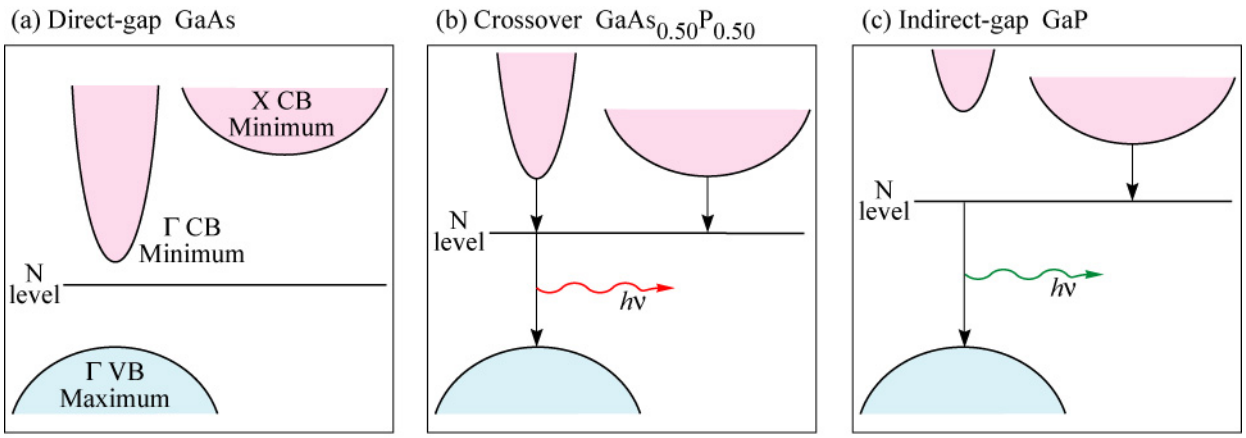

Fig. 12.1. Schematic band structure of GaAs, GaAsP, and GaP. Also shown is the nitrogen level. At a P mole fraction of about 45–50 %, the direct–indirect crossover

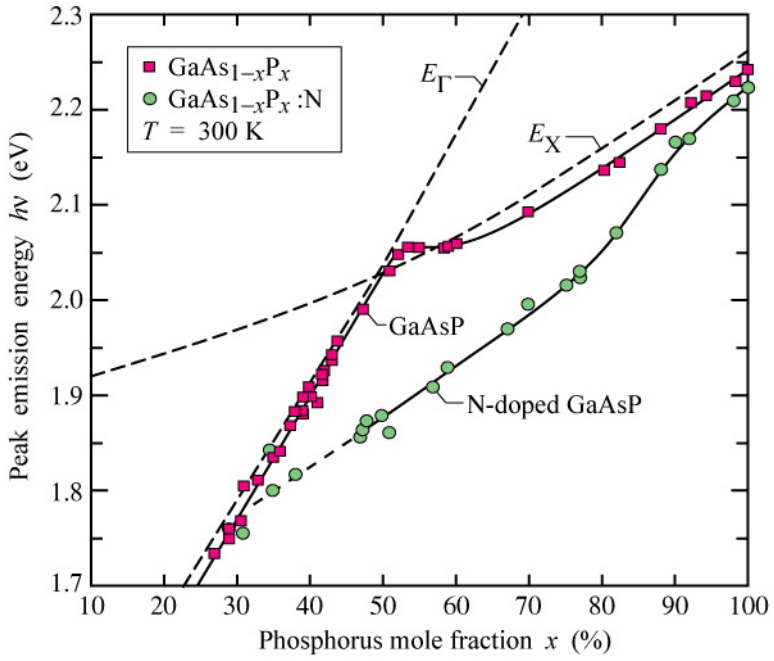

Fig. 12.2. Room-temperature peak emission energy versus alloy composition for undoped and nitrogen-doped GaAsP LEDs injected with a current density of 5 A/cm^2. Also shown is the energy gap of the direct-to-indirect ($E\Gamma$-to-E_X) transition. The direct–indirect crossover occurs at $x \approx 50\,\%$ (after Craford *et al.*, 1972).

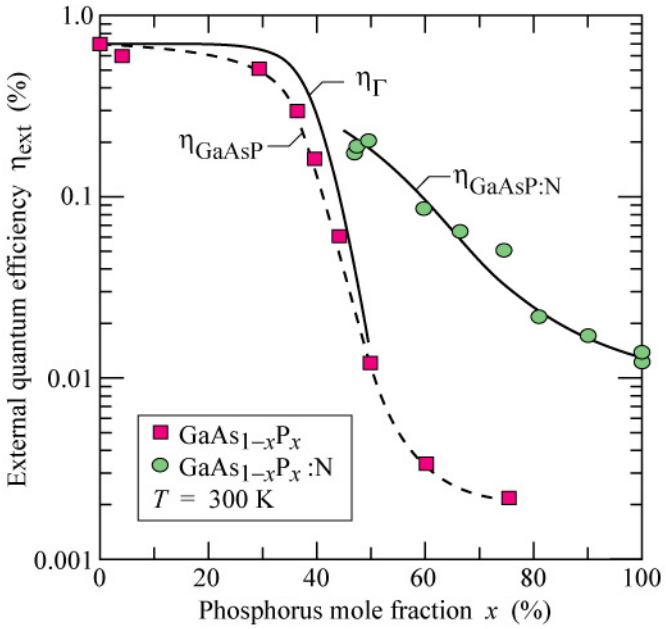

Fig. 12.3. Experimental external quantum efficiency of undoped and N-doped GaAsP versus the P mole fraction. Also shown is the calculated direct-gap (Γ) transition efficiency, η_Γ, and the calculated nitrogen (N) related transition efficiency, η_N (solid lines). Note that the nitrogen-related efficiency is higher than the direct-gap efficiency in the indirect bandgap (x > 50%) regime (after Campbell *et al*., 1974).

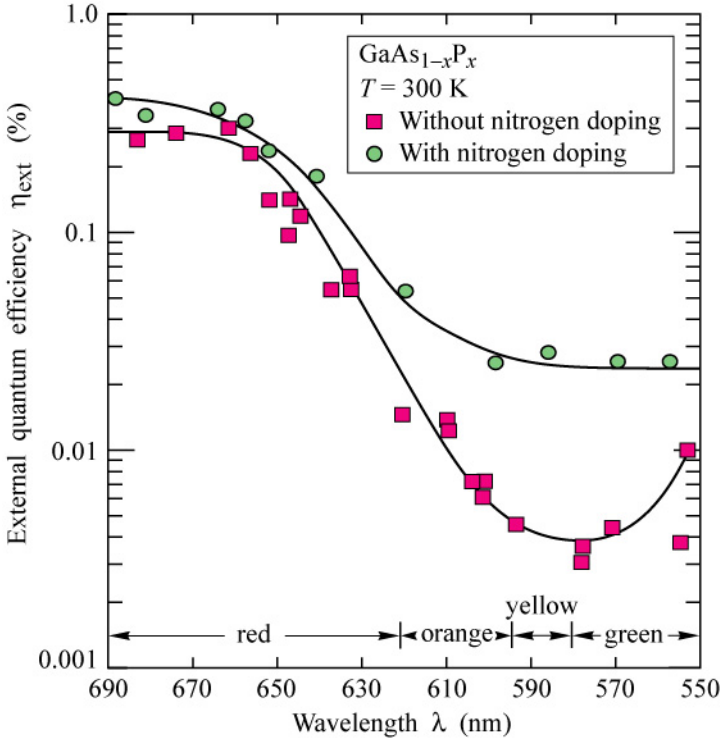

Fig. 12.4. External quantum efficiency versus emission wavelength in undoped and nitrogen-doped $GaAs_{1-x}P_x$ (after Groves *et al*., 1978a, 1978b).

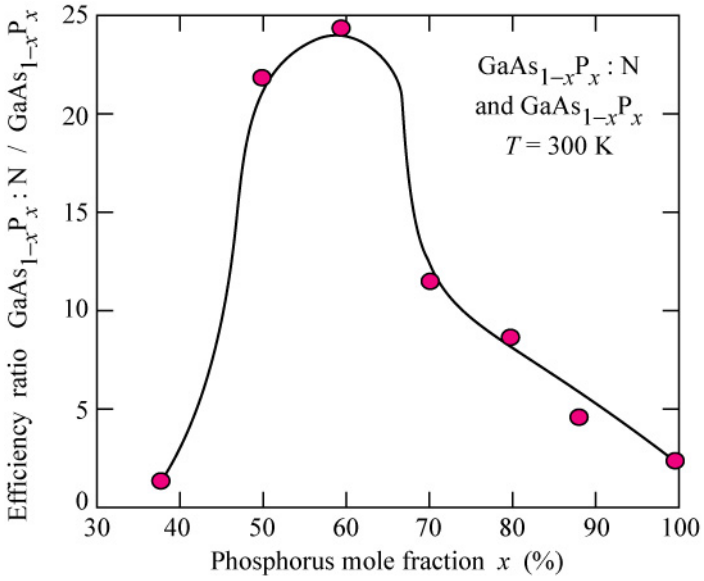

Fig. 12.5. Efficiency ratio between nitrogen-doped and undoped $GaAs_{1-x}P_x$ at 300 K (after Groves *et al.*, 1978a, 1978b).

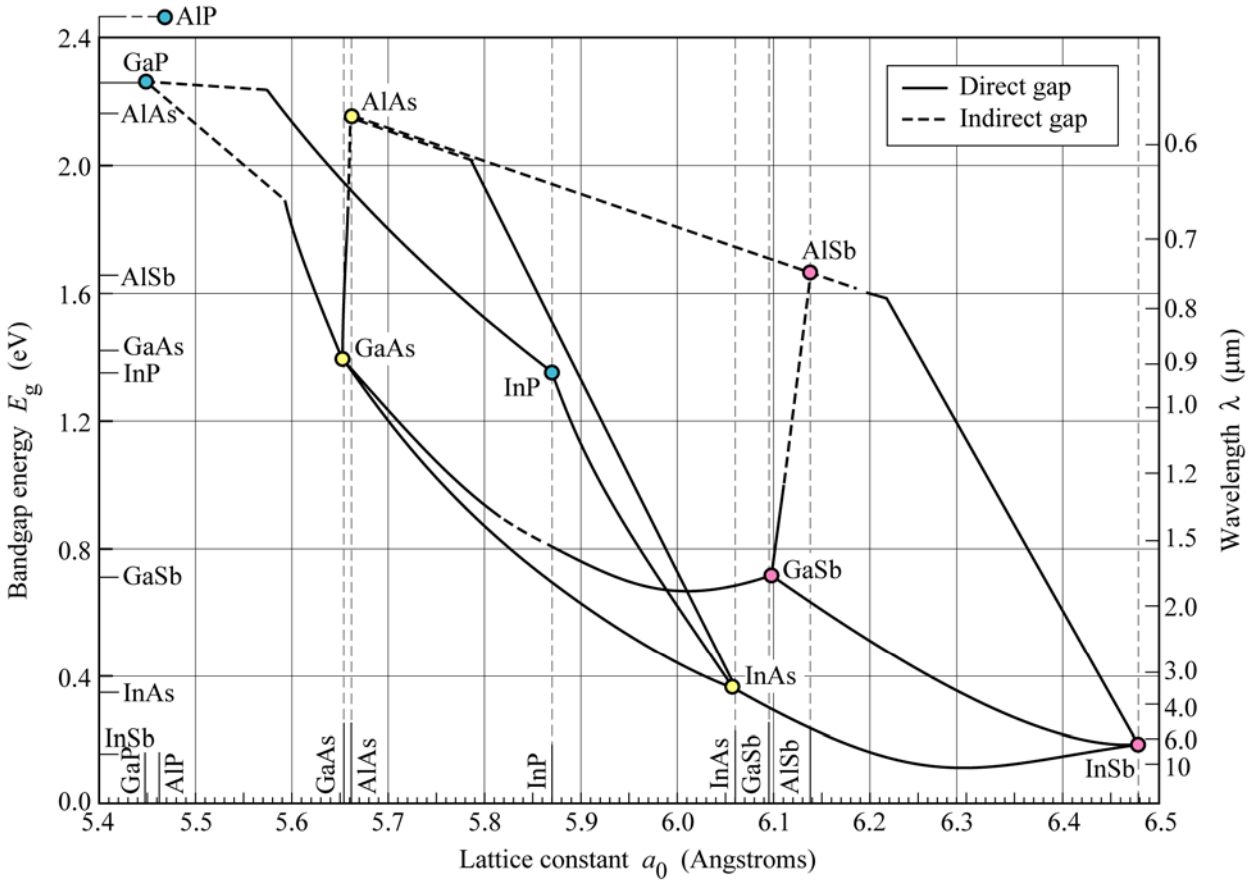

Fig. 12.6. Bandgap energy and lattice constant of various III–V semiconductors at room temperature (adopted from Tien, 1988).

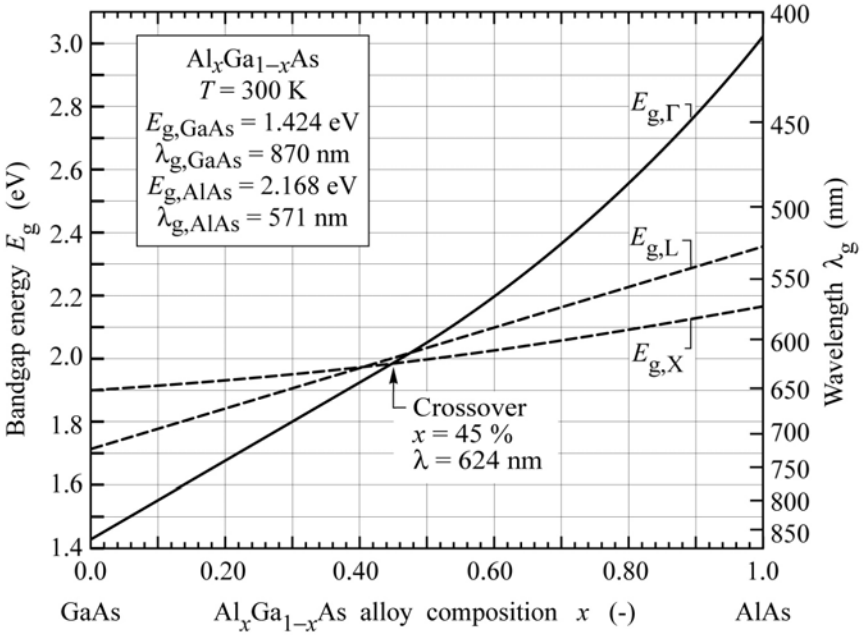

$E_{g,\Gamma}$ /eV = 1.424 + 1.247 x $(0 \le x \le 0.45)$
$E_{g,\Gamma}$ /eV = 1.424 + 1.247x + 1.147$(x - 0.45)$ $(0.45 \le x \le 1.0)$
$E_{g,L}$ /eV = 1.708 + 0.642 x $(0 \le x \le 1.0)$
$E_{g,X}$ /eV = 1.900 + 0.125 x + 0.143 x^2 $(0 \le x \le 1.0)$

Fig. 12.7. Bandgap energy and emission wavelength of AlGaAs at room temperature. E_Γ denotes the direct gap at the Γ point and E_L and E_X denote the indirect gap at the L and X point of the Brillouin zone, respectively (adopted from Casey and Panish, 1978).

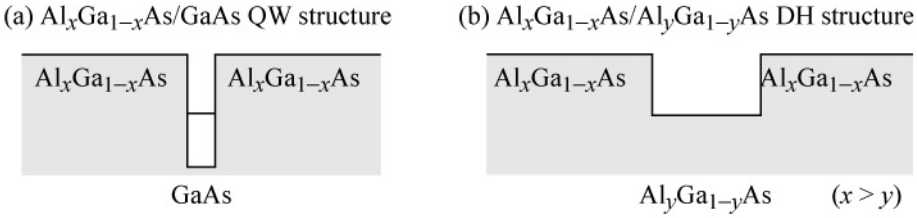

Fig. 12.8. Band diagrams of AlGaAs/GaAs structures suited for emission in the red part of the visible spectrum. (a) AlGaAs/GaAs quantum well (QW) structure with a thin GaAs well. (b) AlGaAs/AlGaAs double heterostructure (DH) with an AlGaAs active region.

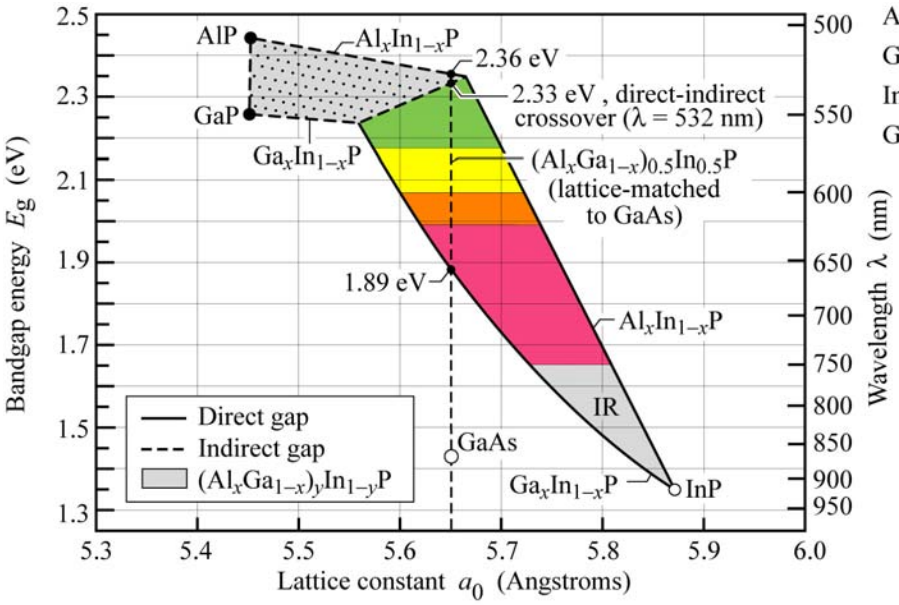

AlP: E_g = 2.45 eV, a_0 = 5.4510 Å
GaP: E_g = 2.26 eV, a_0 = 5.4512 Å
InP: E_g = 1.35 eV, a_0 = 5.8686 Å
GaAs: E_g = 1.424 eV, a_0 = 5.6533 Å

Fig. 12.9. Bandgap energy and corresponding wavelength versus lattice constant of $(Al_xGa_{1-x})_yIn_{1-y}P$ at 300 K. The vertical dashed line shows $(Al_xGa_{1-x})_{0.5}In_{0.5}P$ lattice matched to GaAs (adopted from Chen *et al.*, 1997).

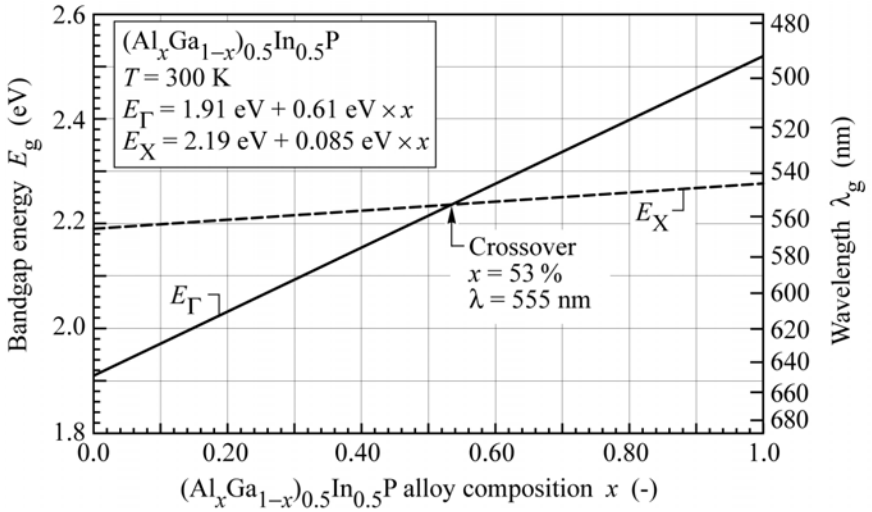

Fig. 12.10. Bandgap energy and emission wavelength of unordered AlGaInP lattice-matched to GaAs at room temperature. E_Γ denotes the direct gap at the Γ point and E_X denotes the indirect gap at the X point of the Brillouin zone (adopted from Prins *et al*., 1995 and Kish and Fletcher, 1997).

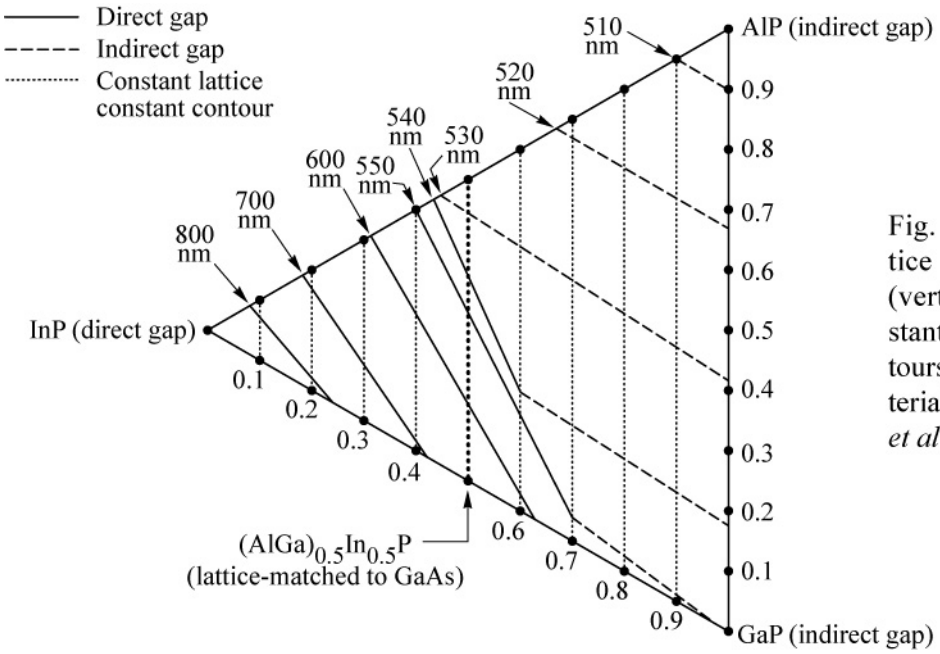

Fig. 12.11. Constant lattice constant contours (vertical lines) and constant emission line contours of the AlGaInP materials system (after Chen *et al*., 1997).

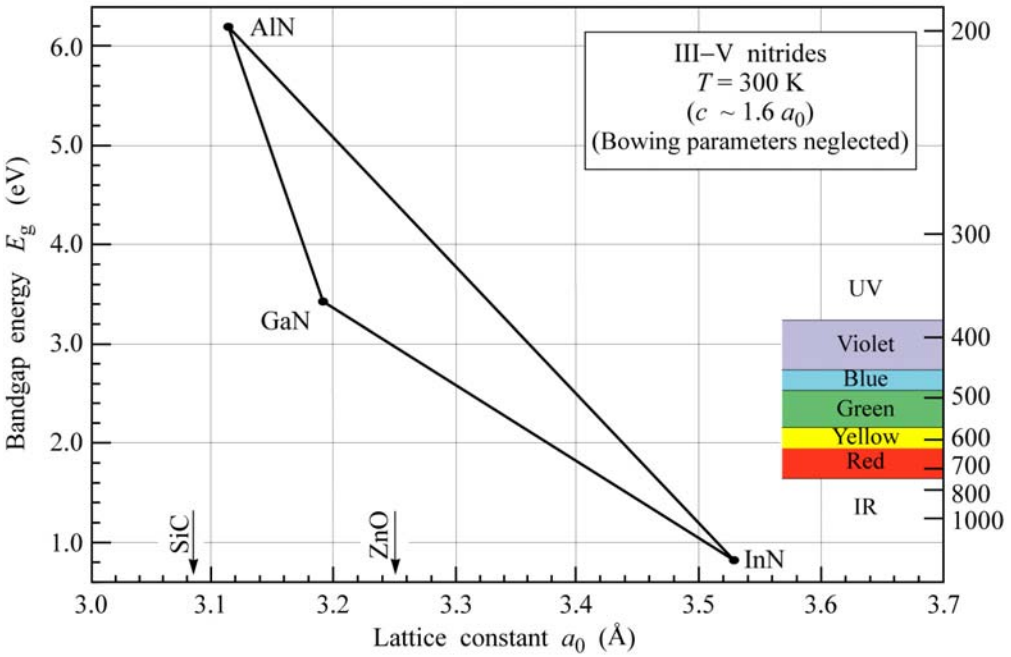

Fig. 12.12. Bandgap energy versus lattice constant of III–V nitride semiconductors at room temperature.

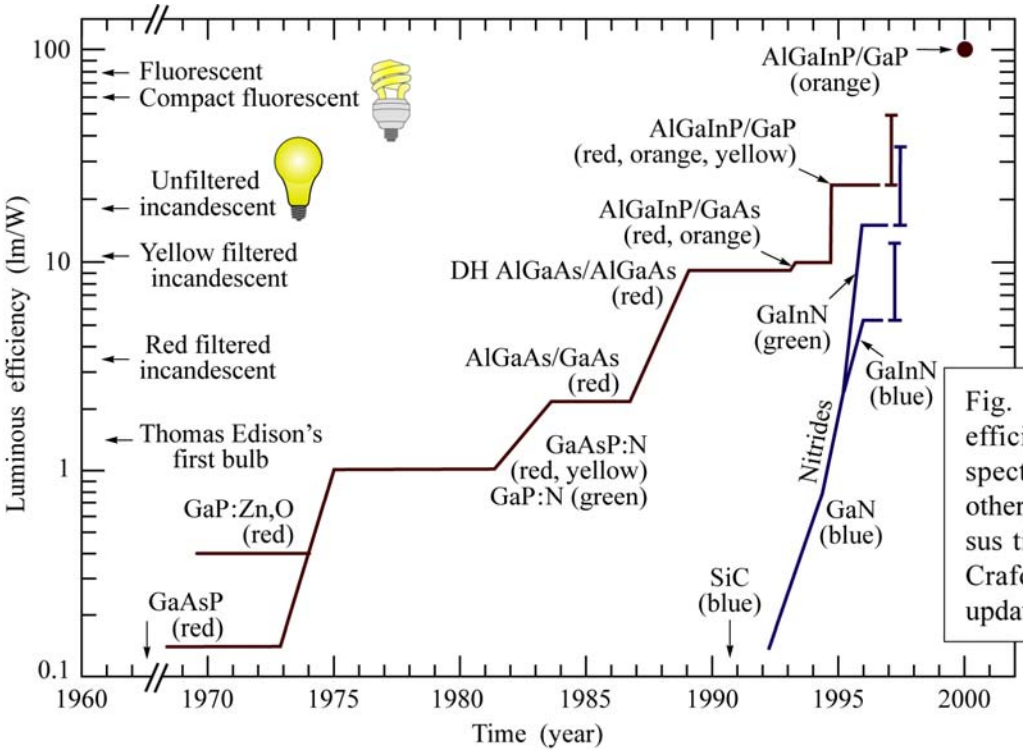

Fig. 12.13. Luminous efficiency of visible-spectrum LEDs and other light sources versus time (adopted from Craford, 1997, 1999, updated 2000).

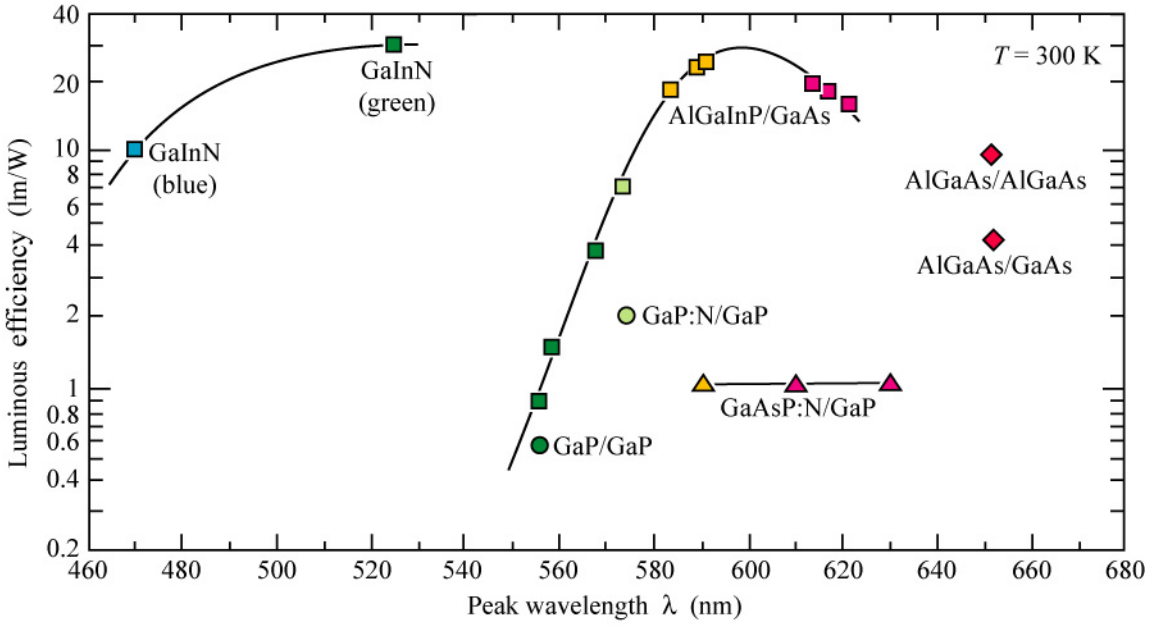

Fig. 12.14. Overview of luminous efficiency of visible LEDs made from the phosphide, arsenide, and nitride material system (adopted from United Epitaxy Corporation, 1999; updated 2000).

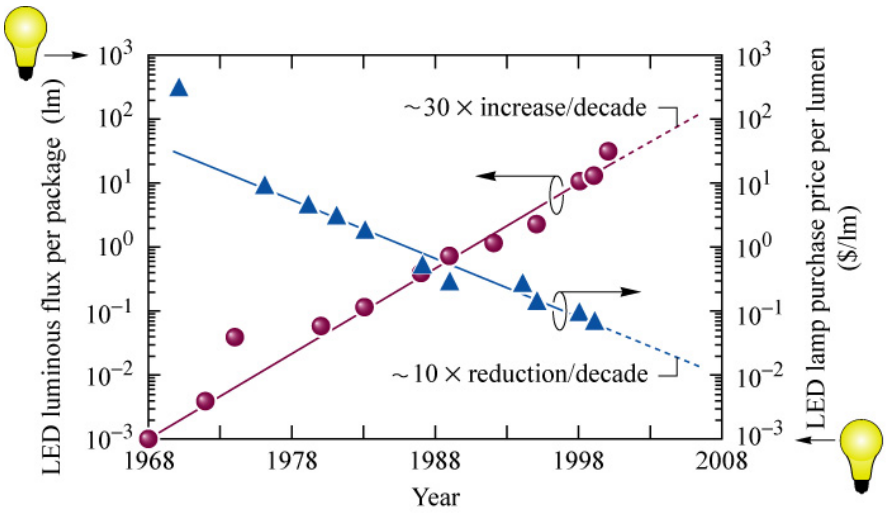

Fig. 12.15. LED luminous flux per package and LED lamp purchase price per lumen versus year. Also shown are the values for a 60 W incandescent tungsten-filament light bulb with a luminous efficiency of ~17 lm/W and a luminous flux of 1000 lm with an approximate price of 1.00 US$ (after Krames *et al.*, 2000).

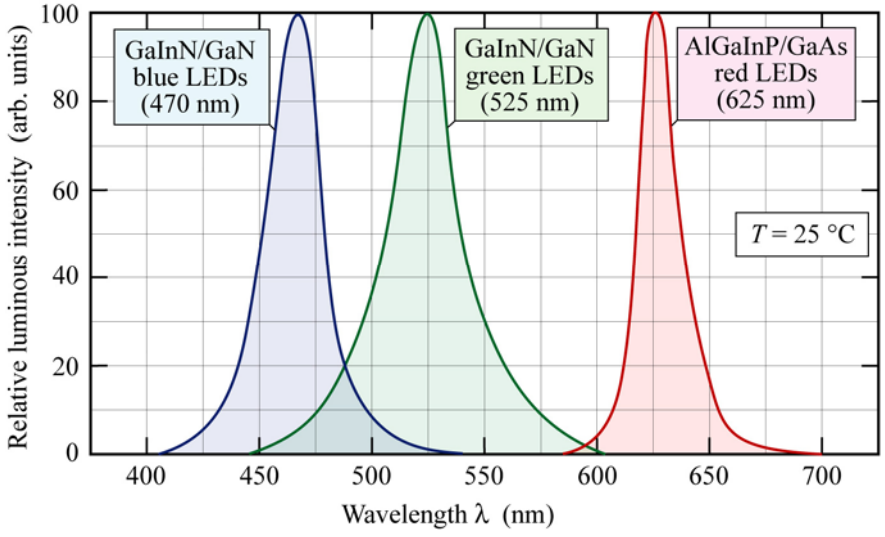

Fig. 12.16. Typical emission spectrum of GaInN/GaN blue, GaInN/GaN green, and AlGaInP/GaAs red LEDs at room temperature (after Toyoda Gosei Corp., 2000).

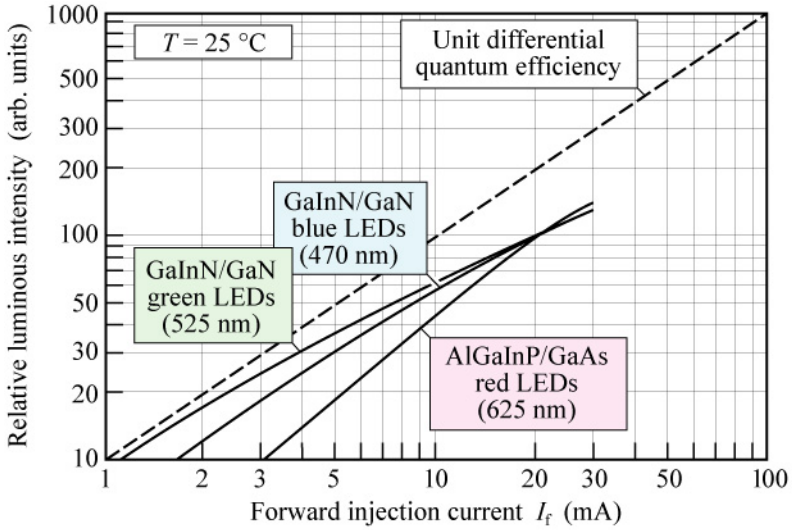

Fig. 12.17. Typical light output power vs. injection current of GaInN/GaN blue, GaInN/GaN green, and AlGaInP/GaAs red LEDs at room temperature (adopted from Toyoda Gosei Corp., 2000).

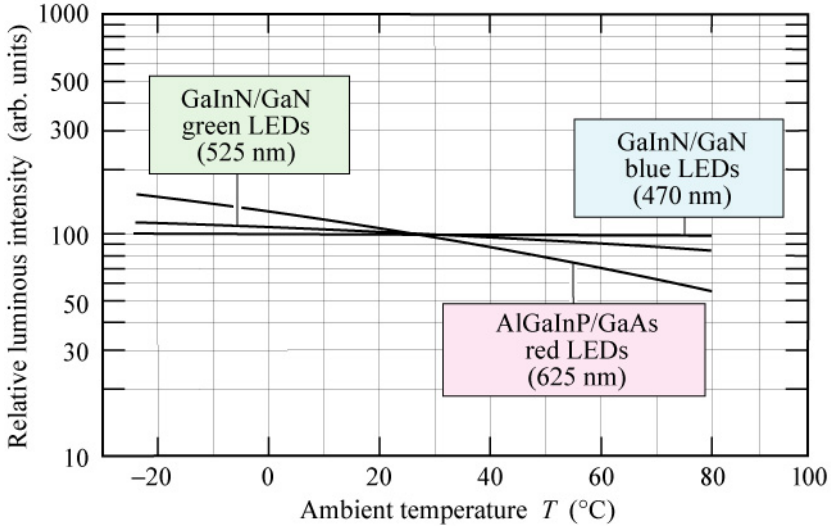

Fig. 12.18. Typical output intensity of GaInN/GaN blue, GaInN/GaN green, and AlGaInP/GaAs red LEDs versus ambient temperature (after Toyoda Gosei Corp., 2000).

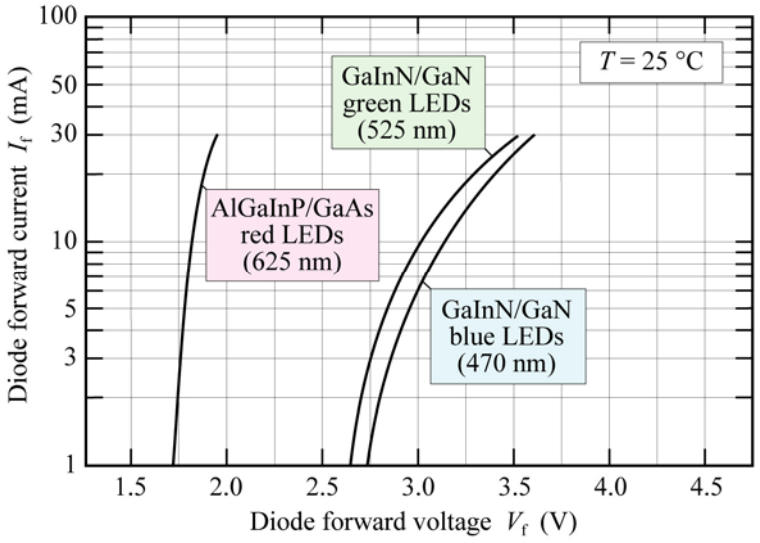

Fig. 12.19. Typical forward current–voltage (I–V) characteristic of GaInN/GaN blue, GaInN/GaN green, and AlGaInP/GaAs red LEDs at room temperature (after Toyoda Gosei Corporation, 2000).

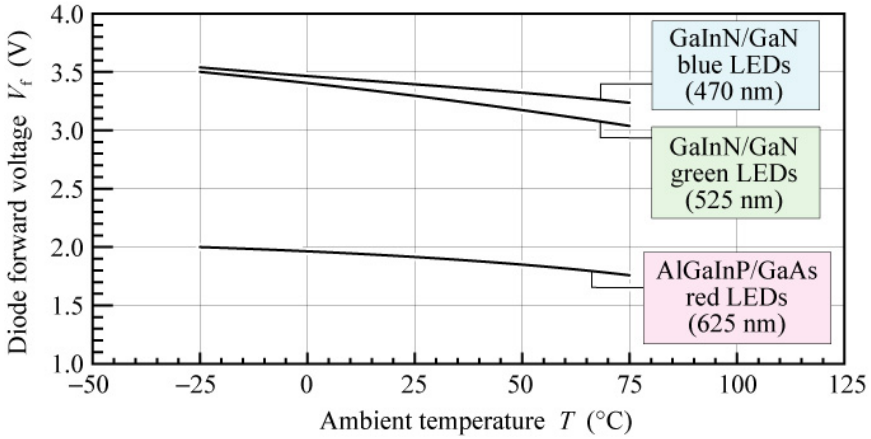

Fig. 12.20. Typical diode forward voltage at a current of 30 mA of GaInN/GaN blue, GaInN/GaN green, and AlGaInP/GaAs red LEDs versus temperature (after Toyoda Gosei Corp., 2000).

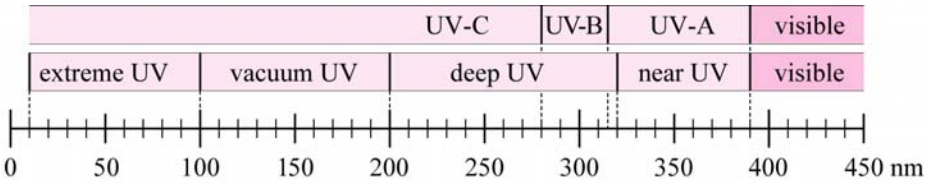

Fig. 13.1. Nomenclature of UV radiation versus wavelength (after International, 1932).

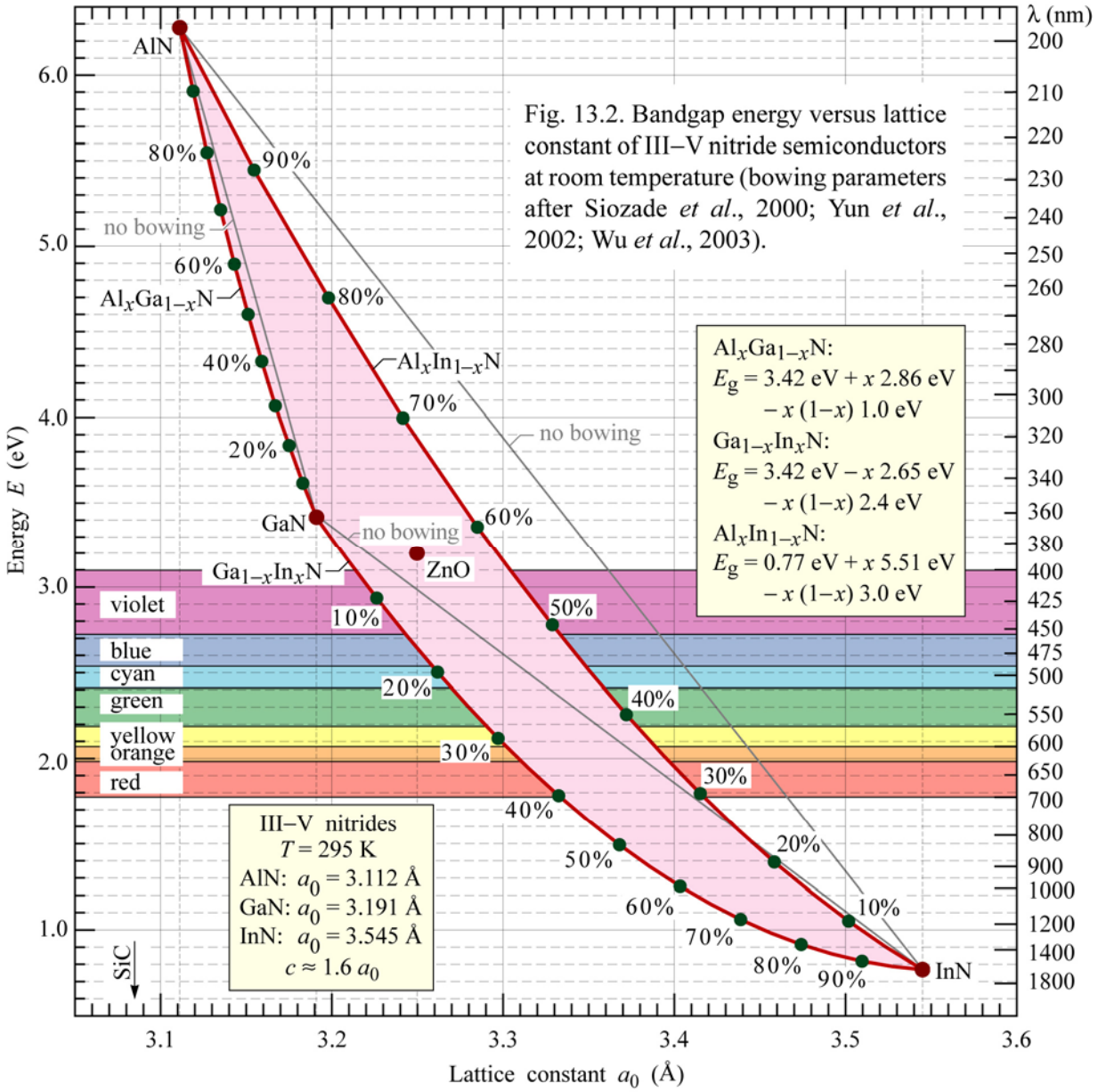

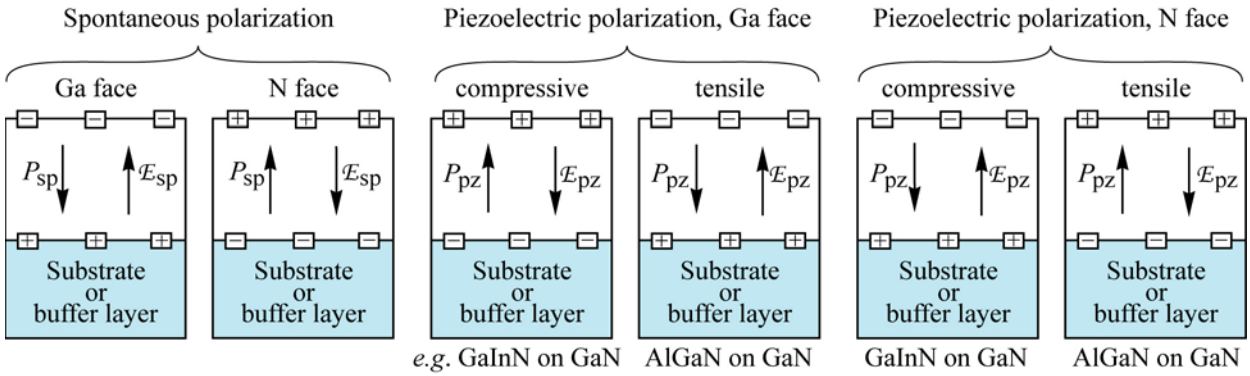

Fig. 13.3. Surface charges and direction of electric field and polarization field for spontaneous and piezoelectric polarization in III–V nitrides for Ga and N face orientation.

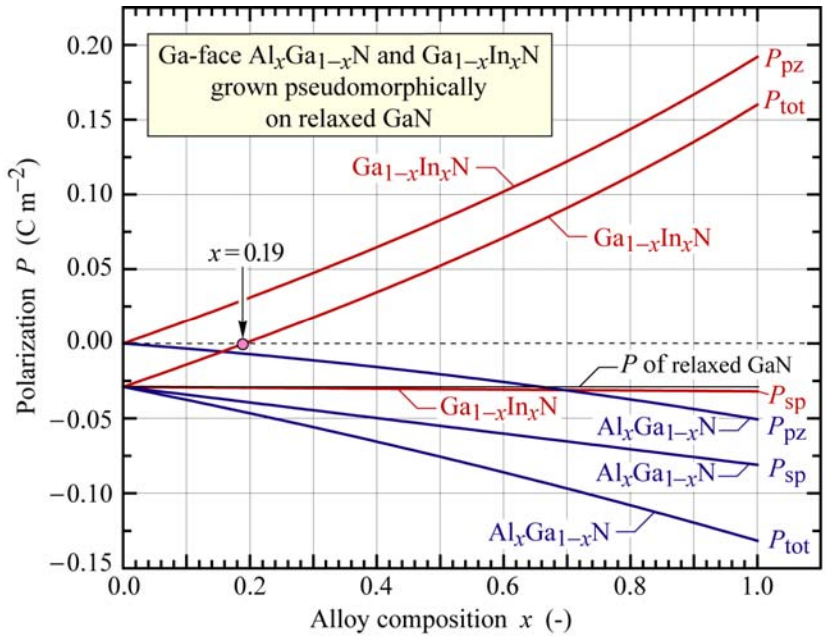

Fig. 13.4. Magnitude and direction of spontaneous and piezoelectric polarization in GaInN and AlGaN grown pseudomorphically on relaxed GaN. Relaxed GaN has a spontaeous polarization, but no piezoelectric polarization (after Gessmann *et al.*, 2002).

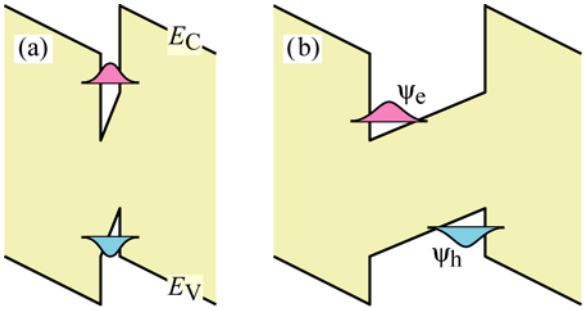

Fig. 13.5. Schematic band diagram of (a) thin and (b) thick AlGaN/GaN active region with poalization fields for Ga-face growth (substrate on right-hand side).

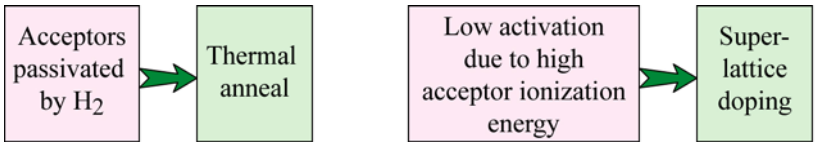

Fig. 13.6. Specific problems of p-type doping in GaN and their solution.

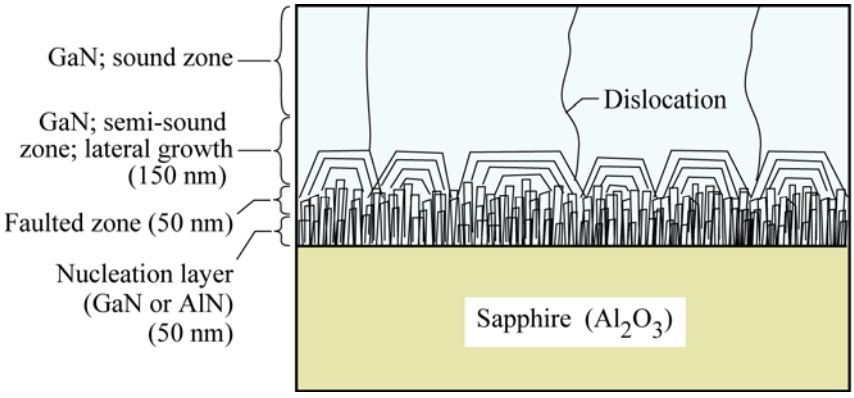

Fig. 13.7. Dislocation structure of a GaN epitaxial layer grown on sapphire by means of the GaN or AlN nucleation layer developed by Amano *et al.* (1986). The nucleation layer is normally grown at 500 °C, much lower than the following GaN epitaxial layers (after Nakamura and Fasol., 1997).

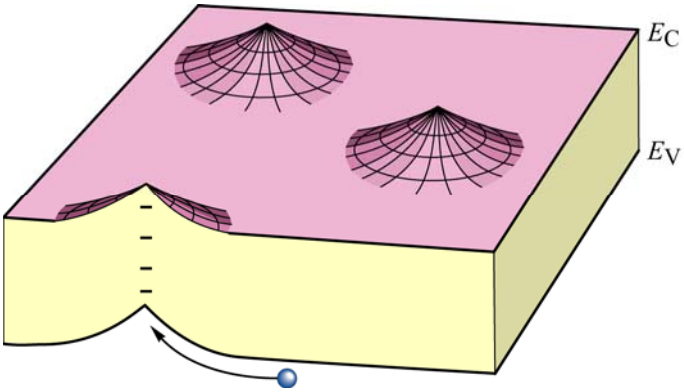

Fig. 13.8. Bandgap diagram of semiconductor having negatively charged dislocations. Holes are attracted to disclocation lines where they must ultimately recombine with electrons.

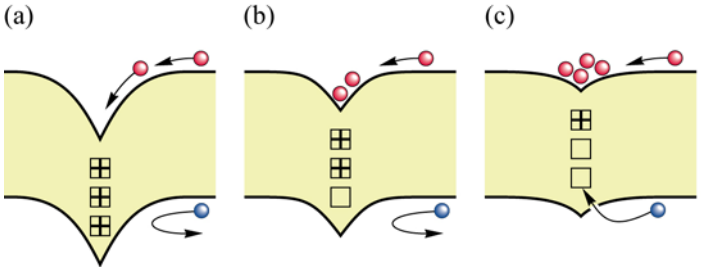

Fig. 13.9. Recombination in a positively charged dislocation. (a)−(c) Sequence shows electrons accumulating in the potential minimum thereby screening the dislocation potential and allowing holes to recombine.

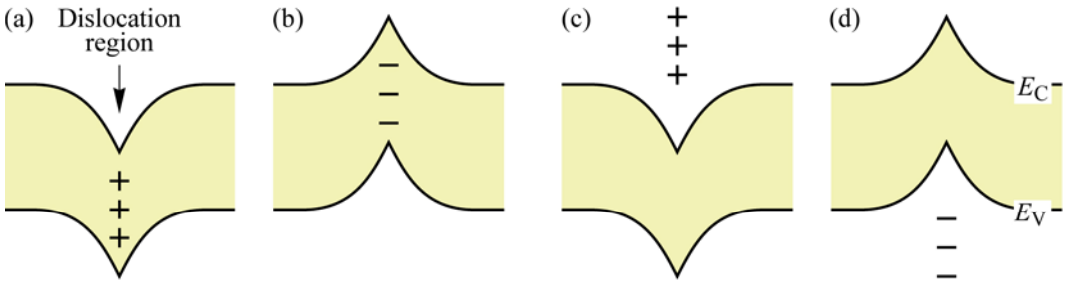

Fig. 13.10. Band diagram of dislocation: (a) donor states in gap, (b) acceptor states in gap, (c) donor states in conduction band, and (d) acceptor states in valence band. Whereas (a) and (b) lead to non-radiative recombination, (c) and (d) no not.

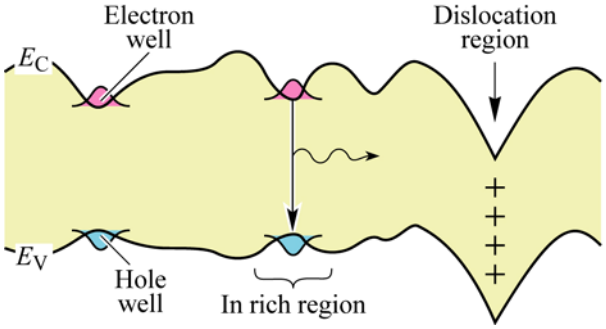

Fig. 13.11. Band diagram of GaInN having clusters of In rich regions which spatially localize carriers and pevent them from diffusing to dislocations.

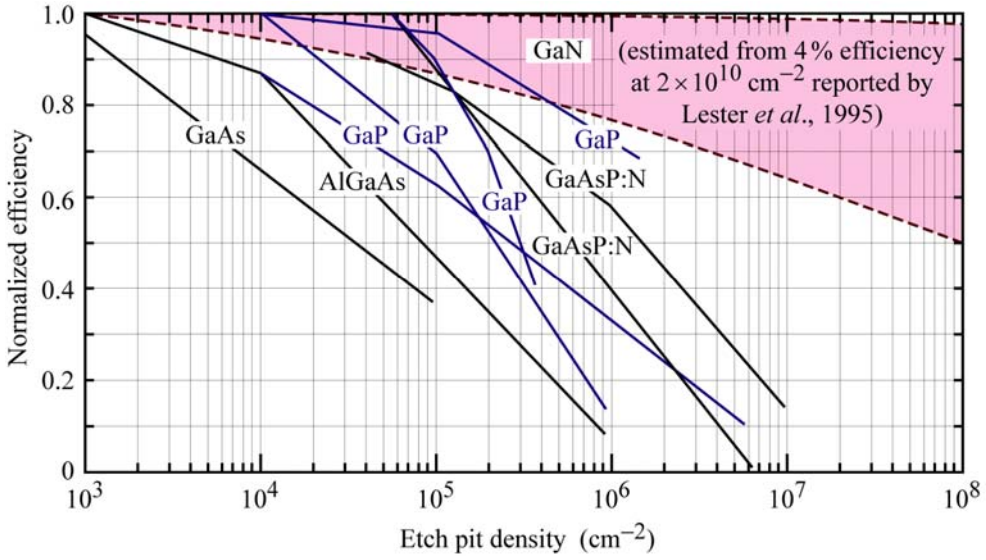

Fig. 13.12. Dependence of radiative efficiency on etch pit density (III–V arsenide and phosphide data adopted from Lester *et al.*, 1995; III–V nitride data estimated by the author of this book).

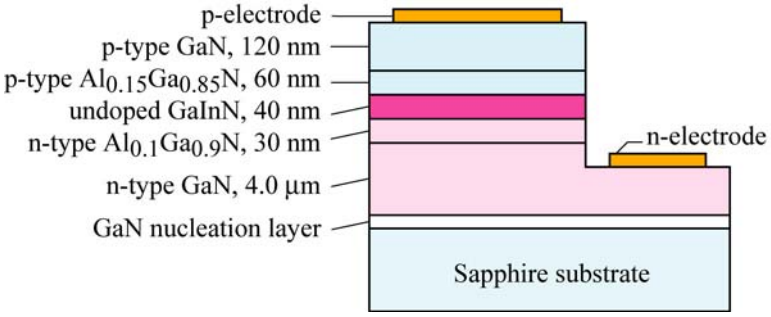

Fig. 13.13. Layer structure of GaInN UV LED grown on saphire substrate emitting at 370 nm (after Mukai *et al.*, 1998).

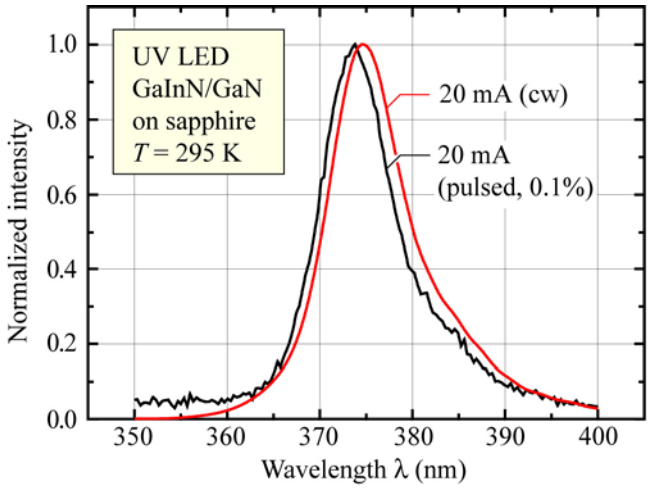

Fig. 13.14. Room temperature emission spectrum of commercial 375 nm UV LED (Nichia Corp.) under cw and pulsed condition.

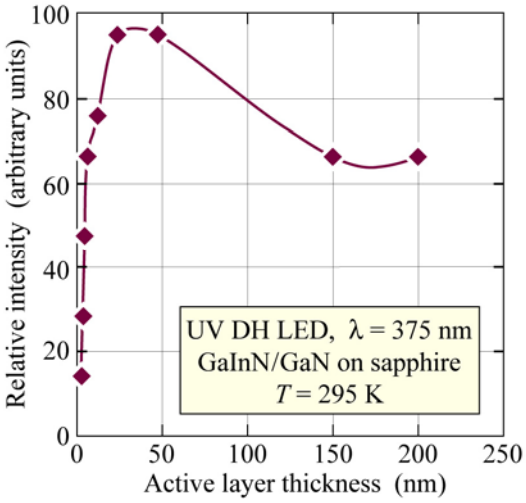

Fig. 13.15. Room temperature emission intensity as a function of GaInN active layer thickness for double heterostructure UV LEDs emitting at 375 nm (after Mukai *et al*., 1998).

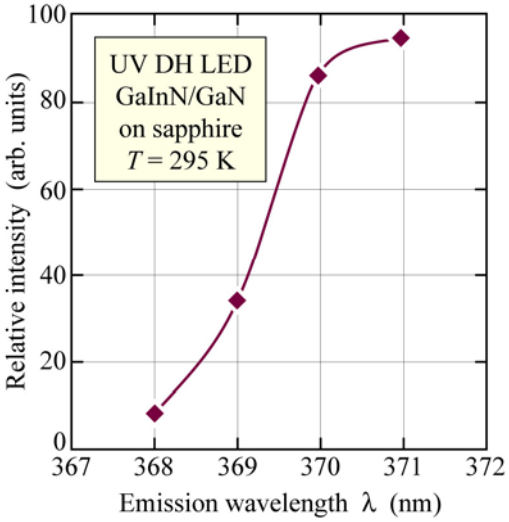

Fig. 13.16. Room temperature intensity as a function of emission wavelength for GaInN double heterostructure UV LEDs (after Mukai *et al*., 1998).

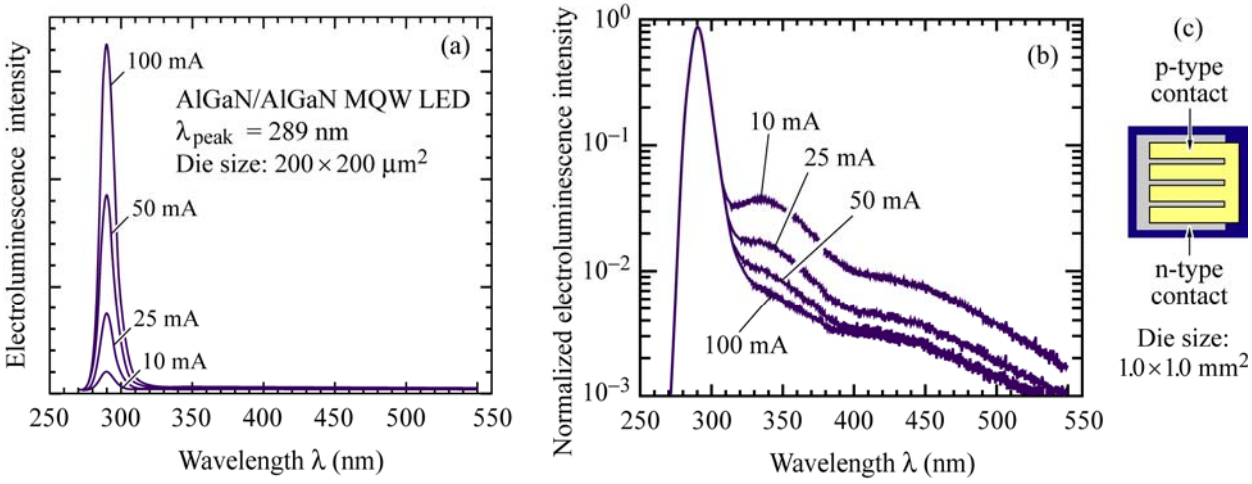

Fig. 13.17. Emission spectrum of deep-UV AlGaN/AlGaN multiple quantum well LED for different injection-currents on (a) linear and (b) logarithmic scale. An interdigitated contact geometry, as shown in (c), was used for large-area dies (after Fischer *et al*., 2004).

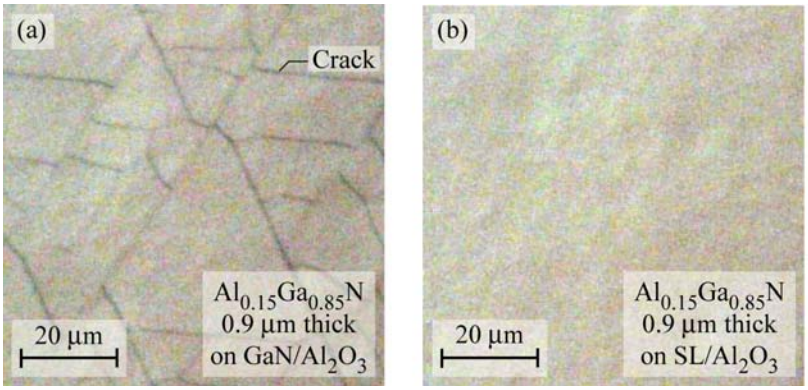

Fig. 13.18. Optical micrograph of $Al_{0.15}Ga_{0.85}N$ layer grown (a) without and (b) with a strain-compensating $AlN/Al_{0.45}Ga_{0.55}N$ superlattice (SL). The SL has 10 periods and equal well and barrier thickness of 10 nm. Angles between crack lines frequently are 60° or 120°.

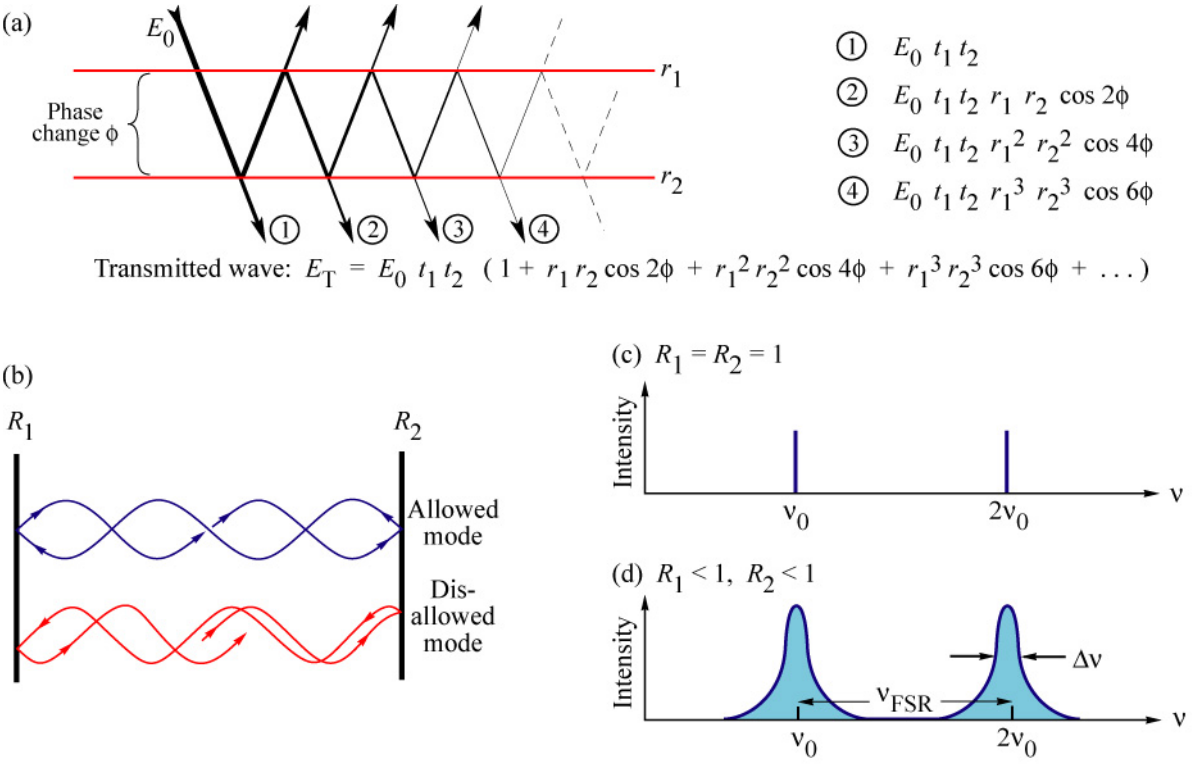

Fig. 14.1. (a) Transmission of a light wave with electric field ampltitude E_0 through a Fabry–Perot resonator. (b) Schematic illustration of allowed and disallowed optical modes in a Fabry–Perot cavity consisting of two coplanar reflectors. Optical mode density for a resonator with (c) no mirror losses ($R_1 = R_2 = 100$ %) and (d) mirror losses.

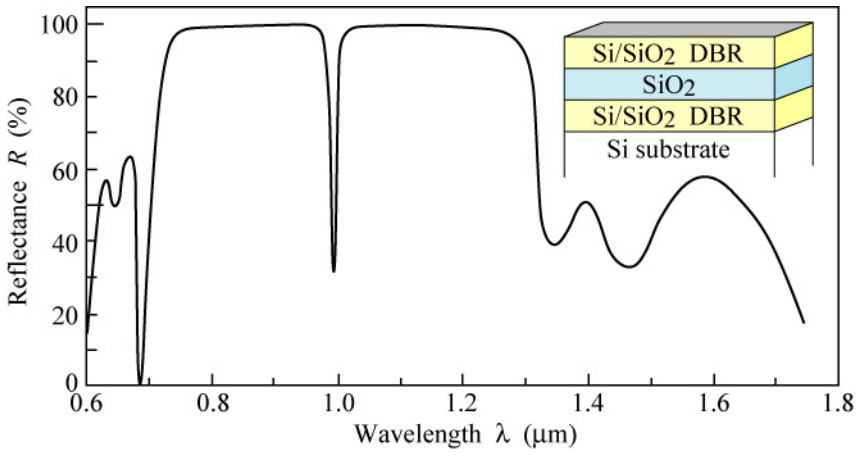

Fig. 14.2. Reflectance of a Fabry–Perot cavity consisting of two Si/SiO_2 reflectors and a SiO_2 center region. At the resonance wavelength ($\lambda \approx 1000$ nm), the reflectivity has a sharp dip.

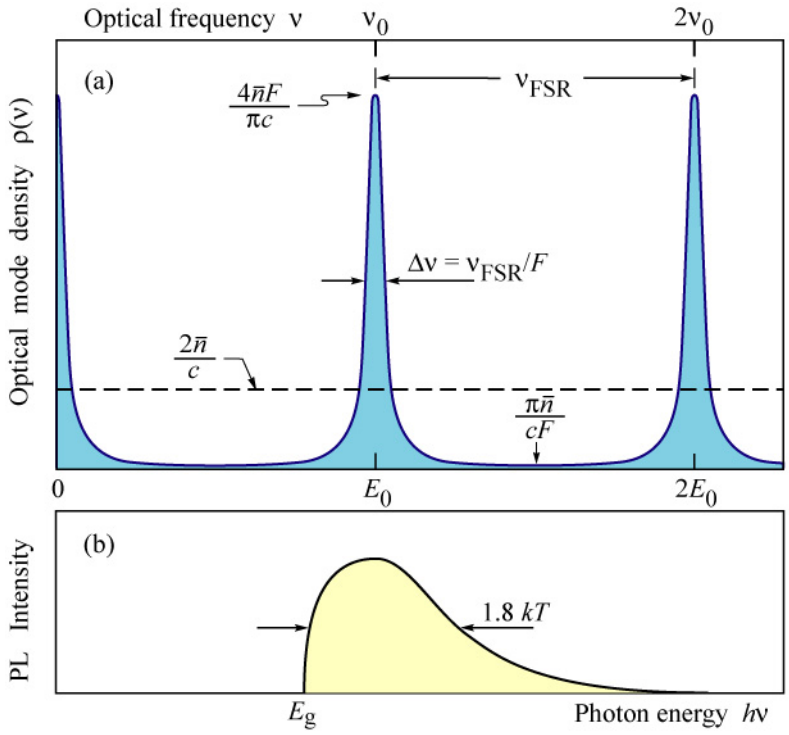

Fig. 14.3. (a) Optical mode density of a one-dimensional planar microcavity (solid line) and of homogeneous one-dimensional space. (b) Theoretical shape of the lminescence spectrum of bulk semiconductors.

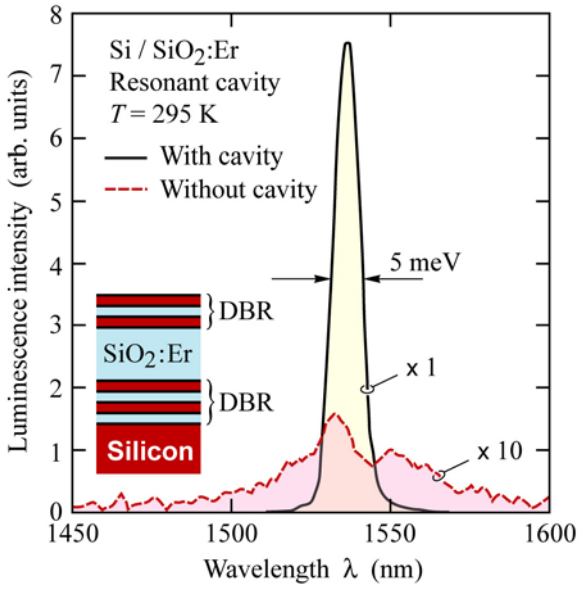

Fig. 14.4. Photoluminescence spectra of Er-doped SiO_2. One of the spectra is for Er-doped SiO_2 located in a cavity resonant at 1540 nm. The other spectrum is without a cavity. An emission enhancement factor greater than 50 is found (after Schubert *et al.*, 1992b).

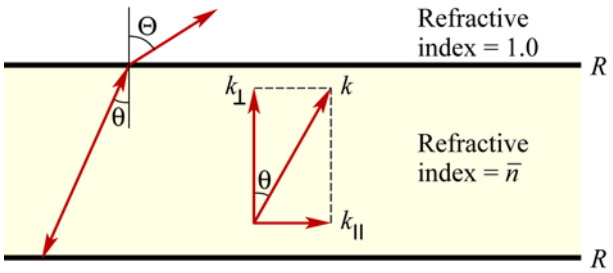

Fig. 14.5. Perpendicular and parallel component of wavevector k for light propagating in resonant cavity.

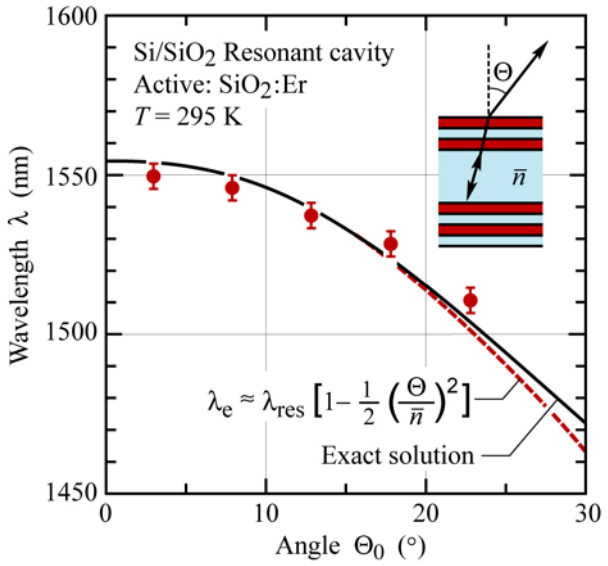

Fig. 14.6. Peak emission wavelength as a function of polar angle for a planar Si/SiO_2:Er resonant cavity (after Schubert *et al.*, 1992b).

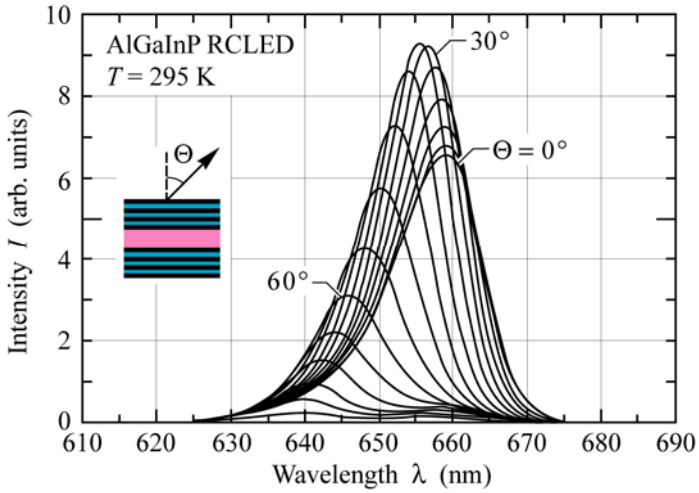

Fig. 14.7. Emission spectra of AlGaInP RCLED for different polar angles. The long-wavelength part of the QW emission is emitted in the forward direction (0°). The shorter wavelengths are emitted off-axis. When measured with an integrating sphere, an 18 nm wide spectrum (FWHM) is found (after Streubel *et al.*, 2002).

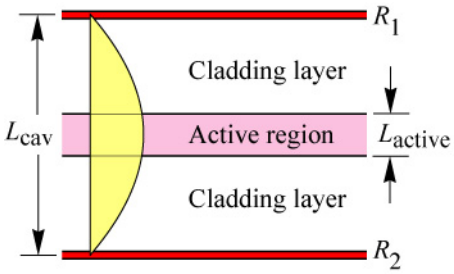

Fig. 15.1. Schematic illustration of a resonant cavity consisting of two metal mirrors with reflectivity R_1 and R_2. The active region has a thickness L_{active} and an absorption coefficient α. Also shown is the standing optical wave. The cavity length is L_{cav} is equal to λ/2.

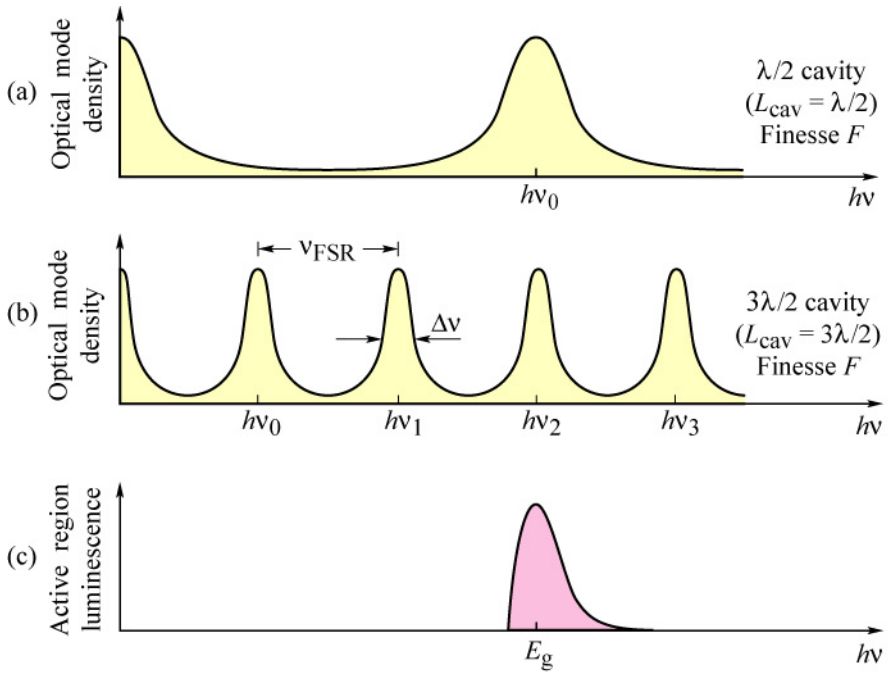

Fig. 15.2. Optical mode density for (a) a short and (b) a long cavity with the same finesse F. (c) Spontaneous free space emission spectrum of an LED active region. The spontaneous emission spectrum has a better overlap with the short-cavity mode spectrum compared with the long cavity mode spectrum.

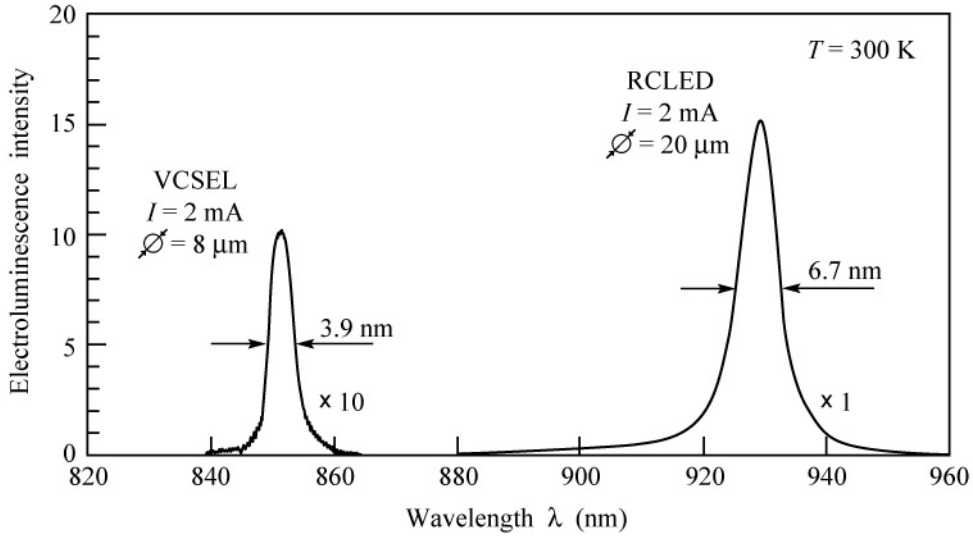

Fig. 15.3. Spontaneous electroluminescence spectrum of a vertical-cavity surface-emitting laser (VCSEL) emitting at 850 nm and of a resonant-cavity light-emitting diode (RCLED) emitting at 930 nm. The drive current for both devices is 2 mA. The VCSEL spectrum is multiplied by a factor of 10. The threshold current of the VCSEL is 7 mA (after Schubert *et al*., 1996).

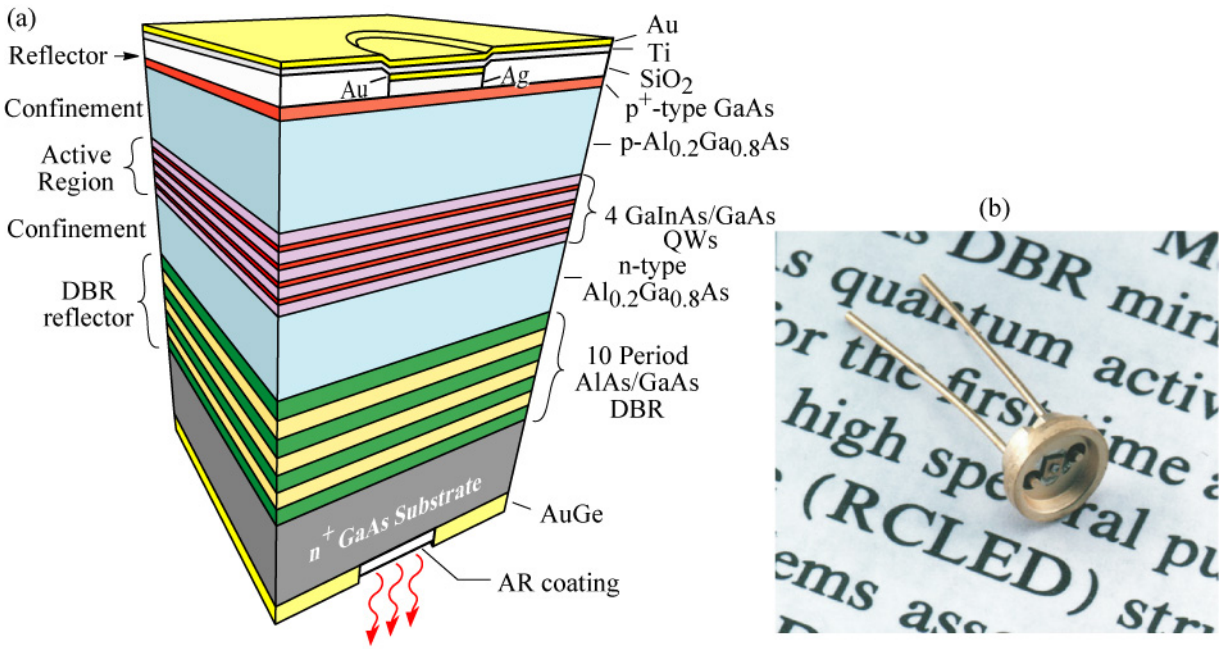

Fig. 15.4. (a) Schematic structure of a substrate-emitting GaInAs/GaAs RCLED consisting of a metal top reflector and a bottom distributed Bragg reflector (DBR). The RCLED emits at 930 nm. The reflectors are an AlAs/GaAs DBR and a Ag top reflector. (b) Picture of the first RCLED (after Schubert *et al*., 1994).

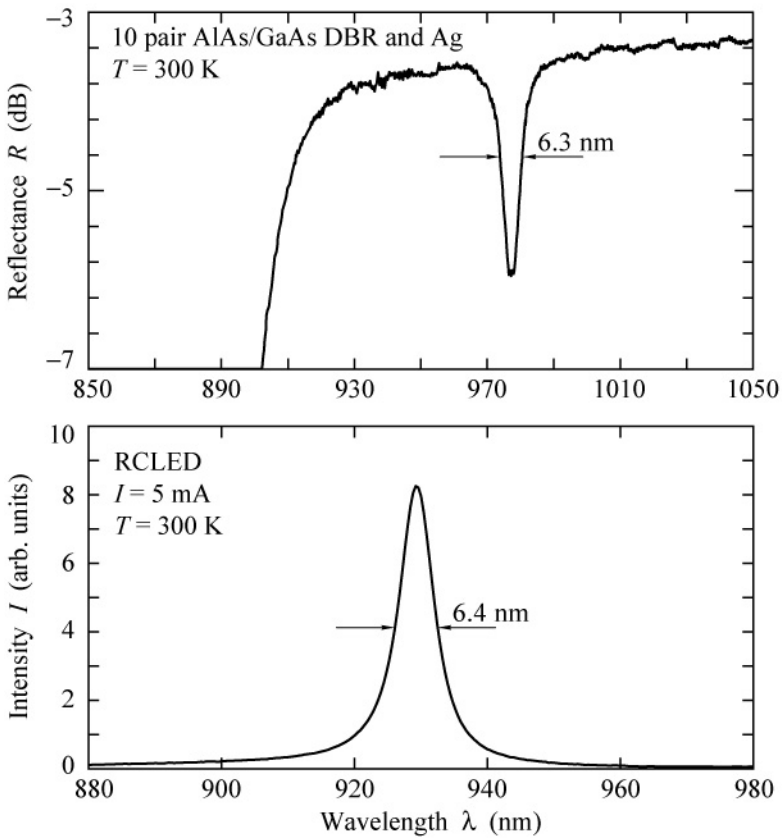

Fig. 15.5. (a) Reflectance of a resonant cavity consisting of a 10-pair AlAs/GaAs distributed Bragg reflector and an Ag reflector. (b) Emission spectrum of a RCLED consisting of a 10-pair AlAs/GaAs distributed Bragg reflector and an Ag reflector (after Schubert *et al*., 1994).

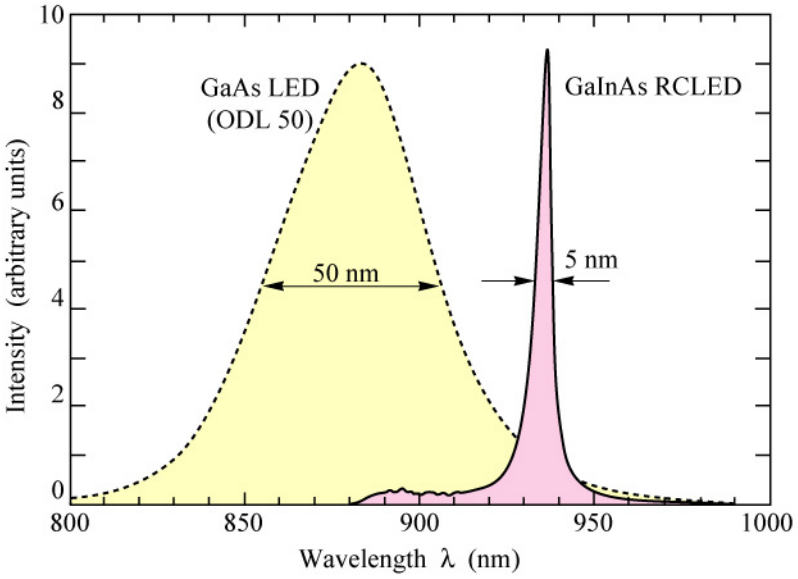

Fig. 15.6. Comparison of the emission spectra of a GaAs LED emitting at 870 nm (AT&T ODL 50 product) and a GaInAs RCLED emitting at 930 nm (after Hunt *et al.*, 1993).

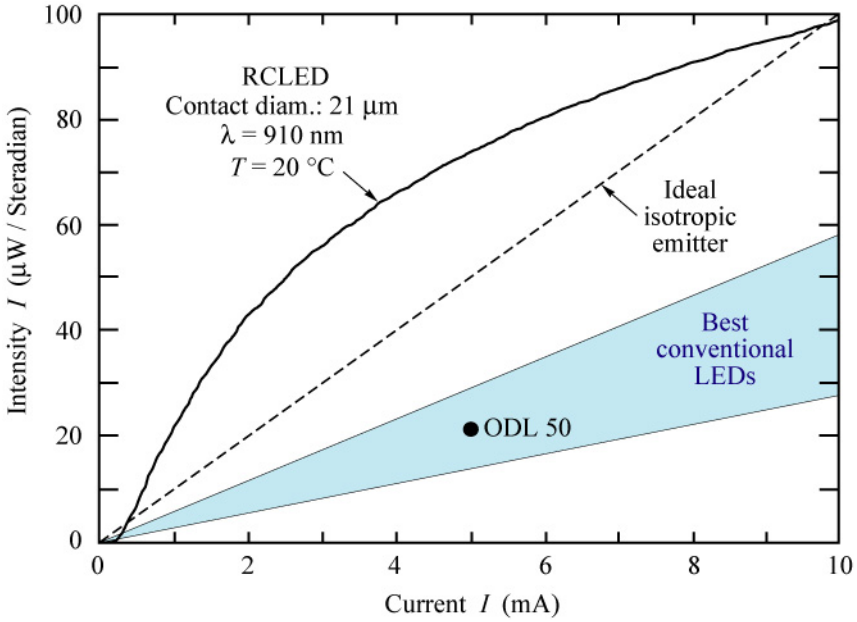

Fig. 15.7. Light-versus-current curves of a GaInAs/GaAs RCLED and of the *ideal isotropic emitter*. The ideal isotropic emitter is a hypothetial device emitting light isotropically with a quantum efficiency of 100%. The shaded region shows the intensity of the best conventional LEDs. The ODL 50 is a commercial LED product (after Schubert *et al.*, 1994).

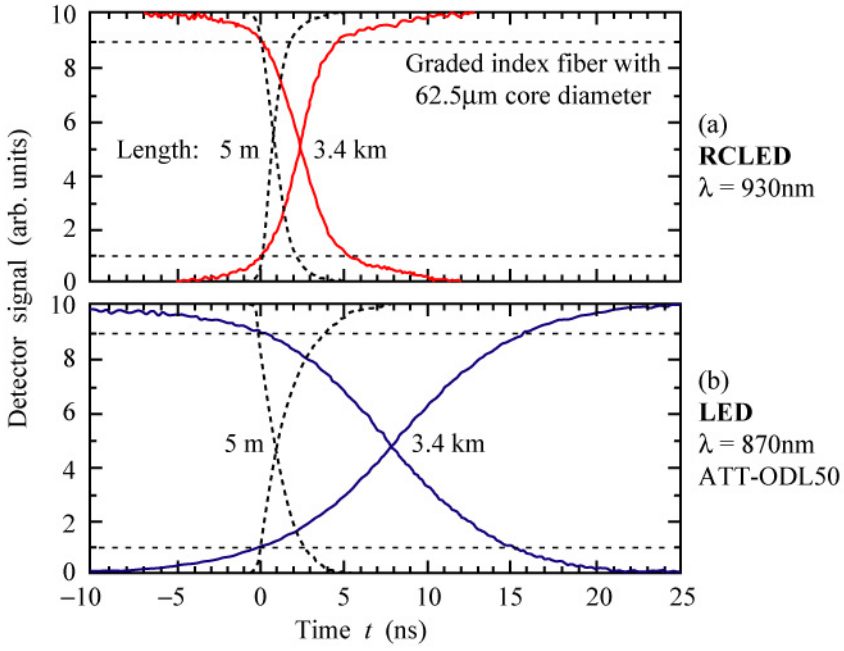

Fig. 15.8. Signal detected at the receiver end of a graded-index multimode fiber with a core diameter of 62.5 μm using an (a) GaInAs RCLED and (b) GaAs LED source. After a short transmission distance of 5 m, no marked difference is found for the two sources. After a trans-mission distance of 3.4 km, the RCLED exhibits much less pulse broadening than the LED (after Hunt *et al*., 1993).

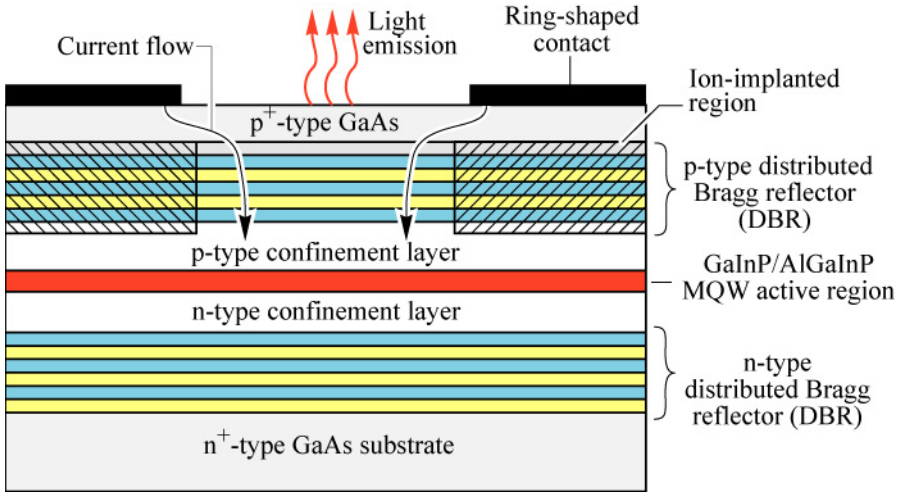

Fig. 15.9. Structure of a GaInP/AlGaInP/GaAs MQW RCLED emitting at 650 nm used for plastic optical fiber applications (after Whitaker, 1999)

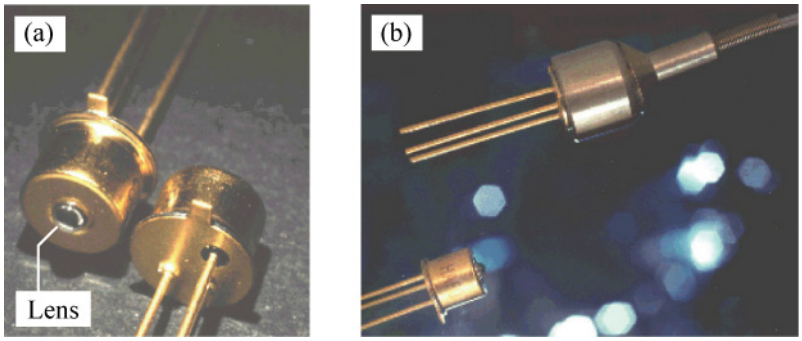

Fig. 15.10. (a) Packaged (TO package) RCLED emitting at 650 nm suited for plastic optical fiber applications. (b) Pig-tailed RCLED (courtesy of Mitel Corporation, Sweden, 1999).

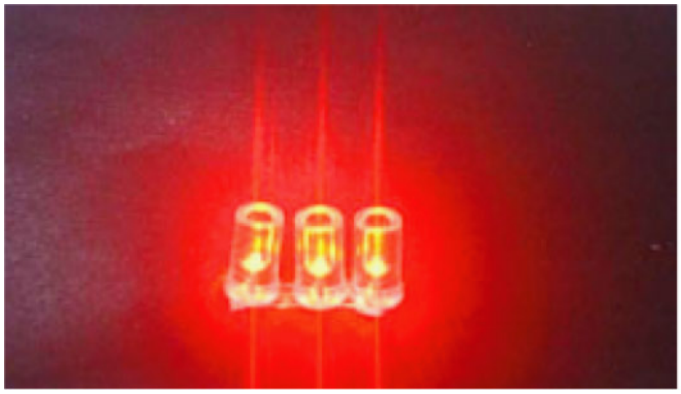

Fig. 15.11. AlGaInP/GaAs RCLEDs emitting at 650nm. Note the forward-directed emission pattern similar to that of a semiconductor laser (courtesy of Osram Opto Semiconductors Corporation, Germany, 1999).

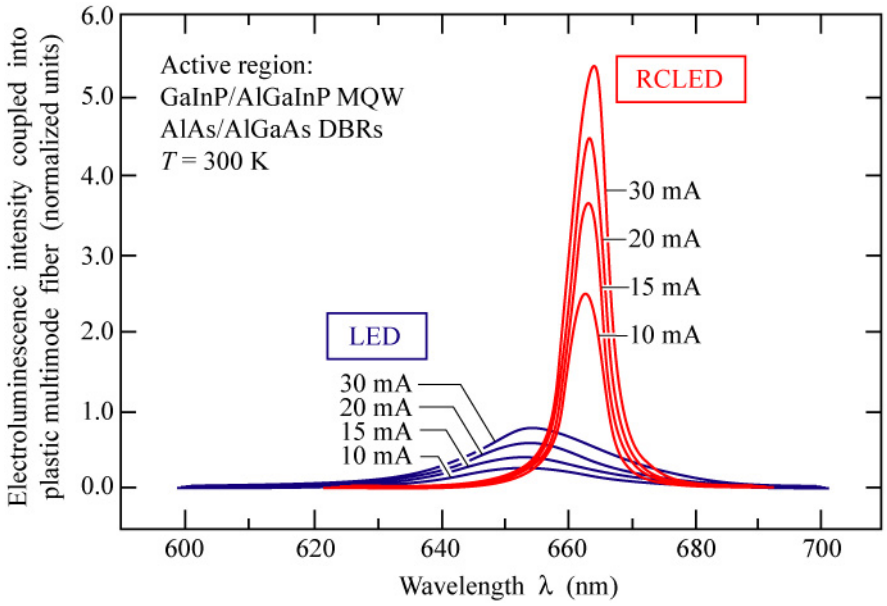

Fig. 15.12. Spectra of light coupled into a plastic optical fiber from an GaInP/AlGaInP MQW RCLED and a conventional GaInP/AlGaInP LED at different drive currents. Note the narrower spectrum and higher coupled power of the RCLED (after Streubel *et al.*, 1998).

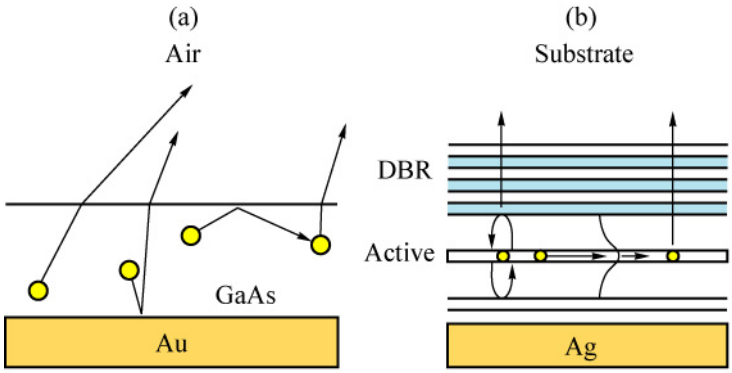

Fig. 15.13. Two approaches to photon recycling LEDs. (a) Bulk epilayer placed on top of gold. Most spontaneous emission that does not escape into air is reabsorbed and has a chance to emit again. (b) Microcavity designed with a waveguiding active region. Waveguided light is reabsorbed after some tens of microns, and has a chance to reemit out of the top of the device.

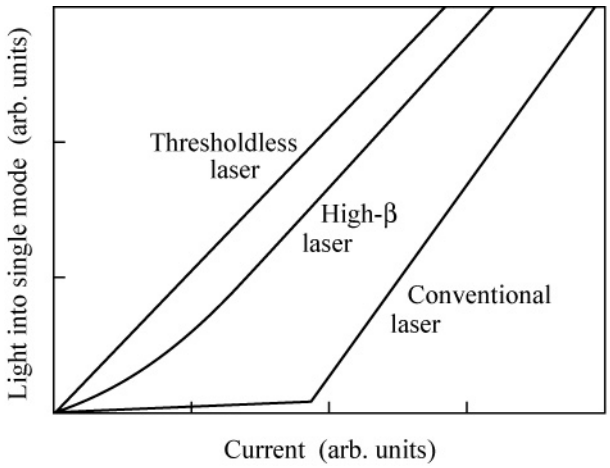

Fig. 15.14. Light-power-versus-current curves for single spatial-mode emission from a (*i*) conventional laser, (*ii*) a high β-factor laser, and (*iii*) a thresholdless laser. The conventional laser has a distinct current threshold. The high β-factor laser has a less distinct threshold. It would be noticeable in the spectrum and device modulation speed, however. A hypothetical thresholdless laser would have a β close to 1, and would somehow suppress all other lossy emission until the carrier density required for gain (or at least transparency) was achieved.

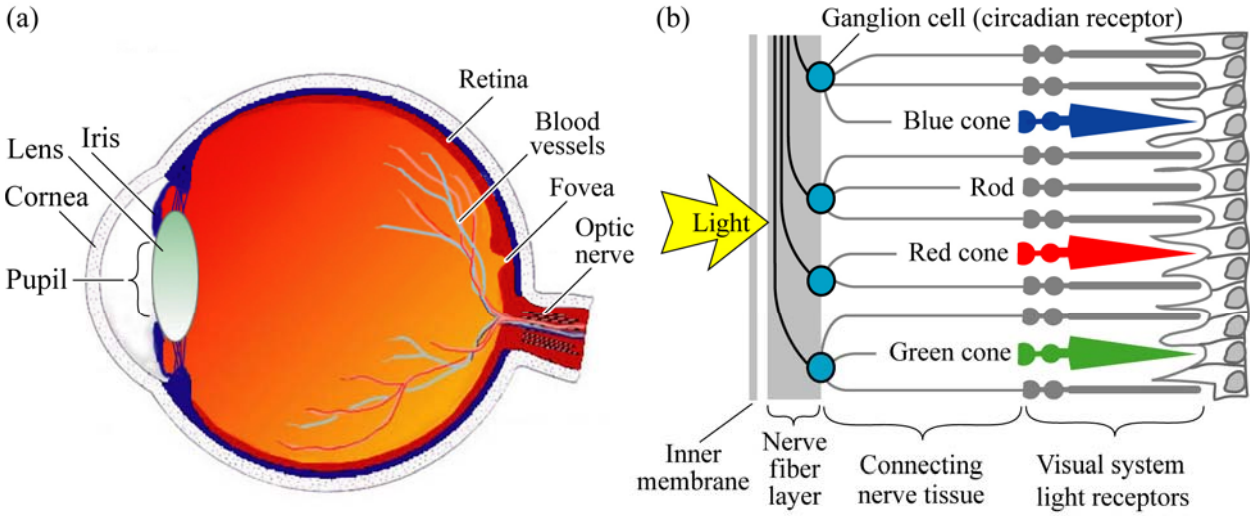

Fig. 16.1. (a) Cross section through a human eye. (b) Schematic view of the retina including rod and cone light receptors (adapted from Encyclopedia Britannica, 1994).

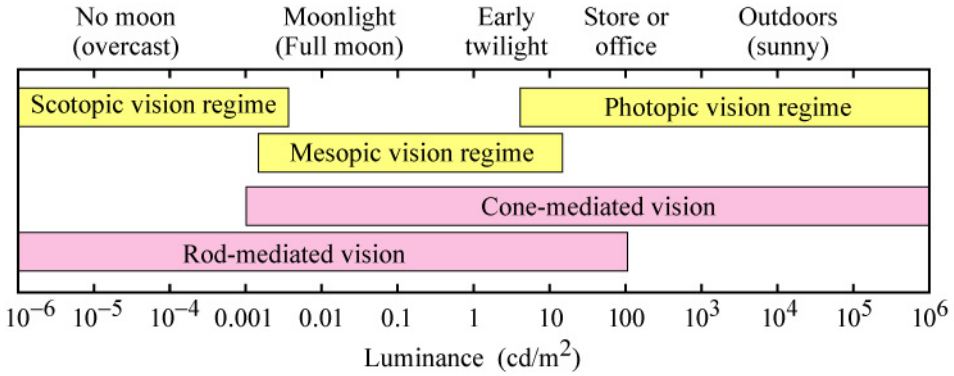

Fig. 16.2. Approximate ranges of vision regimes and receptor regimes (after Osram Sylvania, 2000).

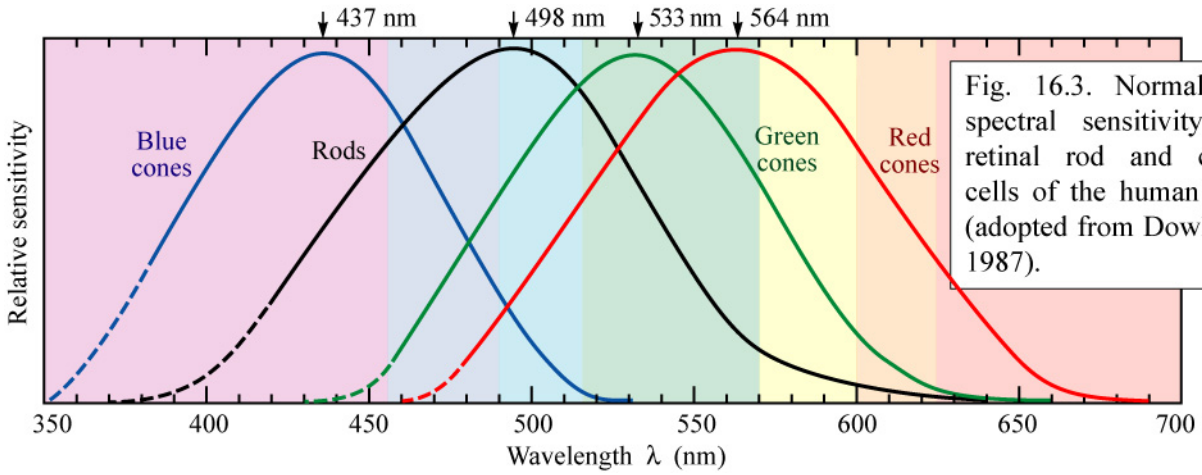

Fig. 16.3. Normalized spectral sensitivity of retinal rod and cone cells of the human eye (adopted from Dowling, 1987).

Fig. 16.4. Plumber's candle as used by plumbers to melt lead when joining water pipes in the 19th century.

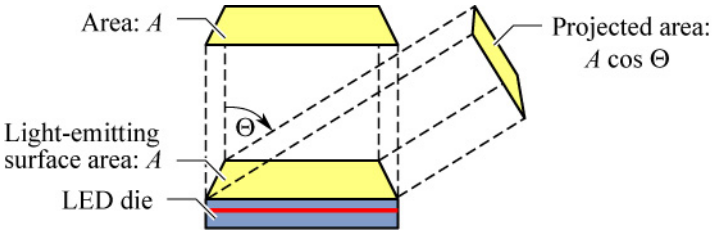

Fig. 16.5. Area of LED, A, and projected area, $A\cos\Theta$, used for the definition of the luminance of an LED.

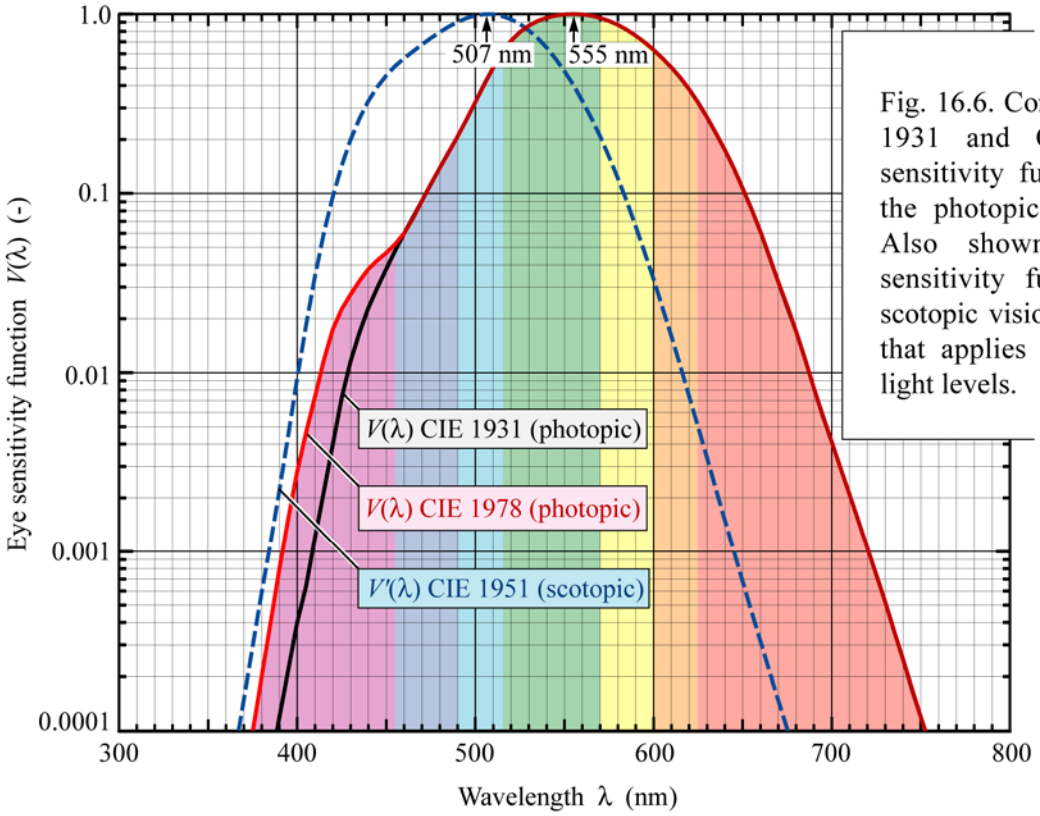

Fig. 16.6. Comparison of CIE 1931 and CIE 1978 eye sensitivity function $V(\lambda)$ for the photopic vision regime. Also shown is the eye sensitivity function for the scotopic vision regime, $V'(\lambda)$, that applies to low ambient light levels.

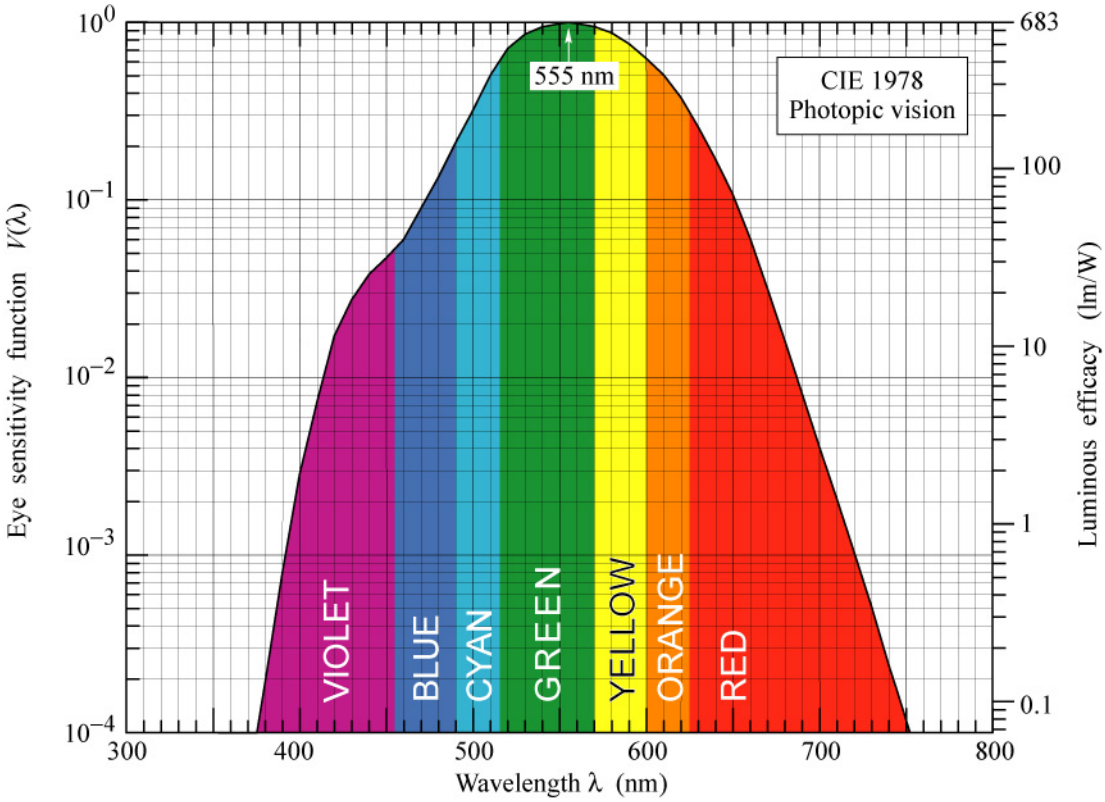

Fig. 16.7. Eye sensitivity function, $V(\lambda)$, (left ordinate) and luminous efficacy, measured in lumens per Watt of optical power (right ordinate). $V(\lambda)$ is greatest at 555 nm. Also given is a polynomial approximation for $V(\lambda)$ (after 1978 CIE data).

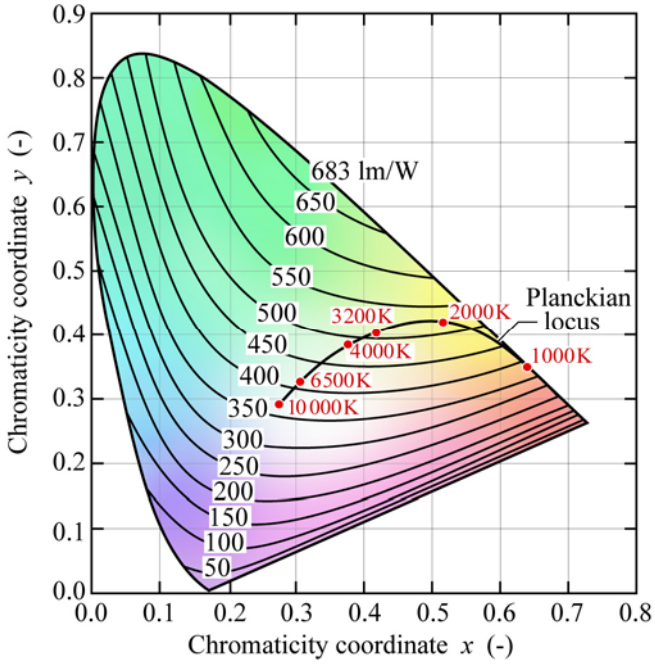

Fig. 16.8. Relation of maximum possible luminous efficacy (lumens per optical Watt) and chromaticity in the CIE 1931 x, y chromaticity diagram (adopted from MacAdam, 1950).

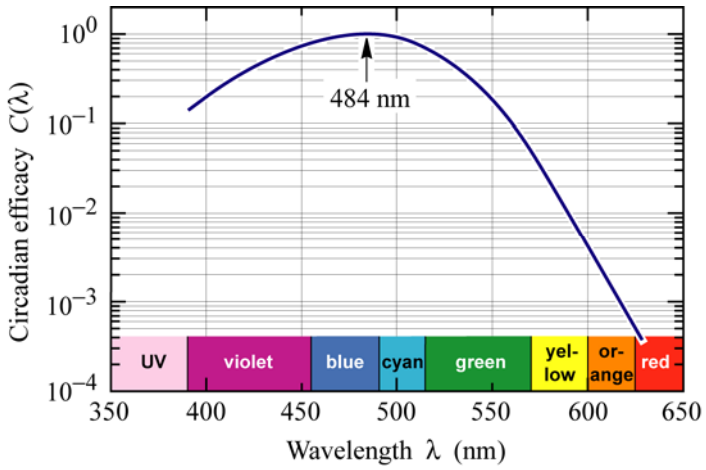

Fig. 16.9. Circadian efficacy curve derived from retinal ganglion cell photoresponse measurements. The ganglion cells on which the measurements were performed originated from mammals (after Berson *et al.*, 2002).

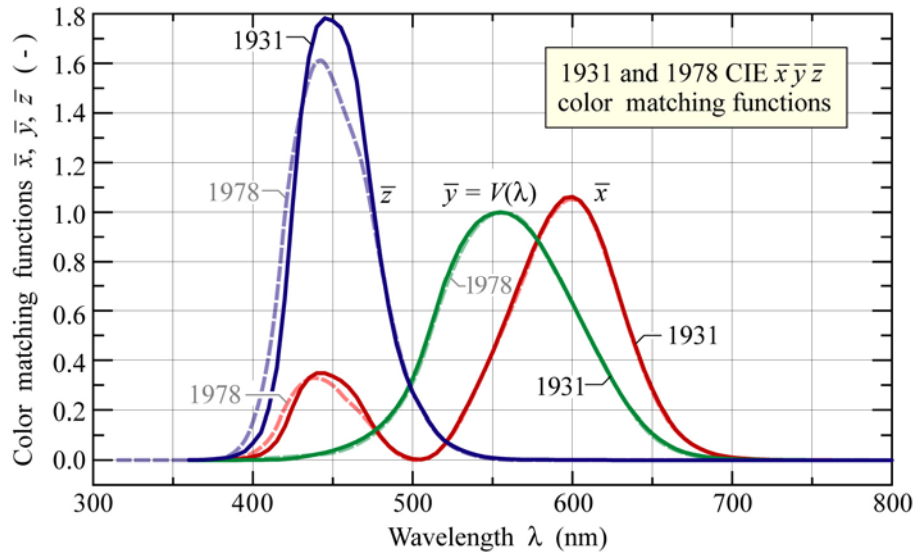

Fig. 17.1. CIE (1931) and CIE (1978) $\bar{x}\bar{y}\bar{z}$ color matching functions (CMFs). The $\bar{y}$ CMF is identical to the eye sensitivity function $V(\lambda)$. Note that the CIE 1931 CMF is the currently valid official standard.

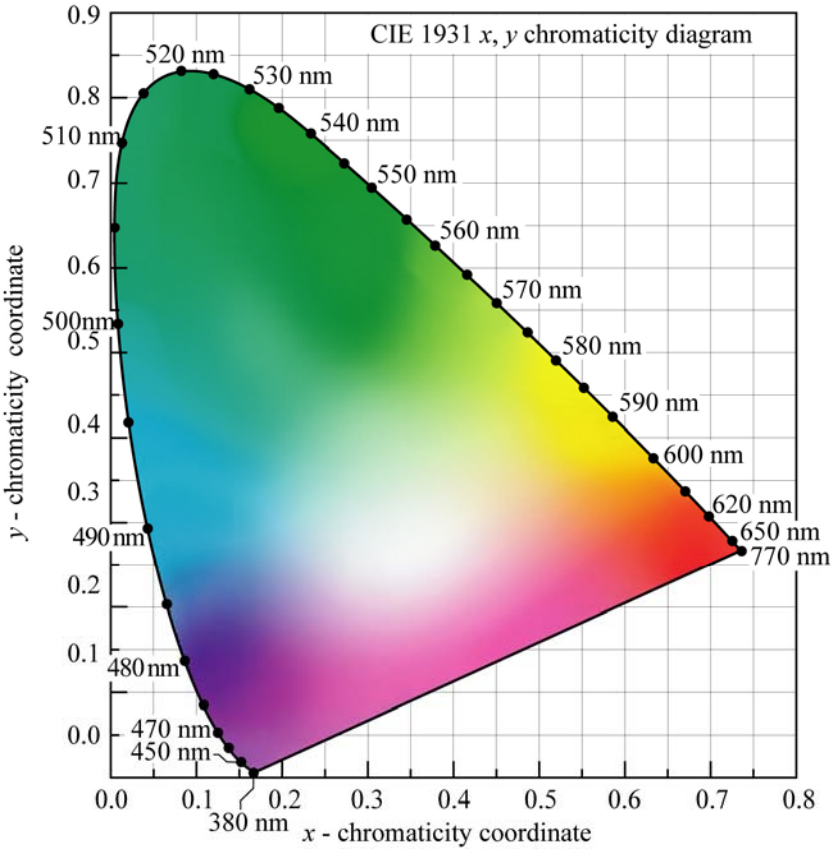

Fig. 17.2. CIE 1931 (x, y) chromaticity diagram. Monochromatic colors are located on the perimeter and white light is located in the center of the diagram.

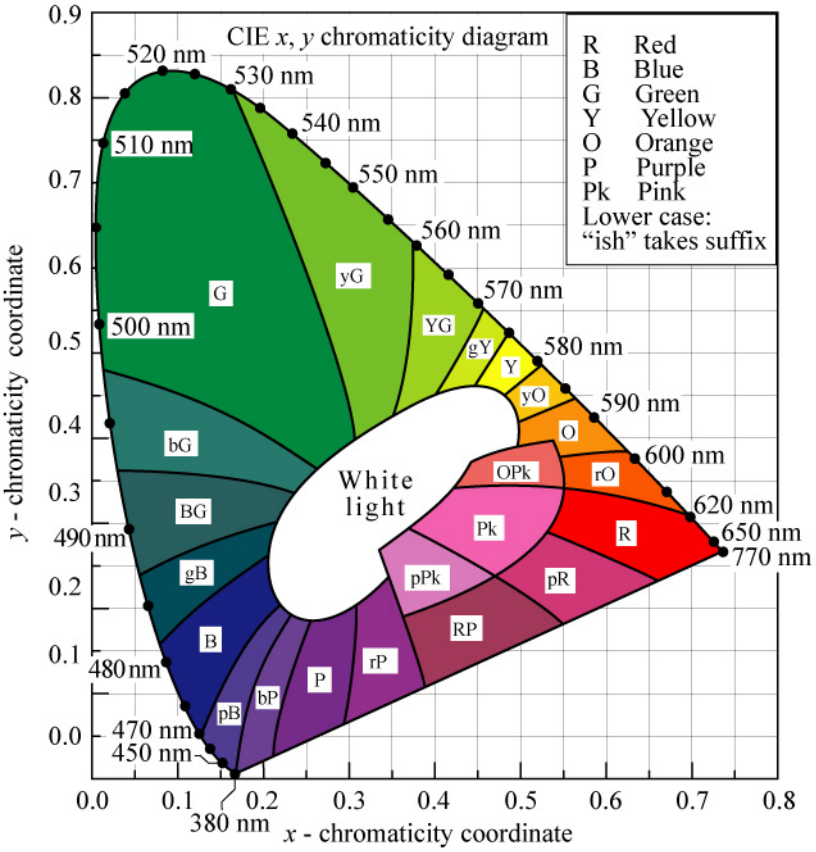

Fig. 17.3. 1931 CIE chromaticity diagram with areas attributed to distinct colors (adopted from Gage *et al.*, 1977).

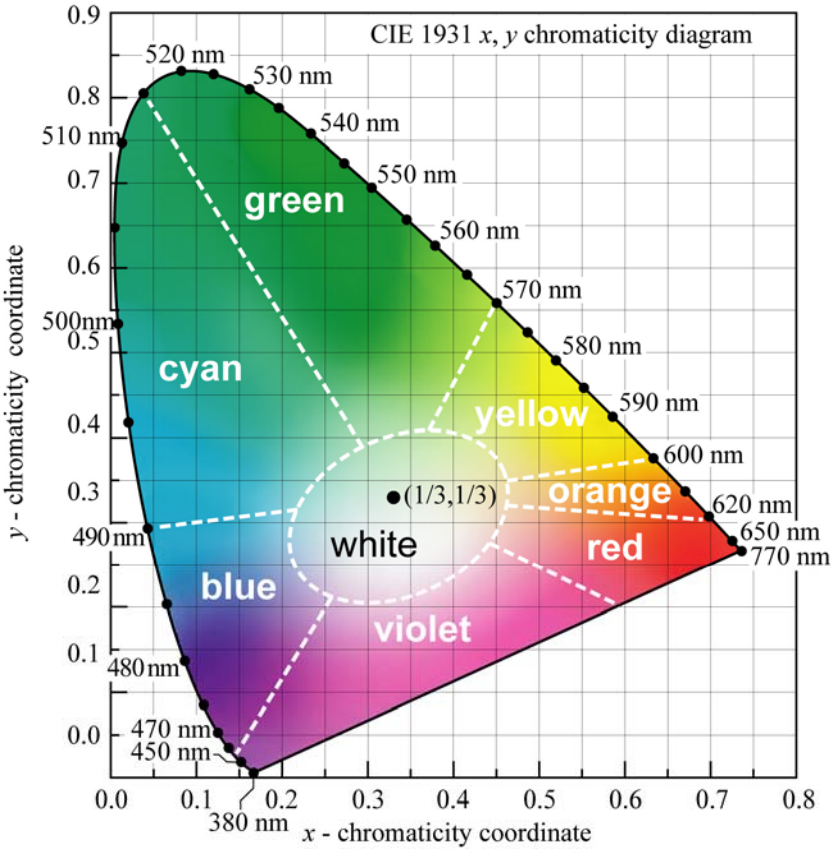

Fig. 17.4. CIE 1931 (x, y) chromaticity diagram. Monochromatic colors are located on the perimeter. Color saturation decreases towards the center of the diagram. White light is located in the center. Also shown are the regions of distinct colors. The equal-energy point is located at the center and has the coordinates (x, y) = (1/3, 1/3).

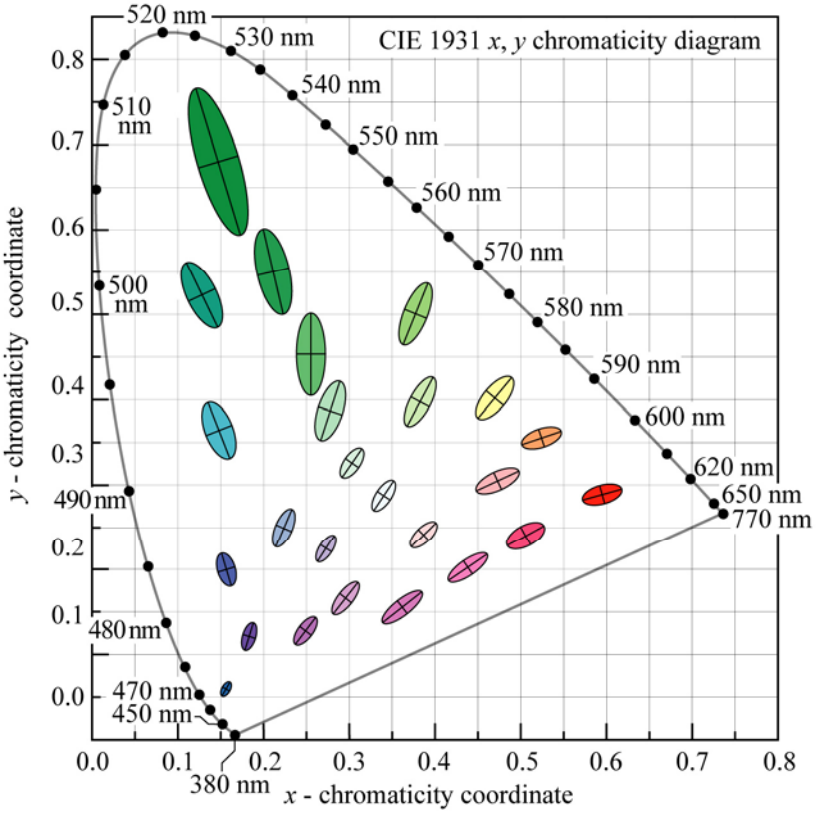

Fig. 17.5. MacAdam ellipses plotted in the CIE 1931 (x, y) chromaticity diagram. The axes of the ellipses are ten times their actual lengths (after MacAdam, 1943; Wright, 1943; MacAdam, 1993).

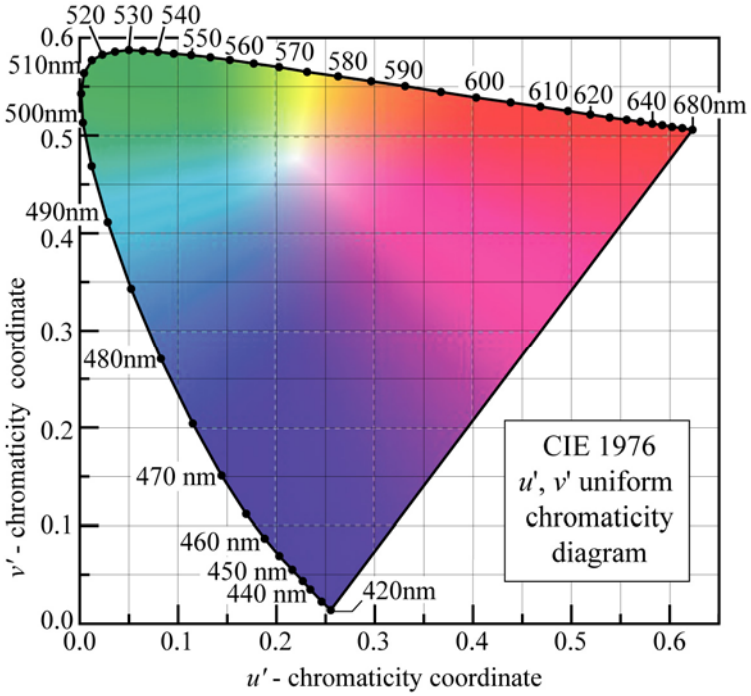

Fig. 17.6. CIE 1976 (u', v') uniform chromaticity diagram calculated using the CIE 1931 2° standard observer.

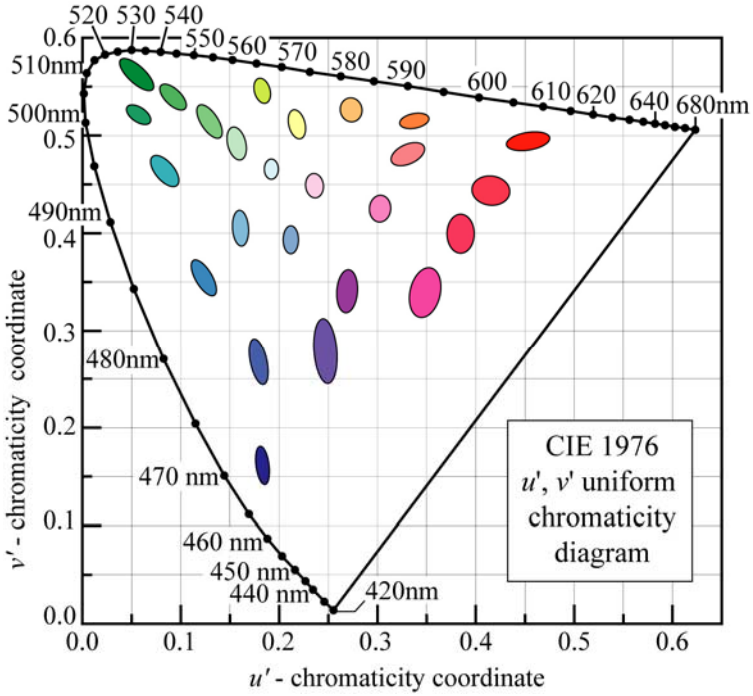

Fig. 17.7. MacAdam ellipses transformed to uniform CIE 1976 (u', v') chromaticity coordinates. For clarity, the axes of the transformed ellipses are ten times their actual lengths. Transformed ellipses are not ellipses in a strict mathematical sense, but their shapes closesly resemble those of ellipses. The areas of the transformed ellipses in the (u', v') diagram are much more similar than the MacAdam ellipses in the (x, y) diagram.

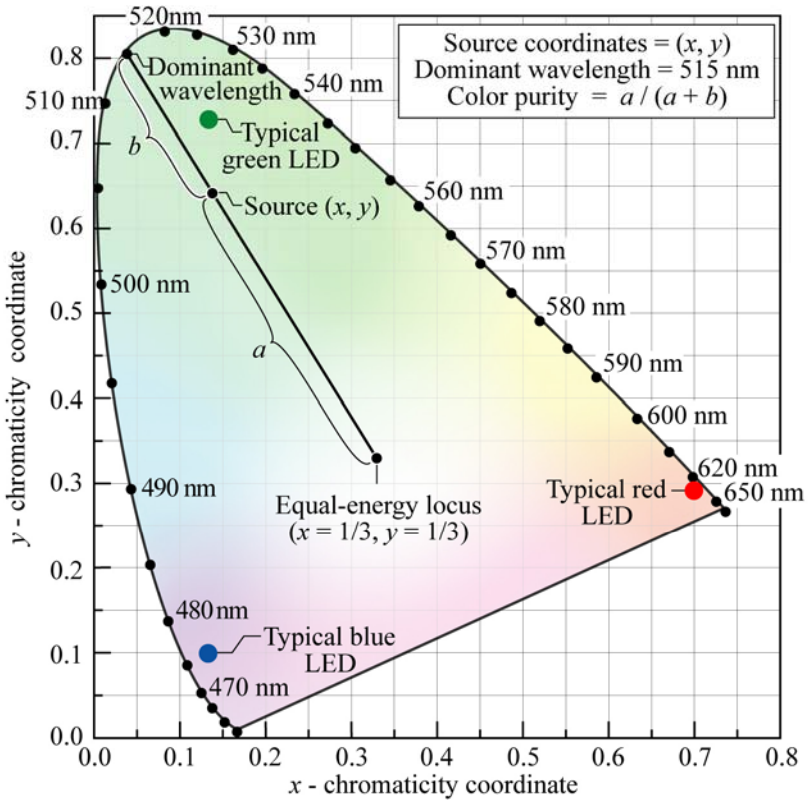

Fig. 17.8. Chromaticity diagram showing the determination of the *dominant wavelength* and *color purity* of a light source with chromaticity coordinates (x, y) using the equal-energy locus (x = 1/3, y = 1/3) as the white-light reference. Also shown are typical locations of blue, green, and red LEDs.

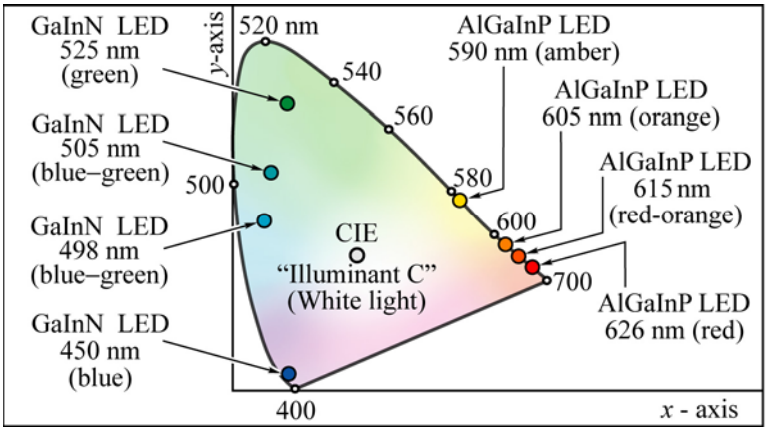

Fig. 17.9. Location of LED light emission on the chromaticity diagram (adopted from Schubert and Miller, 1999).

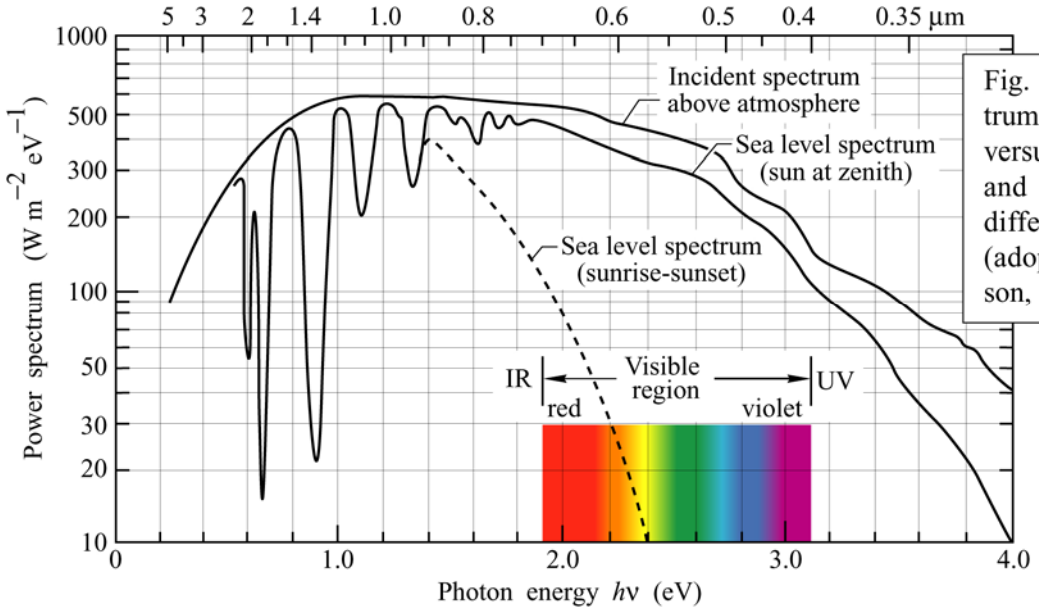

Fig. 18.1. Power spectrum of solar radiation versus photon energy and wavelength for different conditions (adopted from Jackson, 1975).

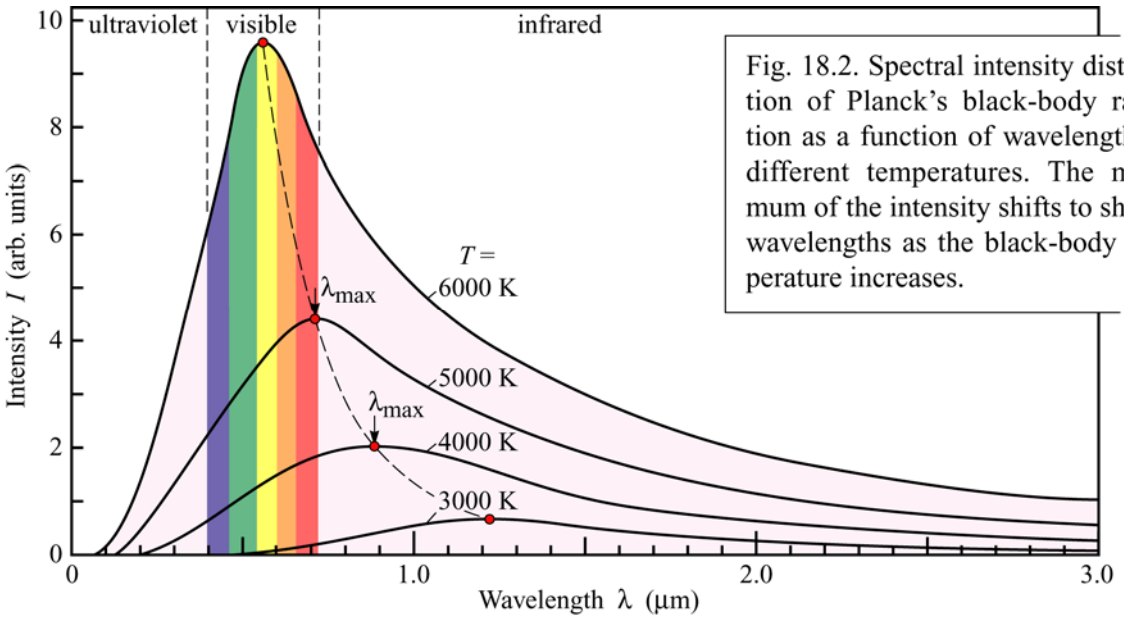

Fig. 18.2. Spectral intensity distribution of Planck's black-body radiation as a function of wavelength for different temperatures. The maximum of the intensity shifts to shorter wavelengths as the black-body temperature increases.

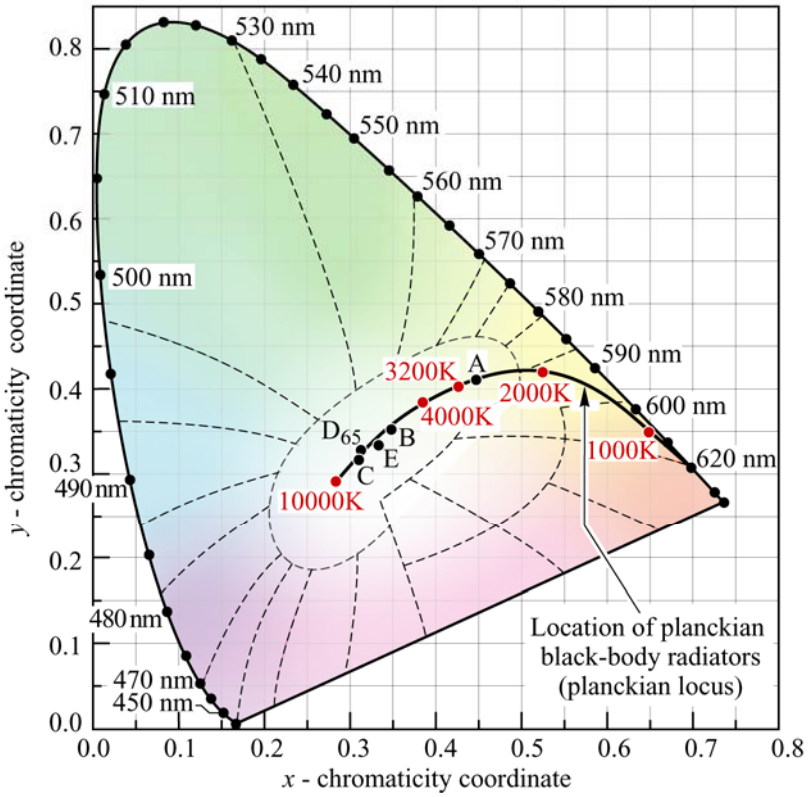

Illuminant A
(x, y) = (0.4476, 0.4074)
(Incandescent source, T = 2856 K)

Illuminant B
(x, y) = (0.3484, 0.3516)
(Direct sunlight, T = 4870 K)

Illuminant C
(x, y) = (0.3101, 0.3162)
(Overcast source, T = 6770 K)

Illuminant D_{65}
(x, y) = (0.3128, 0.3292)
(Daylight, T = 6500 K)

Illuminant E (equal-energy point)
(x, y) = (0.3333, 0.3333)

Fig. 18.3. Chromaticity diagram showing planckian locus, the standardized white Illuminants A, B, C, D_{65}, and E, and their color temperature (after CIE, 1978).

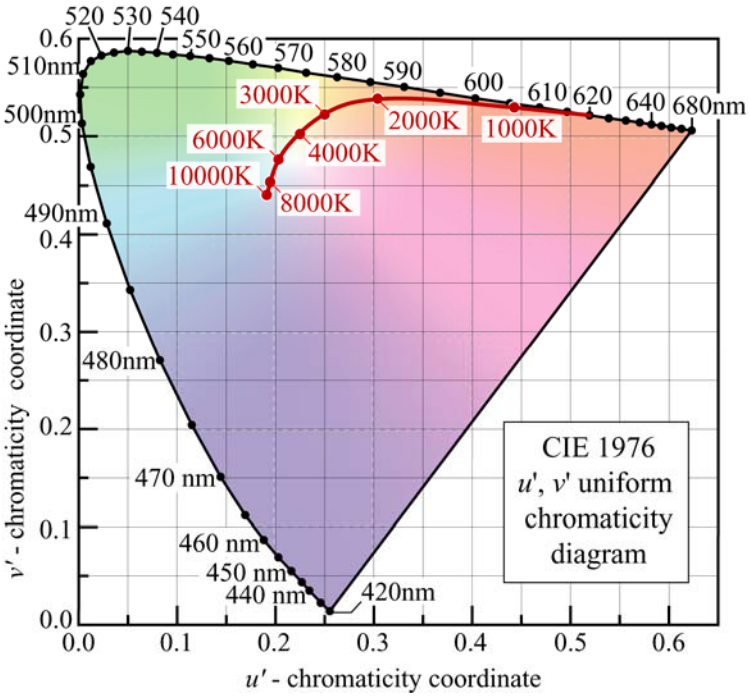

Fig. 18.4. CIE 1976 (u', v') uniform chromaticity diagram calculated using the CIE 1931 2° standard observer and planckian locus.

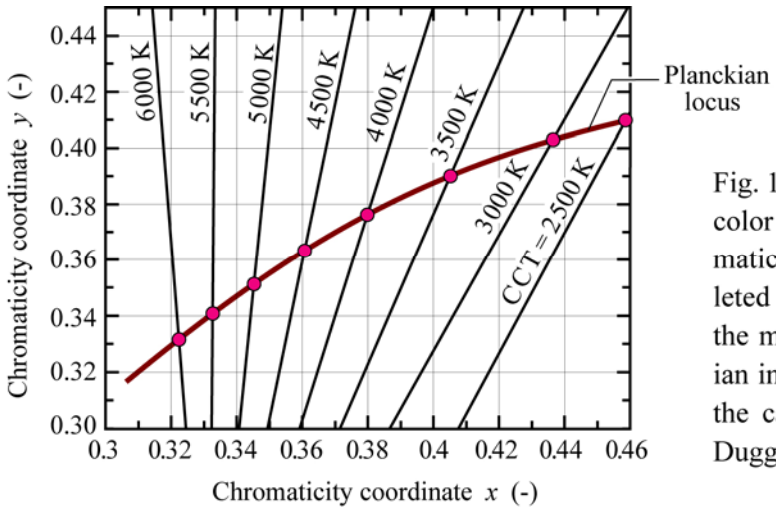

Fig. 18.5. Lines of constant correlated color temperature in the (x, y) chromaticity diagram. Whereas the correleted color temperature follows from the minimum distance to the planckian in the (u', v') diagram, this is not the case in the (x,y) diagram (after Duggal, 2005).

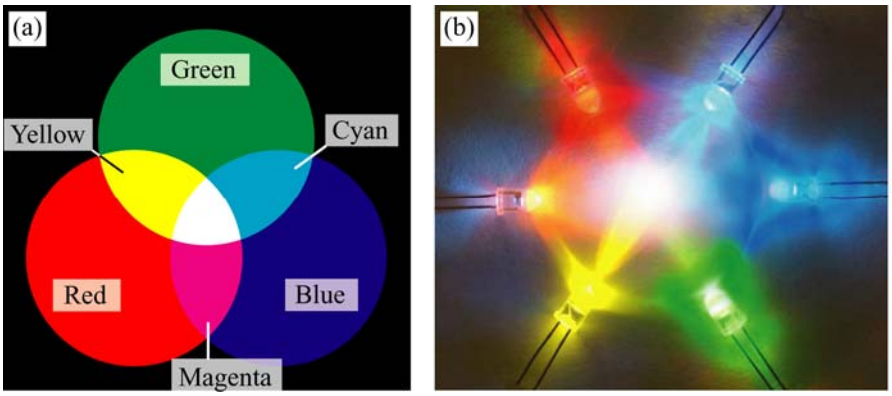

Fig. 19.1. (a) Schematic of additive color mixing of three primary colors. (b) Additive color mixing using LEDs.

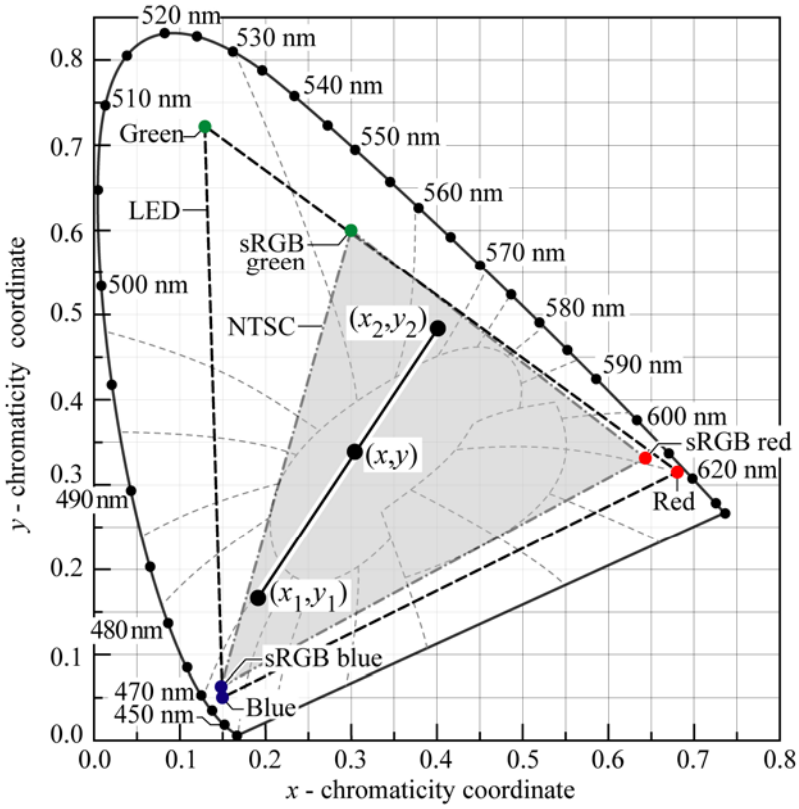

Fig. 19.2. Principle of color mixing illustrated with two light sources with chromaticity coordinates (x_1, y_1) and (x_2, y_2). The resulting color has the coordinates (x, y). Also shown is the triangular area of the chromaticity diagram (color gamut) accessible by additive mixing of a red, green, and blue LED. The locations of the red, green, and blue phosphors of the sRGB display standard (x_r = 0.64, y_r = 0.33, x_g = 0.30, y_g = 0.60, x_b = 0.15, y_b = 0.06) are also shown. The sRGB standard is similar to the NTSC standard.

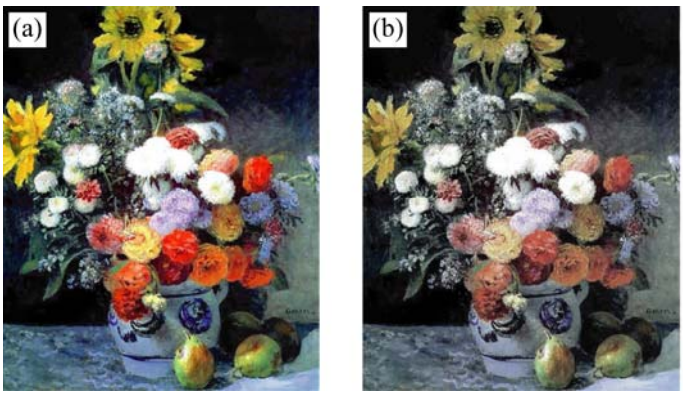

Fig. 19.3. Artwork entitled "Fleurs dans un vase" illuminated with (a) high-CRI source and (b) low-CRI source (Auguste Renoir, French impressionist, 1841–1919) .

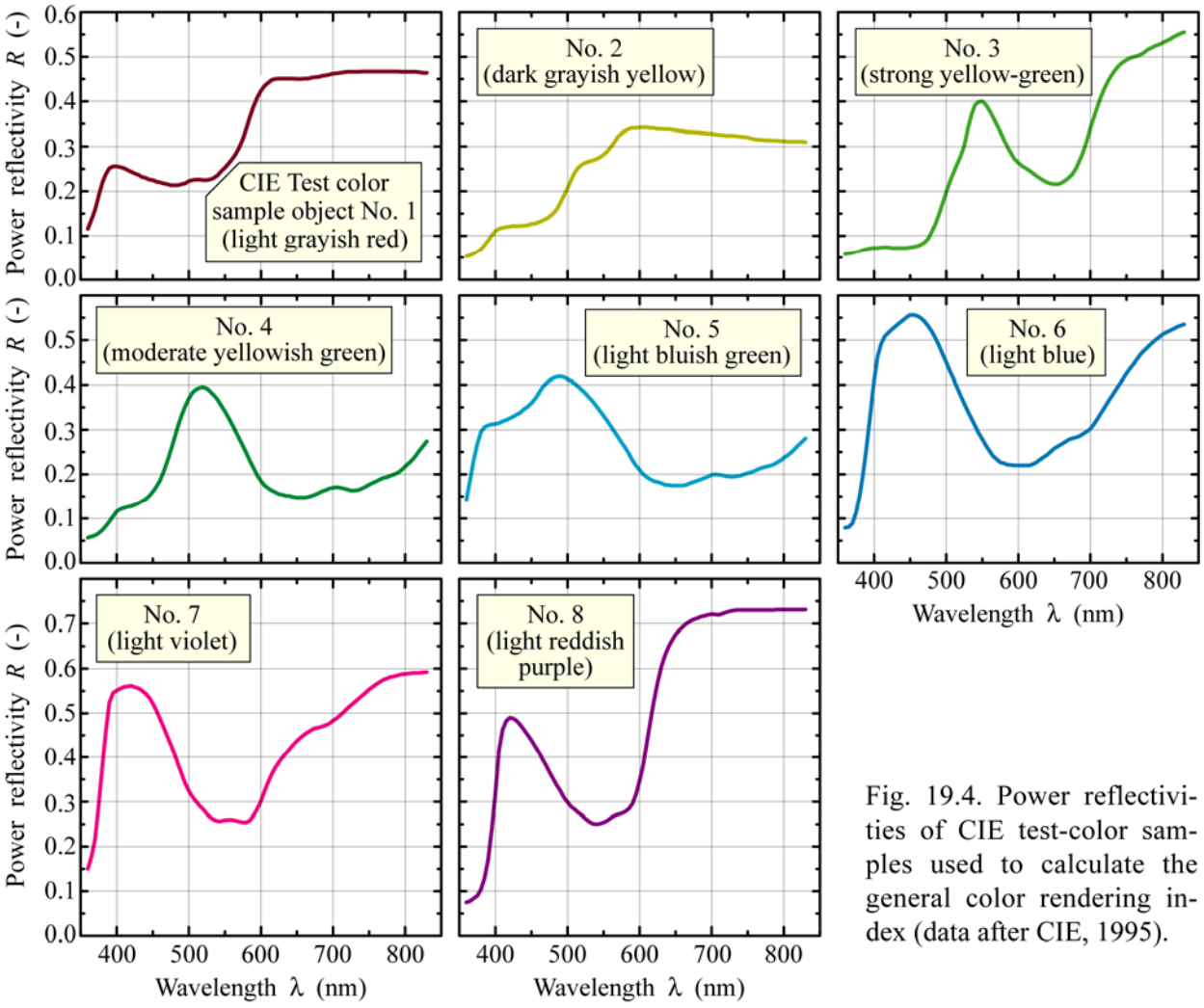

Fig. 19.4. Power reflectivities of CIE test-color samples used to calculate the general color rendering index (data after CIE, 1995).

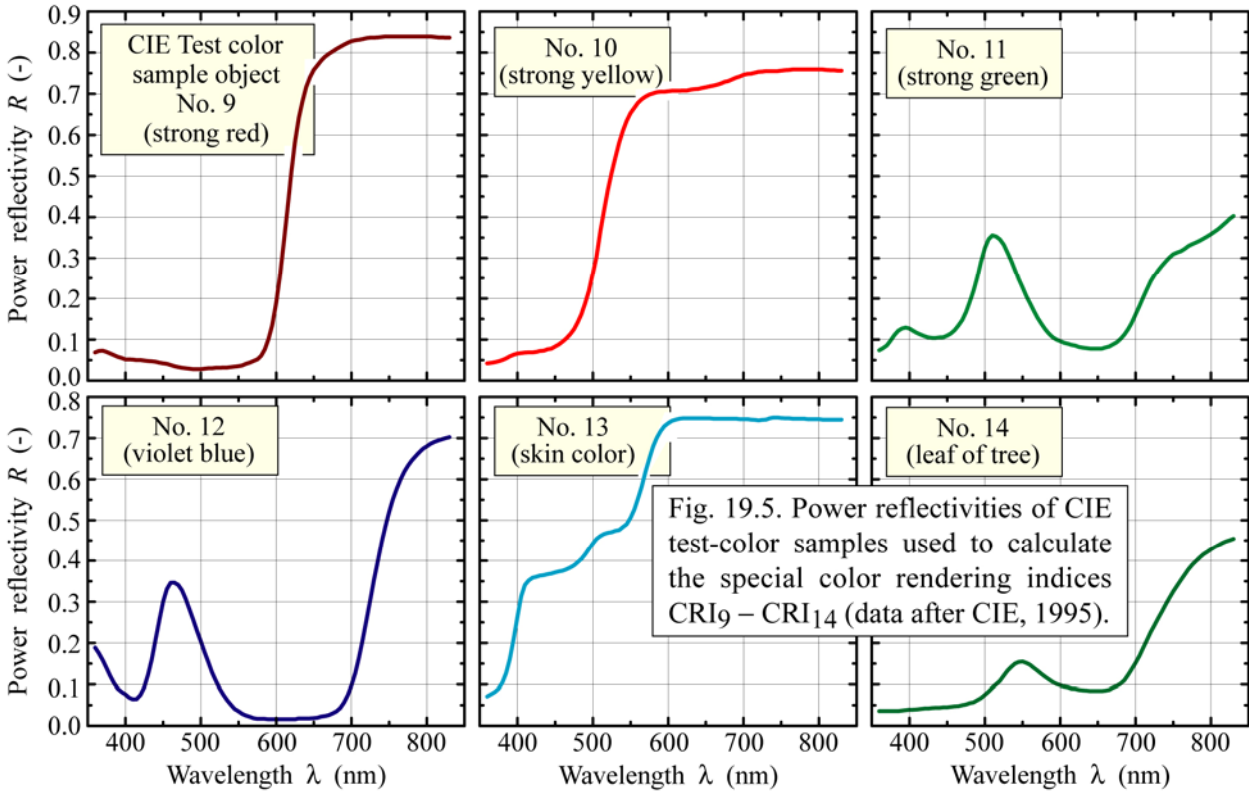

Fig. 19.5. Power reflectivities of CIE test-color samples used to calculate the special color rendering indices $CRI_9 - CRI_{14}$ (data after CIE, 1995).

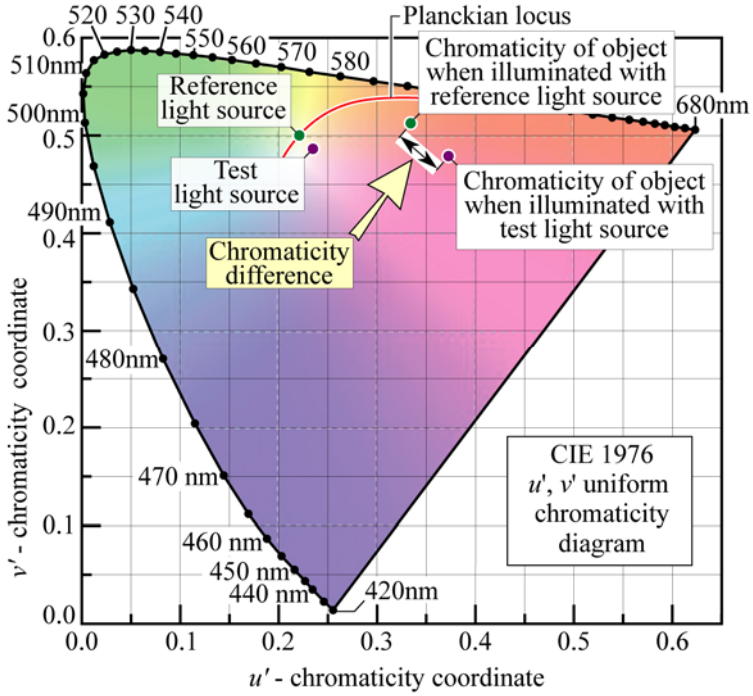

Fig. 19.6. Chromaticity difference resulting from the illumination of an object with a reference and a test light source. In the CIE 1976 u', v' uniform chromaticity diagram, the chromaticity difference is directly proportional to the geometric distance. The reference light source is located on the planckian locus at the correlated color temperature of the test light source.

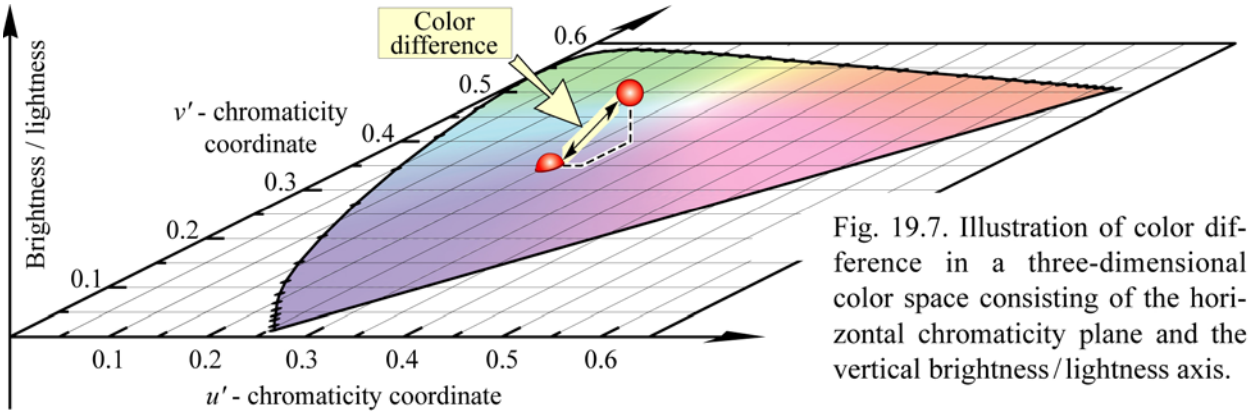

Fig. 19.7. Illustration of color difference in a three-dimensional color space consisting of the horizontal chromaticity plane and the vertical brightness / lightness axis.

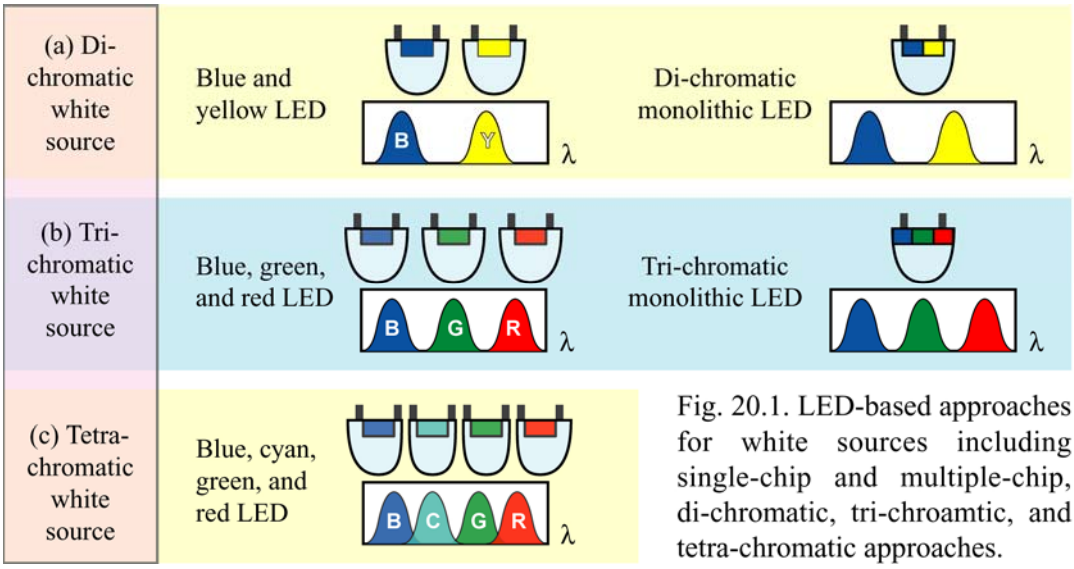

Fig. 20.1. LED-based approaches for white sources including single-chip and multiple-chip, di-chromatic, tri-chroamtic, and tetra-chromatic approaches.

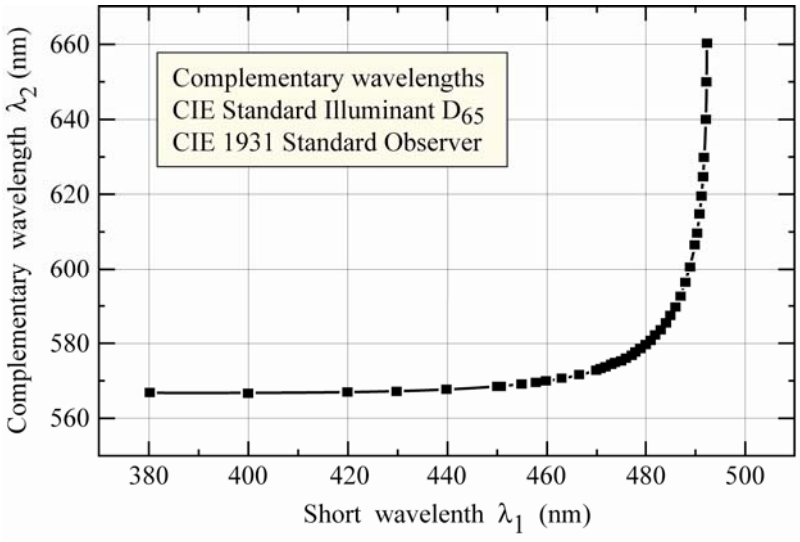

Fig. 20.2. Monochromatic complementary wavelengths resulting in the perception of white light at a certain power ratio (after Wyszecki and Stiles, 1982).

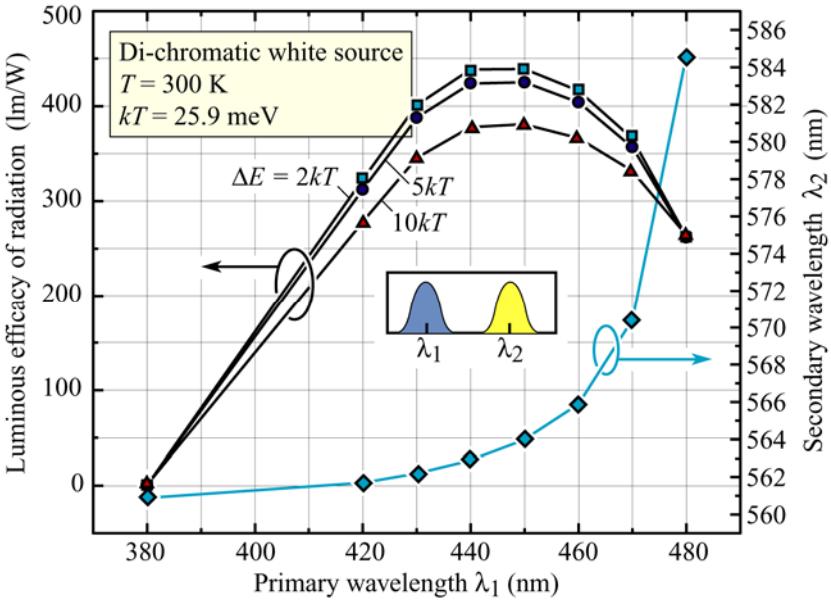

Fig. 20.3. Calculated luminous efficacy of dichromatic white light source (with chromaticity point at D_{65} standard illuminant) for different linewidths ΔE as a function of the primary wavelength. Also shown is the complementary secondary wavelength (after Li *et al.*, 2003).

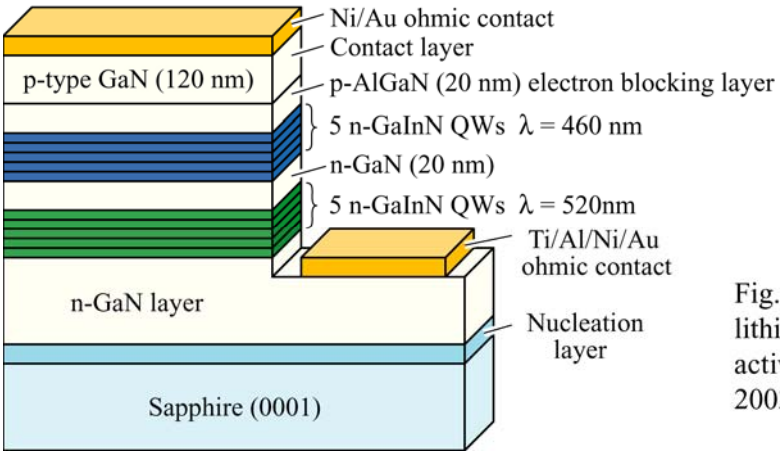

Fig. 20.4. Structure of a monolithic dichromatic LED with two active regions (after Li *et al.*, 2003).

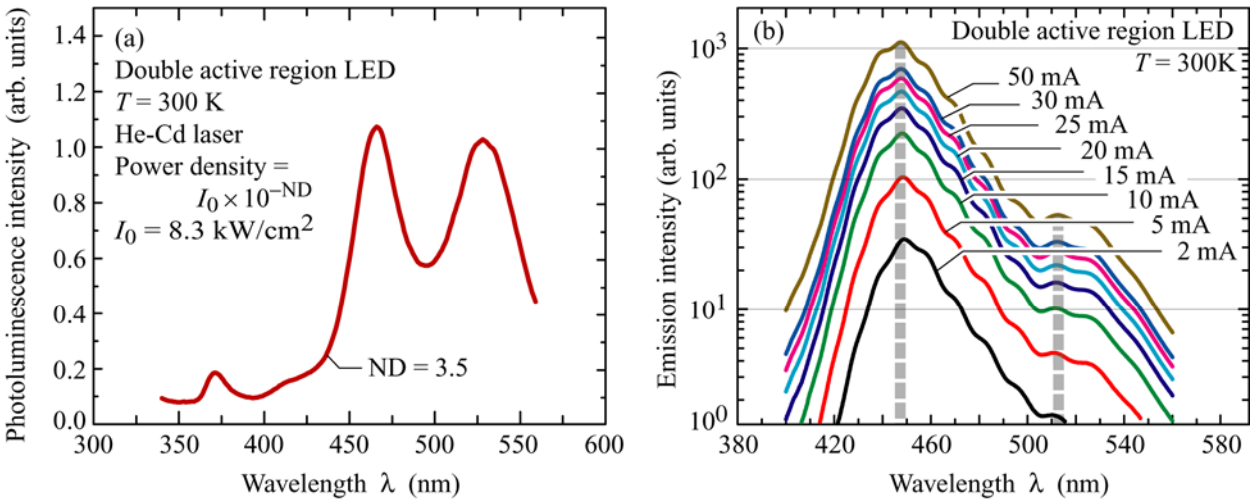

Fig. 20.5. Room temperature (a) photoluminescence and (b) electroluminescence spectra of monolithic dichromatic LED with two active regions (after Li *et al.*, 2003).

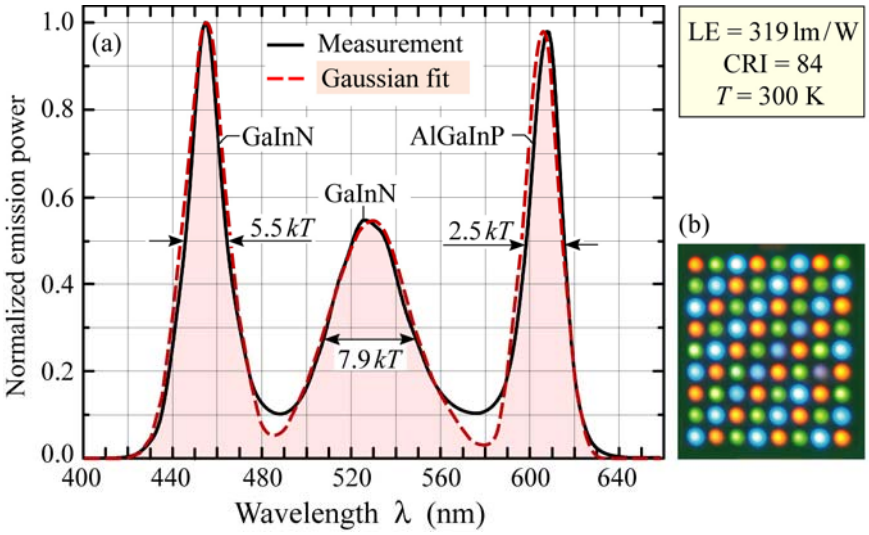

Fig. 20.6. (a) Emission spectrum of tri-chromatic white multi-LED source with color temperature of 6500 K (solid line) and gaussian fit (dashed line). The source has a luminous efficacy of radiation of 319 lm/W and a color rendering index of 84. (b) Photograph of source assembled of 5 mm LEDs (after Chhajed *et al.*, 2005).

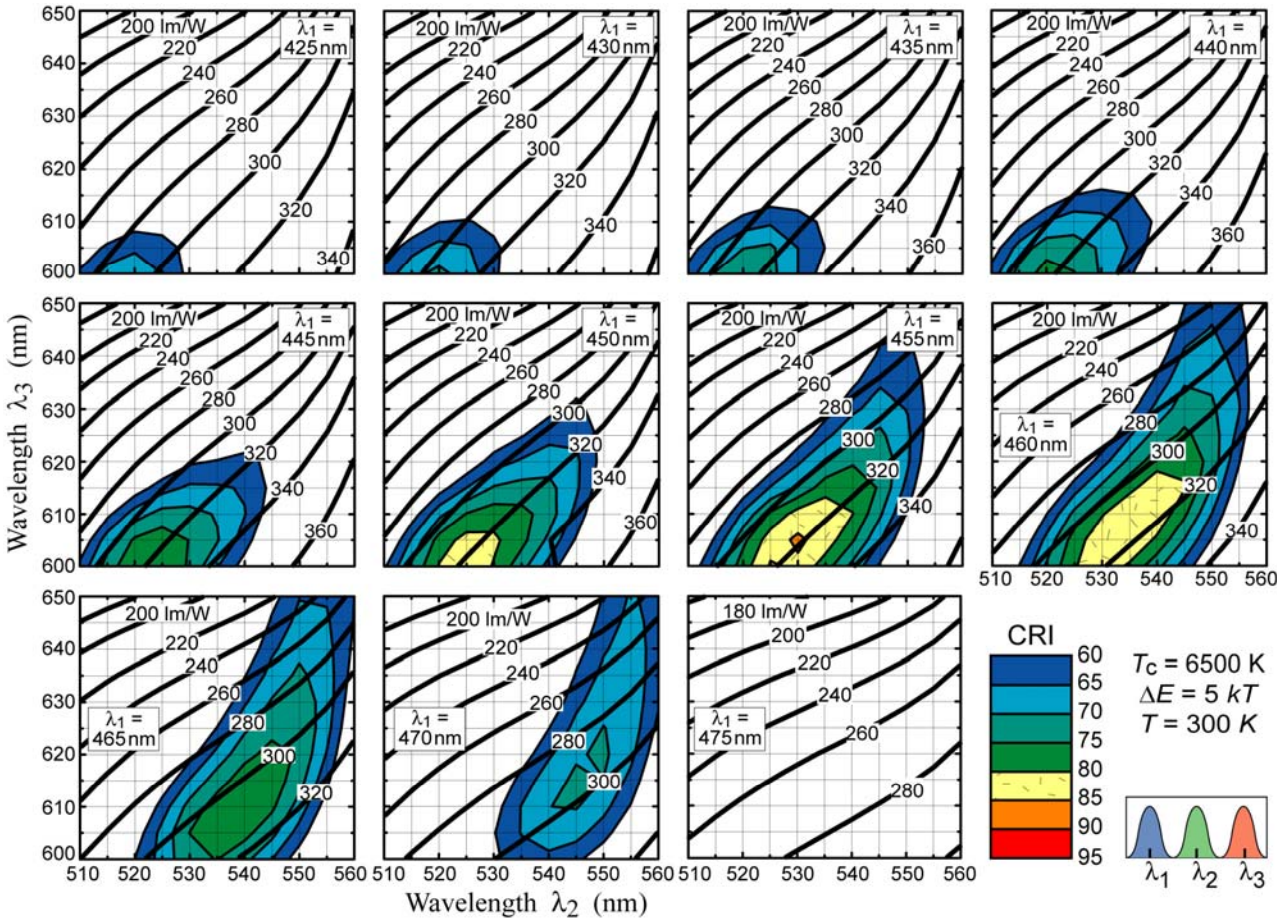

Fig. 20.7. Contour plot of luminous efficacy of radiation and CIE color-rendering index of white trichromatic LED source with color temperature 6500 K as a function of the three wavelengths for a linewidth (FWHM) of 5 *kT* (after Chhajed *et al.*, 2005).

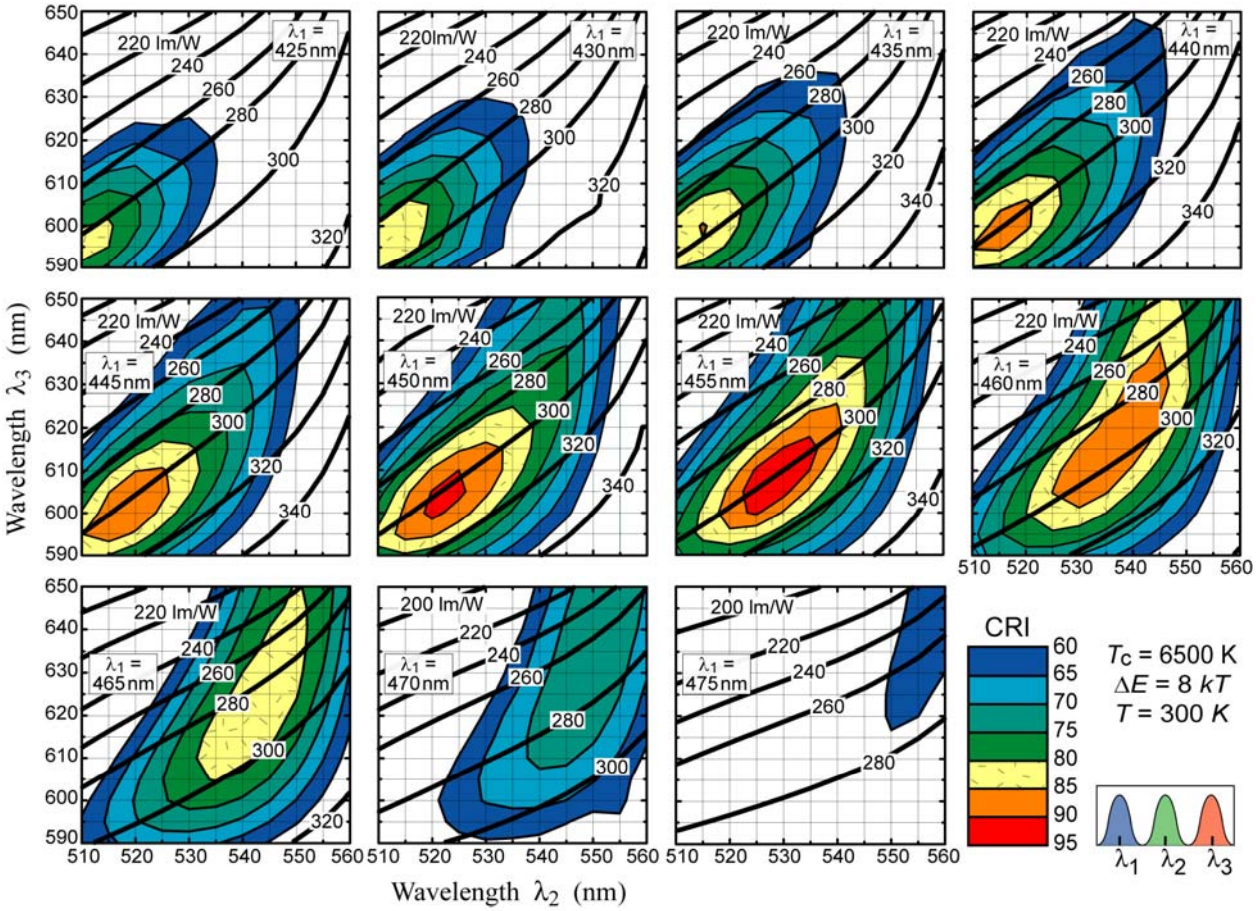

Fig. 20.8. Contour plot of luminous efficacy of radiation and CIE color-rendering index of white trichromatic LED source with color temperature 6500 K as a function of the three wavelengths for a linewidth (FWHM) of 8 *kT* (after Chhajed *et al*., 2005).

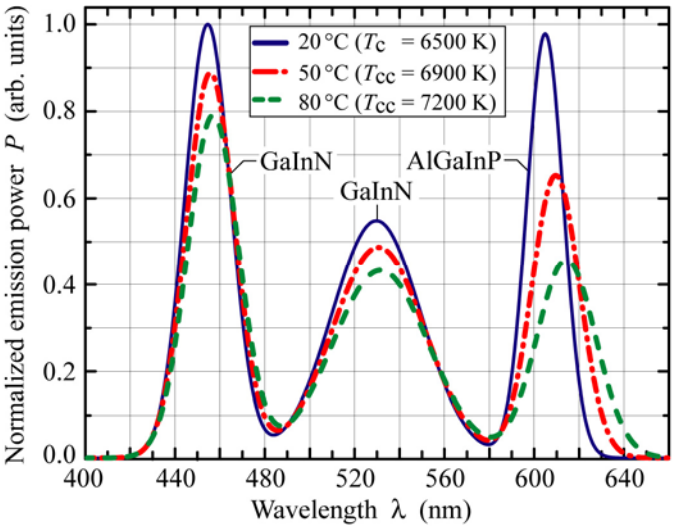

Fig. 20.9. Emission spectrum of trichromatic white LED source for different ambient temperatures (junction heating neglected). Optical power, linewidth, and peak wavelength change with temperature. As a result of these changes, the color temperature of the source increases (after Chhajed *et al*., 2005).

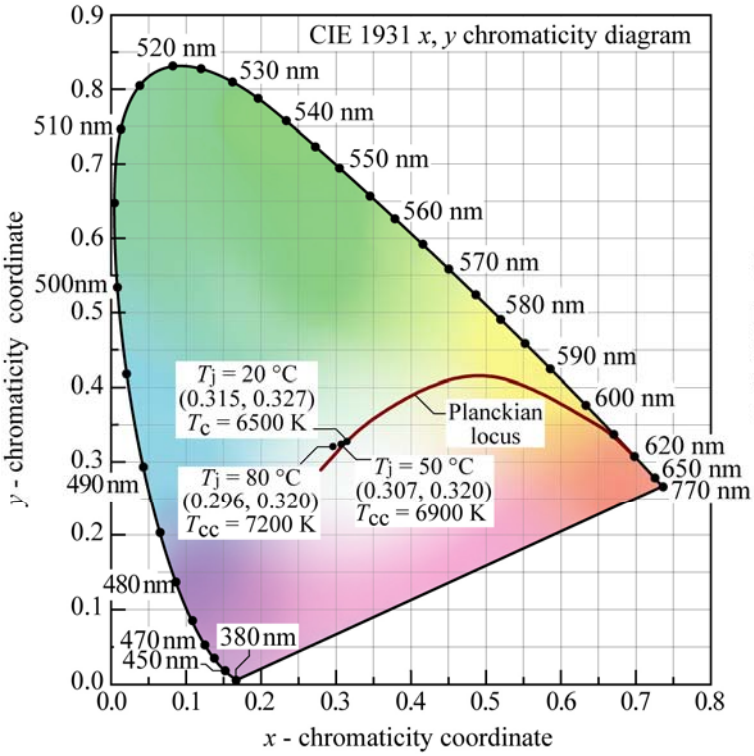

Fig. 20.10. Change in chromaticity of trichromatic white LED-based source. The source color temperature is 6500 K when devices are at room temperature. Due to the dependence of emission power, peak wavelength, and linewidth on temperature, the chromaticity point migrates off the planckian locus as the device temperature increases (after Chhajed *et al*., 2005).

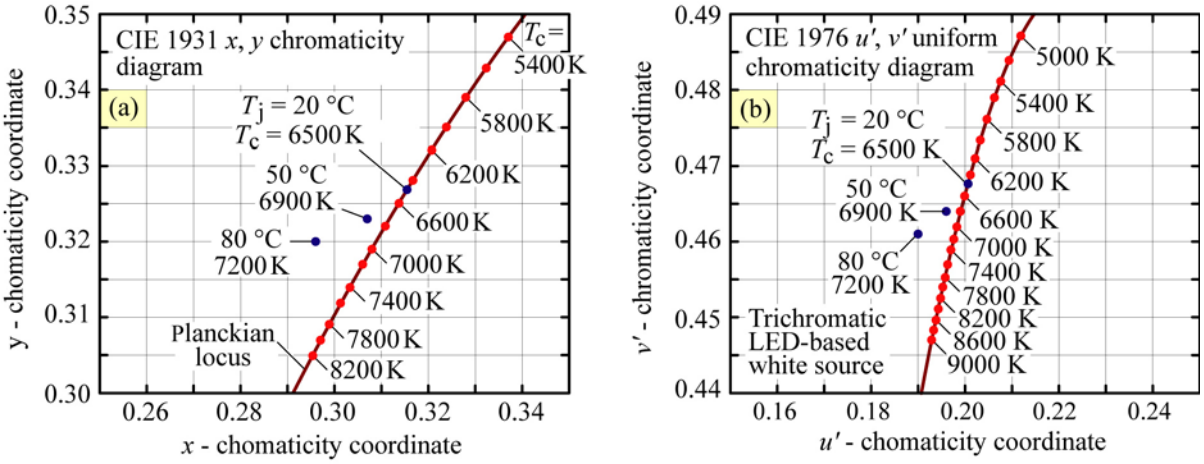

Fig. 20.11. Change in (a) *x*, *y* and (b) *u*′, *v*′ chromaticity of trichromatic white LED source. T_c = 6500 K when p-n junctions are at room temperature (after Chhajed *et al*., 2005).

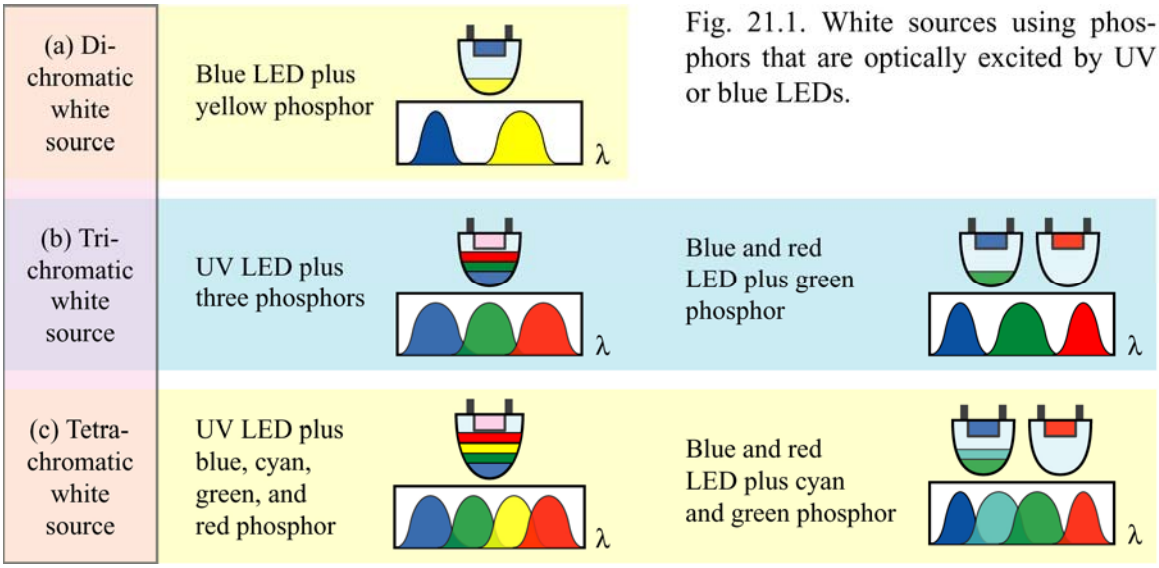

Fig. 21.1. White sources using phosphors that are optically excited by UV or blue LEDs.

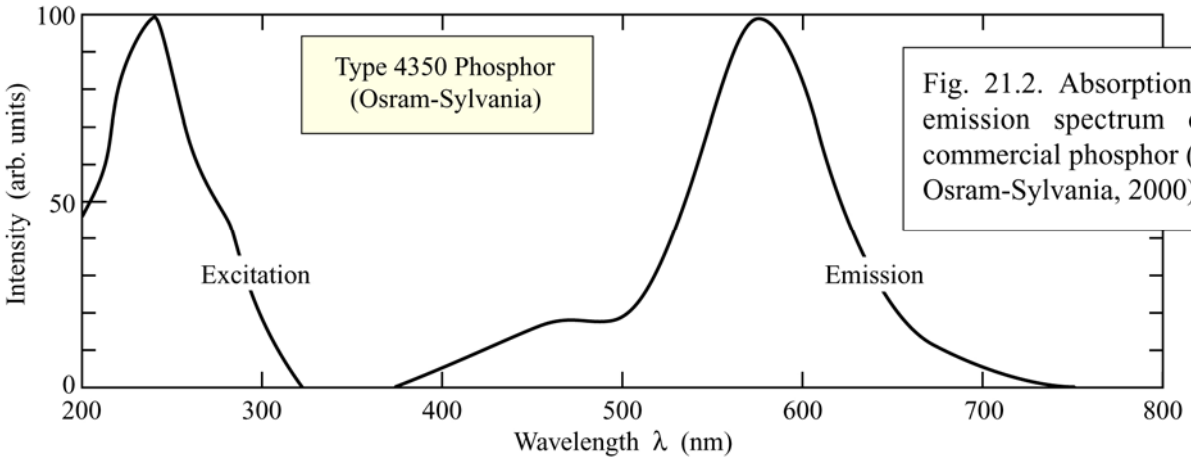

Fig. 21.2. Absorption and emission spectrum of a commercial phosphor (after Osram-Sylvania, 2000).

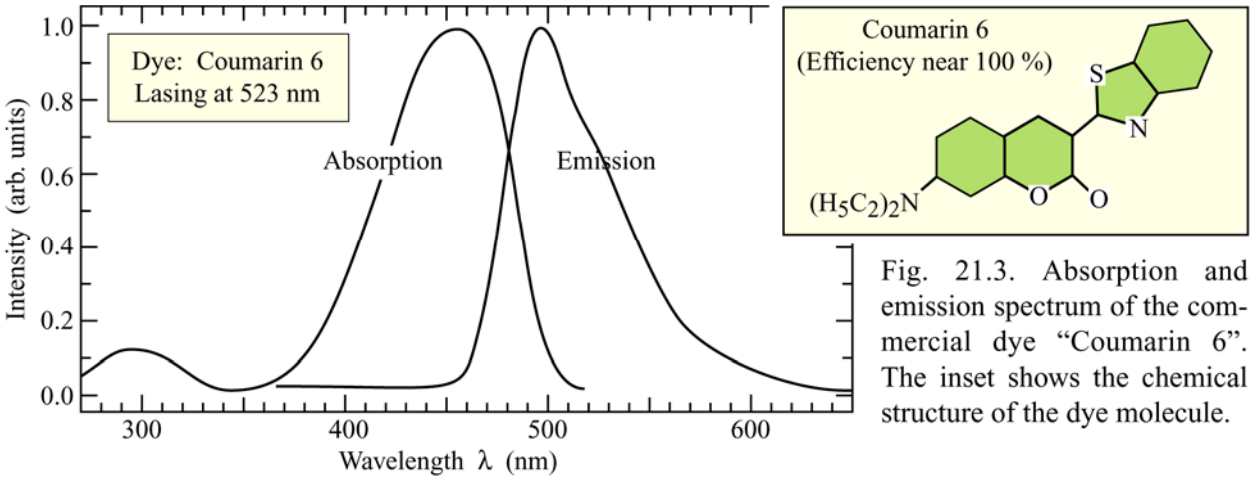

Fig. 21.3. Absorption and emission spectrum of the commercial dye "Coumarin 6". The inset shows the chemical structure of the dye molecule.

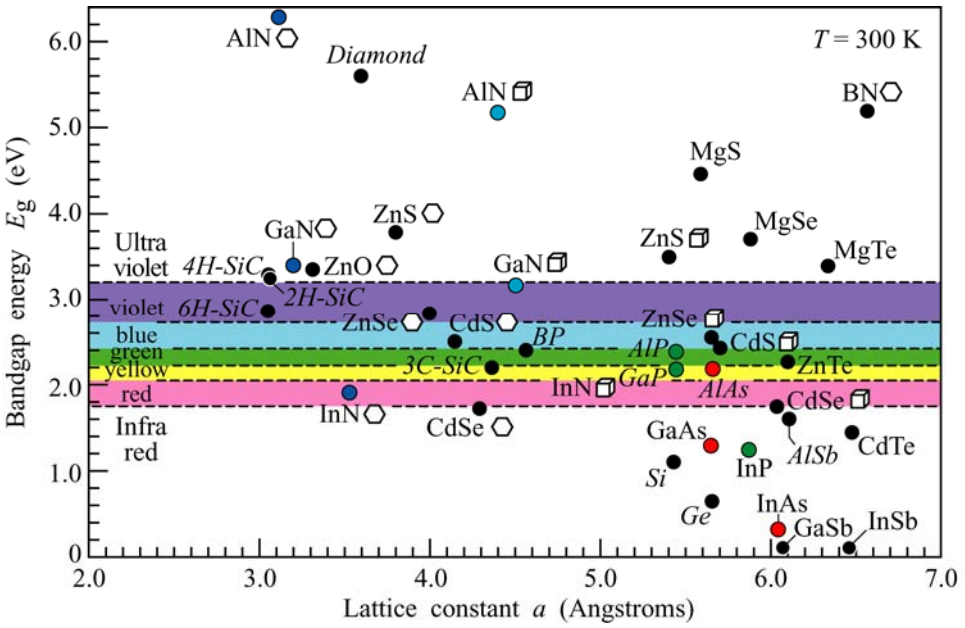

"*Italics*" = indirect gap

"Roman" = direct gap

hexagonal structure

cubic structure

Fig. 21.4. Room-temperature bandgap energy versus lattice constant of common elemental and binary compound semiconductors.

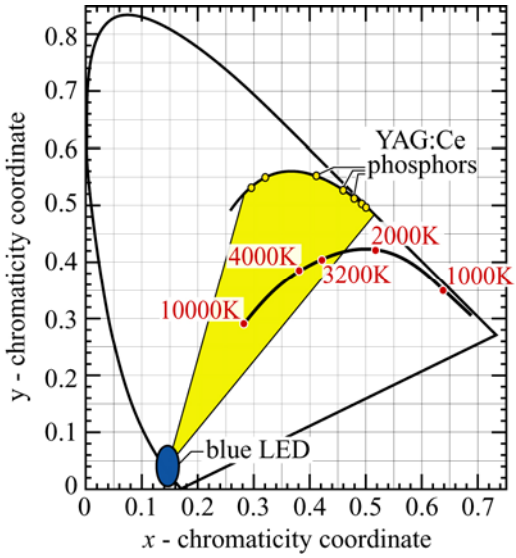

Fig. 21.6. Chromaticity points of YAG:Ce phosphor, and the general area (shaded) accessible to white emitters consisting of a blue LED and YAG:Ce phosphor (adopted from Nakamura and Fasol, 1997). Also shown in the planckian locus with color temperatures.

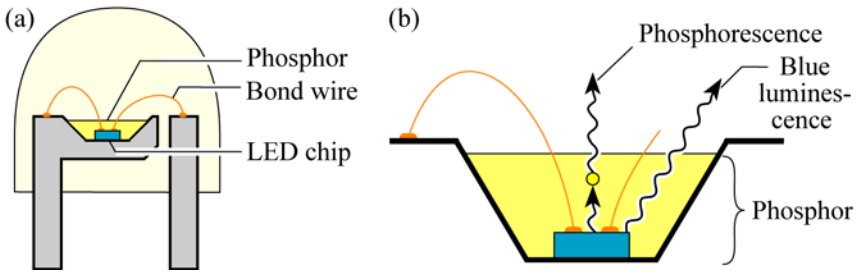

Fig. 21.7. (a) Structure of white LED lamp consisting of a GaInN blue LED chip and a phosphor. (b) Wavelength-converting phosphorescence and blue luminescence (after Nakamura and Fasol, 1997).

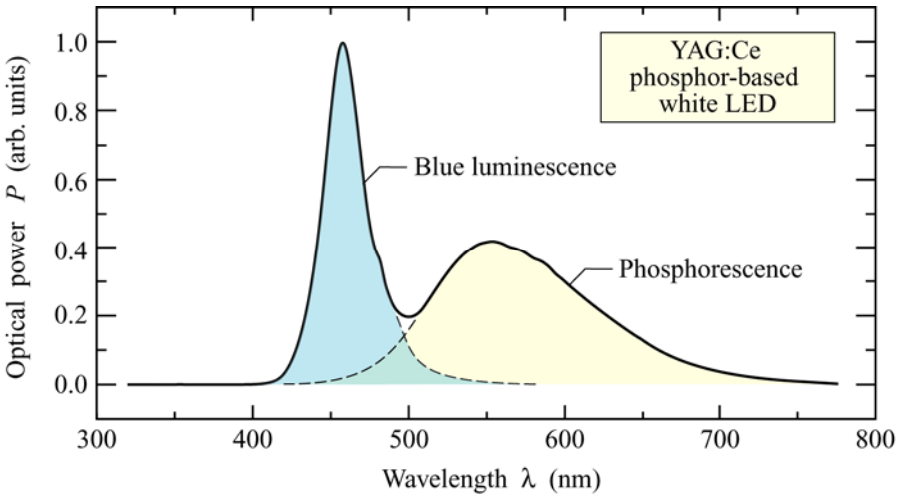

Fig. 21.8. Emission spectrum of a phophor-based white LED manufactured by Nichia Corporation (Anan, Tokushima, Japan).

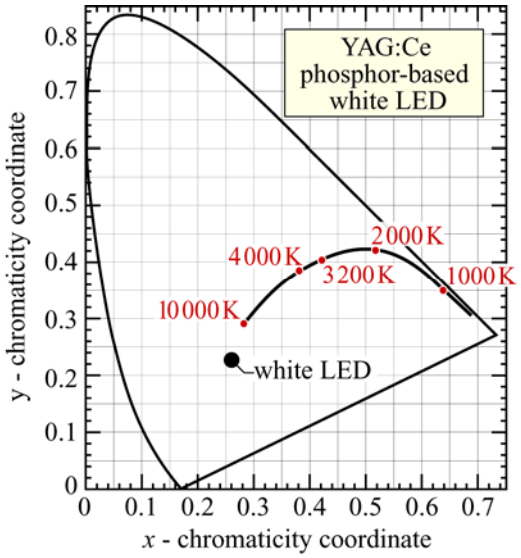

Fig. 21.9. Chromaticity coordinates of a commercial phophor-based white LED manufactured in 2001 by Nichia Corporation (Anan, Tokushima, Japan). Also shown is the planckian locus and associated color temperatures.

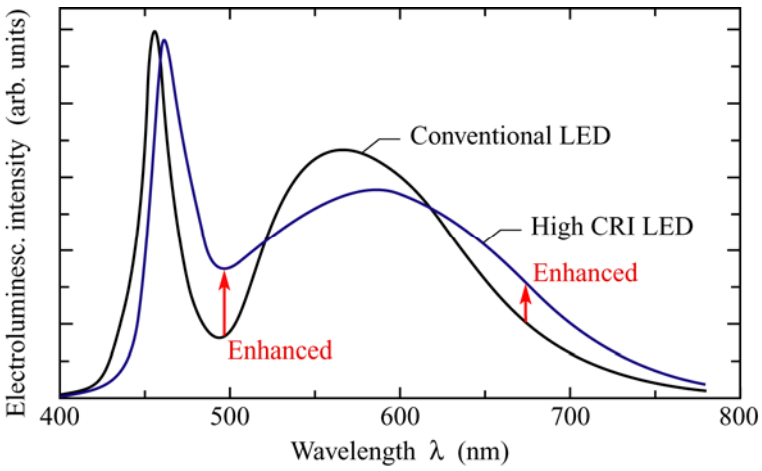

Fig. 21.10. Electroluminescence spectrum of conventional white LED and of high-color-rendering white LED. The high CRI results from the broader emission spectrum and the reduction of the notch in the spectrum (after Narukawa, 2004).

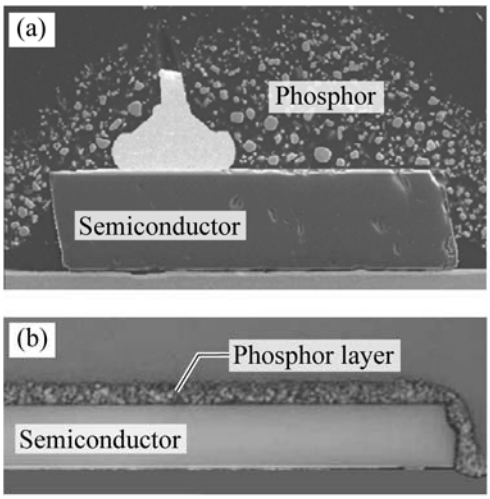

Fig. 21.11. Phosphor distributions in white LEDs: (a) Proximate phosphor distribution. (b) Proximate conformal phosphor distribution. (c) Remote phosphor distribution ((a) and (b) adopted from Goetz, 2003; (c) after Kim *et al.*, 2005).

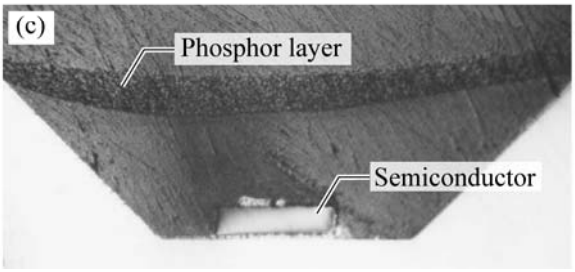

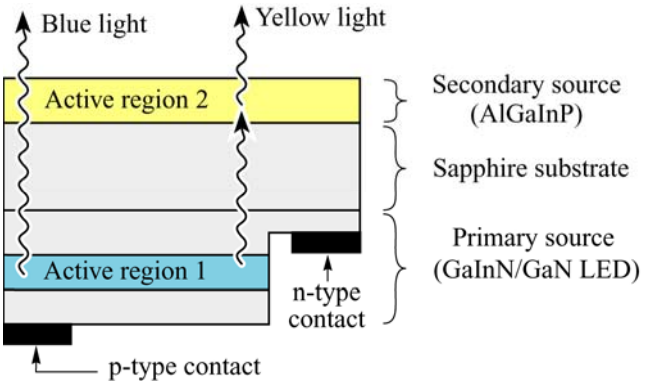

Fig. 21.12. Schematic structure of a photon-recycling semiconductor LED with one current-injected active region (Active region 1) and one optically excited active region (Active region 2) (after Guo *et al.*, 1999).

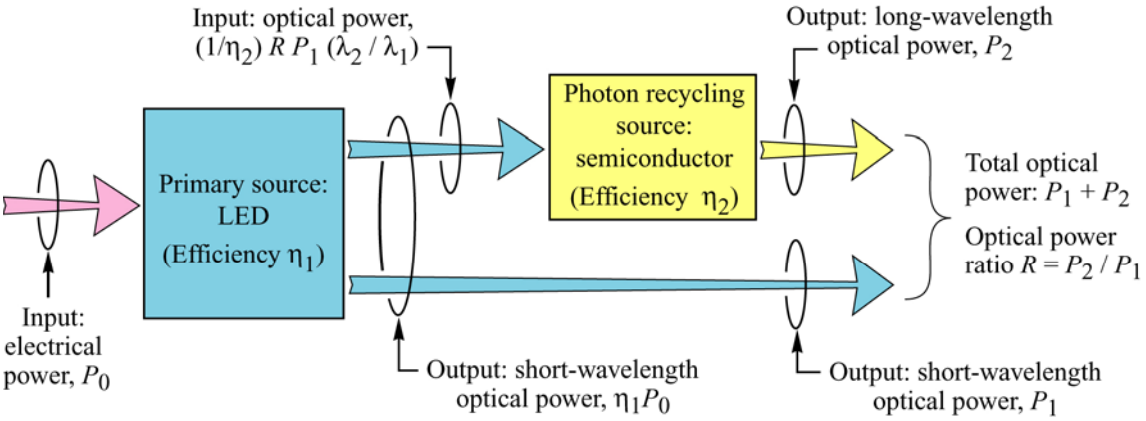

Fig. 21.13. Photon-recycling semiconductor LED power budget with electrical input power P_0 and optical output power P_1 and P_2.

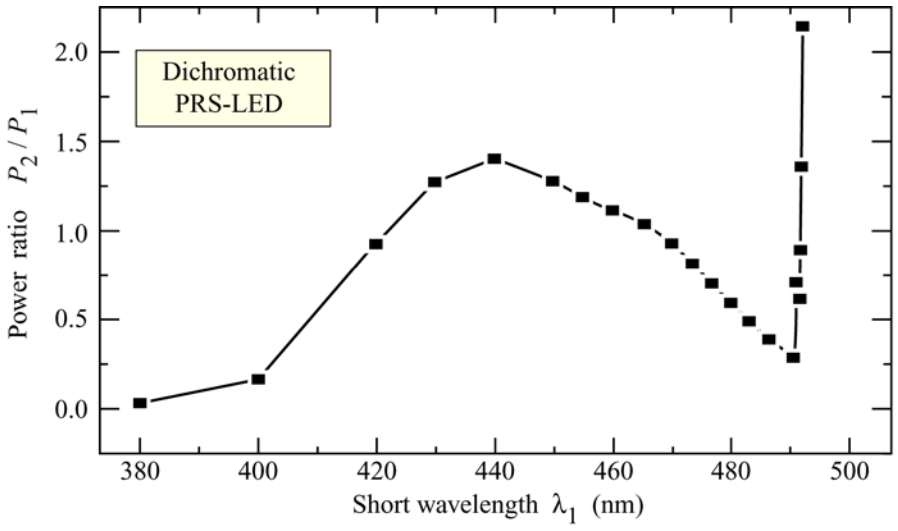

Fig. 21.14. Calculated power ratio between the two optical output powers P_1 and P_2 required to obtain white light emission (after Guo *et al*., 1999).

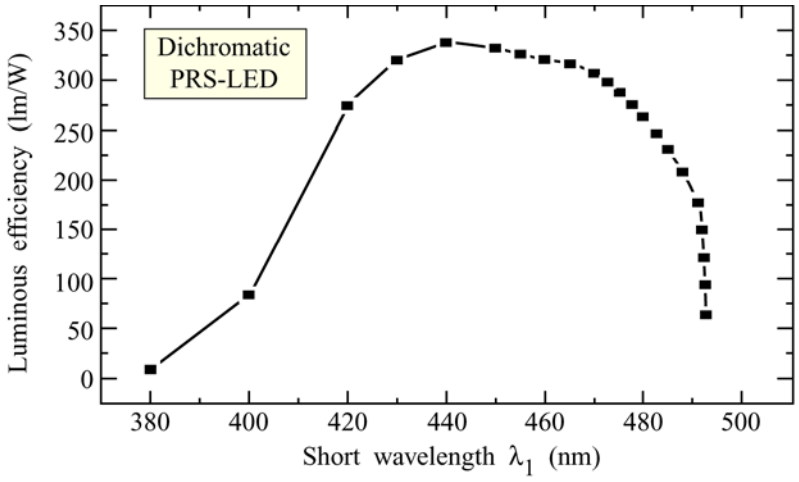

Fig. 21.15. Calculated luminous efficiency of a dichromatic PRS-LED versus its primary emission wavelength (after Guo *et al*., 1999).

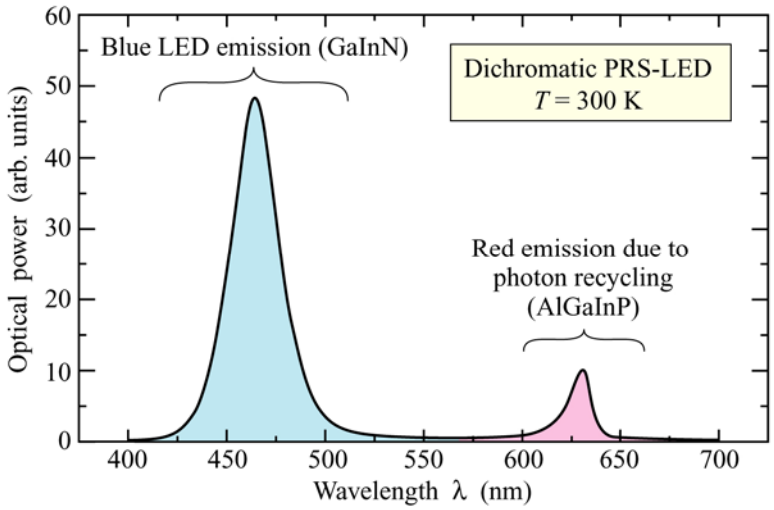

Fig. 21.16. Emission spectrum of dichromatic PRS-LED with current-injected GaInN blue LED primary source and AlGaInP photon recycling wafer (secondary source) emitting in the red (after Guo *et al*., 2000).

(a) ***Step-index multimode fiber***
Simple coupling; large modal dispersion

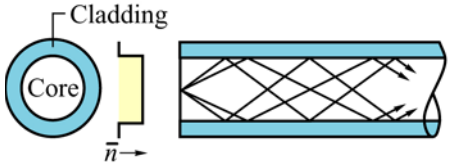

Typical diameters and refractive indices

Core/cladding diameter	62.5/125, 100/140, ... , 1000/1200 µm
Core index	1.45
Index difference	1 % – 2 %

(b) ***Parabolically-graded-index multimode fiber***
Simple coupling; difficult fabrication; low or zero modal dispersion

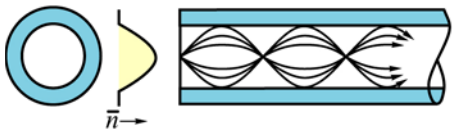

Core/cladding diameter	50/125, 62.5/125, 85/125
Core index at center	1.45
Index difference	1 % – 2 % in graded index profile

(c) ***Step-index single-mode fiber***
Difficult coupling; difficult fabrication; no modal dispersion

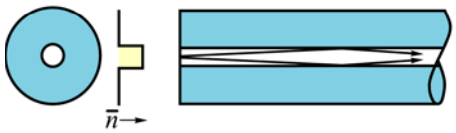

Core/cladding diameter	9/125
Core index	1.45
Index difference	1 % – 2 %

Fig. 22.1. (a) Step-index multimode fibers allow for the propagation of several optical modes. (b) Parabolically graded-index multimode fibers allow for the propagation of several modes with similar propagation constant. Graded-index multimode fibers have a lower modal dispersion than step-index multimode fibers. (c) Step-index single-mode fibers have a small core diameter and no modal dispersion.

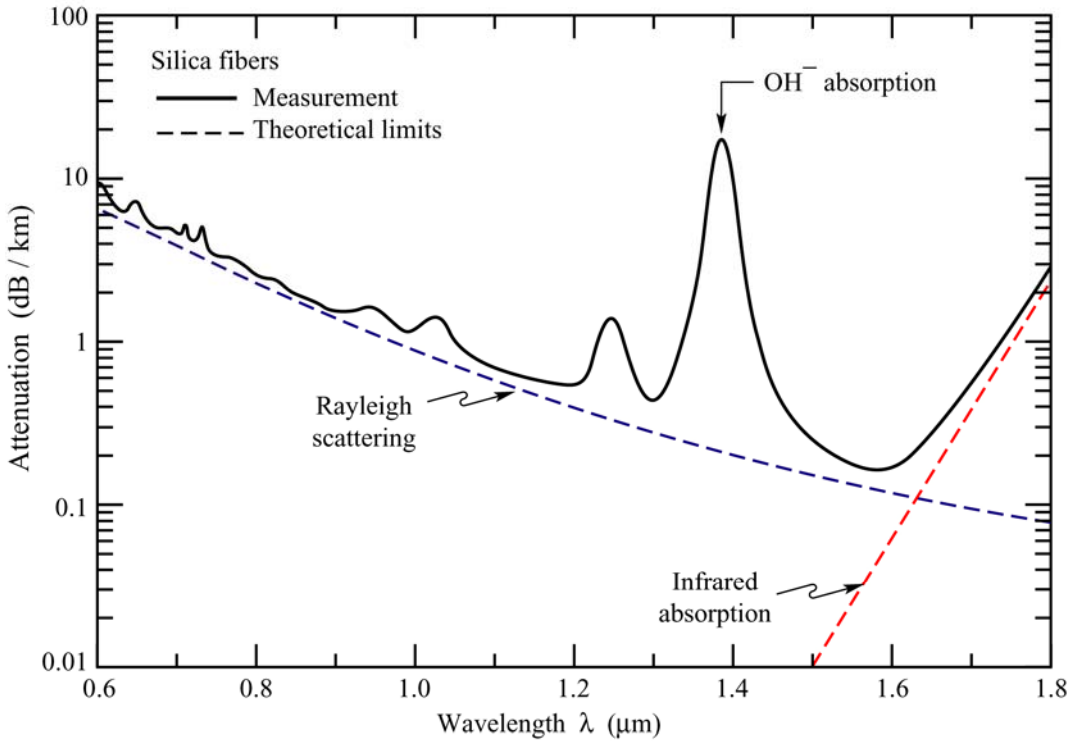

Fig. 22.2. Measured attenuation in silica fibers (solid line) and theoretical limits (dashed lines) given by Rayleigh scattering in the short-wavelength region, and by molecular vibrations (infrared absorption) in the infrared spectral region.

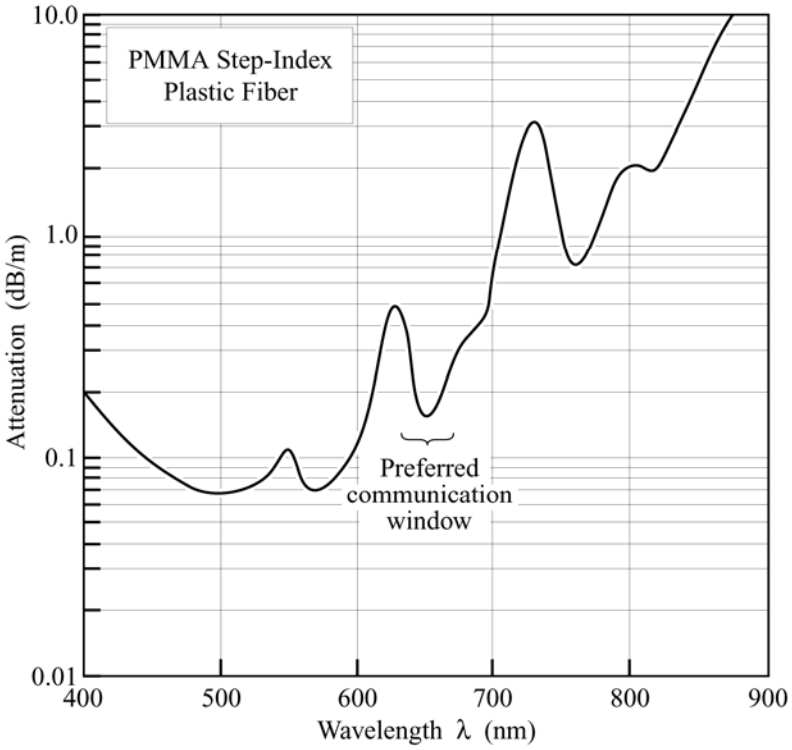

Fig. 22.3. Attenuation of a PMMA step-index plastic optical fiber. At 650 nm, the preferred communication wavelength, the attenuation is about 150 dB/km (after data sheet of Toray Industries Ltd., 2002).

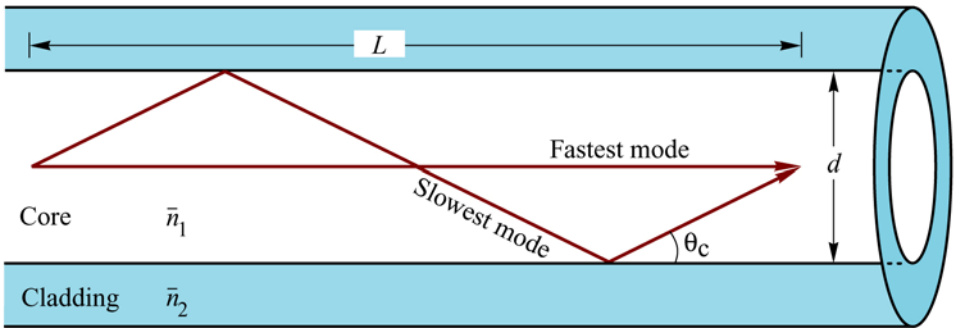

Fig. 22.4. Geometry used for calculation of the modal dispersion in a multimode fiber waveguide.

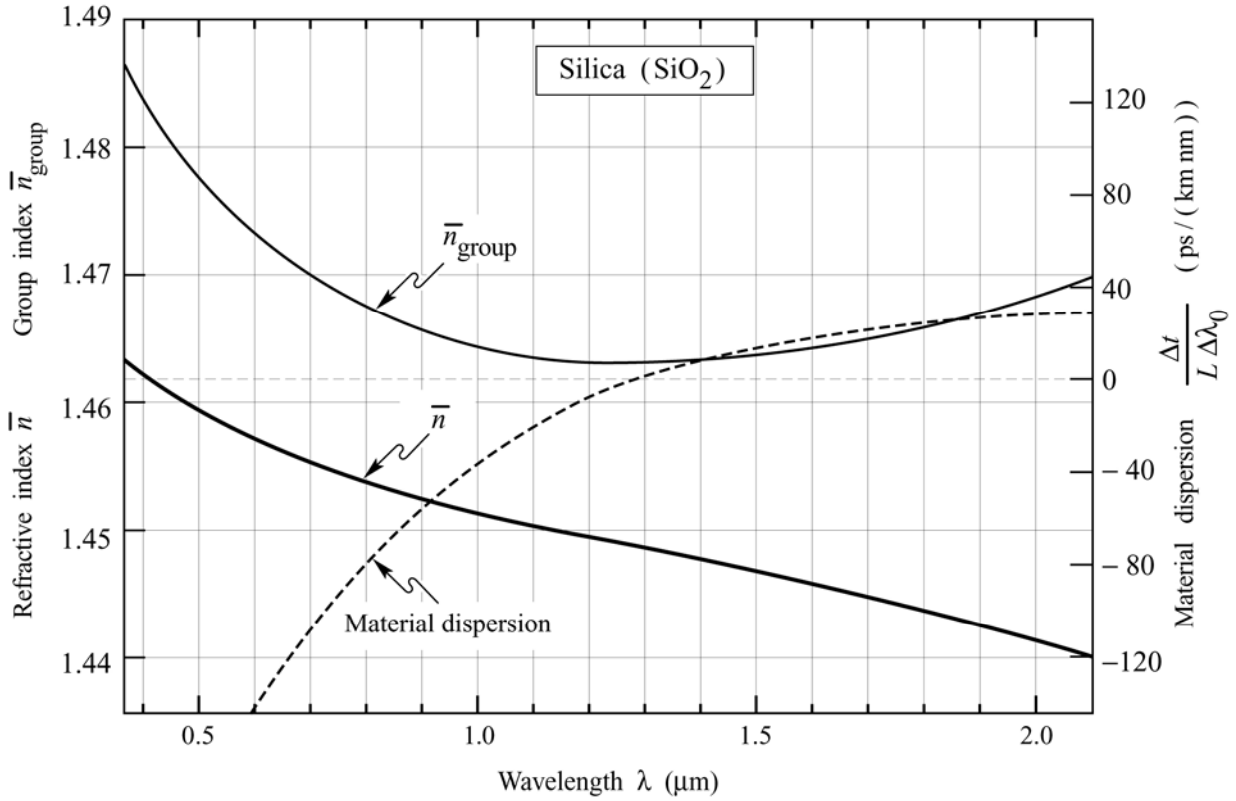

Fig. 22.5. Refractive index, group index, and material dispersion of a silica fibers for an optical signal spectral width $\Delta\lambda_0$ in vacuum. The material dispersion of regular silica fibers is zero at $\lambda = 1.3$ μm.

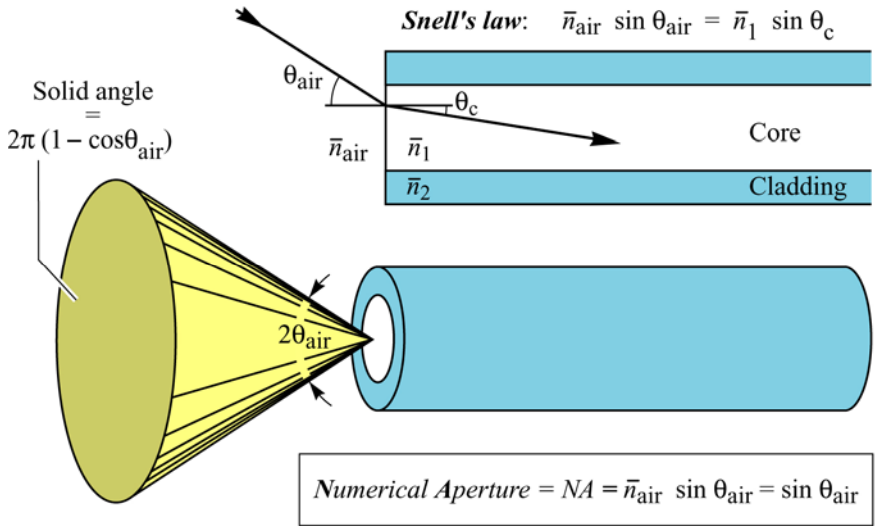

Fig. 22.6. Illustration of the *numerical aperture* (*NA*) of a fiber. For example, the light acceptance angle in air is $\theta_{air} = 11.5°$ for a numerical aperture of $NA = 0.2$.

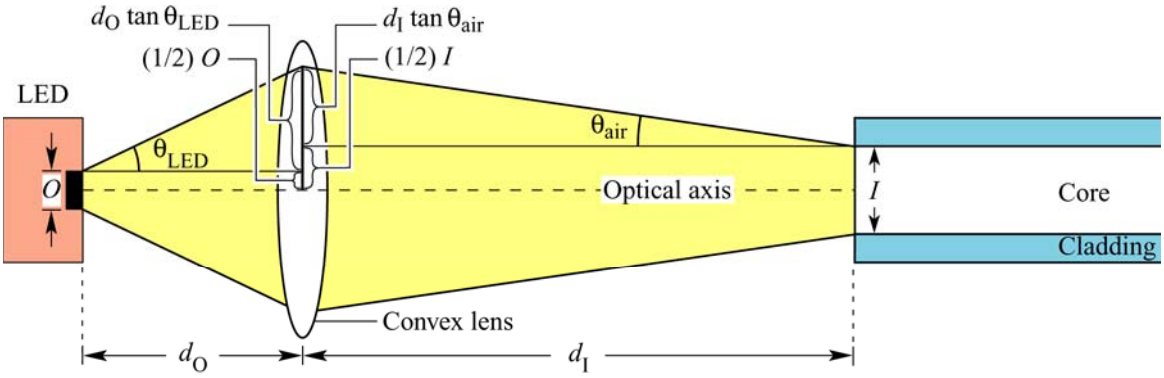

Fig. 22.7. Schematic illustration of coupling with a lens by imaging the light-emitting region of an LED onto the core of an optical fiber. The LED has a circular emission region with diameter O (Object). The emission region is imaged onto the fiber core with diameter I (Image) using a convex lens with focal length f.

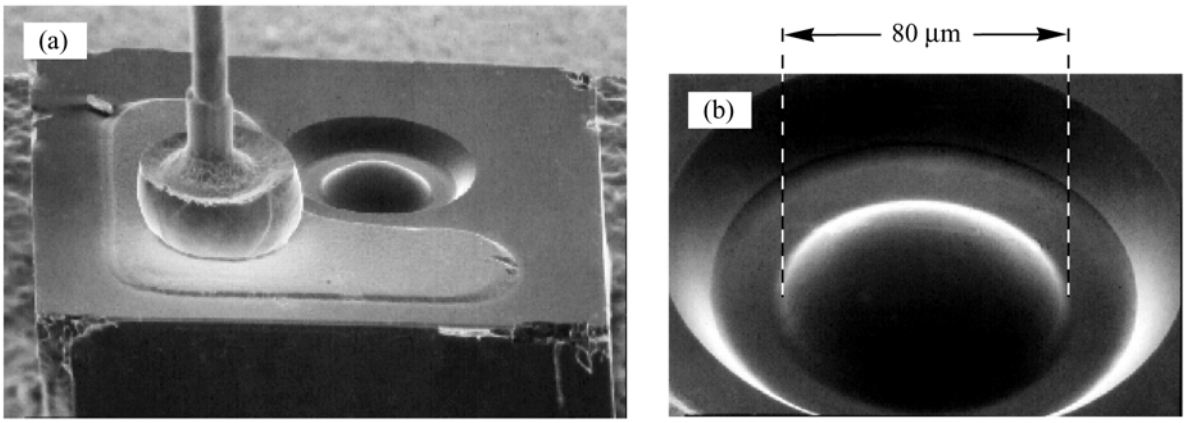

Fig. 22.8. (a) Commercial communication LED chip with integrated lens. (b) Detailed picture of the lens etched by a photochemical process into the GaAs substrate (AT&T ODL procuct line, 1995).

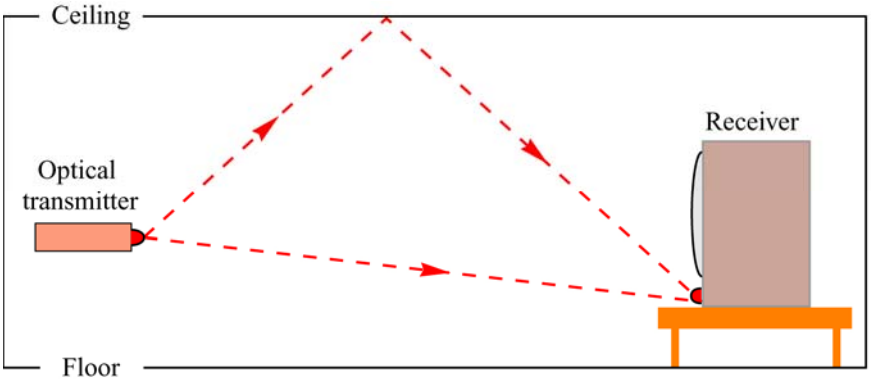

Fig. 22.9. Illustration of multipath distortion of a free-space optical signal, which limits the maximun data rate of the signal.

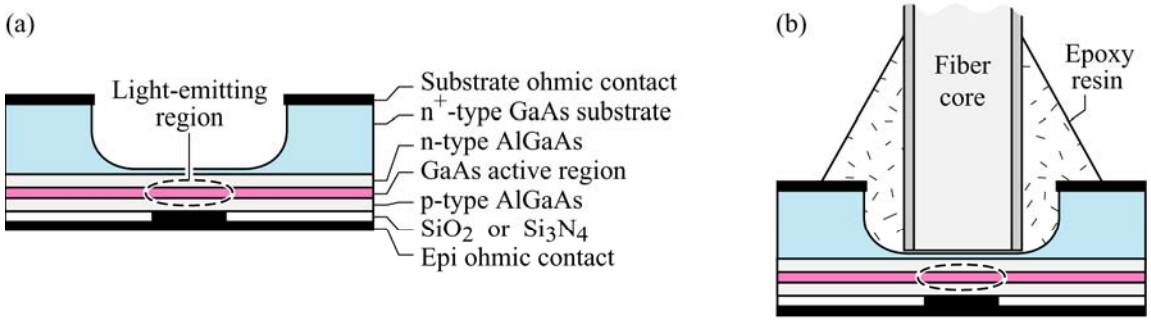

Fig. 23.1. (a) Burrus-type $Al_xGa_{1-x}As/GaAs$ DH LED with the opaque GaAs substrate removed above the active region by wet chemical etching. The Burrus-type LED is mounted substrate-side up. (b) Optical fiber coupled to a Burrus-type LED.

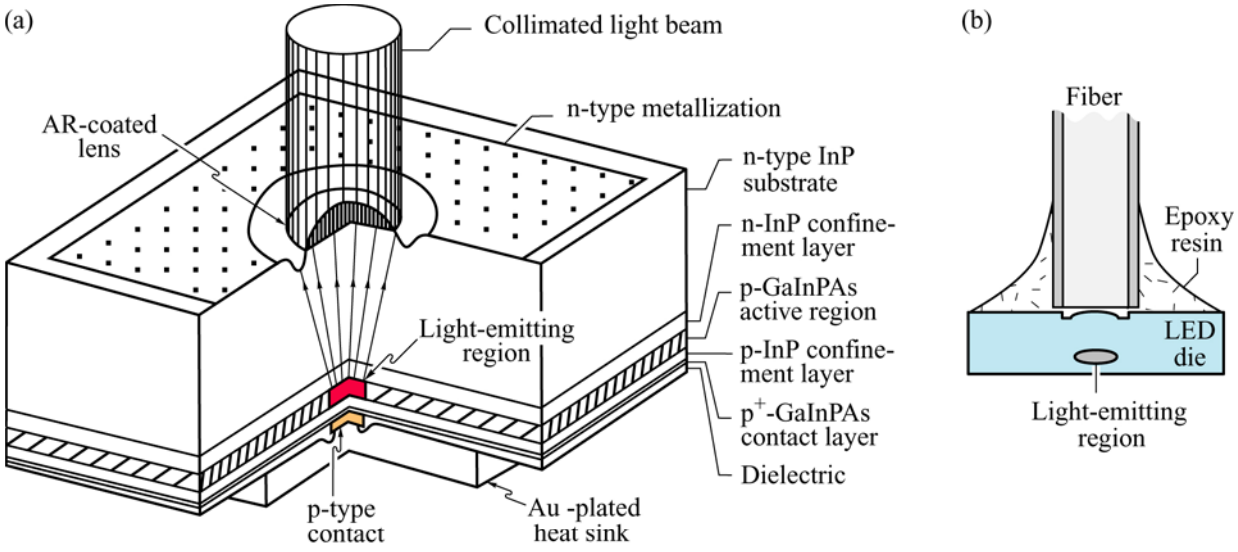

Fig. 23.2. (a) Structure of a communication LED emitting at 1300 nm with a GaInPAs active region lattice-matched to InP. The light generated in the active region is transmitted through the transparent InP substrate. The lateral dimension of the light-emitting region is defined by current injection under the circular ohmic contact with a diameter of 20 μm. An anti-reflection-coated (AR) lens, etched into the substrate, collimates the light beam. (b)Illustration of LED-to-fiber coupling using epoxy resin.

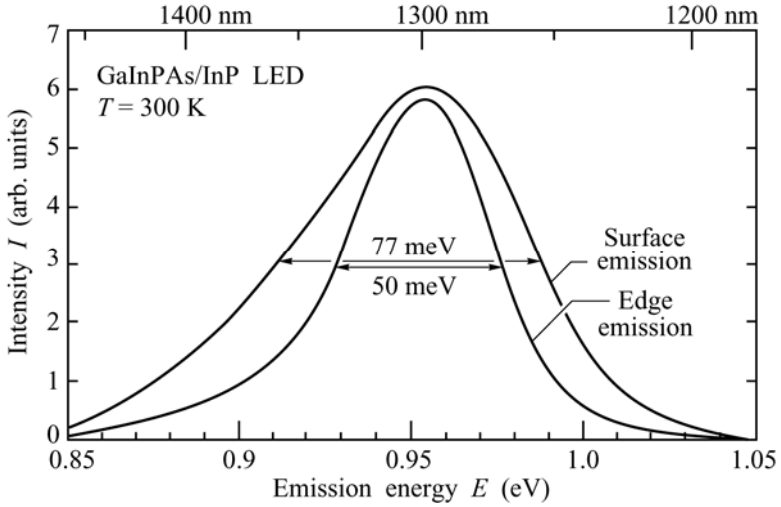

Fig. 23.3. Emission spectrum along the edge and surface of GaInPAs/InP communication LED emitting at 1300 nm. The spectrum emitted along the edge of the LED is narrower due to self-absorption.

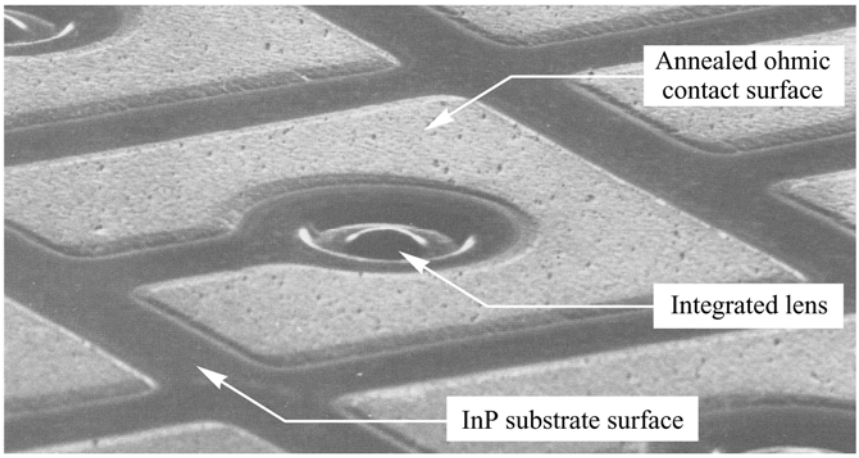

Fig. 23.4. GaInPAs communication LED grown on an InP wafer. The LED has an integrated semiconductor lens. The ohmic contact metal surface has a textured appearance due to the annealing process (after Ostermeyer *et al.*, 1983).

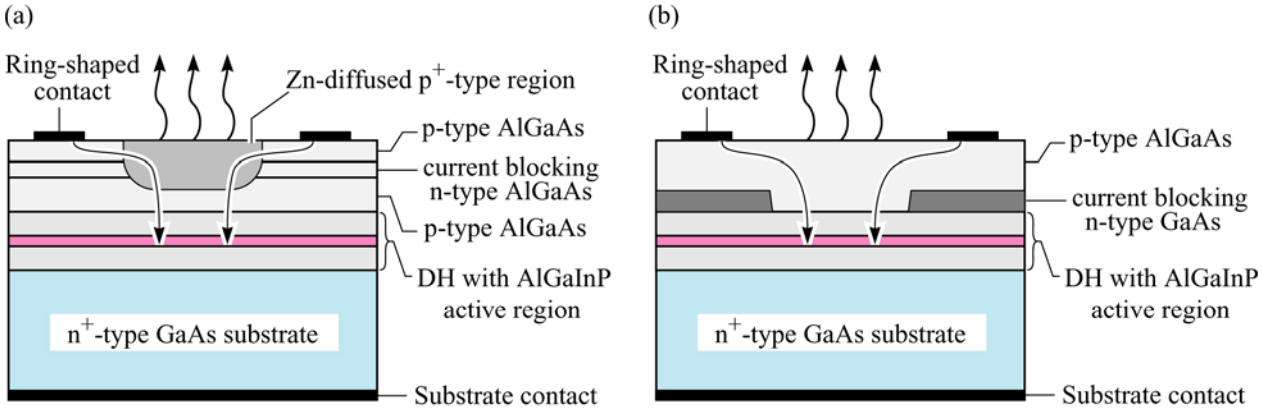

Fig. 23.5. AlGaInP/GaAs LED structures emitting at 650 nm for plastic optical fiber communications. Both LED structures funnel the current to the center of the active region where the emitted light is not obstructed by the top metal contact ring. (a) Structure using an n-type AlGaAs current blocking layer and a p^+-type diffusion region. (b) Structure fabricated by epitaxial regrowth using an n-type GaAs current blocking layer.

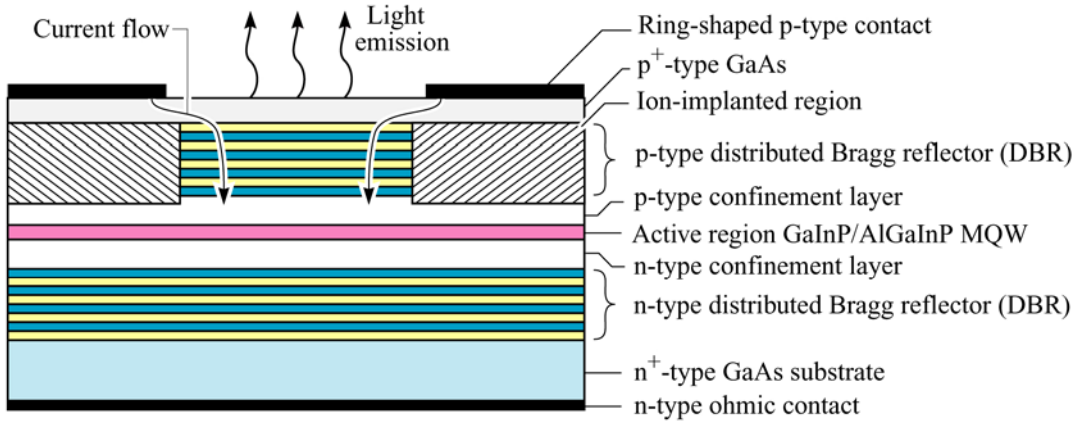

Fig. 23.6. RCLED emitting at 650 nm. Two distributed Bragg reflectors (DBRs) form the cavity. The active region is a GaInP/AlGaInP multiple-quantum well structure (after Whitaker, 1999).

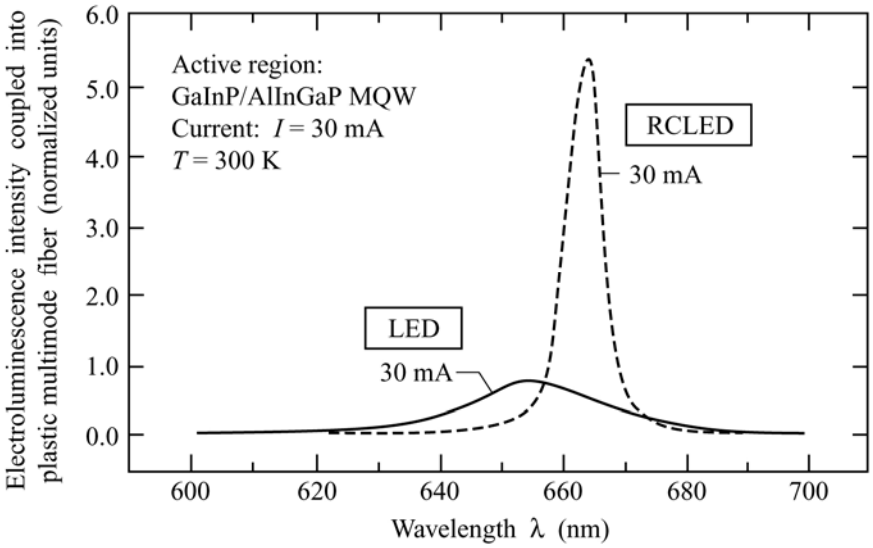

Fig. 23.7. Fiber-coupled ($NA = 0.275$) emission spectrum of RCLED and conventional LED at injection current of 30 mA. The microcavity effect of the RCLED enhances the emission intensity and reduces the emission linewidth, especially for low NA fibers (after Whitaker, 1999).

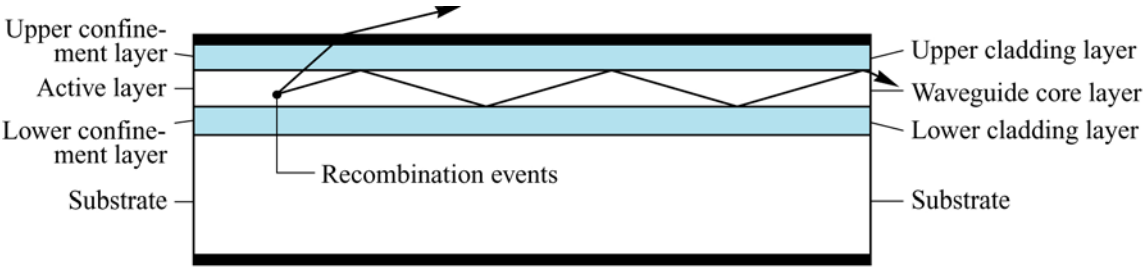

Fig. 23.8. Waveguide geometry showing guided light rays in the core layer with low angles of incidence.

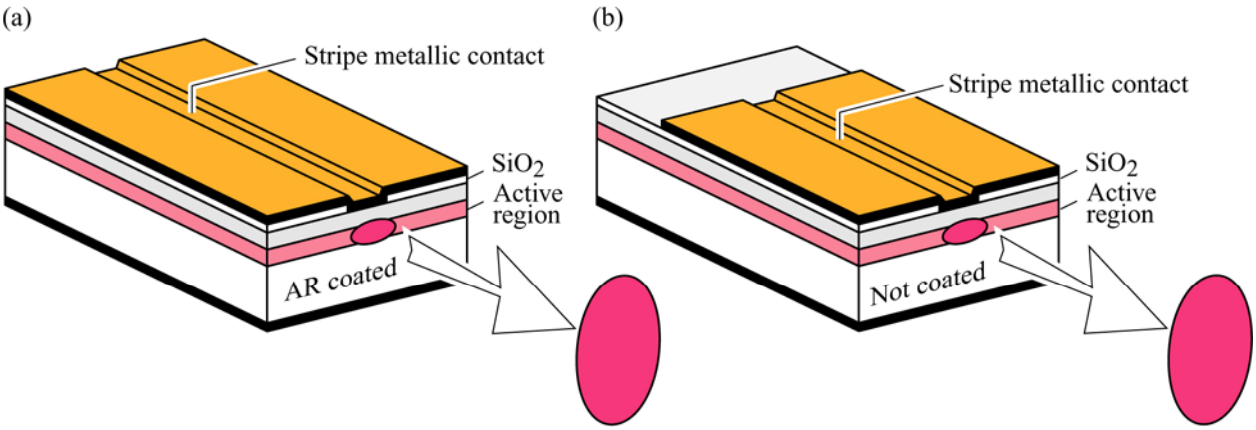

Fig. 23.9. Common structures of superluminescent diodes (SLDs). (a) SLD with cleaved facets coated with anti-reflection (AR) coatings. (b) SLD with cleaved, reflecting facets and stripe contact injecting current over the partial length of the device.

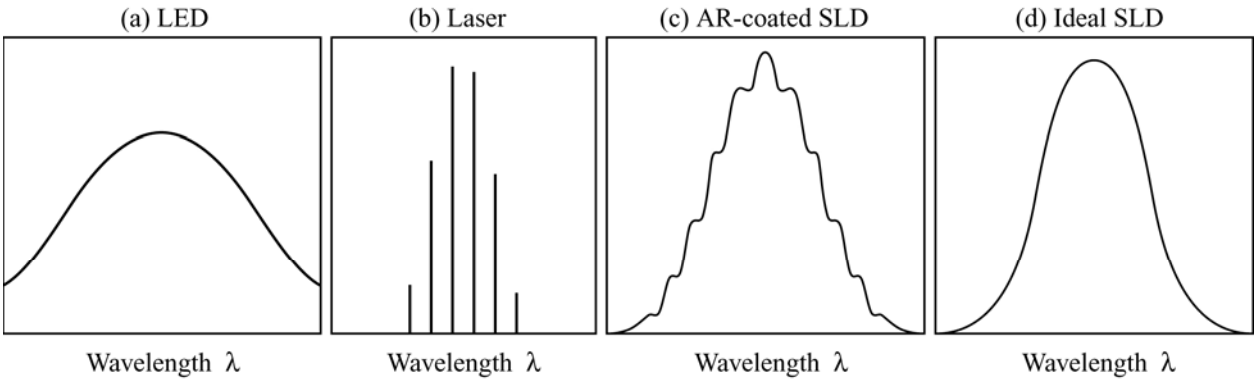

Fig. 23.10. Spectrum of (a) regular LED with a theoretical linewidth of 1.8 *kT,* (b) multimode semiconductor laser, (c) superluminescent diode (SLD) fabricated by AR coating of a multimode laser, (d) ideal SLD with linewidth less than *kT* (after Liu, 2000).

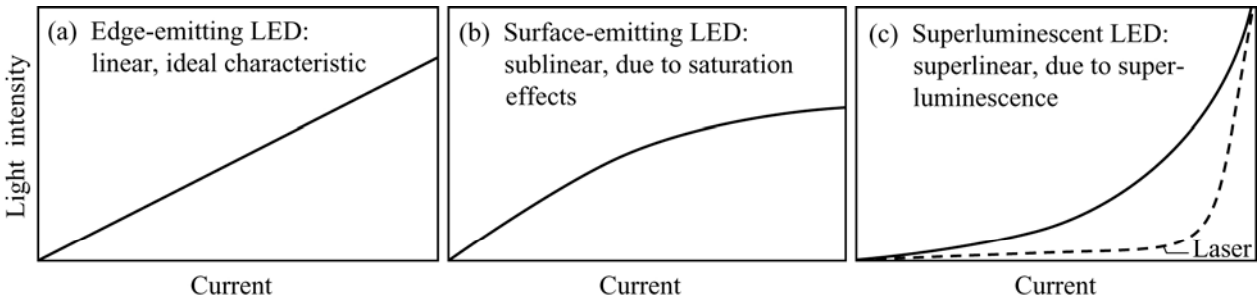

Fig. 23.11. Light-versus-current (*L–I*) characteristic of different LEDs. (a) Edge-emitting LED with little or no saturation effects. (b) Surface-emitting LED with small active area exhibiting saturation effects due to carrier overflow. (c) Superluminescent LED. Also shown is the *L–I* characteristic of a laser that exhibits a distinct threshold current.

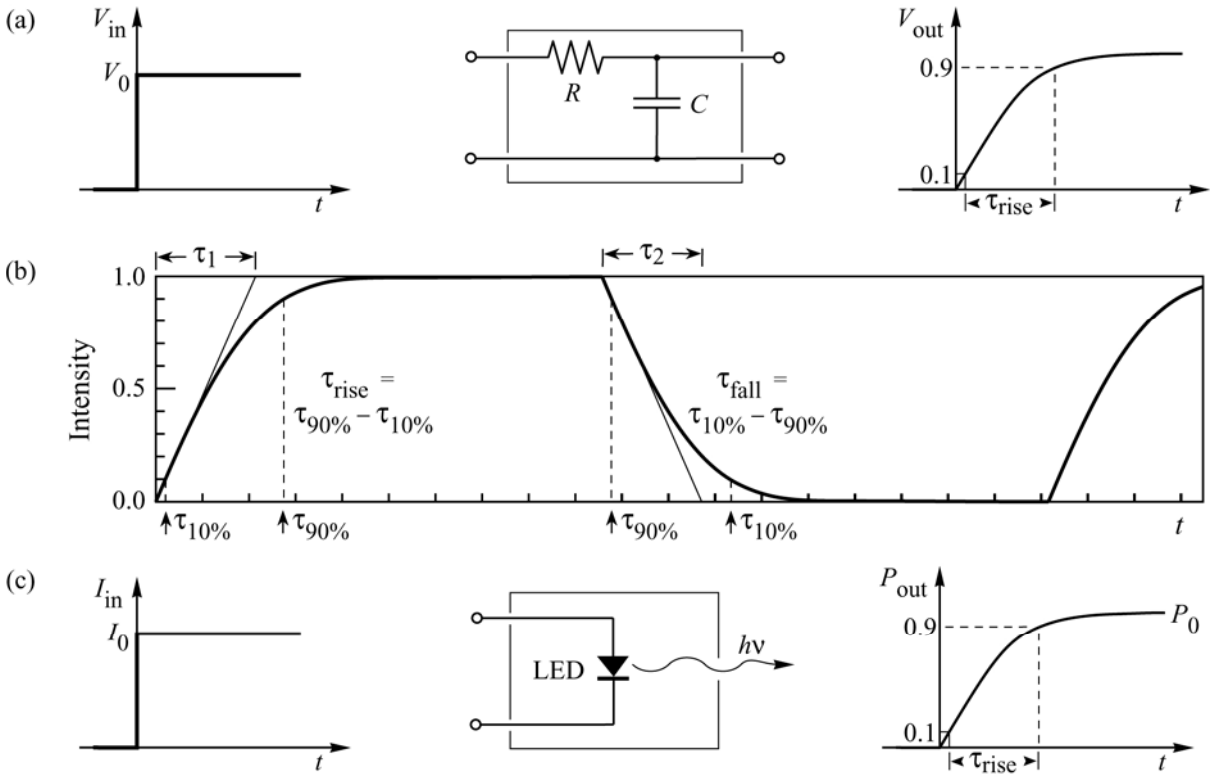

Fig. 24.1. (a) Illustration of the system response of a linear RC system with rise time τ_r. (b) Rise and fall time of a signal with an exponential time dependence and the time constants τ_1 and τ_2. (c) Illustration of the light output power as a function of time for an LED with a rise time of τ_r.

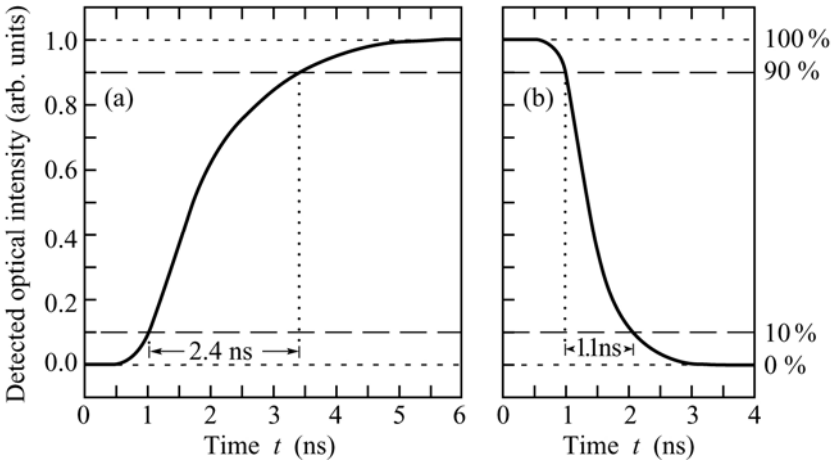

RCLED $T = 300$ K
$V_{on} = 1.4$ V $V_{off} = 0.0$ V
$f_{3dB} = 490$ MHz

Fig. 24.2. Measured (a) rise time (τ_{rise} = 2.4 ns) and (b) fall time (τ_{fall} = 1.1 ns) of an RCLED. The photodetector used in the measurement is much faster than the LED, so that the measured times are essentially the rise and fall times of the LED.

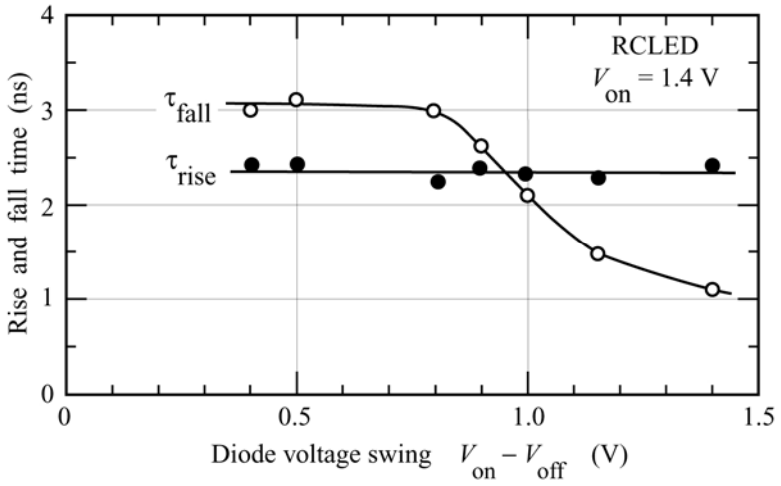

Fig. 24.3. Rise time and fall times as a function of the voltage swing. The fall time of the diode decreases with increasing voltage swing due to sweep-out of carriers out of the active region.

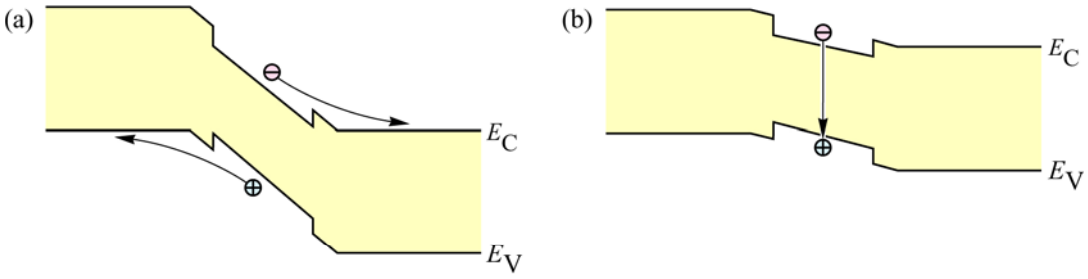

Fig. 24.4. Illustration of two mechanisms determining the fall time. (a) Return to zero bias results in carrier sweep-out of the active region. The sweep-out time can be very short, << 1 ns. (b) If the modulating voltage amplitude is smaller, carriers are *not* swept out of the active region, so that the intensity decay is determined by the spontaneous recombination lifetime.

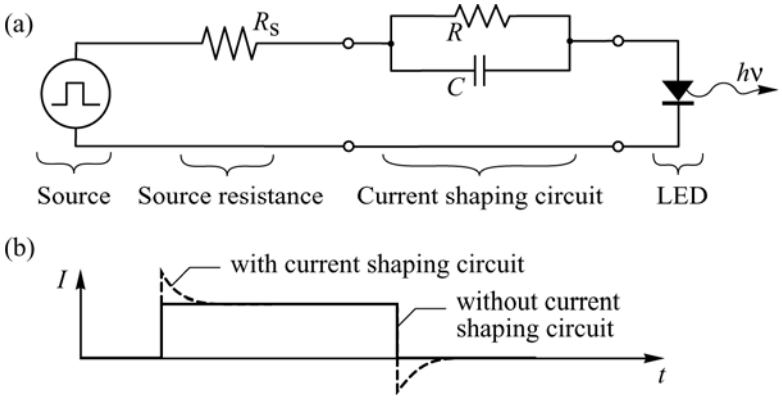

Fig. 24.5. (a) Illustration of an RC "current-shaping circuit" used to decrease the rise time of LEDs. (b) Diode current pulse versus time in the limit of small diode capacitance (solid line) and effect of current shaping circuit on diode current (dashed line).

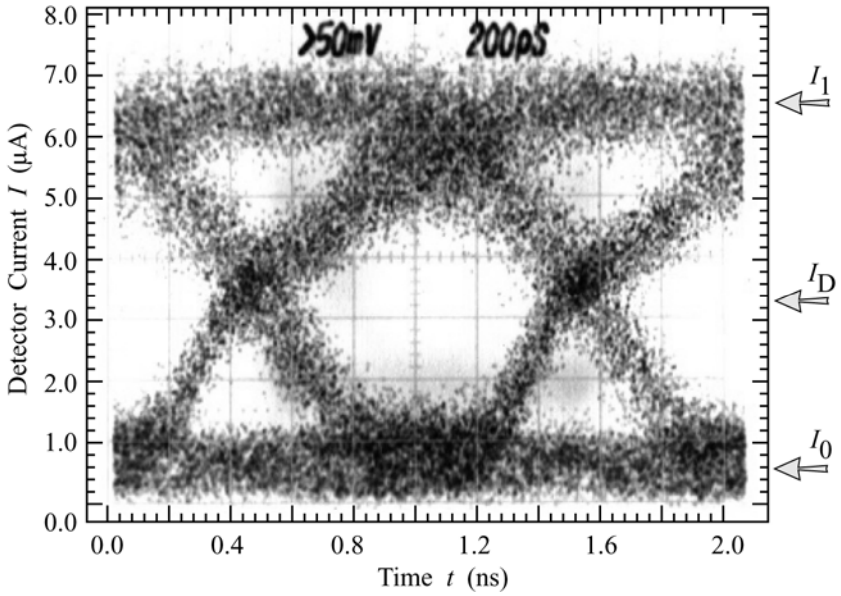

Fig. 24.6. "Eye diagram" of the received optical signal of an RCLED. The optical signal is measured as the photocurrent of a Si photodiode measured with a sampling oscilloscope. The data rate of the RCLED is 622 Mbit/s. Also indicated are the three current levels for the "0" state (I_0), "1" state (I_1), and decision current (I_D).

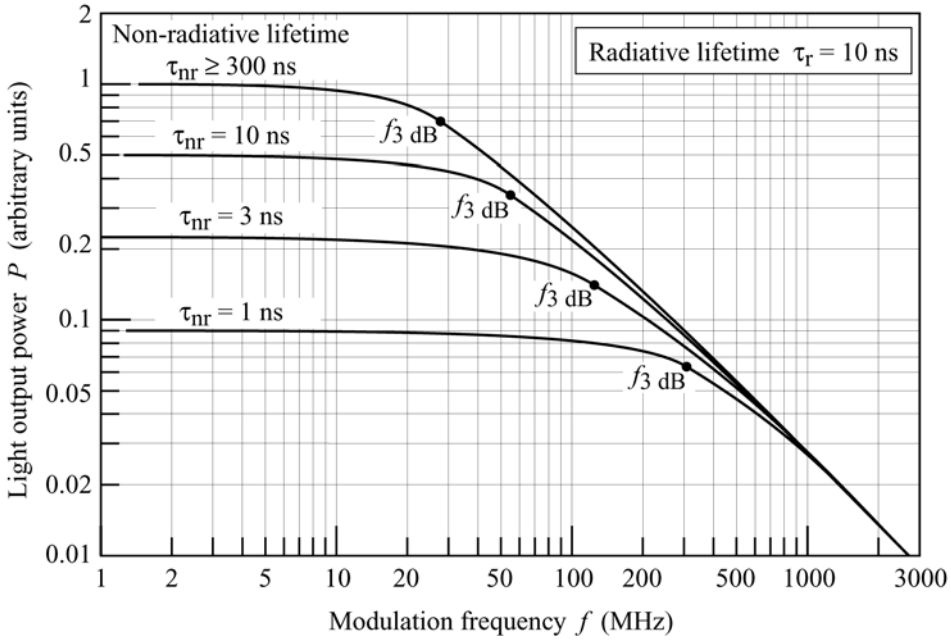

Fig. 24.7. Calculated LED output power versus modulation frequency for different values of the nonradiative lifetime. A radiative lifetime of 10 ns is assumed.